



UNIVERSIDADE D
COIMBRA

Daniela Vanessa Rosendo Lopes

**ELECTROCHEMICAL REDUCTION OF
IRON OXIDES INTO ZERO-VALENT IRON
FOR RED MUD VALORISATION**

Doctoral Thesis of the Doctoral Program in Advanced Materials and Processing, supervised by Professor Doctor Margarida João de Quina, Professor Doctor Jorge Ribeiro Frade and Doctor Andrei Kovalevsky (Kavaleuski) and submitted to the Department of Mechanical Engineering, Faculty of Sciences and Technology of the University of Coimbra

May 2020

Department of Mechanical Engineering, University of Coimbra

Electrochemical reduction of iron oxides into zero-valent iron for red mud valorisation

Daniela Vanessa Rosendo Lopes

Doctoral Thesis of the Doctoral Program on Advanced Materials and Processing

Supervisors:

Professor Doctor Margarida Maria João de Quina, University of Coimbra

Professor Doctor Jorge Ribeiro Frade, University of Aveiro

Doctor Andrei Kovalevsky (Kavaleuski), University of Aveiro

Funding: Fundação para a Ciência e a Tecnologia (Grant PD/BD/114106/2015)

May 2020



UNIVERSIDADE D
COIMBRA

Agradecimentos

Agradeço aos meus orientadores, Professora Doutora Margarida Quina, Professor Doutor Jorge Frade e Andrei Kovalevsky (Kavaleuski) pelo constante apoio, encorajamento, crescimento científico e orientação. À Professora Margarida, com quem tive a oportunidade de dar os meus primeiros passos na Ciência e que é desde há muitos anos um exemplo de motivação e de apoio. Ao Professor Jorge Frade pela sua confiança ao permitir que eu avançasse no mundo desconhecido, até então, da Engenharia dos Materiais e da Eletroquímica, e por me mostrar que há sempre uma maneira diferente de interpretar o que observamos. Ao Doutor Andrei Kovalevsky (Kavaleuski), que teve um papel fundamental no presente trabalho, e a quem agradeço a sua paciência, interessantes discussões e múltiplos ensinamentos que permitiram o meu crescimento científico.

Ao financiamento da Fundação para a Ciência e a Tecnologia (PD/BD/114106/2015) e do projeto SIDERWIN- DLV-768788 - Horizon 2020/SPIRE10, que permitiram a realização deste trabalho.

Aos Departamentos de Engenharia Química da Universidade de Coimbra e de Engenharia de Materiais e Cerâmica da Universidade de Aveiro pelas suas infraestruturas, assim como aos seus Técnicos pelo apoio prestado ao longo dos anos. Em especial, ao Engenheiro Artur Sarabando do DEMaC, pelos ensinamentos e sugestões nos estudos de Difração de Raio-X, e pelas inúmeras análises e repetições.

Aos colegas de laboratório do DEMaC pelo bom ambiente que ultrapassa o local de trabalho, nomeadamente ao Kiryl, Blanca, Inês, Miguel, Maksim e Eduardo pela troca de conhecimentos, sugestões e apoio.

Aos que são insubstituíveis e que estão sempre comigo em todos os momentos, em especial o Jorge. Não poderia deixar de agradecer também à Capoeira, por enriquecer o meu dia e me libertar a mente.

Por último, aos meus Pais e Irmão por acreditarem sempre em mim e me fazerem a pessoa que sou. À Vó e ao Vô que estão muito longe, mas que fazem parte de mim.

A todos o meu sincero agradecimento por terem caminhado ao meu lado até aqui.

This Page Intentionally Left Blank

Abstract

Electrolytic methods such as the electrochemical reduction of iron oxides from its ores in alkaline medium have been investigated as an alternative carbon-lean technology for iron and steel production. Besides, the Fe⁰ production by this route arises as a promising possibility for the iron-recovery from iron-rich wastes. The present Ph.D. thesis aims to assess the prospects for iron recovery from red mud, which is an industrial waste from the alumina production, by electrochemical methods.

In order to understand the fundamental aspects and minimize the unpredictable effects imposed by the complex chemical composition of the waste, most of the studies were performed using synthetic compositions mimicking the main components of the red mud. Highly-porous Fe_{2-x}Al_xO₃ ceramics with cellular microstructures were developed and tested for the bulk electrochemical reduction in alkaline conditions (10M NaOH, 90 °C). The efficiency of the iron reduction was assessed for different electrode concepts. Comparative studies were also performed for electroreduction of the suspensions in similar experimental conditions. The obtained Fe⁰ crystals were characterised based on combined XRD/SEM/EDS studies. The Faradaic efficiencies for the conversion to Fe⁰ were 70%, 55% and 32% for Fe₂O₃, Fe_{1.8}Al_{0.2}O₃, and Fe_{1.4}Al_{0.6}O₃, respectively, suggesting the decrease of the Faradaic efficiency with Al content. Red mud waste in powder was directly used for processing highly-porous ceramics by the emulsification of the waste suspension, aiming further electroreduction or catalytic and environmental remediation applications. Particular attention was given to the percolation in porous structures, affecting the electrochemical reduction rate and potential pollutant separation functionality. Corresponding cellular ceramics were characterised regarding their morphology, crystallography, permeability and surface charge. Successfully produced highly-porous microstructures (70 – 75%) demonstrated potential benefits for environmental applications. The first tests of the prepared red mud samples for phosphate adsorption in wastewater treatment revealed relatively low removal of phosphate (4 mg of phosphate/g from a 400 mg/L phosphate solution). However, the treatment can be substantially improved in the future by coupling adsorption with redox or catalytic reactions. Preliminary tests of the direct bulk electrochemical reduction of the cellular red-mud-based ceramics have demonstrated that slow electroreduction is feasible, but is significantly affected by the presence of insulating phases and phase inhomogeneities.

The obtained results demonstrate that the electrochemical reduction of iron oxides in alkaline medium is feasible when dealing with high iron content in the waste. Electrochemical methods can be directly applied for iron-rich waste valorisation, although additional pre-treatment may be required in the future to decrease the fraction of the low-conductive components.

Keywords: zero-valent iron; iron; electrochemical reduction; ceramic cathodes; iron waste; red mud.

This Page Intentionally Left Blank

Resumo

Os métodos eletrolíticos como a redução eletroquímica em meio alcalino de óxidos de ferro, a partir dos seus minérios, têm vindo a ser investigados como uma possível tecnologia limpa em carbono para a produção de ferro e aço. Para além disso, a produção de Fe^0 por esta via surge como uma alternativa interessante para a recuperação de ferro a partir de resíduos ricos neste elemento. A presente tese de Doutoramento tem como objetivo avaliar a possibilidade de recuperação do ferro presente em lamas vermelhas formadas na produção de alumina, recorrendo a métodos eletroquímicos.

Na perspetiva de compreender os aspetos fundamentais e minimizar os efeitos inesperados impostos pela composição química complexa do resíduo, a maioria dos estudos foram realizados com composições sintéticas para simular os componentes principais das lamas vermelhas. Cerâmicas altamente porosas de $\text{Fe}_{2-x}\text{Al}_x\text{O}_3$ com microestruturas celulares foram desenvolvidas e testadas para a redução eletroquímica em “bulk” (NaOH , 10 M a 90 °C). A eficiência da redução de ferro foi avaliada para diferentes configurações de eléctrodo. Estudos comparativos foram também realizados para a eletroredução de suspensões nas mesmas condições experimentais. Os cristais de Fe^0 foram caracterizados tendo por base estudos combinados de XRD/SEM/EDS. As eficiências Faradaicas para as conversões a Fe^0 foram de 70%, 55% e 32% para as composições de Fe_2O_3 , $\text{Fe}_{1.8}\text{Al}_{0.2}\text{O}_3$ e $\text{Fe}_{1.4}\text{Al}_{0.6}\text{O}_3$, respetivamente, sugerindo a diminuição da eficiência Faradaica com o teor de Al. A lama vermelha em pó foi usada para o processamento de cerâmicas altamente porosas pela emulsificação de suspensões do resíduo, com o objetivo de serem utilizadas para a eletroredução ou aplicações catalíticas e de remediação ambiental. Uma atenção especial foi dada para promover a percolação em estruturas porosas, afetando a taxa de redução eletroquímica e a potencial funcionalidade de segregação de poluentes. As correspondentes cerâmicas celulares foram caracterizadas em relação à sua morfologia, cristalografia, permeabilidade e carga superficial. As estruturas altamente porosas foram bem-sucedidas (70 – 75%), demonstrando ter propriedades adequadas para serem usadas em aplicações ambientais. Os primeiros testes nas amostras preparadas a partir de lamas vermelhas foram realizados para a adsorção de fosfato em tratamento de águas residuais, mostrando baixos valores na remoção de fosfato (4 mg de fosfato/g em 400 mg/L de solução de fosfato). Contudo, o tratamento pode ser substancialmente melhorado no futuro ao acoplar reações de redução-oxidação ou catalíticas à adsorção. Estudos preliminares da redução eletroquímica direta em “bulk” da lama vermelha processada mostraram que a lenta eletroredução é possível, apesar de este processo ser significativamente limitado pela presença de fases isolantes e de fases heterogéneas.

Os resultados obtidos demonstraram que a redução eletroquímica de óxidos de ferro em meio alcalino é eficaz aquando o uso de resíduos com alto teor em ferro. Os métodos eletroquímicos podem ser diretamente aplicados para a valorização de resíduos ricos em ferro, apesar de poder ser necessário um pré-tratamento adicional do resíduo para diminuir a fração de componentes de baixa condutividade.

Palavras-chave: ferro zero-valente; ferro; redução eletroquímica; cátodos cerâmicos; resíduos de ferro; lamas vermelhas.

This Page Intentionally Left Blank

List of contents

Abstract	iii
Resumo	v
List of tables	ix
List of figures	xi
Acronyms	xv
1. Introduction	1
1.1. Scope and objectives of the Thesis.....	4
1.2. Thesis structure	4
1.3. References	5
2. Literature review.....	9
2.1. Electrolytic processes for iron reduction	9
2.1.1. Electroplating in acidic baths.....	9
2.1.2. Molten oxides electrolysis (MOE)	11
2.1.3. Molten salts electrolysis	13
2.1.4. Electrolysis in alkaline aqueous solutions	15
2.2. Electroreduction of iron oxides in alkaline medium: mechanisms of reduction and operation conditions	16
2.2.1. Electrochemical reduction in suspension.....	16
2.2.2. Electrochemical reduction in bulk	23
2.2.3. Challenges and hydrogen evolution reaction.....	32
2.2.4. Design of the electrochemical cell and future industrial applications	36
2.3. Red mud: an overview and related trends.....	38
2.3.1. Sources and environmental concerns.....	39
2.3.2. The phase composition and general chemistry of the red mud.....	40
2.3.3. Current trends of red mud utilization.....	41
2.4. Concluding remarks and outlook of using red mud waste as an iron-source for the electroreduction processes	43
2.5. References	46
3. Processing of highly-porous cellular iron oxide-based ceramics by emulsification of ceramic suspensions	57
3.1. Introduction	58
3.2. Experimental procedure	59
3.3. Results and discussion	62
3.4. Conclusions.....	68
3.5. References	69

4. Electrochemical reduction of hematite-based ceramics in alkaline medium: Challenges in electrode design.....	73
4.1. Introduction.....	74
4.2. Experimental procedure.....	75
4.3. Results and discussion.....	77
4.3.1. Electrochemical behaviour of $\text{Fe}_{1.8}\text{Al}_{0.2}\text{O}_3$ electrode: general aspects.....	77
4.3.2. Nickel-foil supported configuration.....	80
4.3.3. Ag-modified nickel-foil supported configuration.....	84
4.3.4. Nickel-mesh supported configuration.....	87
4.4. Conclusions.....	88
4.5. References.....	89
5. Electrochemical deposition of zero-valent iron from alkaline ceramic suspensions of $\text{Fe}_{2-x}\text{Al}_x\text{O}_3$ for iron valorisation.....	93
5.1. Introduction.....	94
5.2. Experimental procedure.....	95
5.3. Results and discussion.....	96
5.3.1. Structural and microstructural studies of ceramics and powdered samples.....	96
5.3.2. Electrochemical reduction to ZVI.....	99
5.3.3. Conclusions.....	107
5.3.4. References.....	108
6. Direct processing and electroreduction of cellular red-mud-based ceramics for environmental applications.....	113
6.1. Introduction.....	114
6.2. Experimental procedure.....	115
6.3. Results and discussion.....	117
6.3.1. Screening of paraffin-to-suspension ratio and firing temperatures towards microstructural cellular design.....	117
6.3.2. Microstructural development.....	118
6.3.3. Effects of processing conditions on microstructural features and percolation...	122
6.3.4. Phosphate removal from water – preliminary studies.....	127
6.3.5. Electrochemical reduction of the processed red mud in bulk – preliminary studies.....	130
6.4. Conclusions.....	134
6.5. References.....	135
7. General conclusions and forthcoming work.....	141

List of tables

Table 2.1. Overview of the common iron plating baths and its operational conditions, adapted from [5].	10
Table 2.2. General aspects of the researches conducted by molten oxides electrolysis processes.	12
Table 2.3. General aspects of works related to molten salts electrolysis.	14
Table 2.4. Operation conditions used during the Fe ⁰ electrodeposition from alkaline suspensions.	22
Table 2.5. Operation conditions and main results achieved for the electroreduction in bulk of iron oxides.	31
Table 2.6. General composition of red mud from different plants worldwide based on [92].	40
Table 2.7. Most common applications of red mud used in recent years.	42
Table 3.1. Open (x_o) and total porosities (x_t), average cellular cavity sizes (d), resistivity (R_s) and constriction factors (f_c) of Fe _{2-x} Al _x O ₃ and Fe _{3-y} Mg _y O ₄ ceramic materials fired at different temperatures.	67
Table 4.1. Electrode configurations studied.	77
Table 4.2. Results of fitting of the EIS data: the parameters of the equivalent circuit.	80
Table 5.1. Firing conditions and open porosities (x_o) of Fe _{2-x} Al _x O ₃ cellular ceramics.	97
Table 5.2. Onset potential (E_{on}); peak potential (E_p); decay potential (E_d); stored charge of the Fe ⁰ -deposition peak (Q_{Fe}) and estimated current density of hydrogen evolution at the decay potential ($j_{H2,on}$).	101
Table 6.1. Factors and levels used in Taguchi's planning: solid load (S), gelatine (G) and stirring time (t).	116
Table 6.2. L ₉ orthogonal array of Taguchi plan used to study the effects of the solid load of red mud (S), gelatine content (G) and stirring time (t) on the response variables: cellular cavities size (d), open porosity (x_o), linear roughness (R_z) and constriction factor (f_c). Additional experiments were performed with changes in firing temperature, while maintaining the other conditions of experiment E1, and changes in paraffin:suspension ratio, while maintaining conditions of E2.	123
Table 6.3. Correlation matrix of the effects of each factor studied (S, G, t) on the response variables (d, x_o , R_z , f_c) and the coefficient of determination (R^2) of the mathematical models.	125

This Page Intentionally Left Blank

List of figures

Fig. 1.1. Overview of the general steel and ironmaking process scheme [9].	2
Fig. 2.1. Electroplating cells, where several plates were used as cathodes and anodes [4].	10
Fig. 2.2. Liquid Fe ⁰ obtained after the molten oxide electrolysis [11].	13
Fig. 2.3. Pourbaix diagram of the Fe-H ₂ O system at 100 °C [45].	18
Fig. 2.4. (A) Voltammogram of the iron WE in a NaOH (10 M, 90 °C), before (dashed line) and after (solid line) of the addition of 0.3 M of Fe ₂ O ₃ in [52]; (B) SEM image of typical Fe ⁰ deposits from the electrodeposition process in [48].	20
Fig. 2.5. Example of an electrochemical cell used for the electrochemical reduction in bulk [37].	23
Fig. 2.6. Evolution of the atomic crystalline structures during the reduction of α-Fe ₂ O ₃ to α-Fe, based in [60].	25
Fig. 2.7. Schematic model of the three-phase interlines (3PIs) during the electrochemical reduction of a solid-insulator material [66].	27
Fig. 2.8. Electroreduction process of a Fe ₂ O ₃ pellet in the alkaline solution: a typical current-time curve [64].	28
Fig. 2.9. Typical voltammograms curves from Fe ₂ O ₃ pellets recorded at 10 mV/s with (A) 44% of open porosity at 1 M NaOH solution at 25 °C (solid line) and 90 °C (dashed line); (B) 44% of open porosity at 10 M NaOH solution at 90 °C and with 64% of open porosity (inserted figure) at the same conditions, from [40].	30
Fig. 2.10. SEM micrographs of Fe ₂ O ₃ pellets with 44% of open porosity (A) before reduction; (B) and (C) after reduction, from [40].	31
Fig. 2.11. Simulated potential of the H ₂ evolution vs. Hg HgO (V) with temperature (°C) and concentration (mol/kg) of NaOH solution [82].	35
Fig. 2.12. Schematic representation of a typical electrochemical cell for the reduction of iron oxides, where: 1) working electrode (WE); 2) metallic current collector; 3) counter electrode (CE); 4) Luggin capillary; 5) teflon tube for the reference electrode support, filled with the electrolyte; 6) electrochemical Teflon/PTFE cell; 7) heating system, adapted from [40].	37
Fig. 2.13. Scheme of the proposed electrowinning route at the industrial scale [88].	38
Fig. 2.14. Dried red mud in a pond [98].	40
Fig. 2.15. Patented red mud applications from the year 1964 to 2008, based in [112].	41
Fig. 3.1. Representative example of impedance spectra showing de-convolution of the contribution at very high frequency (R _s) and the R ₁ C ₁ term with relaxation frequency close to 1 MHz.	61

Fig. 3.2. Dependence of microstructural contributions R_1 (triangles) and R_5 (closed circles) on open porosity. The results of R_5 for samples fired at highest temperature (1400 °C) are shown as large open circles to emphasize their deviation from the main trends of samples with better cellular microstructures.	61
Fig. 3.3. SEM microstructures of $Fe_{2-x}Al_xO_3$ ceramics obtained at various firing conditions: $Fe_{1.8}Al_{0.2}O_3$ (A, B); $Fe_{1.6}Al_{0.4}O_3$ (C, D) and $Fe_{1.4}Al_{0.6}O_3$ (E,F). The insets show the microstructural evolution in the individual cells (C,D) and EDS mapping results (E,F).	63
Fig. 3.4. SEM microstructures of $Fe_{2.3}Mg_{0.7}O_4$ cellular ceramics obtained at various firing conditions.....	64
Fig. 3.5. XRD patterns of $Fe_{1.8}Al_{0.2}O_3$ (A), $Fe_{1.6}Al_{0.4}O_3$ (B), $Fe_{1.4}Al_{0.6}O_3$ (C) and $Fe_{2.3}Mg_{0.7}O_4$ (D) fired at different temperatures.....	65
Fig. 3.6. $Fe_{1.8}Al_{0.2}O_3$ sample after firing at 1400 °C, showing thermally-induced cracks and defects.	67
Fig. 4.1. CV curves recorded with a scan rate of 10 mV/s for porous $Fe_{1.8}Al_{0.2}O_3$ (60% of open porosity) electrodes in 10 M NaOH at 90 °C in NF-F configuration before (A) and after (B) reduction at cathodic potential $E_{cath} = -1.10$ V.....	79
Fig. 4.2. Nyquist plots for non-reduced 60%-porous $Fe_{1.8}Al_{0.2}O_3$ sample ($t = 0$ h) and the same sample reduced during $t = 2.5$ h and $t = 5$ h at $E_{cath} = -1.10$ V (NF-F electrode configuration) at 90 °C in 10 M NaOH.	80
Fig. 4.3. Current vs. time curves at various cathodic potentials (-1.00 V, -1.05 V and -1.10 V) for 2.5 h (60% of open porosity).	81
Fig. 4.4. Current-time transients recorded for NF-F and NF-R configurations at $E_{cath} = -1.10$ V for 2.5 h (60% of open porosity).	82
Fig. 4.5. Post-mortem studies of the NF-R electrode (60% of open porosity, $E_{cath} = -1.10$ V, 5 h of reduction).	83
Fig. 4.6. Reduction of $Fe_{1.8}Al_{0.2}O_3$ electrode (37% of open porosity, 5 h), previously fired at 1300 °C, with $E_{cath} = -1.075$ V in different orientations towards CE: (A) NFAg-R and (B) NFAg-F; (C) XRD analysis of NFAg-R test; (D) pellet collapse during NFAg-F test.....	85
Fig. 4.7. Microstructural evolution after electroreduction of the electrode in NFAg-R configuration: (A) before reduction (37% of open porosity); (B) after 5 h of reduction (bulk of the electrode).	85
Fig. 4.8. Current-time transients obtained for dense $Fe_{1.8}Al_{0.2}O_3$ samples (3% of open porosity), $E_{cath} = -1.075$ V, in NFAg-R and NFAg-F electrode configuration.....	86
Fig. 4.9. SEM microstructures of dense $Fe_{1.8}Al_{0.2}O_3$ electrode in NFAg-R configuration (A) before reduction (3% of open porosity); and after reduction ($E_{cath} = -1.075$ V): (B) under the Ag layer near the Ni current collector; (C) cross-section starting from the current collector left to the ceramics bulk (right) (D) XRD pattern obtained for the whole ceramic electrode converted to powder.....	87
Fig. 4.10. (A) Current vs. time curves obtained for NMAg-R configuration at $E = -1.075$ V, using a dense electrode (3% of open porosity); (B) SEM images of the microstructural alteration in the cross-section of the electrode: at	

the surface beneath the Ag paste in the contact with Ni-mesh and electrolyte (left part) and structure without reduction (right part).....	88
Fig. 5.1. SEM images of the fractured cellular ceramics: (A) Fe_2O_3 (1100 °C), (B) $\text{Fe}_{1.8}\text{Al}_{0.2}\text{O}_3$ (1300 °C), (C) $\text{Fe}_{1.4}\text{Al}_{0.6}\text{O}_3$ (1300 °C); (D) corresponding XRD patterns.....	97
Fig. 5.2. Size distribution of the powder after crushing.....	98
Fig. 5.3. Powders of $\text{Fe}_{2-x}\text{Al}_x\text{O}_3$ processed ceramics after crushing (A) general view and (B) walls of a previous cavity cell.....	98
Fig. 5.4. Cyclic voltammetry performed at 0.01 V/s after Fe^0 deposition from Fe_2O_3 (black line) and $\text{Fe}_{1.4}\text{Al}_{0.6}\text{O}_3$ (red line). The insert image shows expanded scales of the main cathodic and anodic peaks.....	99
Fig. 5.5. Cyclic voltammograms of $\text{Fe}_{1.4}\text{Al}_{0.6}\text{O}_3$ suspensions at different scan rates. The shaded area represents the stored charge of the cathodic peak per unit area.....	101
Fig. 5.6. Current vs. time curves of Fe^0 electrodeposition from Fe_2O_3 , $\text{Fe}_{1.8}\text{Al}_{0.2}\text{O}_3$ and $\text{Fe}_{1.4}\text{Al}_{0.6}\text{O}_3$ suspensions at -1.08 V (90 °C, NaOH 10 M).....	102
Fig. 5.7. XRD patterns of Ni grids after Fe^0 deposition from Fe_2O_3 , $\text{Fe}_{1.8}\text{Al}_{0.2}\text{O}_3$ and $\text{Fe}_{1.4}\text{Al}_{0.6}\text{O}_3$ suspensions.	104
Fig. 5.8. Microstructural evolution of Fe^0 crystals deposited during (A) 20 min; (B), (C) and (D) 7 h of electroreduction of Fe_2O_3 -based suspensions, where (B) shows the Ni grid covered by Fe^0 crystals, while (C) represents a top view of Fe^0 crystals and (D) a side view.....	105
Fig. 5.9. SEM images of Fe^0 crystals after electrochemical reduction of suspensions containing (A) and (B) $\text{Fe}_{1.8}\text{Al}_{0.2}\text{O}_3$; (C) and (D) $\text{Fe}_{1.4}\text{Al}_{0.6}\text{O}_3$. Images (B) and (D) show EDS mappings.....	106
Fig. 6.1. Effects of paraffin:suspension volume ratio and firing temperatures on SEM microstructures for selected samples: (A) E2: p:s 1.5:1; G = 3.5%; t = 8 min; T = 1100 °C; (B) E13: p:s 0.5:1; G = 3.5%; t = 8 min; T = 1100 °C; (C) E11: p:s 1.5:1; G = 2%; t = 4 min; T = 1200 °C.....	117
Fig. 6.2. SEM micrographs of red mud-based ceramics fired at 1100 °C, paraffin:suspension volume ratio of 1.5:1, with different experimental conditions attending to the Taguchi plan: (A) E1: S = 45%, G = 2%, t = 4; (B) E3: S = 45%, G = 5%, t = 12; (C) E4: S = 50%, G = 2%, t = 8 min; (D) E5: S = 50%, G = 3.5%, t = 12 min; (E) E8: S = 55%, G = 3.5%, t = 4; (F) E9: S = 55%, G = 5%, t = 8.....	119
Fig. 6.3. (A) Flow and viscosity curves of the suspension (S) and (B) flow and viscosity curves for the emulsions from Taguchi plan, E1, and E3, for the red mud processing ceramics.....	120
Fig. 6.4. XRD diffractograms of initial red mud waste (RM_i), processed green samples after burn-out of the organic phase (500 °C) (G) and processed samples after firing (1100 °C and 1200 °C).....	121
Fig. 6.5. (A) Impedance spectra for E1 and E11, and (B) the corresponding alternative representation of Z' vs Z''/f , to obtain the fitting parameters for the “bi” contribution.....	124
Fig. 6.6. Zeta potential as a function of pH for the initial red mud waste (RM_i) and the processed red mud (PRM).	127

Fig. 6.7. Adsorption studies for 20 mg/L and 400 mg/L of phosphate solutions with RM, and PRM at pH 4 and 8: (A) Adsorption capacity of the adsorbents; (B) phosphate removal (%) after 6 h.	129
Fig. 6.8. Cyclic voltammograms of the EI– red-mud-based cathode before (black line) and after (red line) the electrochemical reduction (NaOH, 10 M at 90 °C).	131
Fig. 6.9. Current-density vs. time curves (replicates R1 and R2) of the processed red mud sample (EI) in 10M NaOH at 90 °C).....	132
Fig. 6.10. XRD pattern of the processed EI red mud pellet after the electroreduction.	133
Fig. 6.11. SEM microstructures of the processed EI red mud pellet after 20 h of electroreduction (NaOH, 10 M at 90°C): (A) destruction of the initial cellular cavities; (B) iron crystals; (C) iron crystals with higher magnification; (D) EDS mapping of the iron crystals observed in (B) and (C).....	134

Acronyms

BF	- blast furnace
BOF	- basic oxygen furnace
CE	- counter electrode
CNTs	- carbon nanotubes
CV	- cyclic-voltammetry
DRI	- direct reduced iron
EAF	- electric arc furnace
EDS	- energy dispersive X-ray spectroscopy
EIS	- electrochemical impedance spectroscopy
F.E.	- Faradaic efficiency
HER	- hydrogen evolution reaction
IEP	- isoelectric point
MOE	- molten oxides electrolysis
PTFE	- polytetrafluoroethylene
PRM	- processed red mud
RDE	- rotating disk electrodes
RE	- reference electrode
RIR	- reference intensity ratio
RM	- red mud
RM_i	- initial red mud
SEM	- scanning electron microscopy
TEA	- triethanolamine
WE	- working electrode
XRD	- x-ray diffraction
ZVI	- zero-valent iron
3PIs	- three-phase interlines
YSZ	- yttria-stabilized zirconia

This Page Intentionally Left Blank

I. Introduction

Iron and steel world production reached around 1.8 billion tons in 2018. The production is expected to grow over the years due to the strong impact of the iron and steelmaking industry on the development of the worldwide economy [1]. Thus, the demand for the extraction of quality iron ores continues to increase. Iron ores for the iron and steel production include hematite (Fe_2O_3), magnetite (Fe_3O_4), goethite (FeOOH) and siderite (FeCO_3) components. Higher-grade ores should have above 55% of the total iron content, and the more common ores are mainly rich in Fe_2O_3 and Fe_3O_4 , but fractions of SiO_2 , Al_2O_3 , MgO , CaO , TiO_2 , P_2O_5 , MnO , K_2O or Na_2O are also usually present [2,3].

The main iron and steel production route produces 70% of the total steel, consisting on the carbothermic reduction of the iron ores to liquid iron (“pig iron” or “hot metal”) by using iron ores as raw material combined with layers of limestone and coke (fuel) in blast furnaces (BF). The air inside the BF reacts with coke, producing heat and CO, which will act as a reducing agent for the iron oxides reduction. The temperature inside the BF can reach over 2000 °C. A major fraction of the resulting impurities from this process are removed as slags [4–7]. In order to lower and control the carbon content present in the “pig iron” produced, the latter it is transported to a basic oxygen furnace (BOF) where the excess of carbon is oxidised, as well with other impurities present in the produced steel which are also removed as oxides (silicon, phosphorous and manganese) [8]. Thus, this sector is responsible for massive CO_2 emissions resulting from several aspects such as the combustion of coke as fuel, to maintain very high temperatures and also by limestone decomposition. Alternatively to the BF, non-coke based technologies such as the Electric Arc Furnace (EAF) and the Direct Reduced Iron (DRI) are currently in use. EAF and DRI contribute to the remaining 30% of the iron and steel production worldwide. EAF consists of the recycling of iron by smelting mainly scrap iron or some manufactured iron pieces (“pig iron” and iron from DRI) in high-power electric arc furnaces for liquid steel production. On the other hand, DRI is based on the reduction of the iron ore in solid-state to metallic iron. Natural gas is mixed with gases from previous operations in the furnace to produce CO or H_2 which are used as reducing agents, reducing the iron oxides from the ores to an iron porous material, the “sponge iron”. Despite the DRI process have a less environmental impact when compared to BF/BOF and EAF, “sponge iron” contains impurities that need to be further separated by the EAF process, which increases energy consumptions and CO_2 emissions [3,8]. Fig. 1.1. represents a general scheme of the traditional iron and steelmaking routes previously described.

BF/BOF routes are expected to continue to be the main route for steelmaking in the next years due to its capacity for mass production and the cost-effectiveness of the process. However, steelmaking

industries have been pressured to improve their technologies regarding the use of less raw materials, less energy consumption, and CO₂-lean technologies. Around 2.3 billion tons of CO₂ emissions were accounted in 2007 by the steelmaking industries, but over 3.0 billion of CO₂ emissions are expected in 2050, contributing actively to the greenhouse gas emissions. In fact, iron and steelmaking industries produce about 9% of the global CO₂ emissions [7]. Moreover, significant emissions of SO₂, H₂S, dust with iron particles and slags are also environmental issues inherent to the mentioned technologies. Nowadays, improvements to the BF/BOF are being developed by taking into account different furnace designs, injection of pre-treated biomass to reduce the coke consumption, separation and recycling of the gases produced as well as the recovery of the waste heat [7].

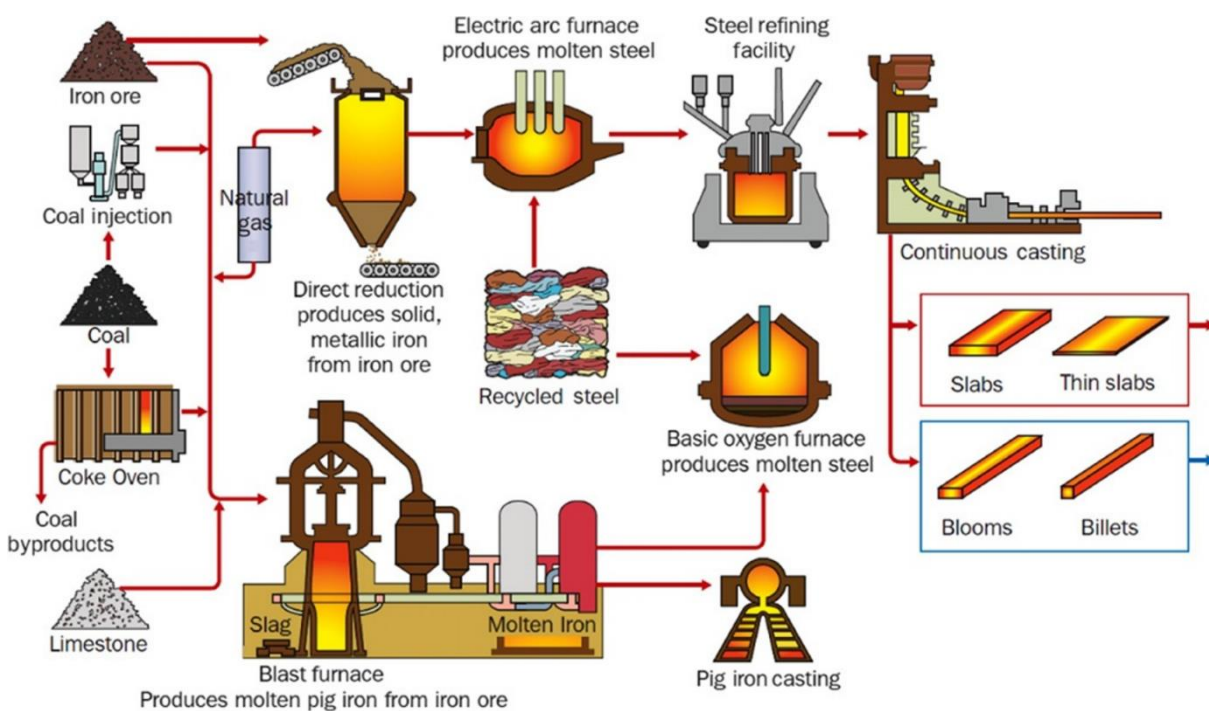


Fig. 1.1. Overview of the general steel and ironmaking process scheme [9].

Several R&D projects have been approved by the European Commission under the Horizon 2020, seeking new CO₂-free technologies with low energy consumption as alternatives to existing main technologies. In this scope, the electrolysis of iron oxides arose as promising technology consisting in the conversion of iron oxides into metallic iron using electric energy. Simultaneously, non-polluting gases such as oxygen and hydrogen are released during the electrochemical reaction. Based on this technology, the SIDERWIN project (previously the ULCOWIN project) intends to use not only iron ores but other iron oxide-based by-products from metallurgical industries and convert them into steel with low energy consumption [10,11].

Using iron oxide-based by-products instead of the ores can be an alternative for lowering the use of raw materials and to increase the recycling and valorisation potential of iron by-products or even iron-rich waste. Interesting industrial symbiosis can be established when using iron-rich waste as raw materials in electrolysis, contributing to the circular economy. In fact, as a result of the high worldwide production of iron and steel, around 700 million tons of metallurgical residues are produced per year [1]. While the major fraction can be recycled (about 83% of the steel produced [12]), some iron or steel materials are discarded due to the high level of contamination. Thus, some iron-rich wastes are disposed of in landfills or incorporated in foundations of buildings [13]. Alumina production industries by the bauxite leaching process (Bayer process) also generate an alkaline problematic iron-rich waste, known as red mud with around 30-60 wt% of Fe_2O_3 and 10-20 wt% of alumina content (Al_2O_3) in its constitution, between others [14]. The world production rate of red mud waste reached near 160 million tons in 2015, and China is the largest producer with 88 million tons per year [15]. Alumina industries are facing major issues when dealing with the storage of the massive amount of waste produced. Moreover, the high alkalinity (up to pH 13) and the presence of toxic metal oxides even in trace amounts, such as chromium or nickel, are responsible for the contamination of soils and water streams [14,15]. However, red mud appears as an interesting iron-rich waste that can be recovered, leading to a decrease in the amount of waste discarded and stored in the soil. .

On the other hand, the reducing properties ($E^0 = -0.44 \text{ V}$ for Fe^{2+}) of the metallic iron (Fe^0) or often called as zero-valent iron (ZVI) when in contact with nitrate [16], pesticides [17], textile dyes [18] and many others, have devoted research lines towards the soil and water decontaminations in the last decades. Its reactivity in contact with pollutants was even proved for the oxidation of organic matter present in wastewaters when coupled with a strong oxidizing agent such as hydrogen peroxide [19], revealing an interesting chemical versatility. Fe^0/ZVI has been produced mainly by chemical reduction from iron salts [20], where several hazardous chemicals are used such as sodium borohydride and by carbothermal reductions routes [21].

During the last decade, the low-temperature electrolysis of Fe_2O_3 has gained particular interest as a suitable and greener alternative to the traditional technologies of iron and steel production [10,22,23]. This appears to be a plausible approach when considering the electroreduction of iron-rich waste such as red mud and an appealing alternative for Fe^0/ZVI production in comparison with the main routes used. Nevertheless, when considering an iron waste, a significant challenge is imposed by the complex composition of the iron waste, containing other redox-stable or redox-active cations. This thesis aims to contribute to the fundamental knowledge of this process, by investigating the electroreduction mechanisms of iron oxides, containing a well-controlled amount of those cations in typical iron waste.

I.1. Scope and objectives of the Thesis

The present work aims to investigate the iron recovery and its valorisation from red mud waste by applying a CO₂-free technology based on the electrochemical reduction of the iron oxides to obtain Fe⁰. Taking into consideration that the produced Fe⁰ particles are usually reactive and can be used for further environmental studies, the specific objectives are:

- i. to process synthetic materials mimicking the composition of red mud waste for electroreduction studies;
- ii. to study the microstructural evolution on the conversion of bulk iron oxides to Fe⁰;
- iii. to assess the possibilities for Fe⁰ production by electrochemical reduction of iron-oxide-based suspensions and evaluate related mechanisms;
- iv. to establish the main factors affecting the Faradaic efficiency for the cases mentioned in ii. and iii.;
- v. to process red mud-based compositions suitable for environmental remediation applications;
- vi. to propose guidelines for the bulk electrochemical reduction of red mud to Fe⁰.

I.2. Thesis structure

The Ph.D. thesis is divided into seven chapters. The first one focuses on the contextualization of the problem, the motivation and the scope of the work. The second part aims to give a literature review on the electrochemical methods with a potential for iron reduction. The electrochemical reduction mechanisms in bulk and suspensions are discussed, as well as its challenges, the effects of the hydrogen evolution in the electrolytic processes and the electrochemical cell design. The literature review also highlights the innovative aspects of the iron valorisation by the electrochemical method and gives attention to the corresponding prospects for red mud valorisation.

Chapters 3, 4, 5 and 6 report the results based on the objectives proposed for the thesis. These chapters are structured in the form of scientific articles. The third chapter is devoted to the processing of porous cellular iron oxide-based materials and its characterisation by mimicking the main components of red mud waste (hematite and alumina). The fourth chapter discusses the bulk electrochemical reduction of highly-porous hematite-based materials in alkaline medium and challenges in the working electrode design for the electrochemical cell. In the fifth chapter, the electrochemical reduction of hematite-based components was assessed in alkaline suspensions. The processing of real red mud waste into a highly-porous cellular matrix, as well as its direct application for phosphate removal from

contaminated water and its use as a ceramic cathode for the bulk electroreduction are discussed in the Chapter 6. General conclusions and forthcoming work are described in Chapter 7.

1.3. References

- [1] L. Fu, H. Gu, A. Huang, M. Zhang, J. Wu, Fabrication of CaO–MgO–Al₂O₃ materials from metallurgical waste industrial residue and their potential usage in MgO–C refractories, *Ceram. Int.* 46 (2020) 959–967. doi:10.1016/j.ceramint.2019.09.057.
- [2] J.K. Mohanty, M.S. Jena, A.K. Paul, Integrated Mineralogical Characterisation of Banded Iron Ores of Orissa and Its Implications on Beneficiation, *J. Miner. Mater. Charact. Eng.* 11 (2012) 1133–1142. doi:10.4236/jmmce.2012.1112122.
- [3] T. Battle, U. Srivastava, J. Kopfle, R. Hunter, J. McClelland, The Direct Reduction of Iron, in: *Treatise Process Metall.*, 1st edition, Elsevier Ltd., 2014: pp. 89–176. doi:10.1016/B978-0-08-096988-6.00016-X.
- [4] B. Yuan, O.E. Kongstein, G.M. Haarberg, Electrowinning of Iron in Aqueous Alkaline Solution Using a Rotating Cathode, *J. Electrochem. Soc.* 156 (2009) D64–D69. doi:10.1149/1.3039998.
- [5] E.C. 2010/75/EU, Industrial Emissions Directive, Best Available Technique (BAT) Reference Document for the Iron and Steel Production, 2010.
- [6] T. Kovacs, G. Bator, W. Schroeyers, J. Labrincha, F. Puertas, M. Hegedus, D. Nicolaidis, M.A. Sanjuán, P. Krivenko, I.N. Grubeša, Z. Sas, B. Michalik, M. Anagnostakis, I. Barisic, C. Nuccetelli, R. Trevisi, T. Croymans, S. Schreurs, N. Todorović, D. Vaiciukyniene, R. Bistrickaite, A. Tkaczyk, K. Kovler, R. Wieggers, R. Doherty, From raw materials to NORM by-products, in: W. Schroeyers (Ed.), *Nat. Occur. Radioact. Mater. Constr. Integr. Radiat. Prot. Reuse (COST Action Tu1301 NORM4BUILDING)*, 1st edition, Woodhead Publishing, 2017: pp. 135–182. doi:10.1016/B978-0-08-102009-8.00006-2.
- [7] E.A. Mousa, Modern blast furnace ironmaking technology: Potentials to meet the demand of high hot metal production and lower energy consumption, *Metall. Mater. Eng.* 25 (2019) 69–104. doi:10.30544/414.
- [8] H. 2020 Project Nr. 693845, EU coordinated MEthods and procedures based on Real Cases for the effective implementation of policies and measures supporting energy efficiency in the Industry (EU-MERCI). Technical analysis – Iron and Steel sector (NACE C24.1-24.2-24-5), 2020.

- [9] American Iron and Steel Institute, Technology Roadmap Research Program for the Steel Industry, 2010.
- [10] A. Allanore, H. Lavelaine, G. Valentin, J.P. Birat, P. Delcroix, F. Lapique, Observation and modeling of the reduction of hematite particles to metal in alkaline solution by electrolysis, *Electrochim. Acta.* 55 (2010) 4007–4013. doi:10.1016/j.electacta.2010.02.040.
- [11] H. Lavelaine, S. Van der Laan, A. Hita, K. Olsen, M. Serna, G. Haarberg, J. Frade, Iron production by electrochemical reduction of its oxide for high CO₂ mitigation (IERO). European Commission, 2016.
- [12] J. Birat, Steel cleanliness and environmental metallurgy, *Metall. Res. Technol.* 113 (2016) 201. doi:10.1051/metal/2015050.
- [13] A. Di Schino, Circular economy aspects related to steel production, *J. Chem. Technol. Metall.* 54 (2019) 239–244.
- [14] Y. Hua, K. V. Heal, W. Friesl-Hanl, The use of red mud as an immobiliser for metal/metalloid-contaminated soil: A review, *J. Hazard. Mater.* 325 (2017) 17–30. doi:10.1016/j.jhazmat.2016.11.073.
- [15] E. Mukiza, L.L. Zhang, X. Liu, N. Zhang, Utilization of red mud in road base and subgrade materials: A review, *Resour. Conserv. Recycl.* 141 (2019) 187–199. doi:10.1016/j.resconrec.2018.10.031.
- [16] D.V. Lopes, M. Sillanpää, C. Wolkersdorfer, Nitrate Reduction of the Siilinjärvi/Finland Mine Water with Zero-valent Iron and Iron Waste as Alternative Iron Sources, *Mine Water Environ.* 39 (2020) 280–290. doi:10.1007/s10230-020-00668-9.
- [17] X. Cong, N. Xue, S. Wang, K. Li, F. Li, Reductive dechlorination of organochlorine pesticides in soils from an abandoned manufacturing facility by zero-valent iron, *Sci. Total Environ.* 408 (2010) 3418–3423. doi:10.1016/j.scitotenv.2010.04.035.
- [18] D.A. Yaseen, M. Scholz, Textile dye wastewater characteristics and constituents of synthetic effluents: a critical review, Springer Berlin Heidelberg, 2019. doi:10.1007/s13762-018-2130-z.
- [19] R. Martins, D. Lopes, M. Quina, R. Quinta-ferreira, Treatment improvement of urban landfill leachates by Fenton-like process using ZVI, *Chem. Eng. J.* 192 (2012) 219–225. doi:10.1016/j.cej.2012.03.053.
- [20] J.T. Nurmi, P.G. Tratnyek, V. Sarathy, D.R. Baer, J.E. Amonette, K. Pecher, C. Wang, J.C. Linehan, D.W. Matson, R.L. Penn, M.D. Driessen, Characterization and properties of metallic iron nanoparticles: Spectroscopy, electrochemistry, and kinetics, *Environ. Sci. Technol.* 39 (2005) 1221–1230. doi:10.1021/es049190u.

- [21] M. Bystrzejewski, Synthesis of carbon-encapsulated iron nanoparticles via solid state reduction of iron oxide nanoparticles, *J. Solid State Chem.* 184 (2011) 1492–1498. doi:10.1016/j.jssc.2011.04.018.
- [22] X. Zou, S. Gu, X. Lu, X. Xie, C. Lu, Z. Zhou, W. Ding, Electroreduction of Iron (III) Oxide Pellets to Iron in Alkaline Media : A Typical Shrinking-Core Reaction Process, *Metall. Mater. Trans. B.* 46B (2015) 1262–1274. doi:10.1007/s11663-015-0336-8.
- [23] Y. Ivanova, J. Monteiro, L. Teixeira, N. Vitorino, A. Kovalevsky, J. Frade, Designed porous microstructures for electrochemical reduction of bulk hematite ceramics, *Mater. Des.* 122 (2017) 307–314. doi:10.1016/j.matdes.2017.03.031.

This Page Intentionally Left Blank

2. Literature review

2.1. Electrolytic processes for iron reduction

Electrolysis was the name given by Michael Faraday in 1833, to the decomposition of compounds during the passage of electricity [1]. This process is based on passing an electric current between two electrodes immersed in an ionic conductor medium (electrolyte), in order to promote electrochemical reactions on the electrodes. The most well-known electrolysis process is water splitting, where H_2 (g) is produced at the cathode or working electrode (negative pole) and O_2 (g) is produced at the anode or counter electrode (positive pole). The electrolysis of iron allowed coatings on metal surfaces since the XIX century. However, only in 1991, Sadoway suggested the use of electrolysis as a greener approach for mainstream iron extraction [2]. The interest in this technology was based on its CO_2 -lean character. Faradaic or current efficiencies are usually reported to ascertain the feasibility of the electrochemical processes. Faradaic efficiencies (F.E.) are typically determined by taking into consideration the ratio between the weight gain of the working electrode (WE) before and after the electrochemical process, and the theoretical mass calculated by the Faraday's law. The F.E. is calculated by Eq. (2.1), where: Δm is the difference of mass of the WE before and after the electrochemical process; Q is the electrical charge passed through the cell defined by the electrical current (I) with time (t), $Q = \int_0^t I dt$; M is the molar mass of iron; z is the number of electrons transferred in the process; and F the Faraday's constant (96485 C/mol) [3].

$$F.E. = \Delta m / (QM/zF) \quad (2.1)$$

Thus, electrowinning processes based on the reduction of iron oxides from the ores to produce iron have been strongly investigated in recent years, as a suitable alternative to the BF/BOF technology. Several electrolytic routes have been explored through time, consisting in electroplating in acidic baths, molten oxides electrolysis, molten salts electrolysis and electrolysis in alkaline aqueous solutions. The mentioned routes will be described in this section.

2.1.1. Electroplating in acidic baths

Iron electrotypes for printing notes based on the iron electroplating were developed by Klein and used by the Russian Mint in 1868 as the first application of the electrolysis technology. In 1934, the

first electrolysis pilot-plant for iron production for commercial purposes was built, where an ammonium sulphate mixture with ferrous salts was used as electrolyte with a pH between 5 and 6. A maximum temperature of 60 °C was used in the electrolytic cells presented in Fig. 2.1, using several steel cathodes and iron anodes simultaneously. Around 45 kg of iron were produced in every 3 days and a half [4]. The iron was produced by electroplating or electrodeposition, which consists in the formation of a metallic coat or film at the surface of a metallic cathode due to the reduction of metal oxides [3]. Acidic bath solutions of ferrous salts (Fe^{2+}) have been used over time as electrical conductive electrolytes, such as FeSO_4 and FeCl_2 . An overview of the traditional iron baths and operational conditions is shown in Table 2.1.



Fig. 2.1. Electroplating cells, where several plates were used as cathodes and anodes [4].

Table 2.1. Overview of the common iron plating baths and its operational conditions, adapted from [5].

Ferrous bath	Operational conditions			Application of the iron deposits
	pH	T (°C)	j (A/dm ²)	
$\text{FeSO}_4 \cdot 7\text{H}_2\text{O}$	1.4	47	6.7	Iron strip
FeCl_2	0.5-4.7	98-106	33-40	
$\text{FeSO}_4 \cdot 7\text{H}_2\text{O}$	2.5	80	3-27.5	
$\text{FeCl}_2 \cdot 4\text{H}_2\text{O}$	5-5.5	25-40	2-5	Electrotype
$\text{FeSO}_4 \cdot 7\text{H}_2\text{O}$	3.5-5.5	40-43	5-10	
$\text{FeCl}_2 \cdot 4\text{H}_2\text{O}$	3.5-5.5	40-43	5-10	

Despite the fact that room or low temperatures were commonly used, an increase of the current densities (j) was observed at about 100 °C. Aluminium, magnesium or sodium sulphate may be added to the baths as well as $\text{Fe}(\text{BF}_4)_2$, $\text{Fe}(\text{H}_2\text{NO}_3\text{S})_2$, between many others, to improve the quality of deposited layers. However, light grey and brittle deposits were frequently obtained, with slow deposition rates [5]. The brittle and pitted iron deposits are often related to the use of acidic pH. In addition, Fe^{2+} and Fe^{3+} co-exist in the acidic electrolytic bath, causing a redox cycle between the iron species, lowering the overall Faradaic efficiency of the process [5,6]. Thus, very few studies were performed in recent years, except for occasional attempts with sulphate [7] and fluoroborate [8] acidic solutions.

2.1.2. Molten oxides electrolysis (MOE)

The molten oxides electrolysis (MOE), previously named as pyroelectrolysis, arose as a direct method for reducing metal oxides at high temperatures to obtain liquid metal [2]. This process overcame a similar type of electrolysis in molten oxides, previously performed with carbon anodes [9]. However, the anodes were consumed during the process leading to the production of CO and CO₂. When using inert anodes, O₂ (g) is the only by-product. This technology is based on the electroreduction of metal oxide in an electrolyte composed of a mixture of molten oxides. The metal oxide to be further reduced is dissolved in the mixture of the molten oxides, at high temperature, reaching the melting point of each metal oxide. First, the metal oxides dissociate in the molten oxide electrolyte into their cations and anions. The following step consists of the transference of the electrons to the cations and removal of electrons from the anions to form neutral atoms. Thus, the metal oxides are reduced to their metallic form, M⁰, at the cathode and in the liquid state due to the high operating temperature used. The generation of O₂ (g) takes place at the anode [10]. When iron oxides are used in MOE, the reductional steps occur as the following: $\text{Fe}_2\text{O}_3 \rightarrow \text{Fe}_3\text{O}_4 \rightarrow \text{FeO} \rightarrow \text{Fe}^0$, where the formation of FeO can be a possible intermediary step [11].

General aspects of the conducted researches are shown in Table 2.2, where temperatures around 1550 °C are used for liquid Fe⁰ production. The molten oxide electrolytes must have good ionic conductivity, appropriate melting temperature (< 1450 °C), low vapor pressure, lower density than liquid iron and it must have lower reduction ability than iron oxides [11,12]. The most common electrolytes for iron production can be alkaline as CaO-MgO-Al₂O₃-SiO₂ or acidic as MgO-Al₂O₃-SiO₂, where a high concentration of the metal cations should be present and less than 10 wt% should be related to the oxide fraction of the content of the total oxide. Moreover, the electrolyte should be in a liquid state to allow O₂ (g) bubbles to float for gas separation from the electrolyte [11,12,13].

Kim et al. [14] compared the use of an acidic (high content in SiO₂, 46 mol%) and alkaline (58 mol% of CaO and 19 mol% of CaO) electrolyte/melt when using iridium as the anode. Regardless of

the mixture of the molten oxides, both cases showed dendritic deposits of Fe^0 as well as for non-metallic materials at the cathode. When CaO was present in the mixture of the molten oxide, $\text{Fe}_{0.49}\text{Ir}_{0.23}\text{Mo}_{0.28}$ was identified in the cathode, while $\text{Fe}_{0.48}\text{Mo}_{0.52}$ was present in the SiO_2 -rich electrolyte content. The anode consumption was clear and visible under alkaline conditions, leading to current efficiencies of 25%.

Table 2.2. General aspects of the researches conducted by molten oxides electrolysis processes.

Cell	Molten oxides	Cathode	Anode	Feedstock	Other aspects	Ref.
Al_2O_3 and MgO	$\text{SiO}_2\text{-CaO-MgO-Al}_2\text{O}_3$ and $\text{CaO-MgO-Al}_2\text{O}_3$	Mo disk	Ir	Fe_2O_3	1600 °C 3.5 A	[14]
YSZ*	$\text{SiO}_2\text{-MgO-Al}_2\text{O}_3$	Pt	$\text{Fe}_{2.3}\text{Al}_{0.2}\text{Mg}_{0.4}\text{O}_4$	Present in the anode	1455 °C 1.3 A/cm ²	[15]
Al_2O_3	$\text{SiO}_2\text{-MgO-Al}_2\text{O}_3$	Pt and Rh	Pt	Fe_3O_4	1550 °C 75 mA	[11]
Al_2O_3	$\text{SiO}_2\text{-MgO-Al}_2\text{O}_3$	Pt and Rh	Pt and Rh	Fe_3O_4	1550 °C 0.25 A/cm ²	[13]

*Yttria-stabilized zirconia

Ferreira et al. [15] tested a consumable anode with iron oxides in its constitution. The $\text{Fe}_{2.3}\text{Al}_{0.2}\text{Mg}_{0.4}\text{O}_4$ ferrosinell acted successfully as a consumable ceramic anode, appropriate for high temperatures, with high electrical conductivity and adequate refractoriness. However, excessive dissolution of the anode was still promoted by chemically-aggressive electrolyte at high temperatures. The harsh conditions of the process did not allow the estimation of the Faradaic efficiency of the electroreduction.

As mentioned previously, the looping of $\text{Fe}^{2+}/\text{Fe}^{3+}$ valence state in the melt or molten oxide electrolyte hampers the electrochemical reduction. However, to guarantee suitable ionic conduction in the cell, one valence state of iron is preferable as feedstock. As can be seen, usually Fe_2O_3 as Fe(III) is used as feedstock. However, Wiencke et al. [11,13] have used Fe_3O_4 (Fe^{3+} and Fe^{2+}) in their works. The researchers used low Fe_3O_4 concentration (15 wt%) in the silica-based electrolyte to diminish the impact on the ionic conduction. Around 131 mg of Fe^0 was produced in [11], with 36% of current efficiency, while in [13] the process was optimized by shortening the distance between the electrodes, which consequently decreased the ohmic losses and maximized the density of current in the cell. The liquid Fe^0 produced at the end of a MOE process is shown in Fig. 2.2.

In general, recent studies are not focused on Fe^0 production optimization. Instead, the search of an appropriate anode has been the most challenging aspect due to the aggressive character of the molten oxide electrolytes at high temperatures. Despite MOE technology shows good prospects for a wide range of metals, including transition metals (iron, nickel, cobalt, manganese), lanthanides, actinides such as uranium, and refractory metals as TiO_2 [2,10,16], its industrial feasibility is far from being convincingly demonstrated. In fact, the best current efficiencies obtained so far were reported by Wiencke et al. [11] (36%), surpassed only by 2% the reported efficiencies from Allanore et al. [17], due to the low electrical conductivity of the electrolytes. MOE brings difficulties not only due to the high amount of energy consumed but also in finding a suitable mixture of molten oxides as well as anodes that can resist the extreme conditions imposed by this technology.

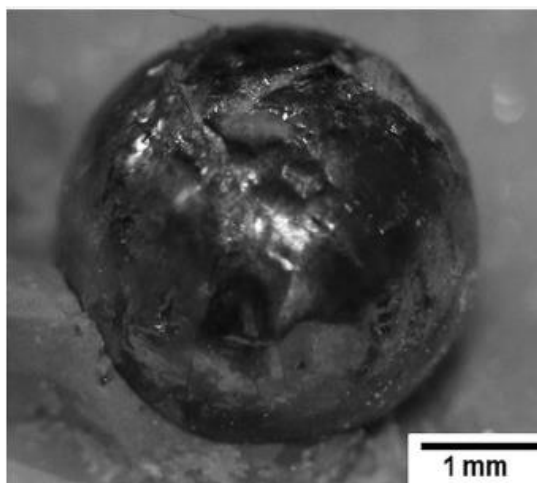


Fig. 2.2. Liquid Fe^0 obtained after the molten oxide electrolysis [11].

2.1.3. Molten salts electrolysis

Molten salts have been extensively used for the electrowinning, electroplating and electrorefining (removal of impurities to produce pure metals) of several metals. This technology is well established for the production of Mg^0 , Na^0 , Li^0 , K^0 , Be^0 , among others [18]. The first attempt to produce Fe^0 was done by Andrieux and Weiss in 1944 but, unfortunately, deposits containing only Fe_3O_4 and sodium were found when using Na_2CO_3 , Na_2O_2 and NaBO_2 as electrolytes at $500\text{ }^\circ\text{C}$ [19]. Years later, Fe^0 deposits were obtained in $\text{KCl-LiCl-FeCl}_2\cdot 4\text{H}_2\text{O}$ at $225\text{ }^\circ\text{C}$ by Ziolkiewicz [20]. Since then, different types of molten salts have been used for electrolysis, including eutectic salts or mixtures of salts, allowing one to work with a wide range of temperatures. Moreover, these salts have suitable electrical conductivity (2 to 9 S/cm) and, in most cases, high solubility, leading to high current densities during electrolysis [16,21,22]. The principle of the electrolysis of molten salts is analogous to the FFC Cambridge process used for the electroreduction of several metals, such as Ti^0 from TiO_2 [23], and it has the same principle

as the MOE previously described. Metal oxides are dissolved in a mixture of molten salts, and the metal is reduced in the cathode while O_2 (g) is generated in the anode. Lower temperatures are required in this case when compared with MOE. The literature for iron production by this type of electrolysis has gained interest in the last years, but studies are still on a laboratory scale. Table 2.3 summarizes general aspects of some studies reported in the literature. Two cathodes (working electrodes) and two anodes (counter electrodes) were used by Haarberg et al. [24] at different temperatures, during the electrolysis experiments and measurements, respectively, when reducing Fe_2O_3 powder to Fe^0 . Despite Fe_3O_4 was found at the cathode, 92% of current efficiencies were achieved. However, the presence of CaF_2 was observed in the Fe^0 due to difficulties in dissolving the salt in the electrolyte. Licht et al. [25] used Li_2CO_3 as an electrolyte, which was suitable to dissolve Fe_2O_3 powder for Fe^0 reduction. However, the electrolysis of the electrolyte resulted in CO (g) formation, despite a 97% of efficiency was attained.

Table 2.3. General aspects of works related to molten salts electrolysis.

Cell	Molten salt	Cathode	Anode	T (°C)	Other aspects	Ref.
Carbon crucible	$CaCl_2$ - CaF_2	Mo and Pt	Fe_3O_4 rod and carbon rod	827 °C and 890 °C	Fe_2O_3 powder 0.5 A/cm ²	[24]
Al_2O_3 crucible	Li_2CO_3	Pt	Ni	800 °C	Fe_2O_3 powder 0.5 A/cm ²	[25]
Vitreous carbon crucible	Eutectic LiF - NaF	Fe_3O_4 pellet with Mo grid	Au	750 °C	0.75 A	[26]
Al_2O_3 crucible	Eutectic $NaCl$ - $CaCl_2$	Fe_2O_3 pellet with stainless steel rod	Graphite rod with stainless	800 °C	0.5 A	[27]

Molten salt electrolysis evolved to an electro-deoxidation approach, where instead of adding iron oxides in powder to the electrochemical cell, a direct solid reduction of the iron oxides is performed [28]. Thus, a solid cathode is assembled as a pellet of iron oxide connected to an electrically conductive wire such as Mo or steel. The mechanism of iron oxides reduction has been the aim of several studies since a solid reduction allows a more controlled understanding of the electrochemical reactions involved. Gibilaro et al. [26] observed a complete reduction to Fe^0 from Fe_3O_4 pellets and suggested a reduction step from Fe_3O_4 to FeO before the complete reduction to Fe^0 . The most consensual model for Fe_2O_3 reduction in pellet seems to be the following one: $Fe_2O_3 \rightarrow Fe_3O_4 \rightarrow FeO \rightarrow Fe^0$, according to Li et al. [27], with 95% of current efficiency. Due to the molten salts electrolyte used and consumption of the anode in [27], Ca^0 deposition and $CaCO_3$ formation decreased the efficiency of the process. As it was concluded previously in MOE, the use of carbon anodes or carbonates molten salts mixture usually have the disadvantage of producing CO and CO_2 during the electrolysis.

A recent study developed by Xie et al. [29] allowed a different approach for iron reduction by using the electro-deoxidation to reduce Fe₂O₃ pellets in molten LiCl at 660 °C. The electrochemical cell used by Xie and collaborators had an entrance for a humid argon atmosphere, where water entered inside the cell along with argon. Thus, H₂ (g) was formed due to water electrolysis and was directly involved in the reduction to Fe⁰, with a current efficiency of 96%. This study introduces a new pathway for future iron production. However, when using molten salts for the electrodeposition and electrowinning purposes, the presence of solidified salts in the Fe⁰ deposits are frequent. Moreover, other disadvantages are related to problems with the solidification of the molten salts when the power supply fails; the corrosive nature of the electrolytes, as in MOE, requires the use of special electrochemical cells along with inert atmospheres in some cases [22].

2.1.4. Electrolysis in alkaline aqueous solutions

The first work on the electrodeposition of iron in an alkaline aqueous solution was a Swedish patent, dated from 1915 [30], where Estelle and co-workers obtained a grey deposit of Fe⁰ after performing electrolysis in a bath constituted by 35% of NaOH, 35% of water and 30% of Fe(III) hydroxide, at 100 °C. In 1952, another patent [31] suggested the use of iron ore instead of Fe(III) hydroxide at the same aqueous medium. Even though the produced Fe⁰ deposits were not characterised in both studies, both patents are considered the starting point of Fe⁰ production by electrolytic processes in alkaline solutions. However, despite the studies performed between the 1940s to 1980s, little attention was given to this process, mainly due to the doubtful and non-consensual mechanism of reduction of iron oxides under alkaline medium [32]. Until recently, the combination of low-temperature electrolysis (≈100 °C) with the insulating properties attributed to Fe₂O₃ (10⁻¹⁴ S/cm [33,34]), the difficulty in dissolving iron oxides in aqueous solutions, together with one single reduction step involving the transference of six electrons (Eq. 2.2), were reasons to discredit this electrolytic process [35–37].



Decades later, significant advances have been made and the electrolysis of alkaline aqueous solutions as electrolytes are now considered one of the advanced technologies for iron production [38–40], despite not being implemented at industrial scale so far.

This type of electrolysis uses concentrated alkaline aqueous solutions such as KOH or NaOH (around 5 to 19 M), for a cathodic reduction of the iron oxides into Fe⁰. Studies have been done both for aqueous suspensions of iron oxides powders and for the direct reduction of solid iron oxide pellets or iron ores. The by-products are H₂ (g) (2H₂O+2e⁻→H₂+2OH⁻) and O₂ (g) (4OH⁻→O₂+2H₂O+4e⁻), which are produced at the cathode and the inert anode, respectively, due to the alkaline water electrolysis

present in the aqueous solution of the electrolyte. The diffusion of OH^- anions during the electrochemical reduction of iron oxides through the electrolyte, is also responsible for promoting O_2 (g) evolution. A three-electrode cell containing cathode or working electrode (WE), reference electrode (RE) and an inert anode or counter electrode (CE), is usually used for this purpose.

Since the work performed in the thesis involved the electrolysis in alkaline media towards valorisation of the iron-rich waste, more detailed information regarding the scientific advances performed through the time in this area will be discussed in the following section.

2.2. Electroreduction of iron oxides in alkaline medium: mechanisms of reduction and operation conditions

2.2.1. Electrochemical reduction in suspension

Despite the mechanism of reduction was not yet understood at that time, considerable progress was made in 1959 by LeDuc and his collaborators regarding the optimization of the process [41] by chronoamperometry methods (current or potential vs. time). The impact on Faradaic efficiency was considered on studying effects of temperature (30 to 120 °C) and alkali concentration (5 to 19 M) during the electrolysis of a Fe_2O_3 suspension (50 g/L). Relatively low Faradaic efficiencies were observed ($\leq 60\%$) at 5 M concentration and at different temperatures, since the Fe_2O_3 powder was not completely solubilized, requiring higher electrolyte concentrations. Moreover, LeDuc et al. concluded that a minimum of 10 M of alkali solution is required for at least 50% of stable Faradaic efficiencies at high temperatures. The maximum of 95% of efficiency was attained in 19 M alkali solution at 90 °C. The temperature was proved to be decisive for increasing the solubility of the iron oxide in the alkali solution. On the other hand, an increase of the current density (galvanostatic mode: fixed current) was demonstrated to decrease the Faradaic efficiencies, possibly due to H_2 (g) generation at the cathode, minimizing the iron deposition. Thus, the lower current density tested (0.043 A/cm^2) was the optimum current density. Dendritic Fe^0 deposits were present at the cathode, which size increased with temperature. These findings lead to pilot scale studies with 80% of Faradaic efficiencies (19 M of NaOH, 88 °C, 64 g/L of Fe_2O_3 powder, 0.048 A/cm^2 , 11 h) for Fe^0 powder production, but large dendrites were obtained as result (> 100 mesh) with a high level of agglomerates. When iron ore was used instead of commercial Fe_2O_3 powder, the efficiencies decreased to around 50% due to the ore impurities. Despite important outcomes were obtained within the conducted research, the reduction mechanism was not clear. The authors suggested the formation of sodium ferrite in the alkaline solution, leading to its

reduction to Fe^0 . However, its low solubility in the alkaline solution was not able to make the mechanism reliable.

Other studies were devoted to the investigation of the mechanism of Fe_2O_3 reduction to Fe^0 based on cyclic voltammetry (CV) analysis (current vs. potential). However, questions were raised in the scientific community due to the low dissolution of Fe_2O_3 in strong alkaline solutions, $\approx 2 \times 10^{-3}$ M (18 M and at 100 °C) [42]. Thus, different iron species were suggested to be part of the pathway of the electrochemical reduction of Fe_2O_3 . Gorbunova and Liamina [32] in 1966, suggested the reduction as $\text{FeO}_2^- \rightarrow \text{FeO}_2^{2-} \rightarrow \text{Fe}^0$ when reducing hydrated iron oxides (III) in suspension in KOH electrolytes up to 13 M. When trying the reduction of Fe(III) in a saturated KOH electrolyte, the hydrate iron oxide was deposited as a compact film on the surface of the cathode, and the presence of Fe_3O_4 was detected by X-ray diffraction (XRD) as an intermediate phase, suggesting that a solid phase plays an active role during the reduction to Fe^0 . Armstrong and Baurhoo [43] investigated Fe^0 dissolution in KOH (10 M) at 70 °C by anodic oxidation to promote the presence of Fe(II) and Fe(III) species in the alkaline solution. Oxidation was observed from Fe^0 to Fe(II) species, such as $\text{Fe}(\text{OH})_2$, and from Fe(II) to Fe(III), where Fe_3O_4 , FeOOH and Fe_2O_3 were identified based on thermodynamic studies. Moreover, other authors, such as [44], supported the formation of the solid phase, $\text{Fe}(\text{OH})_2$, due to the HFeO_2^- and FeO_2^{2-} species as Fe(II) for further FeOOH oxidation as Fe(III), in a KOH electrolyte (4.5 M, 70 °C). Pourbaix diagrams [45], on the other hand, clearly show that $\text{Fe}(\text{OH})_2$ is unstable at higher temperatures (> 65 °C), suggesting that this phase is not formed in alkaline medium at the temperatures used for iron oxides electrolysis.

Although iron oxide (III) reduction seemed to occur from Fe(III) to Fe(II) species and, consequently, to Fe^0 , it is still debatable whether Fe_2O_3 is reduced directly or dissolved in a strong alkaline medium as a first step of the electrochemical reduction. Thermodynamic studies performed by Diakonov et al. [46], proposed $\text{Fe}(\text{OH})_4^-$ as the product of the hydrolysis of Fe_2O_3 at strong alkaline solutions, described as Eq. (2.3):



Nevertheless, little attention was given to this line of electrolysis due to the many uncertainties of the mechanism. After the year 2000s, new studies on the electrodeposition and electrowinning of iron in alkaline aqueous solutions were developed due to the interest in new CO_2 lean technologies for iron production. Allanore et al. [36] studied the reduction mechanism based on the optimization of a previous study from 1980 of Picard et al. [42]. According to Picard, the cathodic reduction reaction occurs in “solid-state”, when the particles of Fe_2O_3 in suspension surround the cathode. Allanore and co-workers supported the dissolution of Fe_2O_3 to $\text{Fe}(\text{OH})_4^-$ (Eq. (2.3)) and proposed the following mechanism (Eqs (2.4) and (2.5)), attending to Pourbaix diagrams of [45,47], represented in Fig. 2.3.

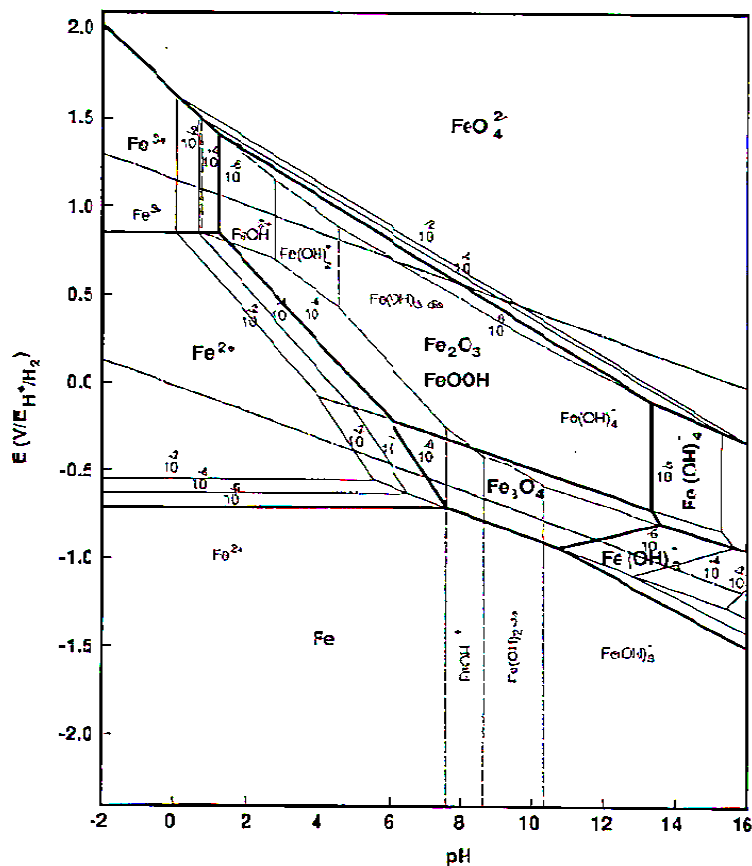


Fig. 2.3. Pourbaix diagram of the Fe-H₂O system at 100 °C [45].

Considering the low level of Fe(III) dissolved in the alkaline conditions tested (2.6×10^{-3} M), low Faradaic efficiencies were obtained ($< 8\%$). A concentrated Fe(III) electrolyte was obtained when an iron anode was used instead of the Pt previously used, increasing the Faradaic efficiency to 70%, where the remaining 30% were attributed to the H₂ (g) generated at the cathode. During the anode dissolution to the electrolyte, Fe(III) and Fe(II) species coexist, leading to the conclusion that Fe₃O₄ can be an intermediary phase, in agreement with Pourbaix diagrams [45,47]. Allanore et al. concluded that the dissolution of Fe₃O₄ might have an important role if there is any solid-phase reaction in the mechanism. Moreover, dendritic shaped Fe⁰ deposits were electrodeposited at the WE.

Research conducted by Yuan et al. [48,49] was based on the same thermodynamic considerations discussed in [36], where Fe(OH)₄⁻ dissolution has a crucial role. Moreover, the iron oxide species dissolved in the electrolyte had different morphology than the initial Fe₂O₃ powder added, encouraging the dissolution as a first step. The investigation led to the optimization of the general conditions of the

electrochemical reduction. Interesting conclusions were made regarding the rotational speed of the rotation electrode disk used as the cathode, which was proved to have a direct impact not only on the Faradaic efficiencies of the electrochemical process, but also on the morphology of Fe^0 deposits. When using the rotating disk electrode at the stationary phase (0 rpm), low reproducibility is attained during the electrochemical tests due to a random number of Fe_2O_3 particles near the WE, leading to fluctuations of the current efficiencies (10% to 94%). An optimized speed range between 1000 to 2000 rpm, led to stable efficiencies above 90%. However, high-speed rates (> 2000 rpm) promoted the air bubbles formation which combined with cathodic H_2 bubbles, caused the passivation of the surface of the WE, decreasing the efficiency to 76%. During the increase of the rotational speed up to 3000 rpm, Fe^0 dendritic deposits proved to have asymmetrical growth. The increase of the initial Fe_2O_3 feedstock concentration from 30 wt% to 50 wt% in the electrolyte, increased the Faradaic efficiency from 90 to 98%. This finding supported the results from [36], where higher iron species present in the electrolyte led to higher efficiencies. On the other hand, more concentrated electrolytes (18 M) led to higher suppressing levels of H_2 , and consequently, to higher efficiencies. Energy consumption was estimated to be around 3 kWh per kg of iron, when using cathodic potentials between -1.13 to -1.19 V (vs. $\text{Hg}|\text{HgO}$). Similar operating conditions were used by Tokushige et al. [50], where the crystal orientation of the Fe^0 was evaluated by XRD. It was concluded that the morphology of the Fe^0 films obtained depends strongly on the current density applied and the transfer rate of the iron oxides particles. Thus, more heterogeneous deposits were obtained at higher current densities (6000 A/m^2) and lower Fe_2O_3 initial feedstock in suspension (33 wt%), where some of the Fe^0 crystals fell into the electrolyte. Based on the fact that a rotating disk was used as cathode and based on the conclusions of [48], possibly the strong H_2 (g) evolution promoted this effect. Zou et al. [51] deposited compact and uniform Fe^0 films on Cu at an optimized temperature of 60°C in 18 M NaOH, due to the dissolution of $\text{Fe}(\text{OH})_4^-$ species in the electrolyte from Fe_2O_3 powder. The iron species dissolved in solution were estimated based on previous thermodynamic studies where the concentrations are 0.34, 0.49 and 0.97×10^{-3} M at 25, 60 and 80°C , respectively.

Different Fe^0 deposits have been obtained by Ivanova et al. [52], where Fe^0 was embedded in carbon nanotubes (CNTs) from Fe_2O_3 suspensions (47.9 g/L) in 10 M (90 $^\circ\text{C}$). Triethanolamine (TEA) additive was used for facilitating the incorporation of CNTs in Fe^0 . CNTs showed to have no effect regarding current efficiencies, but with morphology only. High homogeneity, dense and compact structures of Fe^0 crystals, without pillar-like growth were observed. However, the presence of TEA had a negative impact on the Faradaic efficiency, which decreased from 70-80% (Fe^0 electrodeposition without CNTs and neither TEA) to 20-50%. The dissolution of Fe_2O_3 to $\text{Fe}(\text{OH})_4^-$ was considered as well as its dissolution to $\text{Fe}(\text{OH})_6^{3-}$ ions.

Typical cathodic voltammogram (CV) and common morphology of Fe^0 dendrites formed by the electrolysis of iron oxides suspensions are represented in Fig. 2.4A and 2.4B, respectively. The dashed lined in the CV represents the iron electrode (WE) with the NaOH solution (10 M), while the solid line shows the previously described experimental conditions, but with the addition of Fe_2O_3 (0.3 M) powder to the caustic suspension. A difference of 80 mV from the onset potentials can be observed between the dashed and the solid lines. The onset potentials for both cases are ascribed for the H_2 evolution (cathodic potentials below -1.1 V (vs. $\text{Hg}|\text{HgO}$)). After the addition of Fe_2O_3 (solid line), a shoulder is well visible immediately before -1.1 V, which was identified as the reduction to Fe^0 species in the alkali solution. The micrograph of the Fe^0 dendrites (Fig. 2.4B), shows the perpendicular growth to the WE in the common “needle-like” shape.

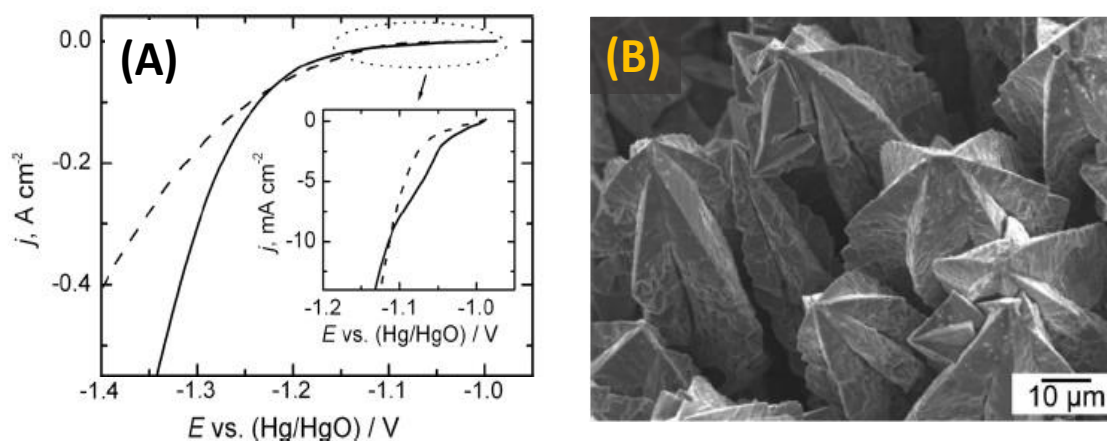


Fig. 2.4. (A) Voltammogram of the iron WE in a NaOH (10 M, 90 °C), before (dashed line) and after (solid line) of the addition of 0.3 M of Fe_2O_3 in [52]; (B) SEM image of typical Fe^0 deposits from the electrodeposition process in [48].

Due to the low solubility of Fe_2O_3 in strongly alkaline conditions, Siebentritt et al. [53] proposed the occurrence of adsorption of the iron oxide particles at the surface of the WE during the electrochemical reduction to Fe^0 . Slightly positive zeta potential measurements were obtained for Fe_2O_3 particles in strong alkaline conditions (10 M, NaOH). Although weak, the adsorption of positively charged Fe_2O_3 particles in contact with the WE (negatively charged) seems to occur by electrostatic forces, contributing actively for the reduction to Fe^0 along with the dissolution of Fe_2O_3 into the electrolyte as $\text{Fe}(\text{OH})_4^-$. The adsorption of Fe_2O_3 particles by a steel cathode immersed during 3 min inside of a hematite-alkaline suspension was also confirmed by another work of Allanore et al. [54], without performing zeta potential measurements. After immersion, the steel substrate was quickly transferred to a separated particle-free NaOH electrolyte (18 M), where a potentiostatic analysis (fixed potential) of 70 seconds was performed at -1.2 V (vs $\text{Hg}|\text{HgO}$), at 110 °C. The current vs. time curve obtained revealed a typical trend of the reductional mechanism from Fe_2O_3 to Fe^0 , with a current increase

up to 0.10 A. The Fe⁰ deposits in the steel substrate were confirmed by XRD analysis, showing a weak dependence with the concentration of the Fe₂O₃ particles suspension. The obtained results were supported by previous literature on the adsorption of Fe₂O₃ particles in a steel surface by a magnetic field [55], that might contribute significantly to the phenomenon.

Suspensions of Fe₂O₃, Fe₃O₄ and goethite (FeOOH) of 10 wt% iron oxide were electroreduced using potentiostatic chronoamperometry methods in NaOH electrolyte solution (18 M) by Feynerol et al. [56]. Both possible adsorption of the particles in the vicinity of the WE and dissolved Fe(OH)₄⁻ and Fe(OH)₃⁻ ions were considered as parts of the iron oxides reduction mechanism to Fe⁰. Despite its low electrical conductivity, Fe₂O₃ reached 1000 A/cm² with the highest Faradaic efficiency (86%), while FeOOH and Fe₃O₄ reached, respectively, 700 A/m² with 66% and 150 A/m² with 5% of current and Faradaic efficiencies. However, according to thermodynamic studies, the solubility of Fe₂O₃, Fe₃O₄ and FeOOH are, respectively, 2.6×10⁻³ M [57], 5.0×10⁻³ M and 1.44×10⁻² M [56] in NaOH at the studied temperature. Low efficiencies observed for FeOOH and Fe₃O₄ suspensions were assigned to several reasons: the FeOOH suspension proved to be highly viscous, hampering the evolution of the large O₂ bubbles; moreover, not only the cathodic potential for the reduction of Fe₃O₄ is more cathodic than other iron oxides, which ultimately leads to higher H₂ evolution reaction, but the magnetic properties of Fe₃O₄ led to a high amount of powder to be settling around the magnetic stirrer, limiting the contact of the powder with surface of the WE. Thus, few deposits were found from Fe₃O₄ suspensions when compared to the other iron oxides suspensions tested, despite its higher electrical conductivity when contrasted with Fe₂O₃.

A very recent study conducted by Maihatchi and his co-workers [58] was performed directly on a red mud suspension and compared to Fe₂O₃ suspension. Despite the first Fe⁰ depositions reached only 20% of Faradaic efficiency in galvanostatic mode ($j = 1000 \text{ A/m}^2$) due to the presence of various impurities (cancrinite, calcite, among others), efficiencies of 71% were reached by decreasing the current density to 45 A/m². Commercial Fe₂O₃ particles were tested in the same experimental conditions of red mud suspensions, where over 80% of efficiency was achieved in the range of 200 to 1000 A/m². Although no justification was given by the authors, one can assume higher H₂ evolution when using higher current densities, hampering the reduction to Fe⁰. On the other hand, the addition of kaolinite and vanadium to the Fe₂O₃ alkali suspension was studied. Kaolinite addition reduced the efficiency of the process to 40% when 30 wt% of kaolinite was added to the Fe₂O₃ suspension. However, a slight decrease was observed with the vanadium addition from 80% to 76%. The presence of impurities in Fe₂O₃ suspensions seemed to act on the surface of the particles, decreasing the reactivity of the suspension.

The operation conditions mostly used for the Fe⁰ electrodeposition in alkaline suspensions are shown in Table 2.4 for the latest carried studies. In general, NaOH (18 M) aqueous solution as electrolyte has been the most used, since it contributes to promote the O₂ evolution [37] and to suppress the H₂

evolution [48], where the last one is commonly associated with the loss of the Faradaic efficiency. Moreover, temperatures between 90 to 114 °C are usually used to improve the solubility of the iron oxides in solution. Different WE and CE can be used, which requires a full optimization for the Fe⁰ deposition in each study.

Table 2.4. Operation conditions used during the Fe⁰ electrodeposition from alkaline suspensions.

Cell	Electrodes	Operation conditions	Faradaic Efficiency/ ZVI deposited	Year/ Ref.
PTFE	WE: PTFE rotating disk with graphite CE: Pt; later substituted by Fe ⁰ foil RE: Hg HgO (10 M, KOH)	KOH (18 M) T = 110 °C 3500 rpm j = 0.1 A/cm ² 10 g Fe ₂ O ₃	F.E.= 70% Dendritic Fe ⁰	2007 [36]
Teflon	WE: rotating disk with graphite CE: Ni mesh RE: Hg HgO (1 M, KOH)	NaOH (18 M) T = 114 °C 1000 rpm j = 4000 A/m ² 33 wt% Fe ₂ O ₃	F.E.= 95% Dendritic Fe ⁰	2009 [48]
Teflon	WE: rotating disk with graphite CE: Ni mesh RE: Hg HgO (0.1 M, NaOH)	NaOH (18 M) T = 110 °C 1000 rpm j = 1000 to 6000 A/m ² 33 and 40 wt% Fe ₂ O ₃	F.E. = 95% at 3000 A/m ² and 40 wt% of Fe ₂ O ₃ Dendritic Fe ⁰	2013 [50]
PTFE	WE: Cu rod CE: Pt RE: Ag AgCl (saturated KCl)	NaOH (6 - 18 M) T = 25 - 80 °C E = -1.8 V t = 3 h Fe(OH) ₄ ⁻ = 0.34 - 0.97 × 10 ⁻³ M	- Fe ⁰ films	2015 [51]
Teflon	WE: Fe CE: Pt RE: Hg HgO (6 M, NaOH)	NaOH (10 M) T = 90 °C 200 rpm t = 30 min j = -0.25 A/cm ² 47.9 g/L of Fe ₂ O ₃ TEA addition	F.E.= 80% Dense and homogeneous Fe ⁰ structures with “spongy” appearance	2015 [52]
PTFE	WE: graphite cylindrical rod CE: Ni RE: Hg HgO (1 M, KOH)	NaOH (18 M) T = 110 °C 600 rpm E = -1.66 V t = 4 h 10 wt% iron oxides	F.E. (Fe ₂ O ₃) = 86% F.E. (FeOOH) = 66% F.E. (Fe ₃ O ₄) = 5% Small columnar crystallites for Fe ₂ O ₃ , denser for FeOOH	2017 [56]
No specified	WE: graphite rod encased by a Ti/Pt grid CE: no specified RE: no specified	NaOH (12.5 M) T = 110 °C 600 rpm j = 45 A/m ² 333.3 g/L red mud	E.F. = 71% No specified morphology of the Fe ⁰ deposits	2020 [58]

2.2.2. Electrochemical reduction in bulk

Research conducted on the electroreduction of iron oxides suspensions in alkaline medium served as a basis for the electroreduction in “bulk”. The increased interest in greener alternatives to the traditional iron production technologies was promoted by the possibility of using solid pieces of iron ores for *in situ* reduction. In fact, the research carried in suspensions medium was considerably improved in the last two decades due to the studies performed for the “bulk” concept. Thus, a more controlled environment allowed one to study closely the reductional mechanism on an iron oxide pellet acting as the cathode (WE) in the electrochemical cell. A schematic electrochemical cell is represented in Fig. 2.5. The iron oxide pellet is usually glued or attached to an electrically conductive wire, foil, grid or electrode material due to the low electrical conductivity of Fe_2O_3 at room temperature (10^{-14} S/cm [33]).

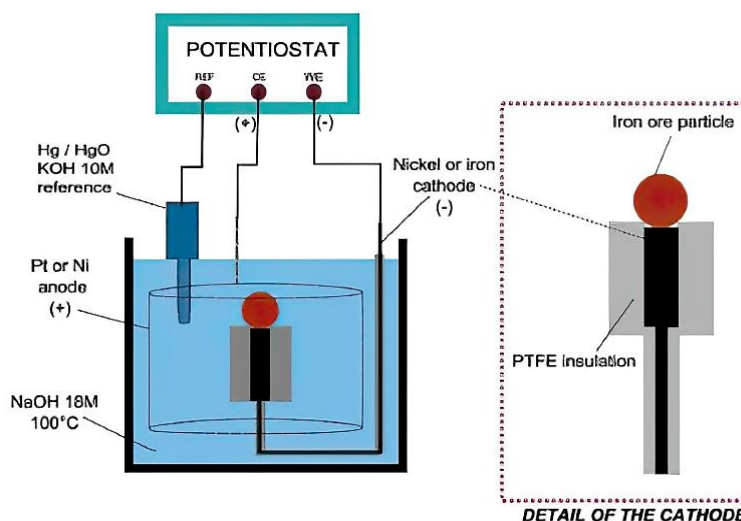


Fig. 2.5. Example of an electrochemical cell used for the electrochemical reduction in bulk [37].

After the work developed for alkaline suspensions previously mentioned [36], Allanore and his co-workers tried to perform a similar electrochemical reduction in bulk with iron ore particles [37]. Iron ores with 66.5 atom% of total iron were used as the WE (Fig. 2.5), where the major impurity was SiO_2 (2.15 atom%). These samples were measured under cathodic polarization (-1.2 V vs. SHE), and the current variations were analysed through time. A significant amount of fluctuations was observed and correlated to the formation of H_2 gas bubbles, affecting mechanically and electrically the contacts between the WE and the iron ore particle.

On the other hand, not only surface changes but also a significant porosity increase was observed at the end of the electrochemical reduction in the ore pellet, revealing a crystallographic rearrangement during the process. The porosity gain was related to the significant density difference between the iron oxide

pellet (5.26 g/cm^3) and metallic iron (7.86 g/cm^3), based on their lattice parameters. Mössbauer spectroscopy revealed the presence of 34 wt% of Fe_2O_3 , 29 wt% of Fe_3O_4 and 37 wt% of Fe^0 in the WE, resulting in 89% of Faradaic efficiency. Magnetite was identified as a partially reduced phase, which confirmed the general concept of Fe_3O_4 to be an intermediary phase during the reduction of Fe_2O_3 to Fe^0 given by Allanore in his previous work related to the suspensions [36]. Despite the high efficiency observed in this new study, the authors assigned the non-complete iron reduction to Fe^0 due to the low diffusion of both oxygen ions and Fe(III) in the electrolyte due to the low temperature used. There was the expectation that Fe_3O_4 phase could be immediately reduced to Fe^0 in the vicinity of the polarized pellet surface. The dissolution of some iron species was considered, but the authors did not explain the complex chemical interactions between the iron oxide and the alkaline solution in the small area of the polarized pellet at that time.

Two years later, similar experimental conditions were used by the same authors to investigate the mechanism of reduction to Fe^0 [6]. Iron ore lumps were used as a feedstock, mainly constituted by Fe_2O_3 (85 wt%) and Fe_3O_4 (5 to 10 wt%), with other minor phases (SiO_2 and Al_2O_3 , 2.5wt% each). During the chronoamperometry studies, three regions in the current (A/cm^2) vs time (s) curve were observed: i) electrolyte reduction (water electrolysis); ii) the current density increased until a maximum; iii) current plateau for larger iron oxide particles or symmetric current density variation for smaller particles.

The electrical insulating properties of Fe_2O_3 impose certain limitations for the electrochemical reduction to proceed. However, the agreed mechanism based not only on Pourbaix diagrams [45,47,59] but also those present in [6,37], relies on the Fe_3O_4 phase formation. The evolution of the crystal structure during the electrochemical reduction is shown in Fig. 2.6, along with the respective space group. The hexagonal crystalline structure of $\alpha\text{-Fe}_2\text{O}_3$ is transformed into the cubic structure of Fe_3O_4 . Further reduction leads to the formation of Fe^0 ($\alpha\text{-Fe}$), with a cubic crystalline structure.

According to [6], the spinel phase, possessing high electrical conductivity (10^3 S/cm [33,35]), undergoes a reductive dissolution leading to Fe(II) species in alkaline conditions, such as $\text{Fe}(\text{OH})_3^-$ (Eq. (2.6)). The formation of Fe^0 occurs due to the reduction of Fe(II) species as shown previously in Eq. (2.5). Moreover, Fe(II) reacts with the neighbouring Fe_2O_3 , forming Fe_3O_4 (Eq. (2.7)). The presence of Fe_3O_4 leads to a current increase, boosting the electrochemical reduction process, which is also self-promoted by the formation of highly-conductive Fe^0 . In fact, the dissolution of Fe_3O_4 to Fe(II) species was previously observed in a sodium perchlorate medium at room temperature [61].



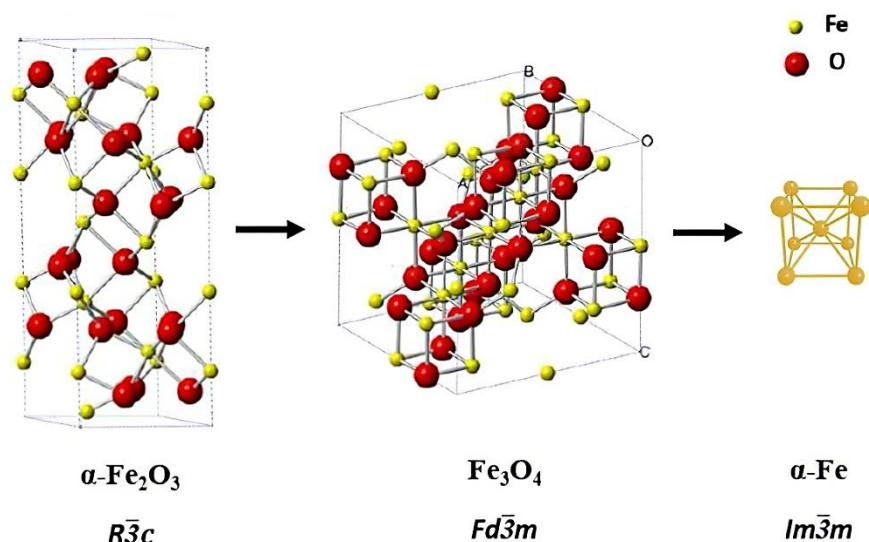


Fig. 2.6. Evolution of the atomic crystalline structures during the reduction of $\alpha\text{-Fe}_2\text{O}_3$ to $\alpha\text{-Fe}$, based in [60].

Furthermore, Allanore et al. suggested that the porosity of the reduced Fe^0 may be promoted by a metal|oxide interface filled with the alkaline electrolyte, where the electrical current passes through the porosity and the Fe_3O_4 particles in contact with the cathode. Higher Faradaic efficiencies (97 ~100%) were observed in comparison with the previous study [37], depending on the dimensions of the pellets. In some cases, the efficiency reached above 100% due to the presence of contaminants in the iron ore pellet, such as SiO_2 precipitates, as well as some electrolyte trapped inside the pores.

The study of the direct reduction of Fe_3O_4 to Fe^0 allowed one to have a better perception of the mechanism. He et al. [62] reduced thin films of Fe_3O_4 previously deposited at an Au cathode in NaOH electrolyte (2 M), at room temperature to 80 °C. Based on lattice parameters, the authors calculated around 52% of volume shrinkage would occur, at low temperatures, for a solid reduction of Fe_3O_4 ($Fd\bar{3}m$) to Fe^0 ($Im\bar{3}m$). The CV analysis indicated the start of the reduction at -1.2 V (vs. Ag|AgCl) at all temperatures. The reduction was proved not to occur at the Fe_3O_4 |electrolyte interface, but at the Au| Fe_3O_4 interface, based on the plane orientations of the metals, in accordance with the XRD analysis. The scanning electrode microscopy (SEM) confirmed a thin layer of Fe^0 between layers of Au and Fe_3O_4 , a new and more conductive $\text{Fe}_3\text{O}_4/\text{Fe}^0$ interface was established, suggesting a possible solid-state reduction. However, the authors clearly stated that was not entirely possible to conclude if the mechanism is a true solid-state reduction or if it follows a dissolution-redeposition route as suggested by Allanore et al. [6] (dissolution of Fe_3O_4 in the electrolyte as Fe(II) species such as $\text{Fe}(\text{OH})_3^-$). When one considers the solid-state route, the mechanism can occur by the direct reduction to Fe^0 (Eq. (2.8)), leading to the O^{2-} diffusion to the surface of the cathode (Eq. (2.9)), and consequent reaction with the aqueous medium, producing OH^- (Eq. (2.10)).



Despite the low O^{2-} diffusion coefficient in the Fe_3O_4 bulk, especially at low temperatures (5.6×10^{-19} cm^2/s at $500^\circ C$), He et al. [62] suggested that the diffusion can occur by electrolyte infiltration through the Fe_3O_4 grains. Haarberg et al. [63] proposed a similar solid-state mechanism, where O^{2-} ions diffused through a sintered Fe_2O_3 pellet ($800^\circ C$). The formation of porosity and fused particles during sintering might be crucial to initiate and propagate the electrochemical reduction through the pellet. On the other hand, isolated particles in the pellet were not expected to be reduced easily. Both Fe^0 and $FeOOH$ were detected by XRD analysis at the end of the electrochemical reduction tests.

Porosity loss from 45% to above 15% with the sintering temperature (700 to $1300^\circ C$) of pressed Fe_2O_3 powders and its effect on the electrochemical reduction was studied by Zou et al. [64], based on the O^{2-} diffusion through the pellet and electrolyte. Pellets sintered at temperatures lower than $1200^\circ C$ had a stable Fe_2O_3 phase present. However, for higher temperatures, both Fe_2O_3 and Fe_3O_4 were identified. Although the electrolyte access inside of the pellet depends strongly on the level of porosity, the pellets sintered at lower temperatures were mechanically unstable for the electrochemical tests. Optimum reduction conditions were attained with pellets sintered at $1100^\circ C$ (15% of porosity) mainly due to the easier access of the electrolyte inside of the cathode, leading to Faradaic efficiencies of nearly 60%. When the solid-state mechanism was investigated, Fe_3O_4 was observed to be formed before the metallic iron, confirming its presence as an intermediate product of the reduction, as suggested in [6]. In fact, the same reduction mechanism was suggested by Zou et al., with an exception of the reduction mechanism of Fe_2O_3 to Fe_3O_4 (Eq. (2.11)) as the first step of reduction, which was not approached in [6].



The reduction of Fe_2O_3 in the bulk pellet was suggested by Zou et al. to follow the three-phase interlines mechanism (3PIs), studied by other researches [65,66] focused on the electrochemical reduction of common solid insulator materials. A schematic representation of the 3PIs model is given in Fig. 2.7 and the corresponding electrochemical reduction of the solid insulator in Eq. (2.12). The general model implies that a solid-insulator material (represented as a cylinder) can only be reduced by an electrochemical reaction when it establishes a combined interface with the electrical conductor (*e.g.* metal wire connected to the insulator material – current collector) and an ionic conductor (liquid electrolyte) in order to form the three-phase interlines: current collector|solid insulator|electrolyte.

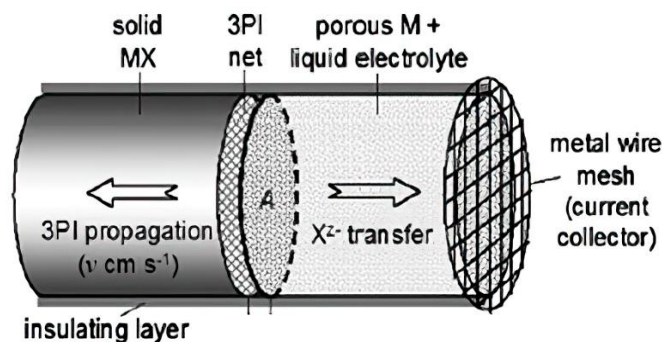


Fig. 2.7. Schematic model of the three-phase interlines (3PIs) during the electrochemical reduction of a solid-insulator material [66].

In this case, the general equation presented in Eq. (2.12) is valid,



where MX refers to the metal compound (not necessarily a metal oxide), M^0 is the solid metal, and X^{z-} is the anion transferred to the electrolyte. The starting point of the reduction of iron oxides is when a current collector (*e.g.* Pt, Ni wires, or grids) establishes an interface between the insulating Fe_2O_3 pellet and the electrolyte: current collector| Fe_2O_3 pellet|electrolyte. Thus, when the metal oxide (MX) is reduced to Fe^0 (M^0), a decrease of volume and increase of density promote porosity in the metal [37, 40, 66]. Simultaneously, O^{2-} (X^{z-}) anion is diffusing through the bulk electrolyte to promote O_2 evolution in the CE. During the reduction to Fe^0 , the electrolyte enters inside of the formed pores establishing new 3PIs. The mechanism progresses until the full conversion of the pellet to Fe^0 .

SEM micrographs suggest that the electroreduction process occurs first in the outside layer of the pellet (starting from the 3PIs from the current collector and further spreading along the surface) and, once the outside layer is converted into Fe^0 , the metallic iron acts as an extended conductor, leading to an eventual complete reduction to Fe^0 in the core of the pellet. This reduction process was called by Zou and his co-workers as the “shrinking-core reaction”. Current-time curves reported by the authors are represented in Fig. 2.8 and demonstrate three periods (i to iii) occurring during the electroreduction:

- i. 0 to 1 h: current increases, that can be divided into two stages. The first 0.5 h represents the electrolyte access to the external layer of the pellet and the second 0.5 h (until 1 h) due to the expanding of the 3PIs reaction along the surface;
- ii. 1 to 3 h: the maximum of current is reached due to full reduction to Fe^0 in the all surface of the pellet and the core remains unreacted;
- iii. 3 to 4.5 h: shrinking of the pellet while the core is reduced to Fe^0 . Since the area of the pellet decreases due to the shrinking, the current decreases until a complete reduction to Fe^0 and the current stabilizes (residual current).

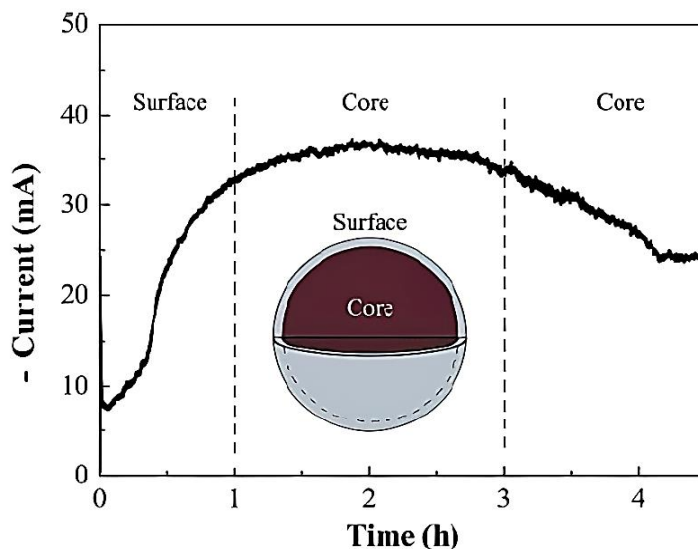


Fig. 2.8. Electroreduction process of a Fe_2O_3 pellet in the alkaline solution: a typical current-time curve [64].

Tuning the porosity of the WE has gained interest since the 3PIs interface can be easily enhanced by increasing the accessibility of the electrolyte through the insulator iron oxide pellet. Monteiro et al. [39] studied and compared the electrochemical reduction of dense (1% vol. of open porosity) and porous (22% vol. of open porosity) Fe_3O_4 pellets to Fe^0 , previously sintered at 1100 °C and 1400 °C, respectively. When the porosity of the pellet precursor is higher, more complete is the reduction process since the samples with higher porosity proved to have higher electrolyte impregnation rate and electrochemical activity, leading to faster reduction rates. Thus, a higher Faradaic efficiency was obtained (85%) for higher porosities (22%). Another interesting point of this study was the range of low temperatures tested (22, 50 and 90 °C) for -1.15 V (vs. $\text{Hg}|\text{HgO}$), where it was possible to observe that when increasing the temperature, higher current densities were attained, which consequently led to more efficient Fe^0 production. The weak point appeared to be the fact that the Fe^0 obtained is too fragile due to the high porosity of the pellets.

So far, one could not find clear evidence confirming the direct reduction of Fe_3O_4 to Fe^0 in alkaline conditions. The first step apparently corresponds to the reduction to Fe(II) species, supported by Monteiro and co-workers. Studies performed in acidic conditions reported the same two-step concept for Fe_3O_4 [61,67,68]. Instead, several Fe(II) species are suggested to participate in the reduction mechanism in alkaline conditions, based on Pourbaix diagrams [45,59], such as HFeO_2^- (Eq. (2.13) and (2.14)).



It should be noticed that Fe_3O_4 is slightly soluble in alkaline medium leading to $\text{Fe}(\text{OH})_4^-$ species (Eq. (2.4)) and consequently reduces to Fe(II) as $\text{Fe}(\text{OH})_3^-$ [69] (Eq. (2.5)), as it is for Fe_2O_3 . Thus, the dissolution-redeposition process ($\text{Fe}_3\text{O}_4 \rightarrow \text{Fe}(\text{OH})_4^- \rightarrow \text{Fe}(\text{OH})_3^- \rightarrow \text{Fe}^0$) was also proposed to occur during the electrochemical reduction of Fe_3O_4 [70,71]. The presence of $\text{Fe}(\text{OH})_2$ as Fe(II) species at high temperatures ($> 65^\circ\text{C}$) was opposed by the thermodynamic studies of Le and Ghali [45], as previously mentioned in the section of electrochemical reduction of alkaline suspensions. However, its presence at lower temperatures is observed in several works, especially in the works devoted to the anodic oxidation of Fe^0 electrodes [72,73]. On the other hand, works such as [39,40,43,74] refer to a possible presence of $\text{Fe}(\text{OH})_2$, based on the voltammograms obtained at higher temperatures. In fact, the oxidation of $\text{Fe}(\text{OH})_2$ to Fe_3O_4 was predicted by thermodynamic studies at temperatures higher than 288°C , and at the highest level of H_2 evolution [69]. The following cathodic (Eq. (2.15)) and anodic (Eqs. (2.16) and (2.17)) reactions are expected to occur, mainly at temperatures below 65°C .



Regarding the current density, it was verified that these values are proportional to the electrochemically active area of the cathodes, which, on the other hand, is directly related to the porosity of the sample, since higher open porosities led to higher surface areas available for the reduction.

Residual porosity resulting from the sintering conditions has proved to have an important role during the electrochemical reduction in bulk samples. However, the porosities over 45% (due to sintering at 700°C in [64]) were not studied until 2017. The investigation of the impact of higher porosity levels during the electroreduction was conducted by Ivanova et al. [40]. Cellular-designed Fe_2O_3 materials were successfully processed by emulsification of Fe_2O_3 suspensions in water (50% of solids) with an organic phase (liquid paraffin) to promote the open porosity after burnout of the organic phase and firing up to 1200°C , based on previous studies with alumina powders [75–77]. The paraffin allowed for a proper cellular skeleton, with high open porosity (64%) and high interconnectivity between pores, which promoted the entrance of the electrolyte into the porous structure. The typical cyclic-voltammetry analysis results are shown in Fig. 2.9 and demonstrate the main differences between the cathodic and anodic peaks at different electrolyte concentrations, temperatures and open porosities. At both temperatures tested, 25°C and 90°C , and at 1 M of NaOH (Fig. 2.9A), two cathodic peaks were identified as the reduction of Fe_2O_3 to Fe(II) species ($C_1 \approx -1.0\text{ V}$) and reduction to Fe^0 ($C_2 < -1.1\text{ V}$). Slightly higher current densities were observed when increasing the temperature up to 90°C , where the H_2 evolution (current B) is more prominent. The anodic processes, on the reverse of the curves, were

more visible at 90 °C, where two peaks related to the Fe⁰ oxidation to Fe(II) species such as Fe(OH)₂ and/or Fe₃O₄, and possibly FeOOH, can be observed. Increasing the concentration of the electrolyte to 10 M (Fig. 2.9B), promoted a high impact on the current density, possibly due to the reported solubility of iron oxides when increasing the concentration and temperature of the electrolyte. Increasing the porosity up to 64% provided more electrolyte infiltration inside the pore structures and a considerably higher surface area.

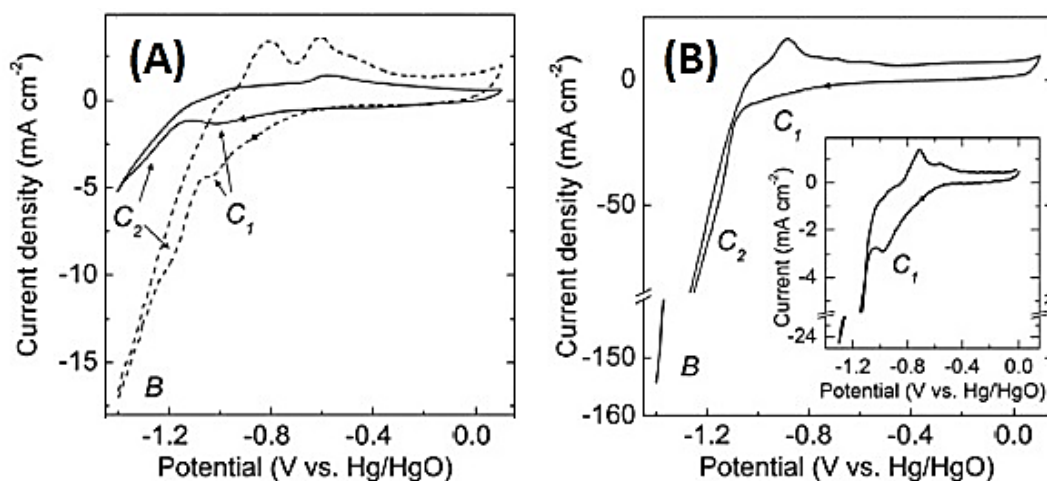


Fig. 2.9. Typical voltammograms curves from Fe₂O₃ pellets recorded at 10 mV/s with (A) 44% of open porosity at 1 M NaOH solution at 25 °C (solid line) and 90 °C (dashed line); (B) 44% of open porosity at 10 M NaOH solution at 90 °C and with 64% of open porosity (inserted figure) at the same conditions, from [40].

The porosity improvement facilitated the reduction of Fe₂O₃ to Fe₃O₄, and later the formation of Fe⁰ crystals in the porous structure, as can be seen in Fig. 2.10. Cubic particles (1 to 2 μm) of Fe⁰ were formed after the electrochemical reduction (Fig. 2.10B and C), also confirmed by XRD. However, at polarizations of -1.5 V and -1.15 V, Faradaic efficiencies of 21% and 39%, respectively, were fairly low, mostly due to side reaction of H₂ evolution. After the electrochemical reduction, the ceramic cathode shrank in volume, increasing the porosity as mentioned in previous studies. The generated porosity allows the escape of H₂ and provides new interfaces for the reduction.

Due to the limited insulating properties of Fe₂O₃ to trigger the electrochemical reduction, the dimensions of the pellets needed to be controlled, while relatively low areas were often used. A colloidal iron oxide electrode developed by Wang et al. [78] is a possible alternative. For this purpose, a solution of Fe₂O₃ particles, NaOH aqueous solution and a dispersion agent were mixed. The suspension was added to glass carbon to develop a 3D percolating electrical conducting network. The resulting colloidal film (1 μm) was then coated on a Ti plate to work as the WE. Based on good electrical properties, higher currents were expected to be achieved, in comparison with the electrochemical reduction in bulk or suspension. Thus, the area of the current collector can be increased due to the improved transference of

electrons and ions. The colloidal electrode was able to be reduced to Fe_3O_4 and Fe^0 , but the current achieved was around -23 mA/cm^2 . A full conversion to Fe^0 was not achieved, and the authors attributed it to the high H_2 evolution during the reduction. The Faradaic efficiency was not quantified, allowing one to assume a relatively low efficiency.

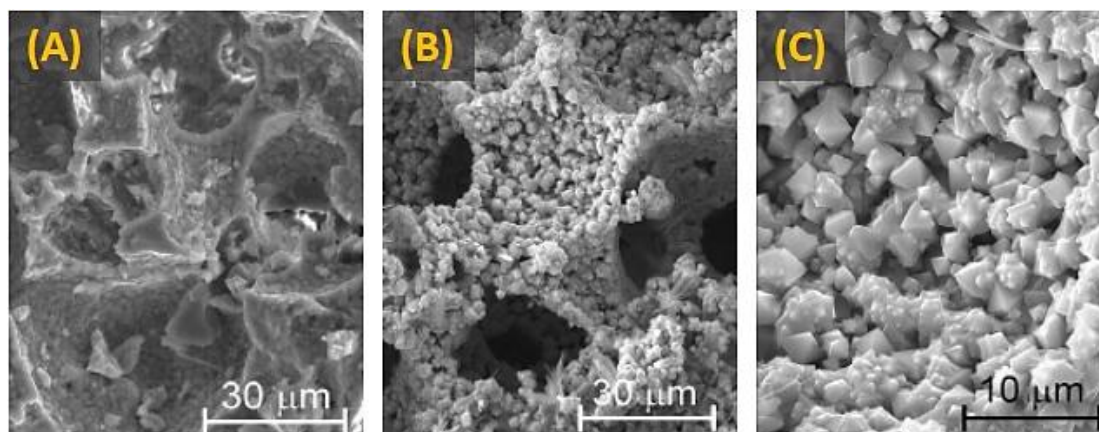


Fig. 2.10. SEM micrographs of Fe_2O_3 pellets with 44% of open porosity (A) before reduction; (B) and (C) after reduction, from [40].

Table 2.5 summarizes the work conducted on the electrochemical reduction of bulk iron oxides cathodes so far. Despite the differences in the cathode designs, high electrical conductivity wires based on Ni, Au, Pt or Ti have been used as current collectors on the insulator iron oxide pellets. Different approaches can be found in different studies. However, the temperatures between $80 \text{ }^\circ\text{C}$ to $110 \text{ }^\circ\text{C}$ are the most frequently used, as well as highly concentrated electrolytes ($\geq 10 \text{ M}$), except for the reduction of thin Fe^0 films. Nearly 100% of current efficiency was attained with 18 M in [6].

Table 2.5. Operation conditions and main results achieved for the electroreduction in bulk of iron oxides.

Cell	Electrodes	Operation conditions	Faradaic Efficiency/ ZVI produced	Year/ Ref.
-	WE: iron ore connected to Ni wire, covered by PTFE CE: Pt RE: Hg HgO (10 M, KOH)	NaOH (18 M) T = $100 \text{ }^\circ\text{C}$ t = 23 min E = -1.2 V (vs. SHE) WE _{area} = 3.1 mm^2 WE _{weight} = 1.7 mg	E.F. = 86% 34 wt% of Fe_2O_3 29 wt% of Fe_3O_4 37 wt% of Fe^0	2008 [37]
Glass beaker	WE: Horizontal disk made of Fe_2O_3 ore lumps with Ni wire CE: Pt RE: Hg HgO (10 M, KOH)	NaOH (18 M) T = $100 \text{ }^\circ\text{C}$ t = 17 min E = -1.2 V (vs. SHE) WE _{area} = $0.034\text{--}0.134 \text{ mm}^2$ WE _{weight} = $0.162\text{--}1.31 \text{ mg}$	E.F. = 53–100% 0.07–0.90 wt% of Fe_2O_3 0.05–0.51 wt% of Fe_3O_4 0.02–0.64 wt% of Fe^0	2010 [6]

Table 2.5. Operation conditions and main results achieved for the electroreduction in bulk of iron oxides (cont.).

Cell	Electrodes	Operation conditions	Faradaic Efficiency/ ZVI produced	Year/ Ref.
-	WE: Thin films of Fe ₃ O ₄ predeposited in an Au cathode CE: - RE: Ag AgCl (1 M, KOH)	NaOH (2 M) T = 25 - 80 °C 200 rpm E = -1.22 V (vs. Ag AgCl) 600 nm of Fe ₃ O ₄ in the WE	- 200 nm of Fe ⁰ deposition	2011 [62]
Teflon	WE: Fe ₂ O ₃ sintered pellet (800 °C) surrounded by a Pt wire CE: Ni metal mesh RE: Hg HgO (1 M, KOH)	NaOH (18 M) T = 110 °C t = 29.5 h j = 300 mA WE _{area} = 78.5 mm ²	- Fe ⁰ and FeOOH	2014 [63]
PTFE	WE: Fe ₂ O ₃ sintered pellet (700 to 1300 °C) covered in porous nickel foil CE: Pt RE: -	NaOH (18 M – 30 M) T = 110 °C t = 2.5 h E = -1.7 V WE _{diameter} = 3.6 mm WE _{weight} = 60 mg	E.F. = 40–70% Fe ₃ O ₄ and Fe ⁰	2015 [64]
-	WE: Ti plate with colloidal Fe ₂ O ₃ film with C network CE: Pt foil RE: Hg HgO	NaOH (16 M) T = 110 °C t = 5 h E = -1.7 V WE _{area} = 1.2 cm ²	- Fe ₃ O ₄ and Fe ⁰	2015 [78]
Teflon	WE: Fe ₃ O ₄ pellets with nickel foil and silver paste CE: Pt RE: Hg HgO NaOH (1 M)	NaOH (10 M) T = 90 °C t = 5.5 h E = -1.15 V	E.F. = 85% for pellets with high porosity (22% of open porosity) Fe ₃ O ₄ and Fe ⁰	2016 [39]
Teflon	WE: Fe ₂ O ₃ highly-porous pellets (fired at 1100–1200 °C); glued with silver paste to Ni foil CE: Pt RE: Hg HgO NaOH (1 M)	NaOH (10 M) T = 90 °C t = 100 s E = -1.5 and -1.15 V	E.F. = 21% (-1.5 V) and 39% (-1.15 V) Fe ₃ O ₄ and Fe ⁰	2017 [40]

2.2.3. Challenges and hydrogen evolution reaction

Although the mechanisms of electrochemical reduction of iron oxides to Fe⁰ in alkaline medium appear to be mostly agreed nowadays, its application at the industrial level is still believed to be far to occur. Several challenges imposed by both systems (suspensions and bulk) are needed to be solved to improve the Faradaic efficiencies, especially towards hydrogen evolution.

During the reduction in alkaline suspensions of iron oxides particles under stirring conditions, not only a poor dissolution can be expected as mentioned previously [69,79], but also a poor adhesion to the WE might take place [53]. In fact, the diffusion of Fe₂O₃ particles can be described by a Stokes-Einstein equation, giving a slow diffusivity of 10⁻¹⁴ m²/s in strong alkaline medium, at 100 °C [78]. On the other

hand, the Fe⁰ electrodeposition in the WE depends not only on the effective area of the electrode, but also on the WE material, which can actively contribute to H₂ evolution itself. With time, rotating cathodes were implemented in the electrochemical cell [36,48,73], increasing the contact between the WE and the suspended particles effectively, until a certain controlled level of speed that does not hamper the current efficiencies (2000 rpm [48]). The rotation speed was proved to be an important parameter, since the particles tend to sediment at the bottom of the cell at low stirring level, while high rotation speeds can promote gas bubbles around the WE. However, and in a general way, electrode disks are hard to implement at a large scale, due to the high energy consumption and complicated setup of the cell.

During the electroreduction of iron oxides in bulk, the main issue seems to be related to the insulating properties of Fe₂O₃, leading to the limitations of the pellet dimensions for attaining suitable current efficiencies. Moreover, electrically conductive wires/grid/supports surrounding the pellets are needed to establish the current collector interface with the insulator pellet. Pressed pellets and artificially porous structures are frequently prepared for designing iron oxides as cathodes at laboratory scales, which is unlikely to occur at industrial scales with large quantities of iron oxides.

The production of hydrogen during cathodic polarizations in alkaline media is by far one of the main issues for this type of electrolysis and is a well-known side reaction. This parasitic effect, usually referred to as hydrogen evolution reaction (HER), occurs at superimposed potentials of the reduction to Fe⁰, leading to a cathodic current competition. HER occurs due to water electrolysis in alkaline media as shown in Eq. 2.18. [32,36,40].



Moreover, metals used as cathodes such as Fe, Ni, Co, Ag, Cu or Au have a moderate activity for HER when compared to noble metal HER electrodes (Pt, Pd or Ru), which are known for their lower activity. Other metals such as Ti, Zn, Sn or Pb are known for their high overpotential [52,80]. On the other hand, one must take into account that most studies of HER are based on acidic electrolysis (Eq. 2.19. [81]), rather than in an alkaline medium.



Hydrogen evolution may also depend mainly on microstructural features of the Fe⁰ deposit, if one considers complete coverage of the cathode substrate with a nearly impervious and adherent Fe⁰ layer. In this case, the Fe⁰ deposit becomes the effective cathode, and its morphology determines the effective electrode area. In addition, poorly adherent Fe⁰ deposits may also affect Faradaic efficiency, as loose Fe⁰ particles may detach from the substrate, losing cathodic protection and reoxidising. Thus, hydrogen evolution and its impact on Faradaic efficiency is a complex issue, which may include

dependence on the nature and morphology of the substrate itself, on operating conditions which determine competing effects on hydrogen evolution and deposition of Fe^0 , as well as its morphology. The initial stage may play a greater effect since it is most likely to determine the adherence and morphology of deposited Fe^0 .

In the alkaline medium cases, HER is responsible for lowering the Faradaic efficiency of the iron oxides electroreduction, down to the values of around 7% to 39%, as reported in [40]. However, this may depend on whether the operating mode is galvanostatic or potentiostatic, and the corresponding potential range. Nickell et al. [82] simulated the H_2 evolution potentials vs Hg|HgO reference electrode in alkaline conditions, based on the overall cell reaction from Eq. (2.20) by the Nernstian analysis represented in Eq. (2.21). One should take into consideration that the potential of the RE strongly depends on the activity of OH^- ions. Nevertheless, the overall cell equation represents the combination of the half-cell potentials from Hg|HgO reference electrode ($\text{Hg} + 2\text{OH}^- \rightarrow \text{HgO} + \text{H}_2\text{O} + 2\text{e}^-$) and the half-cell alkaline water reduction from Eq. (2.18) occurring in the cathode, leading to the elimination of the OH^- factor in the Nernst equation applied. In Eq. (2.21), the $E_{\text{H}_2, \text{HgO}}^0$ is the standard potential of H_2 evolution vs Hg|HgO (-0.926 V), R is the universal gas constant (8.314 J/(K.mol)), T is the temperature (K), F the Faraday constant (96485 C/mol), α_{H_2} and $\alpha_{\text{H}_2\text{O}}$ are the chemical activity of H_2 and H_2O , respectively.



$$E_{\text{H}_2, \text{HgO}} = E_{\text{H}_2, \text{HgO}}^0 - \frac{RT}{2F} \ln \frac{\alpha_{\text{H}_2}}{\alpha_{\text{H}_2\text{O}}} \quad (2.21)$$

Fig. 2.11 shows the calculated values of H_2 evolution potential, increasing to more cathodic values, when increasing both temperature and NaOH concentration in the electrochemical cell. When performing the alkaline electrolysis at 90 °C, more concentrated media should be used to prevent H_2 evolution to less cathodic potentials. Thus, the calculated potential for H_2 evolution with a NaOH solution of 10 M, at 90 °C is around -0.910 V (vs. Hg|HgO), when considering only water electrolysis inside the cell and a Pt plate as a cathode. According to literature studies, the onset potentials of around ≈ -1.09 V or -1.1 V (vs. Hg|HgO) to higher cathodic potentials [48,52,83] in the cyclic-voltammetry analysis are frequently associated with H_2 evolution during iron oxides reductions in alkaline conditions. Thus, some considerable H_2 evolution should be already present even at less cathodic values below -1.09 V, leading to a decrease of the Faradaic efficiencies.

According to [36], the first 10^4 s of the cathodic polarization in alkaline media is detrimental to HER. Hydrogen is adsorbed on the surface of the WE, creating higher overvoltages. When using a rotation cathode, H_2 was appointed as the reason causing over negative potentials (-4 V vs. Hg|HgO), when cathodic rotation rates increased from 2000 to 3000 rpm, due to the coverage of the surface of the

cathode in [48]. A drop in the current efficiency from 95% (< 1000 rpm) to 76% (3000 rpm) was observed. In [6], the current drops were observed during the study due to the evolution of H₂ bubbles, causing the vibration of the iron oxide pellet used as a ceramic cathode.

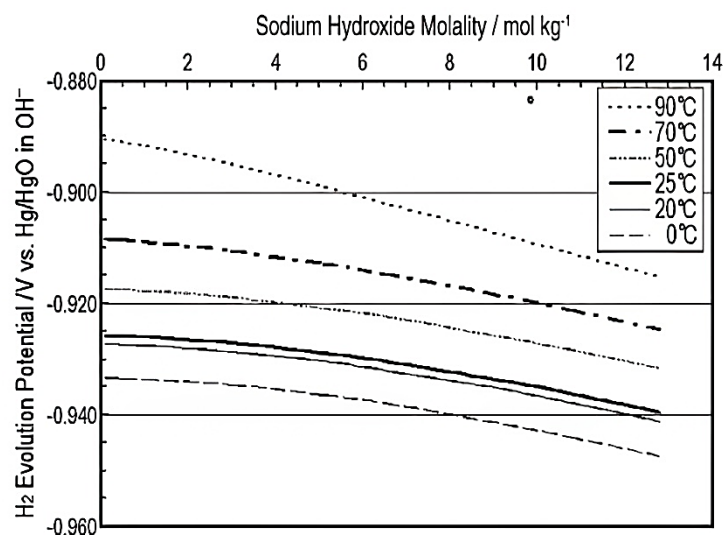


Fig. 2.11. Simulated potential of the H₂ evolution vs. Hg/HgO (V) with temperature (°C) and concentration (mol/kg) of NaOH solution [82].

In order to minimize the effect of HER, research has been conducted to improve the working electrode for the electrochemical reduction. Thus, in some studies the surface of the cathode was modified by adding porosity, increasing the active area for the reduction, and allowing H₂ to escape from the pores. With around 72 vol.% of open porosity [40] and adding carbon to the Fe₂O₃ ceramic cathodes [52] was proved to have a beneficial impact towards higher Faradaic efficiency.

Despite being considered a disadvantage of the aqueous alkaline Fe electrolysis, one may also consider alternative concepts based on co-electrolysis of Fe and H₂, which is a valuable commodity and can be used to store renewable energy. In fact, hydrogen production by alkaline water electrolysis is also a promising technology, but its current efficiency remains low at temperatures in the range between 30 to 80 °C, and typical electrolyte concentration of about 30 wt% (KOH or NaOH). Thus, other options are based on the operation at higher temperatures and in pressurized conditions, with prospects to generate pressurized gases (H₂ and O₂) directly, and relying on separation membranes; this adds higher costs associated with its installation, safety and maintenance. On the other hand, similar operation conditions used during the iron oxides electroreduction in alkaline media are proved to generate H₂ due to the use of cathodes with suitable activity for the HER; this raises prospects for co-electrolysis of Fe and H₂ produced simultaneously. Despite no studies were performed so far on the storage of the H₂ produced during Fe electrowinning processes, commercial membranes are available for gas separation

in water electrolysis and similar membranes might be used as well during the electrowinning technology for this purpose [80,84].

2.2.4. Design of the electrochemical cell and future industrial applications

Little progress has been observed in the design of the electrochemical cells for iron oxides reduction with time. The most relevant changes are related to the suspensions medium. For the latter, a rotating disk electrode acting as a cathode was early implemented, at least around the 1950s [41], whilst its negative impact towards the Faradaic efficiency was immediately observed. Air stirring was also attempted. However, splash and CO₂ entrance into the electrolyte from the air were observed. In the mentioned investigation, the rotating disk was substituted by an agitator impeller with a better outcome. Later on, other researchers tried to use rotating disks, but they seemed to agree on the lower efficiency provided by the combination of air bubbles with H₂ (g) bubbles [48]. In the study developed by LeDuc et al. [41], the use of two consumable anodes (Ni and Fe plates which were corroded during the electrochemical process) and two cathodes (steel sheets) were reported, since a high-volume cell was used (4 L). When the same authors tried a pilot-scale approach, the wall of the electrochemical cell (Ni sheet) was used as one of the two anodes utilized. After the study performed by LeDuc, the target of the majority of the conducted research has been devoted to understanding the electrochemical mechanisms around the chemistry of iron oxides. The volume of the electrochemical cells have been about 80 to 250 mL, and a single cathode and one inert anode have been used.

Thinking about a future large-scale application of this electrolytic process, Allanore and co-workers devoted a study towards the engineering aspects of the electrochemical cell for the iron oxides reduction in suspension [85]. Three types of cells were tried, including a design of horizontal parallel electrode plates where the electrolyte was placed between the plates; and two types of rotating disk electrodes, an inner rotating anode surrounded by a fixed cathode; and a fixed anode with a rotating cathode surrounding it. The tests were performed in galvanostatic mode (0.1 A/cm²) at around 110 °C, with 33 wt% of Fe₂O₃ particles in a NaOH (18 M) solution. The electrodes of each cell were made of Ni (CE) and porous graphite (WE). In the parallel plates design, the electrolyte was kept circulating at a fixed rate through the plates with a centrifugal pump. The results showed a minimum of 80% of Faradaic efficiency in all design tested, where the configurations with rotating disk electrodes showed the lowest efficiency. On the other hand, the cell configuration of the parallel plates reached 98% of current efficiency. Moreover, rotating disks proved to have limitations on the transport of the suspended particles near the WE, especially when the rotating surface is the WE. In the latter case, the O₂ gas bubbles generated on the CE are dragged to the rotating WE, leading to the oxidation of the produced metal and, consequently, low efficiencies are attained. In the parallel plates design, the gas is far from the WE and lower electrical energy was consumed. Despite this alternative, the larger-scale cell of

horizontal parallel electrodes configuration tested by Allanore in 2010, it seems to have not been performed ever since, even at a laboratory scale. On the other hand, bulk electroreduction usually does not require stirring, due to its *in situ* reduction.

A typical electrochemical cell is represented in Fig. 2.12. Teflon and PTFE polymers are frequently used nowadays as reactors, suitable for high-temperature alkaline solutions. Although not shown, two free spaces for gas exclusions, H_2 (g) and O_2 (g), are present in the lid of the reactor. The WE consists of an iron oxide pellet attached to an electrically conductive metal (Ni, Au,..) in the bulk medium, or it can be substituted by a plate or mesh of the conductive metal for the iron oxide suspensions medium. The RE is usually a Hg|HgO electrode due to its suitable behaviour in strong alkali solutions without contaminating the WE [82,86]. Thus, this electrode is commonly placed in a separate electrolyte solution, which is connected to the electrolyte inside the cell by an electrolyte bridge. The bridge usually ends in a capillary, the Luggin capillary, that is placed near the WE, preventing the potential drop in the electrolyte between the capillary and the WE [3,87]. The CE is often a Pt or Ni wire or plate, while a heating system surrounds the electrochemical cell.

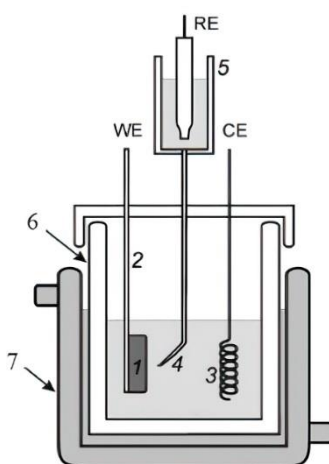


Fig. 2.12. Schematic representation of a typical electrochemical cell for the reduction of ion oxides, where: 1) working electrode (WE); 2) metallic current collector; 3) counter electrode (CE); 4) Luggin capillary; 5) teflon tube for the reference electrode support, filled with the electrolyte; 6) electrochemical Teflon/PTFE cell; 7) heating system, adapted from [40].

Under the scope of the SIDERWIN project, the industrial partner Maizieres-les-Mets R&D ArcelorMittal lab (France) is developing a lamellar anode of Ni coated with 20 μm of Co to decrease the high overvoltage caused during O_2 (g) evolution. The new configuration allows a fast and immediate O_2 gas bubbles removal of the cell, improving the energy efficiency of the electrowinning process. Moreover, recently a pilot-scale cell was developed, capable of producing 3.6 kg of Fe^0 from an iron oxides suspension (ultrafine particles) per electrochemical reduction batch (maximum of 75 h), with 99

wt% of purity with a Ni working electrode. The Fe^0 deposits revealed a compact growth and current efficiencies between 72-91% [88,89].

While the electrowinning technology in the alkaline medium is still far from its industrialization, the general scheme of a future implementation is represented in Fig. 2.13, which is in consideration by the SIDERWIN project. The typical electrochemical cell shown in Fig. 2.12 is expected to be implemented after the processing of the iron ores by grinding and leaching of the undesirable compounds from the ores (gangue), which are mainly SiO_2 . After the cathodic metallic production of iron, steel will be produced by an electric arc furnace technology to melt the Fe^0 . Thus, 1.5 tons of iron ores are expected to produce 1 ton of steel, with global consumption of 3.6 MWh/ton or 13 GJ/ton [88], which is reported to be lower than an efficient blast furnace Fe^0 production route with 19 GJ/ton [90].

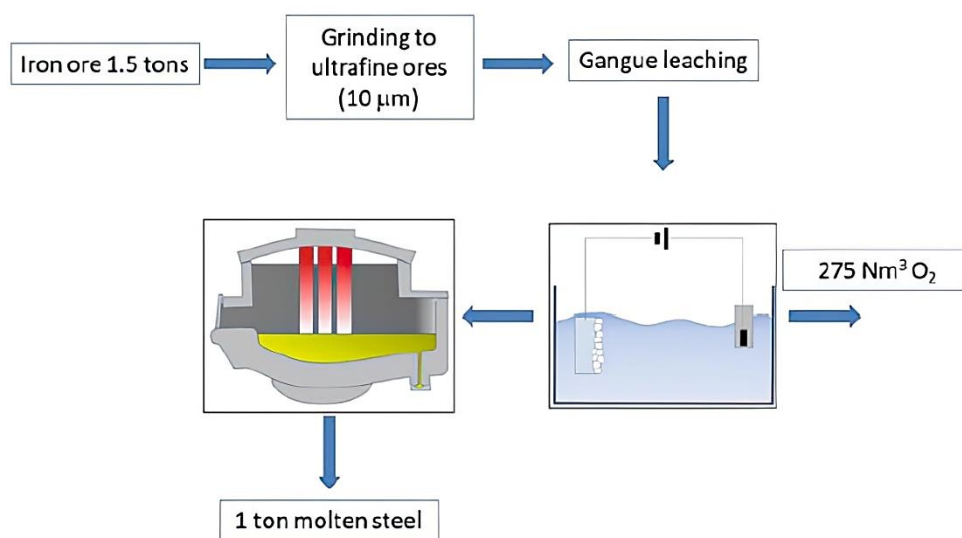


Fig. 2.13. Scheme of the proposed electrowinning route at the industrial scale [88].

2.3. Red mud: an overview and related trends

The alumina industry uses the Bayer process for its extraction from the bauxite ore. However, during the Al_2O_3 extraction from the ore, high volumes of alkaline red mud waste are generated. Around 1.5 tons of red mud are generated per ton of Al_2O_3 produced, leading to the estimation of around 160 million tons of red mud in 2015 [91,92]. Alumina industry is trying to find economical and sustainable ways for the stockpile of high amounts of red mud waste.

2.3.1. Sources and environmental concerns

The bauxite residue (red mud) is obtained after the digesting of the ore with concentrated NaOH (up to 9 M [93]) solution at 240 °C, with 1 to 6 atm of pressure. Bauxite ore is mainly composed of gibbsite ($\text{Al}(\text{OH})_3$), boehmite ($\gamma\text{-AlO}(\text{OH})$), and diaspore ($\alpha\text{-AlO}(\text{OH})$), as well with some insoluble phases such iron oxides and quartz, between others [93,94]. The main composition of the ore contains around 27 wt.% of aluminium oxide phases, 40% of iron oxides and 12% of SiO_2 [95]. During the alkaline digestion, the aluminium-containing phases present in the ore are dissolved as aluminate anion ($\text{Al}(\text{OH})_4^-$) to the solution, and the residue is formed during this stage, which is separated by filtration from the solution. After cooling, $\text{Al}(\text{OH})_3$ and $\text{AlO}(\text{OH})$ precipitates are further decomposed to Al_2O_3 by calcination at 1000 °C [93–95]. The obtained Al_2O_3 is later reduced by an electrolytic method, the Hall-Hérout process, for the metallic aluminium (Al^0) production [94]. China is the highest world producer of red mud, followed by Australia, Brazil, India and Greece [92].

Besides the high volume produced, the high alkalinity of the red mud, the high salinity levels, and the presence of hazardous metal oxides are the major issues attributed to the negative environmental impact [92,96]. The mud is usually disposed of in large ponds for dewatering and posterior drying to reduce the volume of the waste, as shown in Fig. 2.14. Despite being considered a hazardous waste, red mud is usually landfilled after drying, but vast areas of land are needed for this purpose, jeopardizing agriculture fields. In fact, landfilling the sludge causes leakage to the soil and groundwater causing high levels of contamination. Another disposal option considered previously consisted in dumping it into the sea [94,97]. The neutralization of red mud can be an alternative to decrease the environmental impacts due to its high alkalinity. However, the high volume produced makes it an expensive option, since large amount of acidic solutions would be needed for this purpose.

Another concern is the radioactivity of some red mud samples. The trace levels of radioactive elements such as ^{238}U , ^{232}Th , and ^{40}K have been reported by measuring gamma radiation [99,100]. However, the presence of radioactive elements depends strongly on the characterisation of bauxite ore, which will vary considerably from one region to another. Specialised research should be conducted in order to study the leaching behaviour and the irradiation index of the radioactive elements attending to international norms. The safe disposal of red mud is now considered to be an international issue since severe accidents have been reported due to the collapse of the infrastructures where the residue is deposited, not only due to the contaminating of fields and water streams, but also due to injuring and killing lives [96].



Fig. 2.14. Dried red mud in a pond [98].

2.3.2. The phase composition and general chemistry of the red mud

The phase composition of the red mud waste depends significantly on the quality of bauxite ore as well as the Bayer process operating conditions. In fact, the mud can have around 40% of the ore composition [95]. Generally, its composition consists in: Fe_2O_3 (7-65 wt%), Al_2O_3 (6-36 wt%), SiO_2 (3-34 wt%), TiO_2 (trace-15 wt%), Na_2O (2-10 wt%) and CaO (2-38 wt%) [91,92,95,101,102]. Some trace levels of MnO , MgO , K_2O , P_2O_5 or SO_3 can be present [94], besides the presence of V (730 mg/kg), Zr (1230 mg/kg), Ga (60-90 mg/kg), U (50-60 mg/kg), Cr (497 mg/kg), Ni (31 mg/kg), Zn (20 mg/kg), Th (20-30 mg/kg), Sc (60-120 mg/kg) or Y (60-150 mg/kg) [95,102]. Table 2.6 gives an overview of the red mud characterisation from some alumina production plants worldwide concerning the major elements.

Table 2.6. General composition of red mud from different plants worldwide based on [92].

Country	Plant	Composition (wt.%)						Ref.
		Fe_2O_3	Al_2O_3	SiO_2	TiO_2	Na_2O	CaO	
China	Guangxi	34.3	18.9	8.9	6.1	4.4	13.6	[103]
China	Shandong	12.3	6.3	17.8	3.3	2.8	37.5	[104]
India	Narco	51.0	18.0	4.6	9.8	5.3	1.8	[105]
Turkey	Etibank	38.7	19.0	15.6	5.0	10.0	4.3	[106]
Brazil	São Paulo	27.0	22.9	19.2	3.0	8.0	2.2	[107]
Greece	Aluminium of Greece	20.0	40.8	6.8	5.8	2.7	12.6	[108]
Spain	San Ciprián	39.2	19.8	8.8	10.0	5.0	4.5	[109]

The major phases are mainly iron and aluminium oxides or oxy-hydroxides. Thus, goethite (α -FeOOH), maghemite (γ -Fe₂O₃), magnetite (Fe₃O₄) can be found along with Fe₂O₃; and gibbsite (Al(OH)₃), boehmite (γ -AlO(OH)) and diaspore (α -AlO(OH)) can be present along with Al₂O₃. However, the high complexity of the waste can lead to the presence of phase mixtures such as ilmenite (FeO.TiO₂), perovskite (CaTiO₃), aluminosilicates such as kaolinite (Al₂Si₂O₅(OH)₄) or sillimanite (Al₂SiO₅), among many others [102].

The concentrated NaOH solution used for the digestion of the bauxite ore causes the high alkalinity of the residue, characterised by a pH up to 13 [96]. Moreover, red mud presents usually high electrical conductivity, especially due to the relatively high Na⁺ content [96,110], which can vary between 1.4 to 28 mS/cm [110,111].

2.3.3. Current trends of red mud utilization

Despite the environmental concerns towards red mud, its chemical properties, especially related to the high content in metals, have been considered interesting for a wide number of applications. The development of practical applications seems to be a valuable alternative to reduce the amount of sludge discarded in the soil. The overview of the red mud-based applications according to the registered patents from the year 1964 to 2008 are shown in Fig. 2.15, which is the result of 734 patents. The major applications are related to the use of red mud for construction materials (33%), as catalysts and adsorbents (13%), followed by ceramics, coatings or plastics applications as well for water treatments (12%). After 2008 and in a general way, the literature remains more focused on using these materials for construction. However, the applicability as adsorbents and catalysts has been increasing. Table 2.7 summarizes recent studies of the red mud usage.

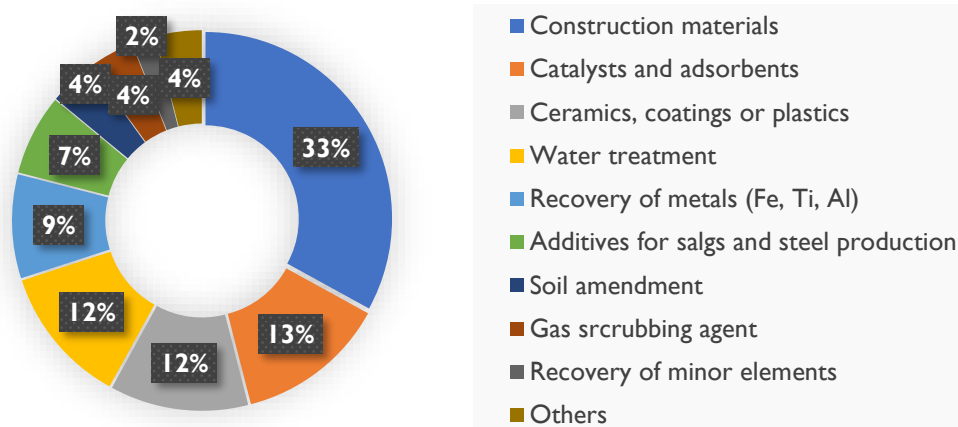


Fig. 2.15. Patented red mud applications from the year 1964 to 2008, based in [112].

Table 2.7. Most common applications of red mud used in recent years.

Applications	Specifications	Ref.
Construction materials	Cement, tiles, bricks, pavement for roads	[92,118–120]
Adsorbents	Removal of metals ions, phenolic compounds, dyes, nitrate, phosphate, fluoride	[113,114]
Catalysis	Hydrogenation, hydrocarbon oxidation, hydrochlorination of organochlorinated compounds, olive mill wastewater	[102,115]
Recovery of metals	Iron, titanium, aluminium, sodium	[116,117]

Red mud incorporation in construction materials (cement, tiles, bricks, and roads) is feasible, but this approach is strongly dependent on its chemical composition and the environmental safety standards for each country. The safe amount of red mud that can be used without leaching problems may vary depending on its properties and concentration of metals, alkalinity and other parameters. Despite the presence of trace radioactive elements in some localized samples as mentioned previously, it can still be incorporated into construction materials but in low amounts. According to [100], up to 60 wt.% and 90 wt.% of the red mud with the presence of ^{238}U , ^{232}Th and/or ^{40}K in trace amounts can be used safely in buildings and roads, respectively.

Properties such as high specific surface area are usually required for adsorbents. Depending on the type of red mud, BET surface areas can reach up to $70\text{ m}^2/\text{g}$ [113], which is suitable for acting as a zero-cost adsorbent for a wide list of metal ions (Cd, Ni, Cr, As, Zn, Pb, Cu), dyes, phenolic compounds, nitrate, phosphate and fluoride anions from water [114]. However, in many cases, the neutralization of red mud with acid or with a thermal pre-treatment is required for better sorption capacity, where the pH of the red mud particles plays an important role. Regeneration of the adsorbent at the end requires further studies.

Red mud has also gained interest as a catalyst due to the zero-costs associated, the Fe_2O_3 and TiO_2 content and specific surface area. Calcination temperatures from 300 to 650 °C are usually applied for activating the red mud by destroying unstable compounds and to remove water from some mineral phases. After that, red mud can act as a catalyst in hydrogenation and hydrogen reactions, hydrochlorination of organochlorinated compounds [102], and has been directly used as a catalyst in Fenton's peroxidation reaction with olive mill wastewaters for organic matter abatement [115].

When the purpose is to recover metals such as Al, Fe, Ti, Na and other valuable elements present in the waste, techniques such as magnetic separation, acidic leaching and solvent extraction are frequently used. Alkali roasting-leaching is specially useful for Al and Na recovery. Rare elements such as vanadium, lanthanum, cerium or scandium can be recovered as well through these methodologies,

according to an active circular utilization of natural resources and industrial wastes in many applications [116,117].

This residue is still been used as a soil amendment, but the application rates higher than 5 wt.% can lead to soil contamination, not only by increasing the Na^+ content of the soil, but also by increasing the concentration of other deleterious metals [96]. Nevertheless, it can be an interesting approach to amend acidic contaminated soils from mining activities, for example, acid mine drainage sludges. In order to prevent leaching of cations from red mud to the soil, a maximum of 10 wt.% of bauxite residue should be added, which proved to be stable for 125 days in [121].

Regardless of the application of red mud, a neutralization, pre-treatment or activation is often needed, especially when using it as adsorbent or catalyst. The major interest in using red mud is the associated low-cost, but its chemical properties can lead to low-efficiency processes when compared with commercial adsorbents or catalysts. Acidic leaching, thermal activation by calcination and sintering, washing it with seawater, the addition of gypsum are some of the pre-treatments used to neutralize the alkaline pH of the waste, increase the specific surface area of the particles and/or increasing the activity of the catalytical species due to the formation of new phases [122]. Sodium or calcium are usually required to be removed during the pre-treatment for a future catalysis application of red mud, since they promote sintering leading to a lower specific surface area of the catalyst at high temperatures [102].

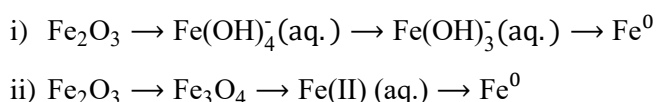
The processing of red mud-based porous ceramics has attracted interest recently. These porous ceramics have the purpose to be incorporated in construction materials such as thermal insulation for houses or road pavements, and filter materials for water treatments [123–127]. Thus, ceramic foams with a wide range of porosities (31 to 80%) have been processed. Guo et al. [125] compared three pore-forming agents, sawdust, NaCO_3 and powdered carbon. Around 53% of apparent porosity was achieved with the optimum pore-former agent tested (12.5 wt% of sawdust) after firing the porous ceramics at 1200 °C. Current studies are devoted to the processing of high porosity and high mechanical strength, where 5 to 49 MPa of pressure are used for flexural strength. Recent works such as Xiang et al. [126] and Wang et al. [123] used CaCO_3 and MgCO_3 , as well as graphite as pore forming agents, respectively. Firing temperatures of the ceramic pieces can go until 1350 °C as in [123].

2.4. Concluding remarks and outlook of using red mud waste as an iron-source for the electroreduction processes

Electrolysis emerged as a cleaner technology with low CO_2 emissions, overcoming the pollutant traditional routes from iron and steelmaking industries. The electrolytic processes of the iron oxides reduction include four main routes such as electroplating in acidic baths, molten oxides electrolysis

(previously pyroelectrolysis), molten salts electrolysis, and electrochemical reduction in strong alkaline medium. In the mentioned routes, one can only consider CO₂ emissions regarding energy consumption, which is related to fossil fuel use and/or when using consumable anodes during the electrochemical process. The most promising electrolytic paths currently under investigation are the molten oxide electrolysis (MOE) and the electroreduction in alkaline solutions. However, both are still far to be implemented at the industrial scale. New inert anodes capable of resisting to the strong corrosive medium of MOE should be tested for further implementation. On the other hand, the electrowinning under alkaline solutions seems to be attractive due to the low operating temperature (≈ 100 °C) when compared with MOE (≈ 1500 °C), requiring simpler electrochemical cells and reactors.

Studies on the electroreduction in strong alkaline media were mainly focused on the reduction mechanisms of iron oxides into Fe⁰ due to several uncertainties of those, both in suspensions and in bulk. Nowadays, the research trends focus on the impacts on the Faradaic efficiencies, provided by the different operation conditions used, the parasitic contribution of H₂ (g), the types and dimensions of the electrodes, as well as their impact on the morphology and purity of the Fe⁰ produced. The general mechanism seems to agree on the following reduction steps:



for the suspensions (i)) and bulk media (ii)), respectively, where establishing a three-phase interlines (current collector|solid insulator|electrolyte) is a crucial step for triggering the reduction of the insulator Fe₂O₃ pellet (bulk). The conducted studies seem not to consider yet the capture and storage of the H₂ produced during the electroreduction process. In fact, not only electrochemical reduction in alkaline solutions may be integrated for storing for the intermittent renewable energy sources, but it may even contribute as the energy source during all the process. Very few pilot-scale studies were performed so far, where the optimization of the experimental conditions and the design of the electrochemical cell were developed, with 51 years apart. A recent pilot-scale developed under the scope of the SIDERWIN project allowed the Fe⁰ production with current efficiencies between 72-91%. However, engineering studies seems to be missing since they are of great relevance for future large-scale applications. Additional studies on the flow of the iron oxides particles in the alkaline suspensions, the dissolution and diffusion of iron species in the electrolyte, as well as the motion of the gases produced and its impacts on the current efficiencies, among many others parameters, must be investigated.

The recovery and valorisation of waste have been strongly encouraged by the European Commission due to the recent circular economy agenda. Red mud has been considered for construction materials, as an adsorbent, catalyst and for the recovery of metals. In this scope, iron-rich wastes emerge as suitable raw material along with iron ores for the electrowinning by an alkaline medium. Red mud

waste showed to have an appropriate iron oxide content, that can go up to 65 wt%. Moreover, many environmental concerns towards red mud, mainly due to the massive worldwide production of the waste, highlight the great need for its valorisation. Thus, the electrochemical reduction arises as a suitable approach for its valorisation, mainly when considering the strong alkalinity of the mud itself, which is a major concern for some valorisation alternatives. However, the literature review on the electroreduction of iron oxides in alkaline medium revealed certain uncertainties in the mechanism when using pure iron oxides, as Fe_2O_3 . The highly complex chemistry of red mud may impose several difficulties during the electrochemical reduction. In order to fully understand the impact of red mud complexity during the proposed valorisation route, one should consider synthetic compositions to mimic the major components of red mud waste. Depending on the chemical composition of the Bayer process, a wide amount of phases can be present in red mud. The very recent and only study conducted with red mud and Fe_2O_3 powder suspensions in an alkaline medium for the electrowinning process showed the impact of kaolinite and vanadium additions on the Fe_2O_3 suspensions based on the Faradaic efficiencies. In fact, kaolinite ($\text{Al}_2\text{Si}_2\text{O}_5(\text{OH})_4$), an alumina-silicate-based composition, revealed to decrease the efficiency by 40%. However, the authors justified the negative impact on the current efficiency based on the presence of kaolinite particles at the surface of Fe_2O_3 , without a clear demonstration of this concept. The conducted research on the addition of kaolinite was probably very complex as a first step to evaluate the mechanism of reduction. Since Al_2O_3 is often the second major phase after Fe_2O_3 , increasing the interest in mimicking these two phases in the synthetic waste, different nominal compositions of a ceramic composite $\text{Fe}_{2-x}\text{Al}_x\text{O}_3$, allow one to study the effect of the Al_2O_3 addition itself by electrochemical testing.

Recent investigations on the electroreduction of iron oxides in bulk suggested the use of porous pellets to facilitate the electrolyte access through the porous cavities, favouring the electroreduction of the iron. Based on the interesting results obtained for the electrochemical reduction of highly-porous Fe_2O_3 , a novel designed porosity on the synthetic red mud composition seems to be a significantly innovative approach for the proposed electrowinning technology and waste valorisation investigation. Thus, the recycling of red mud by processing a porous ceramic material can act in two routes, where the first consists of the iron recovery by the electrowinning methods in strong alkaline solutions and a second one, based on the direct application of the processed ceramic for environmental applications.

The simulated red mud composition ($\text{Fe}_{2-x}\text{Al}_x\text{O}_3$) arises as a novel approach to study the electrochemical reduction in an alkaline medium for waste valorisation. Thus, an interesting symbiotic process is expected to be performed during the thesis by using waste as a raw material for Fe^0 or zero-valent iron production (ZVI), which can be further used for several environmental applications [128], beyond steel production. Although mostly stronger alkaline conditions were often used in this approach, as described in the literature review, the use of 10 M as the electrolyte concentration and 90 °C appear

as promising operation conditions to be used in the present work, when taking into account lower costs and energy consumption in the electrowinning technology.

2.5. References

- [1] E. Canby, A history of electricity. Vol. 6, First Edit, Hawthorn Books Inc., New York, 1963.
- [2] D.R. Sadoway, The electrochemical processing of refractory metals, *J. Met.* 43 (1991) 15–19. doi:10.1007/BF03220614.
- [3] Y. Gamburg, G. Zangari, Theory and practice of metal electrodeposition, Springer Science+Business Media, LLC 2011, 2011. doi:10.1017/CBO9781107415324.004.
- [4] W. Shafer, C. Harr, Electrolytic Iron Powders-Production and Properties, *J. Electrochem. Soc.* 105 (1958) 413–417. doi:10.1149/1.2428876.
- [5] M. Izaki, Electrodeposition of iron and iron alloys, in: M. Schlesinger, M. Paunovic (Eds.), *Mod. Electroplat.*, 5th editio, John Wiley & Sons, Inc., 2010: pp. 309–326. doi:10.1007/BF01022244.
- [6] A. Allanore, H. Lavelaine, G. Valentin, J.P. Birat, P. Delcroix, F. Lapique, Observation and modeling of the reduction of hematite particles to metal in alkaline solution by electrolysis, *Electrochim. Acta.* 55 (2010) 4007–4013. doi:10.1016/j.electacta.2010.02.040.
- [7] S.L. Díaz, J.A. Calderón, O.E. Barcia, O.R. Mattos, Electrodeposition of iron in sulphate solutions, *Electrochim. Acta.* 53 (2008) 7426–7435. doi:10.1016/j.electacta.2008.01.015.
- [8] C. wei Su, F. jiao He, H. Ju, Y. bin Zhang, E. li Wang, Electrodeposition of Ni, Fe and Ni-Fe alloys on a 316 stainless steel surface in a fluorborate bath, *Electrochim. Acta.* 54 (2009) 6257–6263. doi:10.1016/j.electacta.2009.05.076.
- [9] R. Aiken, Process of making iron from ore. US Patent No 816, 142, 1906.
- [10] A. Allanore, Features and Challenges of Molten Oxide Electrolytes for Metal Extraction, *J. Electrochem. Soc.* 162 (2015) E13–E22. doi:10.1149/2.0451501jes.
- [11] J. Wiencke, H. Lavelaine, P.J. Panteix, C. Petitjean, C. Rapin, Electrolysis of iron in a molten oxide electrolyte, *J. Appl. Electrochem.* 48 (2018) 115–126. doi:10.1007/s10800-017-1143-5.
- [12] A. Allanore, Electrochemical engineering of anodic oxygen evolution in molten oxides, *Electrochim. Acta.* 110 (2013) 587–592. doi:10.1016/j.electacta.2013.04.095.
- [13] J. Wiencke, H. Lavelaine, P.J. Panteix, C. Petitjean, C. Rapin, The Impact of Iron Oxide Concentration on the Performance of Molten Oxide Electrolytes for the Production of Liquid Iron Metal, *Metall. Mater. Trans. B Process Metall. Mater. Process. Sci.* 51B (2020) 365–376.

- doi:10.1007/s11663-019-01737-3.
- [14] H. Kim, J. Paramore, A. Allamore, D.R. Sadoway, Electrolysis of Molten Iron Oxide with an Iridium Anode: The Role of Electrolyte Basicity, *J. Electrochem. Soc.* 158 (2011) E101–E105. doi:10.1149/1.3623446.
- [15] N.M. Ferreira, A. V. Kovalevsky, M.C. Ferro, F.M. Costa, J.R. Frade, A new concept of ceramic consumable anode for iron pyroelectrolysis in magnesium aluminosilicate melts, *Ceram. Int.* 42 (2016) 11070–11076. doi:10.1016/j.ceramint.2016.04.004.
- [16] D.R. Sadoway, New opportunities for metals extraction and waste treatment by electrochemical processing in molten salts, *J. Mater. Res.* 10 (1995) 487–492. doi:10.1557/JMR.1995.0487.
- [17] A. Allamore, L. Yin, D.R. Sadoway, A new anode material for oxygen evolution in molten oxide electrolysis, *Nature*. 497 (2013) 353–356. doi:10.1038/nature12134.
- [18] B. Mishra, D.L. Olson, Molten salt applications in materials processing, *J. Phys. Chem. Solids*. 66 (2005) 396–401. doi:10.1016/j.jpcs.2004.06.049.
- [19] L. Andrieux, G. Weiss, Productions of electrolysis of molten salts with an iron anode, *Comptes Rendu*. 217 (1944) 615.
- [20] S. Ziolkewicz, Preparation of iron from a molten eutectic KCl-LiCl+ FeCl₂·4H₂O, *Comptes Rendu*. 247 (1958) 1604.
- [21] R. Abdulaziz, *Electrochemical Reduction of Metal Oxides in Molten Salts for Nuclear Reprocessing*, University College London, 2016.
- [22] X. Yan, J. Fray, Molten Salt Electrolysis for sustainable metals extraction and materials processing - a review, in: S. Kuai, J. Meng (Eds.), *Electrolysis Theory, Types Appl.*, 1st edition, Nova Science Publishers, Inc., 2010: p. 49.
- [23] G. Chen, D. Fray, T. Farthing, Direct electrochemical reduction of titanium dioxide to titanium in molten calcium chloride, *Nature*. 407 (2000) 361–364. doi:10.1038/35030069.
- [24] G. Haarberg, E. Kvalheim, S. Rolseth, T. Murakami, S. Pietrzyk, S. Wang, Electrodeposition of Iron from Molten Mixed Chloride/Fluoride Electrolytes, *ECS Trans.* 3 (2007) 341–345. doi:10.1149/1.2798677.
- [25] S. Licht, B. Wang, High solubility pathway for the carbon dioxide free production of iron, *Chem. Commun.* 46 (2010) 7004–7006. doi:10.1039/c0cc01594f.
- [26] M. Gibilaro, J. Pivato, L. Cassayre, L. Massot, P. Chamelot, P. Taxil, Direct electroreduction of oxides in molten fluoride salts, *Electrochim. Acta.* 56 (2011) 5410–5415. doi:10.1016/j.electacta.2011.02.109.

- [27] H. Li, L. Jia, J.-L. Liang, H.-Y. Yan, Z.-Y. Cai, R. Reddy, Study on the Direct Electrochemical Reduction of Fe₂O₃ in NaCl-CaCl₂ Melt, *Int. J. Electrochem. Sci.* 14 (2019) 11267–11278. doi:10.20964/2019.12.68.
- [28] K.S. Mohandas, Direct electrochemical conversion of metal oxides to metal by molten salt electrolysis: A review, *Trans. Institutions Min. Metall. Sect. C Miner. Process. Extr. Metall.* 122 (2013) 195–212. doi:10.1179/0371955313Z.00000000069.
- [29] K. Xie, A.R. Kamali, Electro-reduction of hematite using water as the redox mediator, *Green Chem.* 21 (2019) 198–204. doi:10.1039/c8gc02756k.
- [30] A. Estelle, Swedish Patent No 42,849, Förfarande för framställning av järn genom elektrolytisk reduktion i lösning av kaustiskt alkali, 1915.
- [31] E. Angel, US Patent No 2,622,063, Electrolytic production of iron and iron alloys, 1952.
- [32] K.M. Gorbunova, L.I. Liamina, On the mechanism of iron reduction from alkaline solutions, *Electrochim. Acta.* 11 (1966) 457–467.
- [33] K.K. Lee, S. Deng, H.M. Fan, S. Mhaisalkar, H.R. Tan, E.S. Tok, K.P. Loh, W.S. Chin, C.H. Sow, α -Fe₂O₃ nanotubes-reduced graphene oxide composites as synergistic electrochemical capacitor materials, *Nanoscale.* 4 (2012) 2958–2961. doi:10.1039/c2nr11902a.
- [34] F. Morin, Electrical properties of α -Fe₂O₃ and α -Fe₂O₃ containing Titanium, *Phys. Rev.* 83 (1951) 1005–1010. doi:https://doi.org/10.1103/PhysRev.83.1005.
- [35] R.M. Cornell, U. Schwertmann, The iron oxides: structures, properties, reactions, occurrences and uses, Second Edi, Wiley–VCH, Weinheim, 2003. doi:10.1002/3527602097.
- [36] A. Allanore, H. Lavelaine, G. Valentin, J.P. Birat, F. Lapique, Electrodeposition of metal iron from dissolved species in alkaline media, *J. Electrochem. Soc.* 154 (2007) E187–E193. doi:10.1149/1.2790285.
- [37] A. Allanore, H. Lavelaine, G. Valentin, J.P. Birat, F. Lapique, Iron Metal Production by Bulk Electrolysis of Iron Ore Particles in Aqueous Media, *J. Electrochem. Soc.* 155 (2008) E125–E129. doi:10.1149/1.2952547.
- [38] C.I. Müller, K. Sellschopp, M. Tegel, T. Rauscher, B. Kieback, L. Röntzsch, The activity of nanocrystalline Fe-based alloys as electrode materials for the hydrogen evolution reaction, *J. Power Sources.* 304 (2016) 196–206. doi:10.1016/j.jpowsour.2015.11.008.
- [39] J. Monteiro, Y. Ivanova, A. Kovalevsky, D. Ivanou, J. Frade, Reduction of magnetite to metallic iron in strong alkaline medium, *Electrochim. Acta.* 193 (2016) 284–292. doi:10.1016/j.electacta.2016.02.058.

- [40] Y. Ivanova, J. Monteiro, L. Teixeira, N. Vitorino, A. Kovalevsky, J. Frade, Designed porous microstructures for electrochemical reduction of bulk hematite ceramics, *Mater. Des.* 122 (2017) 307–314. doi:10.1016/j.matdes.2017.03.031.
- [41] J.A.M. LeDuc, R.E. Loftfield, L.E. Vaaler, Electrolytic Iron Powder from a Caustic Soda Solution, *J. Electrochem. Soc.* 106 (1959) 659–667. doi:10.1149/1.2427465.
- [42] G. Picard, D. Oster, B. Tremillon, Electrochemical reduction of iron oxides in suspension in water-sodium hydroxide mixtures between 25 and 140 °C. II: Experimental study, *J. Chem. Res.* 8 (1980) 252–253.
- [43] R. Armstrong, Baurhoo, The dissolution of iron in concentrated alkali, *J. Electroanal. Chem. Interfacial Electrochem.* 40 (1972) 325–338. doi:10.1016/S0022-0728(72)80377-2.
- [44] B. Andersson, L. Öjefors, Slow Potentiodynamic Studies of Porous Alkaline Iron Electrodes, *J. Electrochem. Soc.* 123 (1976) 824. doi:10.1149/1.2132940.
- [45] H. Le, E. Ghali, Interpretation des diagrammes E-pH du système Fe-H₂O en relation avec la fragilisation caustique des aciers, *J. Appl. Electrochem.* 23 (1993) 72–77. doi:10.1007/BF00241579.
- [46] I.I. Diakonov, J. Schott, F. Martin, J.C. Harrichourry, J. Escalier, Iron(III) solubility and speciation in aqueous solutions. Experimental study and modelling: Part 1. Hematite solubility from 60 to 300 °C in NaOH-NaCl solutions and thermodynamic properties of Fe(OH)₄(aq), *Geochim. Cosmochim. Acta.* 63 (1999) 2247–2261. doi:10.1016/S0016-7037(99)00070-8.
- [47] B. Beverskog, I. Puigdomenech, Revised Pourbaix diagrams for iron at 25–300 °C, *Corros. Sci.* 38 (1996) 2121–2135. doi:10.1016/S0010-938X(96)00067-4.
- [48] B. Yuan, O.E. Kongstein, G.M. Haarberg, Electrowinning of Iron in Aqueous Alkaline Solution Using a Rotating Cathode, *J. Electrochem. Soc.* 156 (2009) D64–D69. doi:10.1149/1.3039998.
- [49] B. Yuan, G. Haarberg, Electrodeposition of Iron in Aqueous Alkaline Solution: An Alternative to Carbothermic Reduction, *ECS Trans.* 16 (2009) 31–37.
- [50] M. Tokushige, O.E. Kongstein, G.M. Haarberg, Crystal Orientation of Iron Produced by Electrodeoxidation of Hematite Particles, *ECS Trans.* 50 (2013) 103–114. doi:10.1149/05052.0103ecst.
- [51] X. Zou, S. Gu, H. Cheng, X. Lu, Z. Zhou, C. Li, W. Ding, Facile Electrodeposition of Iron Films from NaFeO₂ and Fe₂O₃ in Alkaline Solutions, *J. Electrochem. Soc.* 162 (2015) D49–D55. doi:10.1149/2.0751501jes.
- [52] Y. Ivanova, J. Monteiro, A. Horovistiz, D. Ivanou, D. Mata, R. Silva, J. Frade, Electrochemical deposition of Fe and Fe / CNTs composites from strongly alkaline hematite suspensions, *J. Appl.*

- Electrochem. 45 (2015) 515–522. doi:10.1007/s10800-015-0803-6.
- [53] M. Siebentritt, P. Volovitch, K. Ogle, G. Lefèvre, Adsorption and electroreduction of hematite particles on steel in strong alkaline media, *Colloids Surfaces A Physicochem. Eng. Asp.* 440 (2014) 197–201. doi:10.1016/j.colsurfa.2012.09.002.
- [54] A. Allanore, J. Feng, H. Lavelaine, K. Ogle, The Adsorption of Hematite Particles on Steel in Strongly Alkaline Electrolyte, *J. Electrochem. Soc.* 157 (2010) E24–E30. doi:10.1149/1.3273198.
- [55] M.. Haque, N. Kallay, V. Privman, E. Matijević, Magnetic effects in particle adhesion, *J. Colloid Interface Sci.* 137 (1990) 36–47. doi:10.1016/0021-9797(90)90041-L.
- [56] V. Feynerol, H. Lavelaine, P. Marlier, M.N. Pons, F. Lapique, Reactivity of suspended iron oxide particles in low temperature alkaline electrolysis, *J. Appl. Electrochem.* 47 (2017) 1339–1350. doi:10.1007/s10800-017-1127-5.
- [57] A. Allanore, Etude expérimentale de la production électrolytique de fer en milieu alcalin : mécanisme de réduction des oxydes et développement d’une cellule, 2007.
- [58] A. Maihatchi, M.-N. Pons, Q. Ricoux, F. Goettmann, F. Lapique, Electrolytic iron production from alkaline suspensions of solid oxides: compared cases of hematite, iron ore and iron-rich Bayer process residues, *J. Electrochem. Sci. Eng.* 10 (2020) 95. doi:10.5599/jese.751.
- [59] J.E. Verink, Simplified Procedure for Constructing Pourbaix Diagrams, in: R. Revie (Ed.), *Uhlig’s Corros. Handb. Second Ed.*, John Wiley & Sons, Inc., New Jersey, 2000: pp. 111–124. doi:10.1002/9780470872864.ch7.
- [60] W. Zhu, J. Winterstein, I. Maimon, Q. Yin, L. Yuan, A.N. Kolmogorov, R. Sharma, G. Zhou, Atomic structural evolution during the reduction of α -Fe₂O₃ nanowires, *J. Phys. Chem. C.* 120 (2016) 14854–14862. doi:10.1021/acs.jpcc.
- [61] P.D. Allen, G.J. Bignold, N.A. Hampson, The electrodisolution of magnetite: Part III. Iron Nucleation processes on magnetite electrodes, *J. Electroanal. Chem.* 112 (1980) 239–246. doi:10.1016/S0022-0728(80)80405-0.
- [62] Z. He, R. V Gudavarthy, J.A. Koza, J.A. Switzer, Room-Temperature Electrochemical Reduction of Epitaxial Magnetite, *J. Am. Chem. Soc.* 133 (2011) 12358–12361.
- [63] G.M. Haarberg, B. Yuan, Direct Electrochemical Reduction of Hematite Pellets in Alkaline Solutions, *ECS Trans.* 58 (2014) 19–28. doi:10.1149/05820.0019ecst.
- [64] X. Zou, S. Gu, X. Lu, X. Xie, C. Lu, Z. Zhou, W. Ding, Electroreduction of Iron (III) Oxide Pellets to Iron in Alkaline Media : A Typical Shrinking-Core Reaction Process, *Metall. Mater. Trans. B.* 46B (2015) 1262–1274. doi:10.1007/s11663-015-0336-8.

-
- [65] Y. Deng, D. Wang, W. Xiao, X. Jin, X. Hu, G.Z. Chen, Electrochemistry at conductor/insulator/electrolyte three-phase interlines: A thin layer model, *J. Phys. Chem. B.* 109 (2005) 14043–14051. doi:10.1021/jp044604r.
- [66] W. Xiao, X. Jin, Y. Deng, D. Wang, G.Z. Chen, Three-phase interlines electrochemically driven into insulator compounds: A penetration model and its verification by electroreduction of solid AgCl, *Chem. - A Eur. J.* 13 (2007) 604–612. doi:10.1002/chem.200600172.
- [67] P.D. Allen, N.A. Hampson, G.J. Bignold, The electrodisolution of magnetite. Part I. The electrochemistry of Fe₃O₄/C discs-potentiodynamic experiments, *J. Electroanal. Chem.* 99 (1979) 299–309. doi:10.1016/S0022-0728(79)80094-7.
- [68] P.D. Allen, N.A. Hampson, G.J. Bignold, The electrodisolution of magnetite Part II. The oxidation of bulk magnetite, *J. Electroanal. Chem.* 111 (1980) 223–233. doi:10.1016/0368-1874(80)80255-3.
- [69] S. Ziemniak, M. Jones, K. Combs, Magnetite solubility and phase stability in alkaline media at elevated temperatures, *J. Solution Chem.* 24 (1995) 837–877. doi:10.1007/BF00973442.
- [70] N. Sato, K. Kudo, T. Noda, Single layer of the passive film on Fe, *Corros. Sci.* 10 (1970) 785–794. doi:10.1016/S0010-938X(70)80002-6.
- [71] P. Schmuki, S. Virtanen, A. Davenport, C. Vitus, In situ X-ray absorption near-edge spectroscopic study of the cathodic reduction of artificial iron oxide passive films, *J. Electrochem. Soc.* 143 (1996) 574–582.
- [72] R.S. Schrebler Guzmán, J.R. Vilche, A.J. Arvía, The potentiodynamic behaviour of iron in alkaline solutions, *Electrochim. Acta.* 24 (1979) 395–403. doi:10.1016/0013-4686(79)87026-7.
- [73] H. Zhang, S.M. Park, Rotating Ring-Disk Electrode and Spectroelectrochemical Studies on the Oxidation of Iron in Alkaline Solutions, *J. Electrochem. Soc.* 141 (1994) 718–724. doi:10.1149/1.2054798.
- [74] H. Kitamura, L. Zhao, B.T. Hang, S. Okada, J. Yamaki, Effect of Charge Current Density on Electrochemical Performance of Fe/C Electrodes in Alkaline Solutions, *J. Electrochem. Soc.* 159 (2012) A720–A724. doi:10.1149/2.049206jes.
- [75] N. Vitorino, C.C.J. Abrantes, J.R. Frade, Cellular ceramics processed by paraffin emulsified suspensions with collagen consolidation, *Mater. Lett.* 98 (2013) 120–123. doi:10.1016/j.matlet.2013.02.020.
- [76] M.F. Sanches, N. Vitorino, J.C.C. Abrantes, J.R. Frade, J.B.R. Neto, D. Hotza, Effects of processing parameters on cellular ceramics obtained by paraffin emulsified suspensions, *Ceram. Int.* 40 (2014) 9045–9053. doi:10.1016/j.ceramint.2014.01.117.
-

- [77] M.F. Sanches, N. Vitorino, C. Freitas, J.C.C. Abrantes, J.R. Frade, J.B. Rodrigues Neto, D. Hotza, Cellular ceramics by gelatin gelcasting of emulsified suspensions with sunflower oil, *J. Eur. Ceram. Soc.* 35 (2015) 2577–2585. doi:10.1016/j.jeurceramsoc.2015.03.008.
- [78] Q. Wang, Y. Zhu, Q. Wu, E. Gratz, Y. Wang, Low temperature electrolysis for iron production via conductive colloidal electrode, *RSC Adv.* 5 (2015) 5501–5507. doi:10.1039/C4RA14576C.
- [79] K. Ishikawa, T. Yoshioka, T. Sato, A. Okuwaki, Solubility of hematite in LiOH, NaOH and KOH solutions, *Hydrometallurgy.* 45 (1997) 129–135. doi:10.1016/S0304-386X(96)00068-0.
- [80] M.M. Rashid, M.K. Al Mesfer, H. Naseem, M. Danish, Hydrogen Production by Water Electrolysis: A Review of Alkaline Water Electrolysis, PEM Water Electrolysis and High Temperature Water Electrolysis, *Int. J. Eng. Adv. Technol.* (2015) 2249–8958.
- [81] M. Schalenbach, G. Tjarks, M. Carmo, W. Lueke, M. Mueller, D. Stolten, Acidic or alkaline? Towards a new perspective on the efficiency of water electrolysis, *J. Electrochem. Soc.* 163 (2016) F3197–F3208. doi:10.1149/2.0271611jes.
- [82] R.A. Nickell, W.H. Zhu, R.U. Payne, D.R. Cahela, B.J. Tatarchuk, Hg/HgO electrode and hydrogen evolution potentials in aqueous sodium hydroxide, *J. Power Sources.* 161 (2006) 1217–1224. doi:10.1016/j.jpowsour.2006.05.028.
- [83] P. Periasamy, B.R. Babu, S.V. Iyer, Electrochemical behaviour of Teflon-bonded iron oxide electrodes in alkaline solutions, *J. Power Sources.* 63 (1996) 79–85. doi:10.1016/S0378-7753(96)02449-4.
- [84] S. Shiva Kumar, V. Himabindu, Hydrogen production by PEM water electrolysis – A review, *Mater. Sci. Energy Technol.* 2 (2019) 442–454. doi:10.1016/j.mset.2019.03.002.
- [85] A. Allanore, H. Lavelaine, J.P. Birat, G. Valentin, F. Lapicque, Experimental investigation of cell design for the electrolysis of iron oxide suspensions in alkaline electrolyte, *J. Appl. Electrochem.* 40 (2010) 1957–1966. doi:10.1007/s10800-010-0172-0.
- [86] J. Balej, Determination of the oxygen and hydrogen overvoltage in concentrated alkali hydroxide solutions, *Int. J. Hydrogen Energy.* 10 (1985) 365–374. doi:10.1016/0360-3199(85)90062-X.
- [87] E. Gileadi, *Electrode Kinetics for Chemists, Chemical Engineers and Materials Scientists*, Wiley-VCH, New York, 1993.
- [88] P. Cavaliere, *Clean Ironmaking and Steelmaking Processes*, First edit, Springer International Publishing, Lecce, Italy, 2019. doi:10.1007/978-3-030-21209-4.
- [89] H. Lavelaine, S. Van der Laan, A. Hita, K. Olsen, M. Serna, G. Haarberg, J. Frade, Iron production by electrochemical reduction of its oxide for high CO₂ mitigation (IERO). European Commission, 2016.

-
- [90] J. de Beer, Potential for Industrial Energy-Efficiency Improvement in the Long Term, Vol. 5 Eco-Efficiency in Industry and Science, First edit, Springer, Dordrecht, Utrecht, Netherlands, 2000. doi:10.1007/978-94-017-2728-0.
- [91] M.S.S. Lima, L.P. Thives, V. Haritonovs, K. Bajars, Red mud application in construction industry: Review of benefits and possibilities, IOP Conf. Ser. Mater. Sci. Eng. 251 (2017) 0–10. doi:10.1088/1757-899X/251/1/012033.
- [92] E. Mukiza, L.L. Zhang, X. Liu, N. Zhang, Utilization of red mud in road base and subgrade materials: A review, Resour. Conserv. Recycl. 141 (2019) 187–199. doi:10.1016/j.resconrec.2018.10.031.
- [93] G. Power, M. Gräfe, C. Klauber, Bauxite residue issues: I. Current management, disposal and storage practices, Hydrometallurgy. 108 (2011) 33–45. doi:10.1016/j.hydromet.2011.02.006.
- [94] S.N.M. Hairi, G.N.L. Jameson, J.J. Rogers, K.J.D. MacKenzie, Synthesis and properties of inorganic polymers (geopolymers) derived from Bayer process residue (red mud) and bauxite, J. Mater. Sci. 50 (2015) 7713–7724. doi:10.1007/s10853-015-9338-9.
- [95] Y. Zhang, Y. Qi, J. Li, Aluminum Mineral Processing and Metallurgy: Iron-Rich Bauxite and Bayer Red Muds, in: K. Cooke (Ed.), Alum. Alloy. Compos., 2018: p. 21. doi:10.5772/intechopen.78789.
- [96] Y. Hua, K. V. Heal, W. Friesl-Hanl, The use of red mud as an immobiliser for metal/metalloid-contaminated soil: A review, J. Hazard. Mater. 325 (2017) 17–30. doi:10.1016/j.jhazmat.2016.11.073.
- [97] S. Wang, H.M. Ang, M.O. Tadé, Novel applications of red mud as coagulant, adsorbent and catalyst for environmentally benign processes, Chemosphere. 72 (2008) 1621–1635. doi:10.1016/j.chemosphere.2008.05.013.
- [98] M.A. Harris, Dust reduction in Bauxite Red Mud waste using carbonation, gypsum and flocculation, in: Geobiotechnological Solut. to Anthropog. Disturbances, Springer, 2016: pp. 21–48. doi:10.1007/978-3-319-30465-6_2.
- [99] A. Akinci, R. Artir, Characterization of trace elements and radionuclides and their risk assessment in red mud, Mater. Charact. 59 (2008) 417–421. doi:10.1016/j.matchar.2007.02.008.
- [100] T. Croymans, W. Schroeyers, P. Krivenko, O. Kovalchuk, A. Pasko, M. Hult, G. Marissens, G. Lutter, S. Schreurs, Radiological characterization and evaluation of high volume bauxite residue alkali activated concretes, J. Environ. Radioact. 168 (2017) 21–29. doi:10.1016/j.jenvrad.2016.08.013.
- [101] W. Wang, W. Chen, H. Liu, C. Han, Recycling of waste red mud for production of ceramic floor

- tile with high strength and lightweight, *J. Alloys Compd.* 748 (2018) 876–881. doi:10.1016/j.jallcom.2018.03.220.
- [102] M.A. Khairul, J. Zanganeh, B. Moghtaderi, The composition, recycling and utilisation of Bayer red mud, *Resour. Conserv. Recycl.* 141 (2019) 483–498. doi:10.1016/j.resconrec.2018.11.006.
- [103] W. Liu, X. Chen, W. Li, Y. Yu, K. Yan, Environmental assessment, management and utilization of red mud in China, *J. Clean. Prod.* 84 (2014) 606–610. doi:10.1016/j.jclepro.2014.06.080.
- [104] N. Zhang, H. Sun, X. Liu, J. Zhang, Early-age characteristics of red mud-coal gangue cementitious material, *J. Hazard. Mater.* 167 (2009) 927–932. doi:10.1016/j.jhazmat.2009.01.086.
- [105] G. Sridevi, S. Sahoo, S. Sen, Stabilization of Expansive soil with red mud and lime, in: T. Thyagaraj (Ed.), *Gr. Improv. Tech. Geosynth.*, Springer Nature Singapore Pte Ltd, 2019: pp. 85–94. doi:10.1007/978-981-13-0559-7.
- [106] S. Piskin, A.K. Figen, E. Ozkan, U. Ozcay, Structural characterization of seydisehir red mud to utilization in roof tile manufacturing, in: *16th IFAC Symp. Autom. Mining, Miner. Met. Process.* August 25-28, San Diego, California, USA, IFAC, 2013: pp. 484–487. doi:10.3182/20130825-4-US-2038.00010.
- [107] M.L.P. Antunes, S.J. Couperthwaite, F.T. Da Conceição, C.P.C. De Jesus, P.K. Kiyohara, A.C.V. Coelho, R.L. Frost, Red mud from Brazil: Thermal behavior and physical properties, *Ind. Eng. Chem. Res.* 51 (2012) 775–779. doi:10.1021/ie201700k.
- [108] P.E. Tsakiridis, S. Agatzini-Leonardou, P. Oustadakis, Red mud addition in the raw meal for the production of Portland cement clinker, *J. Hazard. Mater.* B116 (2004) 103–110. doi:10.1016/j.jhazmat.2004.08.002.
- [109] L. Pérez-Villarejo, F.A. Corpas-Iglesias, S. Martínez-Martínez, R. Artiaga, J. Pascual-Cosp, Manufacturing new ceramic materials from clay and red mud derived from the aluminium industry, *Constr. Build. Mater.* 35 (2012) 656–665. doi:10.1016/j.conbuildmat.2012.04.133.
- [110] L. Wang, N. Sun, H. Tang, W. Sun, A Review on Comprehensive Utilization of Red Mud, *Minerals.* 9 (2019) 362. doi:doi.org/10.3390/min9060362.
- [111] E. Di Carlo, A. Boullemant, R. Courtney, A field assessment of bauxite residue rehabilitation strategies, *Sci. Total Environ.* 663 (2019) 915–926. doi:10.1016/j.scitotenv.2019.01.376.
- [112] C. Klauber, M. Gräfe, G. Power, Bauxite residue issues: II. options for residue utilization, *Hydrometallurgy.* 108 (2011) 11–32. doi:10.1016/j.hydromet.2011.02.007.
- [113] L. Wang, G. Hu, F. Lyu, T. Yue, H. Tang, H. Han, Y. Yang, R. Liu, W. Sun, Application of red mud in wastewater treatment, *Minerals.* 9 (2019) 281. doi:10.3390/min9050281.

-
- [114] A. Bhatnagar, V.J.P. Vilar, C.M.S. Botelho, R.A.R. Boaventura, A review of the use of red mud as adsorbent for the removal of toxic pollutants from water and wastewater, *Environ. Technol.* 32 (2011) 231–249. doi:10.1080/09593330.2011.560615.
- [115] E. Domingues, N. Assunção, D. V. Lopes, J.R. Frade, M.J. Quina, R.M. Quinta-ferreira, R.C. Martins, Catalytic Efficiency of Red Mud for the Degradation of Olive Mill Wastewater through Heterogeneous Fenton's Process, *Water*. 11 (2019) 1–13. doi:https://doi.org/10.3390/w11061183.
- [116] X. Zhu, Z. Niu, W. Li, H. Zhao, Q. Tang, A novel process for recovery of aluminum, iron, vanadium, scandium, titanium and silicon from red mud (in press), *J. Environ. Chem. Eng.* (2019). doi:10.1016/j.jece.2019.103528.
- [117] F. Lyu, L. Wang, J. Gao, H. Tang, W. Sun, Y. Hu, R. Liu, L. Sun, Comprehensive Utilization of Red Mud Through the Recovery of Valuable Metals and Reuse of the Residue, in: A. Tomsett (Ed.), *Light Met. 2020*, Springer, Cham, 2020: pp. 129–135. doi:https://doi.org/10.1007/978-3-030-36408-3_18.
- [118] M. Ghalehnovi, N. Roshan, E. Hakak, E.A. Shamsabadi, J. de Brito, Effect of red mud (bauxite residue) as cement replacement on the properties of self-compacting concrete incorporating various fillers, *J. Clean. Prod.* 240 (2019) 118213. doi:10.1016/j.jclepro.2019.118213.
- [119] W. Wang, K. Sun, H. Liu, Effects of different aluminum sources on morphologies and properties of ceramic floor tiles from red mud, *Constr. Build. Mater.* 241 (2020) 118119. doi:10.1016/j.conbuildmat.2020.118119.
- [120] Y. Kim, Y. Lee, M. Kim, H. Park, Preparation of high porosity bricks by utilizing red mud and mine tailing, *J. Clean. Prod.* 207 (2019) 490–497. doi:10.1016/j.jclepro.2018.10.044.
- [121] M. Paradis, J. Duchesne, A. Lamontagne, D. Isabel, Using red mud bauxite for the neutralization of acid mine tailings: A column leaching test, *Can. Geotech. J.* 43 (2006) 1167–1179. doi:10.1139/T06-071.
- [122] M. Taneez, C. Hurel, A review on the potential uses of red mud as amendment for pollution control in environmental media, *Environ. Sci. Pollut. Res.* 26 (2019) 22106–22125. doi:10.1007/s11356-019-05576-2.
- [123] W. Wang, W. Chen, H. Liu, Recycling of waste red mud for fabrication of SiC/mullite composite porous ceramics, *Ceram. Int.* 45 (2019) 9852–9857. doi:10.1016/j.ceramint.2019.02.024.
- [124] H. Zhang, H. Li, Y. Zhang, D. Wang, J. Harvey, H. Wang, Performance enhancement of porous asphalt pavement using red mud as alternative filler, *Constr. Build. Mater.* 160 (2018) 707–713. doi:10.1016/j.conbuildmat.2017.11.105.
-

- [125] W. Guo, Y. Zhang, B. Cui, The preparation and characterization of red mud-based porous materials with pore-forming agents, in: 5th Int. Conf. Bioinforma. Biomed. Eng. ICBBE 2011, IEEE, 2011: pp. 1–4. doi:10.1109/icbbe.2011.5781454.
- [126] W. Xiang, Q. Ding, G. Zhang, Preparation and characterization of porous anorthite ceramics from red mud and fly ash, *Int. J. Appl. Ceram. Technol.* 17 (2018) 113–121. doi:10.1111/ijac.13148.
- [127] R. Liu, T. Xu, C. an Wang, A review of fabrication strategies and applications of porous ceramics prepared by freeze-casting method, *Ceram. Int.* 42 (2016) 2907–2925. doi:10.1016/j.ceramint.2015.10.148.
- [128] R. Mukherjee, R. Kumar, A. Sinha, Y. Lama, A.K. Saha, A review on synthesis, characterization, and applications of nano zero valent iron (nZVI) for environmental remediation, *Crit. Rev. Environ. Sci. Technol.* 46 (2016) 443–466. doi:10.1080/10643389.2015.1103832.

3. Processing of highly-porous cellular iron oxide-based ceramics by emulsification of ceramic suspensions

Iron oxides are attractive for a variety of applications, since they offer unique physical and chemical properties, while being abundant and environmentally friendly. Some of those potential applications, including electrochemical and catalytic systems, require ceramics with designed porosity and well-developed percolation networks. In the present work, representative Al- and Mg-substituted hematite and magnetite- based cellular ceramics were processed by emulsification of mixed oxide suspensions. Reactive firing conditions were adjusted to attain a reasonable compromise between designed porosity, percolation and phase composition. The impact of firing conditions on the cellular ceramics microstructure, porosity, phase content and interconnectivity of the cells was studied and discussed. Thus, the applicability of the proposed emulsification of ceramic suspensions method was demonstrated for iron oxide-based ceramics.

Keywords: Cellular ceramics; designed porosity; emulsification; hematite; magnetite.

This chapter is based on the following publication:

D.V. Lopes, A.V. Kovalevsky, M.J. Quina, J.R. Frade, Processing of highly-porous cellular iron oxide-based ceramics by emulsification of ceramic suspensions, *Ceram. Int.* 44 (2018) 20354–20360. doi:10.1016/j.ceramint.2018.08.024.

3.1. Introduction

Iron oxides attract huge interest, provided by wide range of potential applications, combined with corrosion resistance, environmental friendliness, cost effectiveness and flexibility to impart a diversity of properties. These characteristics are relevant for electrical or electrochemical, catalytic, magnetic, spectroscopic and other functionalities. Representative examples include prospective applications as electrodes [1–3], in lithium-ion batteries [4], gas sensors [5], catalysts [6,7], magnetic separation [8], adsorbents [9] for many environmental remediation purposes, and even for photovoltaics [10].

Iron oxides are widely available as natural raw materials, mostly based on hematite or magnetite, while they also represent a significant fraction in industrial wastes, such as red mud from the alumina industry [11] or slags from metallurgical industries [12]. In these cases, iron oxides are combined with other components, such as alumina, silica, calcium and magnesium oxides, thus requiring separation of iron oxides from unwanted components and contaminants. One of the promising concepts implies cathodic in-situ reduction of porous iron oxide-based ceramics [1,3]. Alternatively, one may attempt to combine iron oxides with other components present in those residues to seek enhanced properties or functionalities, often dependent on suitable composition changes and corresponding structural and redox effects. For example, substitution of iron with magnesium and aluminium was shown to improve the spinel Fe_3O_4 phase in terms of refractoriness and phase stability [13], without significant deterioration of electrical properties.

Plausible applications in catalysis, filtration, energy conversion, etc. usually require highly porous materials or foams with suitable microstructures, possessing high specific surface area, and permeability to fluids; this has been addressed by different processing methods such as direct foaming [14] or emulsification of ceramic powder suspensions with different organic phases such as alkanes [15], paraffins [16,17] or edible oils [18]. Emulsification of mixed powder suspensions also allows processing of cellular multicomponent phases by reactive firing, as demonstrated for MgAl_2O_4 [19], NiAl_2O_4 [20] and Al_2TiO_5 or $\text{Al}_2\text{TiO}_5\text{-Al}_2\text{O}_3$ [21]. Being economically more advantageous as compared to the traditional solid state route, the reactive firing processing implies that the target ceramic composition is formed within one-cycle thermal treatment of the precursor powders, provided by their chemical reactivity and sufficient homogenization. Though these methods are most often developed to process nominally inert supports (Al_2O_3 , MgAl_2O_4 , etc.) for subsequent functionalization with the active components, emulsification of mixed powder precursors is also versatile for direct processing of the active phases with designed highly porous microstructures [17]. In this case, emulsification is also expected to provide better mixing and homogenization of the precursor powders, allowing larger reaction area, faster inter-diffusion of the cations and thus facilitating the reactive sintering and one-step formation of the target reaction product. Consequently, the present work was focused on demonstrating the applicability of emulsification of mixed powders to process iron oxide-derived functional ceramics

with designed cellular microstructures. This includes materials with hematite- and magnetite-derived structures, for greater flexibility in materials design.

3.2. Experimental procedure

The selected model materials included hematite- and magnetite-based ceramics, $\text{Fe}_{2-x}\text{Al}_x\text{O}_3$ and $\text{Fe}_{3-y}\text{Mg}_y\text{O}_4$, with nominal compositions $\text{Fe}_{1.8}\text{Al}_{0.2}\text{O}_3$, $\text{Fe}_{1.6}\text{Al}_{0.4}\text{O}_3$, $\text{Fe}_{1.4}\text{Al}_{0.6}\text{O}_3$ and $\text{Fe}_{2.3}\text{Mg}_{0.7}\text{O}_4$. These were prepared by emulsification of the corresponding oxide suspensions with liquid paraffin, based on guidelines from previous works [16,17,19,21]. The powders of hematite (Fe_2O_3) (Gute Chemie, abcr GmbH, 99.8%), aluminium oxide (Al_2O_3) (Alcoa CT3000, 99.8%) and magnesium oxide (MgO) (Sigma-Aldrich, -325 mesh, 99+%) were used as precursors. Preliminary thermal treatments of the precursors, followed by milling to improve the homogeneity of the mixture, were performed in the case of $\text{Fe}_{2.3}\text{Mg}_{0.7}\text{O}_4$, namely calcination in air, at 900 °C (heating and cooling rate of 2 °C/min, dwell of 2 h), 1000 °C (heating and cooling rate of 5 °C/min, dwell of 5 h,) and 1100 °C (heating and cooling rate of 5 °C/min, dwell of 5 h). Before preparation of corresponding suspensions and their emulsification, the powder mixtures (Fe_2O_3 - Al_2O_3 or Fe_2O_3 -MgO) were ball-milled with ethanol (AGA - Álcool e Géneros Alimentares, S.A., 99.5%) for 4 h to decrease the particles sizes ($< 0.5 \mu\text{m}$). Aqueous suspensions of powdered mixtures were prepared using 40% of solids load with 10% (v/v) of a commercial dispersant agent, Dolapix PC-67 (Zschimmer & Schwarz), under stirring with a mechanical stirrer (Heidolph RZR 2020) at 1000 rpm. The emulsification of each aqueous suspension was performed by adding liquid paraffin (Valente e Ribeiro Lda.), with a paraffin:suspension volume ratio of 1.5:1; 19% (v/v) and 6% (v/v) of sodium lauryl sulfate surfactant (1 g/L, Sigma-Aldrich L-6026) in case of Fe_2O_3 - Al_2O_3 mixture and Fe_2O_3 -MgO, respectively; and collagen (Oxoid Lda., LP0008) (5% related to water volume of the suspension) as shape stabilizer. Each emulsification was performed during 8 to 10 min under stirring rate of 1300 rpm at room temperature in the case of $\text{Fe}_{2-x}\text{Al}_x\text{O}_3$ -based ceramics and at 80 °C for $\text{Fe}_{2.3}\text{Mg}_{0.7}\text{O}_4$. The emulsified samples were then cooled to induced gelcasting promoted by collagen, stored at room temperature for two days and then subsequently dried at 70 °C for two days.

The organic phase was burned out by slow heating (1 °C/min) up to 300°C, followed by dwell for 3 h, then heating up to 500 °C at 0.8 °C/min, and natural cooling down to room temperature. This procedure allowed better observation of the microstructural development of green samples after elimination of the dispersed organic phase. The final step of reactive firing was performed at 1000 to 1400 °C, using fixed dwell time of 2 h and cooling/heating rates of 5 °C/min.

Hitachi SU-70 scanning electron microscopy (SEM) combined with energy dispersive spectroscopy (EDS) analysis (Bruker Quantax 400 detector) was used to characterize relevant microstructural features, such as the cellular sizes, interconnectivity between the cells depending on

processing conditions, and to reveal local phase inhomogeneities. The phase composition of each ceramic sample, grinded to powder, was determined from X-ray diffraction analysis (XRD), using a Rigaku D/Max-B diffractometer system (CuK α radiation) ($2\theta = 10 - 80^\circ$). Phase content was estimated in Panalytical HighScore Plus 4.1 (PDF-4) software using the reference intensity ratio (RIR) method [22], using corundum as reference. The strongest peaks of each phase were used for analysis and the corresponding scale factors were taken from the PDF-4 database.

The Archimedes method [16,17,21,23] was applied to measure open (x_o) and total (x_t) porosities of the samples (from 0 to 1, where 1 represents 100%), calculated using Eqs. (3.1) and (3.2),

$$x_o = \frac{wt_2 - wt_1}{wt_2 - wt_3} \quad (3.1)$$

$$x_t = 1 - \frac{\rho_w}{\rho_{th}} \times \frac{wt_1}{wt_2 - wt_3} \quad (3.2)$$

where wt_1 , wt_2 and wt_3 are weights of the dry sample, the sample impregnated with water and the sample immersed in water, respectively; ρ_w and ρ_{th} are the water density (0.997 g/cm³ at 25 °C) and the theoretical density of the sample. The ρ_{th} was calculated based on the densities of the precursor powders, provided by the suppliers, and considering the general rule of mixtures.

Stereology studies were performed using *Estereologia* software [24] to measure the average size of cellular cavities, \bar{d} , by using random lines over planar sections of SEM microstructures, in order to mark the interceptions of the cellular cavities.

The percolation between interconnected cells was studied based on their electrical response [16,25], using a solution of sodium acetate (5% w/w) for impregnation of the processed cellular ceramics. After impregnation under vacuum, the disc-shaped sample was clamped between two plastic plates with thick aluminium foil in between the sample and plastic surface, and corresponding arrangements for electrical measurements. During sample placement and measurement the solution was retained inside the cellular ceramics by capillary forces, while the electrical contact between top and bottom aluminium foils and solution inside the sample was ensured by applied pressure and foil deformation. The studies relied on impedance spectroscopy, performed using a Hewlett Packard 4284A impedance bridge in a frequency range from 20 Hz – 10⁶ Hz. Impedance spectra were fitted to deconvolute different contributions of the electric response, separating the true electrical response of the ionic conducting liquid, which percolates across interconnected cells, from the contribution of the electrode processes. Typical Nyquist plots (Fig.3.1) show a partially resolved arc, which is nearly described by an ideal resistor-capacitor (R_1C_1) contribution, with typical relaxation frequency $f_1=(2\pi R_1C_1)^{-1}$ in the order of 1 MHz, and onset of the electrode contribution at intermediate frequencies. Still, impedance spectra also reveal a prevailing contribution out of the frequency range of the

impedance bridge; this apparently resistive contribution (R_S) is revealed by extrapolation of the resolved arc to its interception with the real axis.

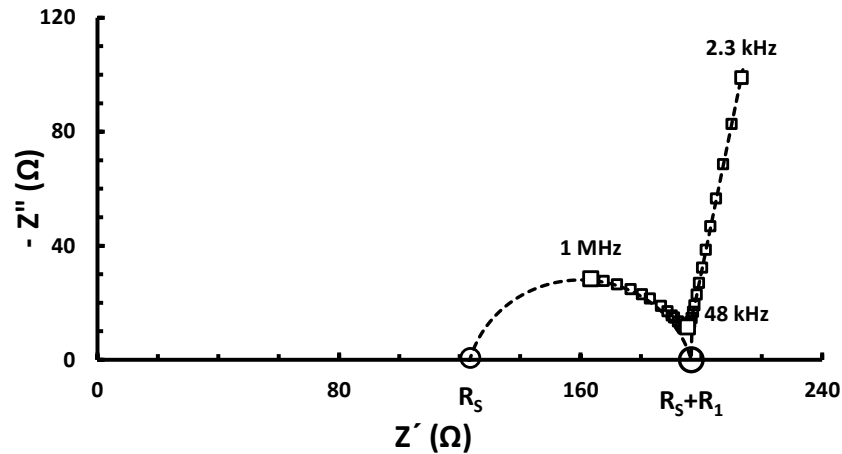


Fig. 3.1. Representative example of impedance spectra showing de-convolution of the contribution at very high frequency (R_S) and the R_1C_1 term with relaxation frequency close to 1 MHz.

Though the precise nature of the R_1 and R_S contributions is unclear, the capacitance values (C_1L/A) are typically in the order of 10 nF/cm^2 , suggesting that this may be ascribed to internal interfaces. In addition, the microstructural nature of the R_S term is also demonstrated by its dependence on open porosity (Fig. 3.2).

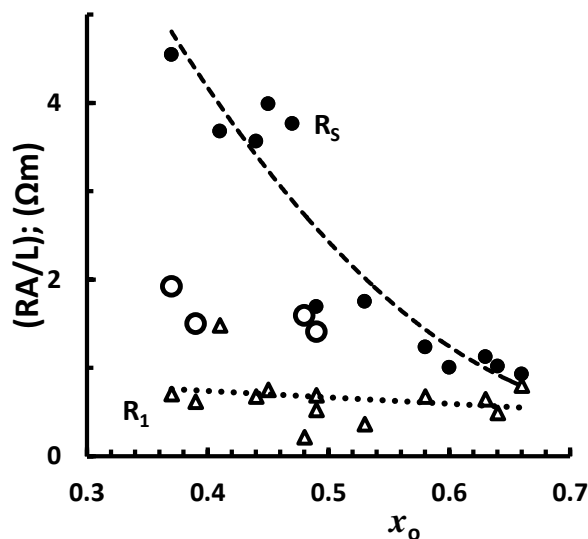


Fig. 3.2. Dependence of microstructural contributions R_1 (triangles) and R_S (closed circles) on open porosity. The results of R_S for samples fired at highest temperature ($1400 \text{ }^\circ\text{C}$) are shown as large open circles to emphasize their deviation from the main trends of samples with better cellular microstructures.

Thus, the sum of both contributions (R_S+R_I) was taken as a measure of limitations in percolation, and a constriction factor, f_c , described by Eq. (3.3) was then calculated as the ratio between the measured resistance of the impregnated ceramic matrix with current constrictions at narrow interconnecting windows (R), and the ideal response for a model parallel behaviour without constrictions R_{par} . The fraction of conducting salt solution was taken as the open porosity (x_o), and on assuming parallel organization of the conducting solution along with highly resistive ceramic walls, one obtains:

$$f_c = \frac{R}{R_{par}} = x_o \frac{A}{L} \frac{R}{\rho_{salt}} \quad (3.3)$$

where ρ_{salt} is the resistivity of sodium acetate solution ($32.4 \Omega \text{ cm}$), estimated from the data on electric conductivity at $20 \text{ }^\circ\text{C}$ presented in [26], and A/L corresponds to the area:thickness geometric ratio. At least three impedance measurements were performed for different ceramic samples processed at a given temperature, to ensure reproducibility.

3.3. Results and discussion

Fig. 3.3 shows representative SEM micrographs of ceramics with nominal $\text{Fe}_{1.8}\text{Al}_{0.2}\text{O}_3$, $\text{Fe}_{1.6}\text{Al}_{0.4}\text{O}_3$ and $\text{Fe}_{1.4}\text{Al}_{0.6}\text{O}_3$ compositions after firing under various conditions. These results clearly confirm the feasibility of the proposed method to process hematite-based cellular ceramics by suspension emulsification followed by reactive firing. Well-defined cellular microstructures are present for all compositions processed at temperatures up to $1300 \text{ }^\circ\text{C}$, with evidence of interconnecting windows in cell walls, as required for percolation. While still retaining the cellular structure, the firing temperature significantly affects the walls thickness and interconnectivity between cells. Microstructural rearrangements and undue grain growth occur at excessively high temperatures, with impact on narrower windows and wall thickening. These changes are clearly demonstrated by the micrograph insets in the Fig. 3.3B, C, showing grain growth by increasing the firing temperature. Apparently, suitable conditions for the development of cellular microstructures with cell interconnectivity are achieved at $1200 \text{ }^\circ\text{C}$, while more pronounced grain growth at $1300 \text{ }^\circ\text{C}$, results in partial collapse of the small intercellular windows. The presence of Al as a secondary phase can be observed as green inclusions by SEM-EDS chemical mapping of samples sintered at 1300 or $1400 \text{ }^\circ\text{C}$, while the distribution of iron is represented in red (Fig. 3.3E, F).

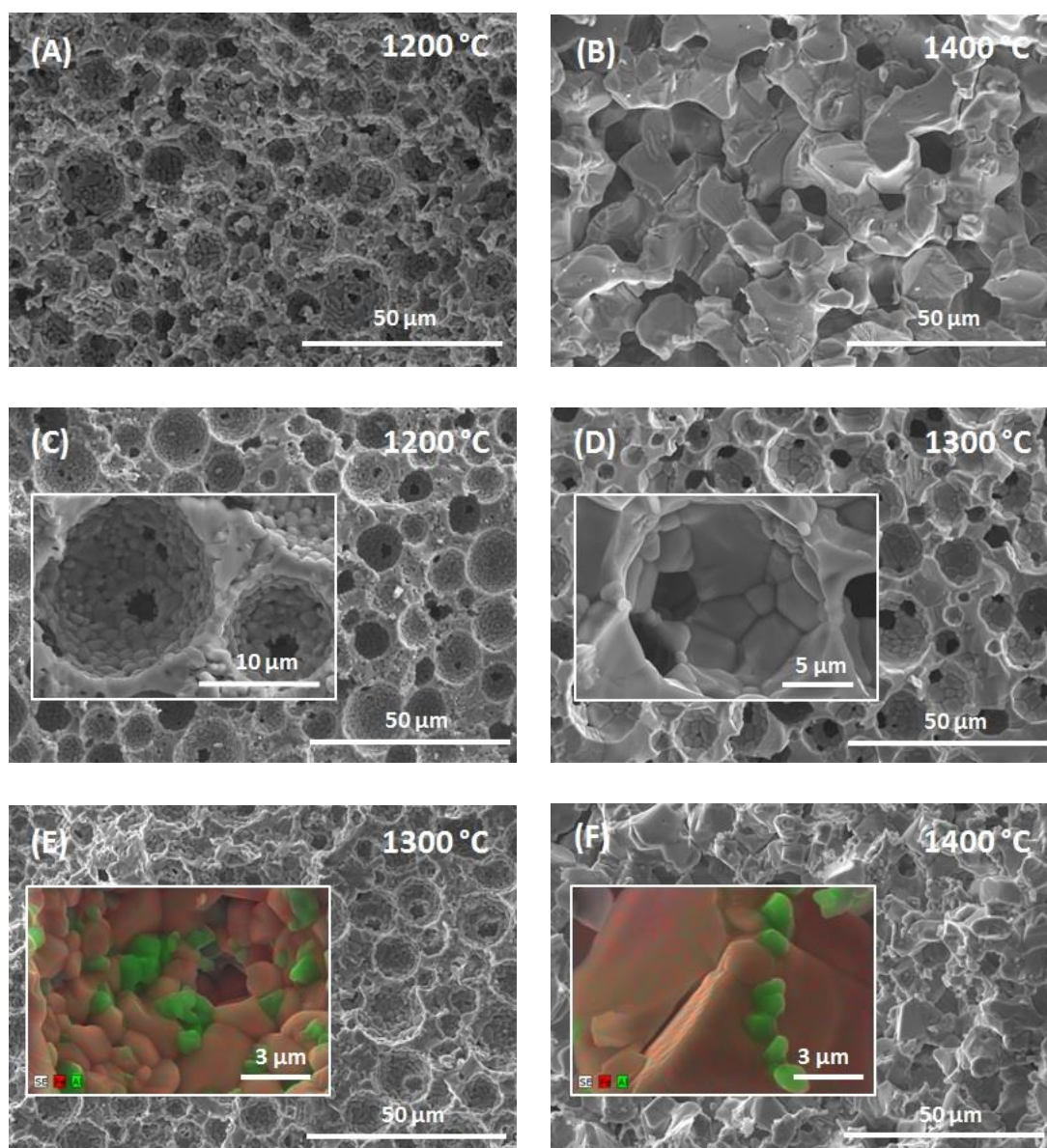


Fig. 3.3. SEM microstructures of $\text{Fe}_{2-x}\text{Al}_x\text{O}_3$ ceramics obtained at various firing conditions: $\text{Fe}_{1.8}\text{Al}_{0.2}\text{O}_3$ (A, B); $\text{Fe}_{1.6}\text{Al}_{0.4}\text{O}_3$ (C, D) and $\text{Fe}_{1.4}\text{Al}_{0.6}\text{O}_3$ (E,F). The insets show the microstructural evolution in the individual cells (C,D) and EDS mapping results (E,F).

Similar microstructural evolution with sintering temperature was observed in the case of spinel with nominal $\text{Fe}_{2.3}\text{Mg}_{0.7}\text{O}_4$ composition (Fig. 3.4). Cellular microstructures are observed at temperatures up to 1300 °C, with significant grain growth in the cell walls. At 1400 °C the cellular structure was suppressed by significant microstructural rearrangements.

Target applications of cellular ceramics imply a reasonable compromise between mechanical resistance to sustain stresses imposed by pressure gradients under the intended gas/liquid flow, and the required phase composition. Although no mechanical studies were performed in the present work, one expects that the moderate grain growth observed at 1200-1300 °C for both hematite- and magnetite-

based compositions is favourable to reach sufficient mechanical strength, based on handleability of the ceramic samples.

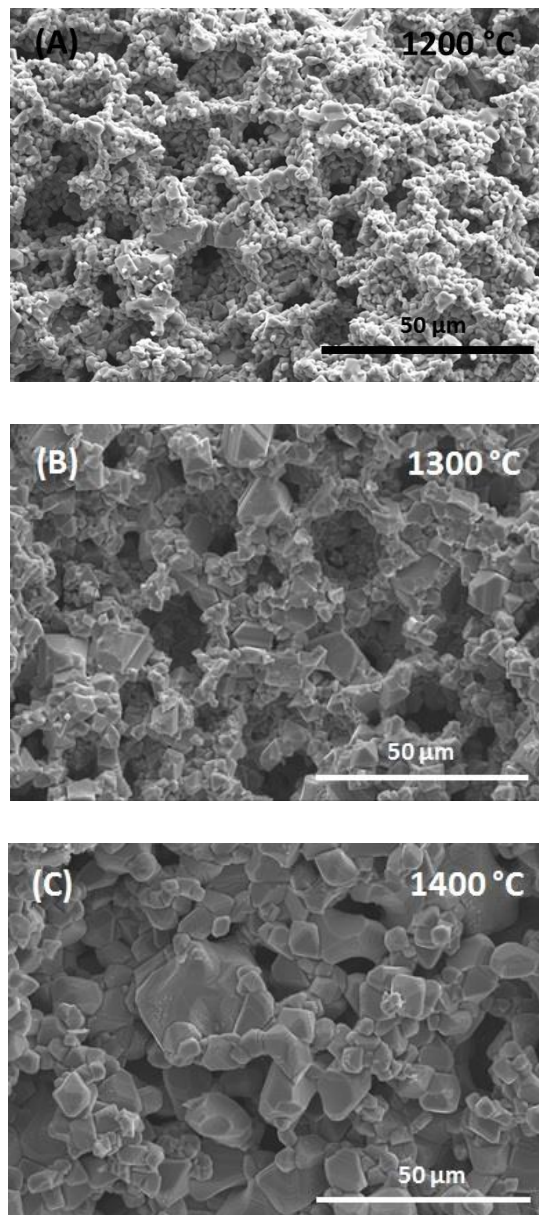


Fig. 3.4. SEM microstructures of $\text{Fe}_{2.3}\text{Mg}_{0.7}\text{O}_4$ cellular ceramics obtained at various firing conditions.

The phase diagrams [27,28] predict limited and temperature dependent solubility of aluminium and magnesium cations in hematite and magnetite structure, respectively, at firing temperatures, and these trends are in good agreement with XRD results shown in Fig. 3.5A-C.

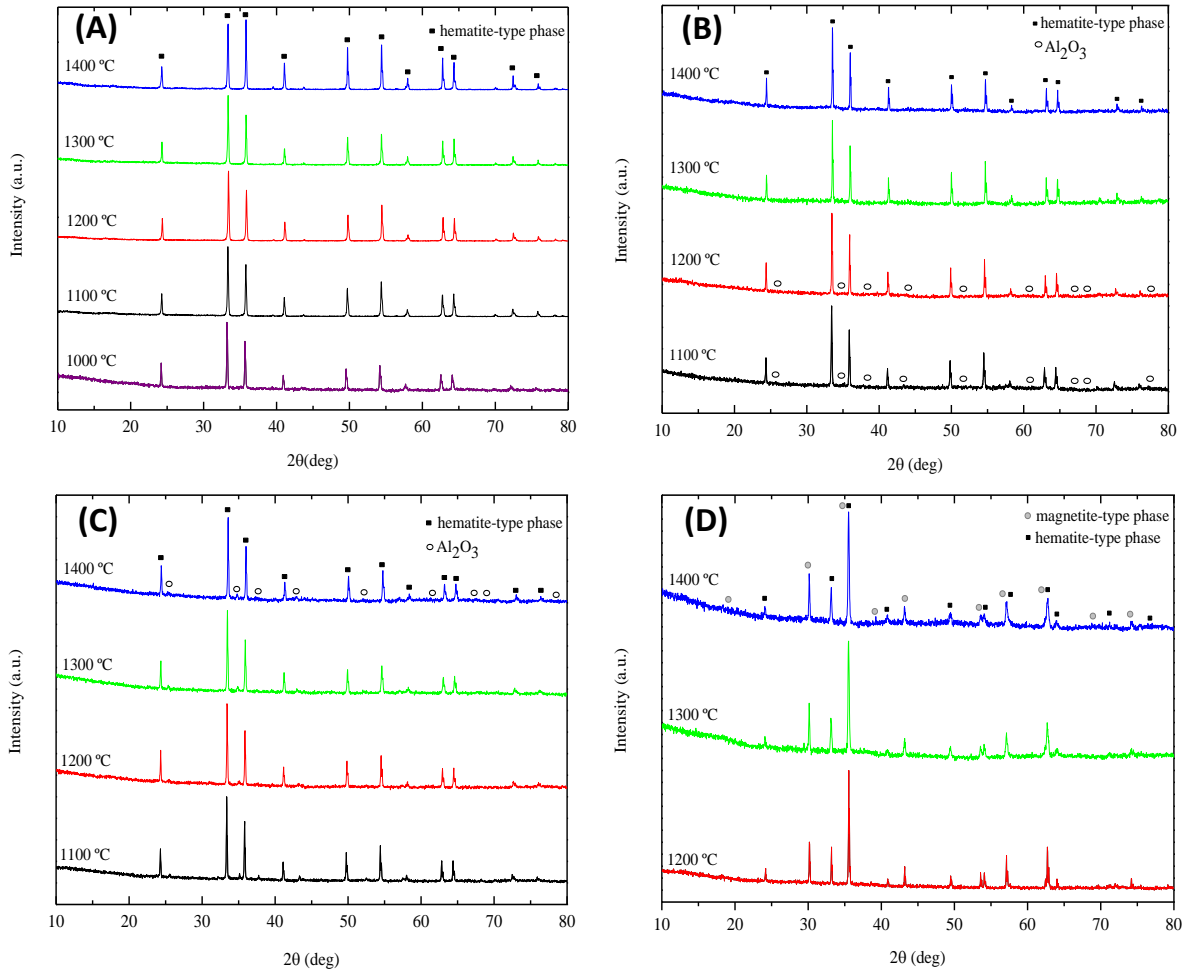
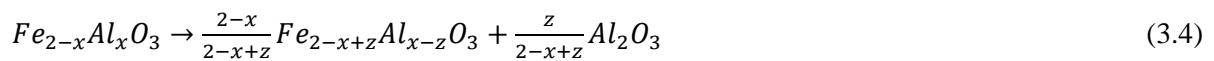


Fig. 3.5. XRD patterns of $\text{Fe}_{1.8}\text{Al}_{0.2}\text{O}_3$ (A), $\text{Fe}_{1.6}\text{Al}_{0.4}\text{O}_3$ (B), $\text{Fe}_{1.4}\text{Al}_{0.6}\text{O}_3$ (C) and $\text{Fe}_{2.3}\text{Mg}_{0.7}\text{O}_4$ (D) fired at different temperatures.

While $\text{Fe}_{1.8}\text{Al}_{0.2}\text{O}_3$ ceramics is single phase for all firing temperatures (Fig. 3.5A), onset of a secondary corundum (Al_2O_3) phase is observed on increasing the aluminium content. Correspondingly, the amount of Al_2O_3 admixture increases on lowering the firing temperature, again in accordance with phase diagrams [27,28]; this may be described as Eq. (3.4):



Approximate quantitative guidelines regarding phase composition of sintered samples were provided by RIR method. The estimated fraction of segregated corundum was up to 12.6 % wt. at 1100 °C and 7.0 % wt. at 1200 °C in $\text{Fe}_{1.6}\text{Al}_{0.4}\text{O}_3$, and up to 22.1 % wt. at 1100 °C, 13.9 % wt. at 1200 °C, 4.3 % wt. at 1300 °C, and 1.4 % wt. at 1400 °C in $\text{Fe}_{1.4}\text{Al}_{0.6}\text{O}_3$ samples. Indeed, this demonstrates mainly the general tendency for phase evolution at different temperatures, rather than precise composition changes of the (Fe,Al) $_2\text{O}_3$ phase. Moreover, the presence of Al_2O_3 as the only phase impurity indicates that the

hematite-type phase is enriched in iron as compared to the nominal chemical composition. The combined SEM/EDS studies also confirm Al_2O_3 impurities, as shown in Fig. 3.4E, F.

Hematite-based $\text{Fe}_{2-x}\text{Al}_x\text{O}_3$ with moderate aluminium content represent a good example of the system, where single-phase materials can be obtained by reactive firing along with retaining highly-porous cellular microstructure. In the case of $\text{Fe}_{2.3}\text{Mg}_{0.7}\text{O}_4$ spinel, highly-porous ceramics skeleton is maintained up to 1300 °C (Fig. 3.4), though already showing significant grain growth. In accordance with the calculated phase diagram [28], this material should be single-phase spinel at temperatures above 1200 °C. Still, a significant fraction of hematite Fe_2O_3 is present in all sintered samples (Fig. 3.5D), indicating kinetic limitations of the reactive firing process. At the same time, the cellular structure disappears after firing at 1400 °C, as shown in Fig. 3.4. Nevertheless, one expects that these limitations may be minimized by adjusting the firing conditions, e.g., by two-step firing schedules [21].

With emphasis on potential applications, the porosity (open and total), average diameter of cell cavities and constriction factor were further assessed in order to evaluate the percolation of the samples for an aqueous medium. The obtained results are shown in Table 3.1. Open (x_o) and total porosities (x_t) decrease when firing temperature increases, in close agreement with the size of the cellular cavities (\bar{d}), quantified by stereology. The cavities are larger for lower firing temperatures. However, stereology studies do not bring conclusive results for the samples processed at high firing temperatures due to increase in wall thickness at these conditions. These results are in agreement with other works [16,17,19].

Though SEM provides evidence of interconnected cellular microstructures and also reveals typical size ranges for cells and interconnecting windows, this is still insufficient for quantitative description of percolation. Thus, one relied on the measurements of electrical resistance, after impregnation of the open porosity with sodium acetate solution, to evaluate the constriction factor, f_c Eq. (3.3). The electrical resistance was extracted by de-convolution of impedance spectra (Fig. 3.1), which show clear separation between the high frequency arc, ascribed to the true resistance, and the low frequency contributions ascribed to electrode processes. The dependence of constriction factor (Table 3.1) shows that percolation has a tendency to decrease on increasing the sintering temperature of $\text{Fe}_{2-x}\text{Al}_x\text{O}_3$ ceramics up to 1300 °C, in accordance with observed porosity and microstructural evolution (Fig. 3.3). However, the constriction factors, indicating high percolation, show surprisingly low values for all hematite-based samples fired at 1400 °C. As illustrated by Fig. 3.6, these samples revealed the presence of extended cracking after cooling, allowing direct percolation of the solution and, consequently, causing a significant decrease in R_s . These results are also emphasized by noticeable deviations from the main correlations between R_s and open porosity (Fig. 3.2).

Table 3.1. Open (x_o) and total porosities (x_t), average cellular cavity sizes (\bar{d}), resistivity (R_s) and constriction factors (f_c) of $\text{Fe}_{2-x}\text{Al}_x\text{O}_3$ and $\text{Fe}_{3-y}\text{Mg}_y\text{O}_4$ ceramic materials fired at different temperatures.

Ceramic	T_{firing} ($^{\circ}\text{C}$)	x_o	x_t	\bar{d} (μm)	R_s (Ω)	f_c
$\text{Fe}_{1.8}\text{Al}_{0.2}\text{O}_3$	1000	0.66 ± 0.01	0.74 ± 0.01	14.2 ± 0.6	22.51	1.90
	1100	0.60 ± 0.02	0.64 ± 0.02	13.8 ± 0.5	31.37	1.86
	1200	0.47 ± 0.02	0.53 ± 0.02	10.6 ± 0.4	152.7	5.47
	1300	0.37 ± 0.01	0.45 ± 0.02	-	174.9	5.20
	1400	0.39 ± 0.02	0.43 ± 0.01	-	57.75	1.81
$\text{Fe}_{1.6}\text{Al}_{0.4}\text{O}_3$	1100	0.63 ± 0.01	0.70 ± 0.02	17.6 ± 0.8	30.95	2.19
	1200	0.44 ± 0.02	0.55 ± 0.02	13.1 ± 0.6	125.8	4.85
	1300	0.41 ± 0.01	0.51 ± 0.01	11.5 ± 0.6	134.6	4.66
	1400	0.49 ± 0.01	0.53 ± 0.01	-	50.35	2.13
$\text{Fe}_{1.4}\text{Al}_{0.6}\text{O}_3$	1100	0.64 ± 0.02	0.71 ± 0.01	14.8 ± 0.6	25.03	2.01
	1200	0.53 ± 0.01	0.60 ± 0.01	15.2 ± 0.7	55.96	2.87
	1300	0.45 ± 0.01	0.52 ± 0.01	11.8 ± 0.5	139.2	5.55
	1400	0.48 ± 0.01	0.51 ± 0.02	-	57.64	2.37
$\text{Fe}_{2.3}\text{Mg}_{0.7}\text{O}_4$	1200	0.58 ± 0.02	0.61 ± 0.03	18.7 ± 1.0	39.06	2.22
	1300	0.49 ± 0.01	0.54 ± 0.02	19.1 ± 2.3	61.28	2.57
	1400	0.37 ± 0.02	0.43 ± 0.02	-	70.39	2.20

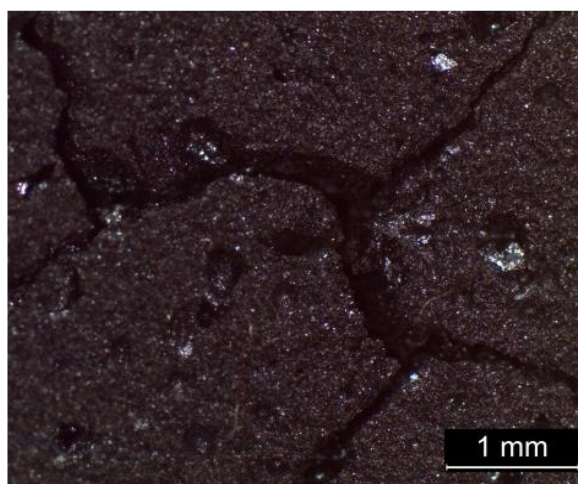


Fig. 3.6. $\text{Fe}_{1.8}\text{Al}_{0.2}\text{O}_3$ sample after firing at 1400 $^{\circ}\text{C}$, showing thermally-induced cracks and defects.

Moreover, the formation of a spinel $(\text{Fe,Al})_3\text{O}_4$ phase might start occurring around 1400 $^{\circ}\text{C}$ [6], which can contribute significantly to the formation of defects due to associated volume changes and chemically-induced stresses. The latter does not occur in the case of $\text{Fe}_{2.3}\text{Mg}_{0.7}\text{O}_4$, for which

corresponding variations in phase composition (Fig. 3.5D) are rather minor. Although higher processing temperatures, in general, reduce the cavities size, this is not expected to be critical for good percolation. Microstructural reconstruction results in collapse of the smaller intercellular windows, which are responsible for connecting two or more adjacent cells. Thus, optimal processing conditions enabling good percolating network in $\text{Fe}_{2-x}\text{Al}_x\text{O}_3$ ceramics correspond to the temperatures below and around 1200 °C. If a good compromise between cells interconnectivity, microstructure and phase composition is considered important, significant improvements may be achieved by optimization of the sintering conditions using Taguchi planning [29,30]. This experimental design method allows optimization of relevant factors for complex problems involving many variables, at different levels, while performing relatively few experiments. Another promising approach may be based on two-step firing, as demonstrated in our recent works [1,17,21].

3.4. Conclusions

Cellular hematite- and magnetite-based ceramics with nominal $\text{Fe}_{1.8}\text{Al}_{0.2}\text{O}_3$, $\text{Fe}_{1.6}\text{Al}_{0.4}\text{O}_3$, $\text{Fe}_{1.4}\text{Al}_{0.6}\text{O}_3$ and $\text{Fe}_{2.3}\text{Mg}_{0.7}\text{O}_4$ composition were processed by emulsification of powder mixtures with liquid paraffin, followed by reactive firing to promote the formation of highly-porous ceramic skeleton. After the burn-out of the organic phase, several firing temperatures were tested in the range of 1000 to 1400 °C with fixed dwell time of 2 h. The formation of single hematite-based phase was observed for $\text{Fe}_{1.8}\text{Al}_{0.2}\text{O}_3$ under selected processing conditions, whereas higher aluminium content resulted in segregation of secondary Al_2O_3 phase, being in accordance with the phase diagrams. On the contrary, while phase diagrams predict a single-phase $\text{Fe}_{2.3}\text{Mg}_{0.7}\text{O}_4$ spinel at temperatures above 1200 °C, the segregation of Fe_2O_3 impurities at these temperatures indicated kinetic limitations during reactive firing.

The cellular ceramics were characterized by XRD/SEM/EDS, for structural, compositional and microstructural features, including average cell sizes, combined with open and closed porosity, obtained by Archimedes method, and percolation testing; this was described by a constriction factor which accounts for the increase in electrical resistance as the percolating phase narrows through the interconnecting windows. Significant grain growth at temperatures reaching 1400 °C resulted in microstructural reconstruction and vanishing the cellular microstructures. In the case of $\text{Fe}_{2-x}\text{Al}_x\text{O}_3$, a decrease in percolation of the cellular network at 1200-1300 °C was attributed to the collapse of the intercellular windows. The results demonstrated the applicability of the proposed method based on emulsification of powder suspensions to obtain cellular iron oxide-based ceramics. Yet, reactive firing conditions still have to be optimized in order to attain better flexibility in terms of designing phase composition while maintaining a highly-porous and percolating network.

Acknowledgments

This work was supported by the FCT grants PD/BD/114106/2015 and IF/00302/2012, projects LEANCOMB (refs. 04/SAICT/2015, PTDC/CTM-ENE/2942/2014) and CICECO-Aveiro Institute of Materials (ref. UID/CTM/50011/2013), financed by COMPETE 2020 Programme and National Funds through the FCT/MEC and when applicable co-financed by FEDER under the PT2020 Partnership Agreement. The authors are grateful to Artur Sarabando (University of Aveiro) for the assistance provided with the XRD analysis.

3.5. References

- [1] Y. Ivanova, J. Monteiro, L. Teixeira, N. Vitorino, A. Kovalevsky, J. Frade, Designed porous microstructures for electrochemical reduction of bulk hematite ceramics, *Mater. Des.* 122 (2017) 307–314. doi:10.1016/j.matdes.2017.03.031.
- [2] C. Girginov, S. Veleva, S. Kozhukharov, C. Girginov, S. Veleva, S. Kozhukharov, A. Stoyanova, E. Lefterova, M. Mladenov, R. Raicheff, A comparative study on application of biogenic hematite and magnetite as electrode materials in hybrid supercapacitors, *J. Chem. Technol. Metall.* 52 (2017) 557–564.
- [3] J. Monteiro, Y. Ivanova, A. Kovalevsky, D. Ivanou, J. Frade, Reduction of magnetite to metallic iron in strong alkaline medium, *Electrochim. Acta.* 193 (2016) 284–292. doi:10.1016/j.electacta.2016.02.058.
- [4] X. Zheng, J. Li, A review of research on hematite as anode material for lithium-ion batteries, *Ionics (Kiel)*. 20 (2014) 1651–1663. doi:10.1007/s11581-014-1262-5.
- [5] X. Hu, J.C. Yu, J. Gong, Q. Li, G. Li, α -Fe₂O₃ nanorings prepared by a microwave-assisted hydrothermal process and their sensing properties, *Adv. Mater.* 19 (2007) 2324–2329. doi:10.1002/adma.200602176.
- [6] M. Maruyama, T. Fukasawa, S. Suenaga, Y. Goto, Vapor-grown carbon nanofibers synthesized from a Fe₂O₃-Al₂O₃ composite catalyst, *J. Eur. Ceram. Soc.* 24 (2004) 463–468. doi:10.1016/S0955-2219(03)00205-X.
- [7] M. Mishra, D.-M. Chun, α -Fe₂O₃ as a photocatalytic material: A review, *Appl. Catal. A Gen.* 498 (2015) 126–141. doi:10.1016/j.apcata.2015.03.023.
- [8] A.H. Lu, E.L. Salabas, F. Schüth, Magnetic nanoparticles: Synthesis, protection, functionalization, and application, *Angew. Chemie Int. Ed.* 46 (2007) 1222–1244. doi:10.1002/anie.200602866.

- [9] H. Su, X. Lv, Z. Zhang, J. Yu, T. Wang, Arsenic removal from water by photocatalytic functional Fe₂O₃-TiO₂ porous ceramic, *J. Porous Mater.* 24 (2017) 1227–1235. doi:10.1007/s10934-017-0362-9.
- [10] E. Borvick, A.Y. Anderson, H.-N. Barad, M. Priel, D.A. Keller, A. Ginsburg, K.J. Rietwyk, S. Meir, A. Zaban, Process-Function Data Mining for the Discovery of Solid-State Iron-Oxide PV, *ACS Comb. Sci.* (2017) 755–762. doi:10.1021/acscombsci.7b00121.
- [11] W. Liu, J. Yang, B. Xiao, Application of Bayer red mud for iron recovery and building material production from aluminosilicate residues, *J. Hazard. Mater.* 161 (2009) 474–478. doi:10.1016/j.jhazmat.2008.03.122.
- [12] M. Skaf, J.M. Manso, Á. Aragón, J.A. Fuente-Alonso, V. Ortega-López, EAF slag in asphalt mixes: A brief review of its possible re-use, *Resour. Conserv. Recycl.* 120 (2017) 176–185. doi:10.1016/j.resconrec.2016.12.009.
- [13] N.M. Ferreira, A. V. Kovalevsky, F.M. Costa, J.R. Frade, L. Gauckler, Processing Effects on Properties of (Fe,Mg,Al)₃O₄ Spinel as Potential Consumable Anodes for Pyroelectrolysis, *J. Am. Ceram. Soc.* 99 (2016) 1889–1893. doi:10.1111/jace.14190.
- [14] T. Fey, U. Betke, S. Rannabauer, M. Scheffler, Reticulated Replica Ceramic Foams: Processing, Functionalization, and Characterization, *Adv. Eng. Mater.* 19 (2017) 1–15. doi:10.1002/adem.201700369.
- [15] S. Barg, C. Soltmann, M. Andrade, D. Koch, G. Grathwohl, Cellular ceramics by direct foaming of emulsified ceramic powder suspensions, *J. Am. Ceram. Soc.* 91 (2008) 2823–2829. doi:10.1111/j.1551-2916.2008.02553.x.
- [16] N. Vitorino, C.C.J. Abrantes, J.R. Frade, Cellular ceramics processed by paraffin emulsified suspensions with collagen consolidation, *Mater. Lett.* 98 (2013) 120–123. doi:10.1016/j.matlet.2013.02.020.
- [17] M.F. Sanches, N. Vitorino, J.C.C. Abrantes, J.R. Frade, J.B.R. Neto, D. Hotza, Effects of processing parameters on cellular ceramics obtained by paraffin emulsified suspensions, *Ceram. Int.* 40 (2014) 9045–9053. doi:10.1016/j.ceramint.2014.01.117.
- [18] M.F. Sanches, N. Vitorino, C. Freitas, J.C.C. Abrantes, J.R. Frade, J.B. Rodrigues Neto, D. Hotza, Cellular ceramics by gelatin gelcasting of emulsified suspensions with sunflower oil, *J. Eur. Ceram. Soc.* 35 (2015) 2577–2585. doi:10.1016/j.jeurceramsoc.2015.03.008.
- [19] N. Vitorino, C. Freitas, A. V Kovalevsky, J.C.C. Abrantes, J.R. Frade, Cellular MgAl₂O₄ spinels prepared by reactive sintering of emulsified suspensions, *Mater. Lett.* 164 (2016) 190–193. doi:http://dx.doi.org/10.1016/j.matlet.2015.10.169.

-
- [20] N.M.D. Vitorino, A. V. Kovalevsky, M.C. Ferro, J.C.C. Abrantes, J.R. Frade, Design of NiAl₂O₄ cellular monoliths for catalytic applications, *Mater. Des.* 117 (2017) 332–337. doi:10.1016/j.matdes.2017.01.003.
- [21] E. Lalli, N.M.D. Vitorino, J.G. Crespo, C. Boi, J.R. Frade, A. V Kovalevsky, Flexible design of cellular Al₂TiO₅ and Al₂TiO₅-Al₂O₃ composite monoliths by reactive firing, *Mater. Des.* 131 (2017) 92–101. doi:http://dx.doi.org/10.1016/j.matdes.2017.06.010.
- [22] C.R. Hubbard, R.L. Snyder, RIR - Measurement and Use in Quantitative XRD, *Powder Diffr.* 3 (1988) 74–77. doi:10.1017/S0885715600013257.
- [23] S.W. Hughes, Archimedes revisited: a faster, better, cheaper method of accurately measuring the volume of small objects, *Phys. Educ.* 40 (2005) 468–474. doi:10.1088/0031-9120/40/5/008.
- [24] J.C.C. Abrantes, Estereologia software, (2001).
- [25] E.A. Moreira, J.R. Coury, The influence of structural parameters on the permeability of ceramic foams, *Brazilian J. Chem. Eng.* 21 (2004) 23–33. doi:10.1590/S0104-66322004000100004.
- [26] D.R. Lide, *CRC Handbook of Chemistry and Physics*, 87th Editi, Taylor&Francis, New York, 2007. doi:10.1080/08893110902764125.
- [27] A. Muan, On the stability of the phase Fe₂O₃.Al₂O₃, *Am.J.Sci.* 256 (1958) 413–422.
- [28] I.H. Jung, S.A. Decterov, A.D. Pelton, Critical thermodynamic evaluation and optimization of the Fe-Mg-O system, *J. Phys. Chem. Solids.* 65 (2004) 1683–1695. doi:10.1016/j.jpcs.2004.04.005.
- [29] G. Taguchi, S. Chowdhury, Y. Wu, *Quality Engineering: The Taguchi Method*, in: Taguchi's Qual. Eng. Handb., John Wiley & Sons, Inc., Hoboken, NJ, USA, 2004: pp. 56–123. doi:10.1002/9780470258354.
- [30] L. Harris, P. Ross, *Taguchi Techniques for Quality Engineering*, in: Q.R.E. Int. (Ed.), Qual. Reliab. Eng. Int., McGraw-Hill Book Company, 1989: p. 249. doi:10.1002/qre.4680050312.

This Page Intentionally Left Blank

4. Electrochemical reduction of hematite-based ceramics in alkaline medium: Challenges in electrode design

Electrochemical reduction of low-conductive hematite-based ceramics represents a novel approach for iron recovery and waste valorisation. The process itself allows a flexible switching between hydrogen generation and iron reduction, important for the intermittent renewable-energy-powered electrolytic process. The present study focuses on the direct electrochemical reduction of aluminium-containing hematite in strong alkaline media. Within this scope, the reduction mechanisms of porous and dense cathodes, with 60%, 37% and 3% of open porosity, were investigated using different types of electrodes configuration: nickel-foil and Ag-modified nickel-foil supported configuration (cathodes facing or against the counter electrode), and nickel-mesh supported configuration. The efficiency of the iron reduction was compared for different electrode concepts. The results highlight the importance of electrolyte access to the interface between the metallic current collector and ceramic cathode for attaining reasonable electroreduction currents. Both excessively porous and dense ceramic cathodes are hardly suitable for such reduction process, showing a necessity to find a compromise between mechanical strength of the electrode and its open porosity, essential for the electrolyte access.

Keywords: Cellular ceramics; hematite; metallic iron; zero-valent iron; cathodic reduction.

This chapter is based on the following publication:

D.V. Lopes, Y.A. Ivanova, A.V. Kovalevsky, A.R. Sarabando, J.R. Frade, M.J. Quina, Electrochemical reduction of hematite-based ceramics in alkaline medium: Challenges in electrode design, *Electrochim. Acta.* 327 (2019) 135060. doi:10.1016/j.electacta.2019.135060.

4.1. Introduction

Iron oxides are available as natural raw materials and are also present in Fe-rich industrial wastes, such as red mud from the alumina refining industry. In the latter case, hematite is combined with other components, such as alumina, silica, calcium and magnesium oxides, requiring further separation from unwanted components and contaminants [1]. Metallurgical industry uses raw iron oxides for steel production and iron-based alloys by reduction in blast furnaces with carbothermal reducing agents resulting in massive CO₂ emissions. Thus, green alternatives to the traditional methods are gaining interest, such as electrochemical deposition of iron in acidic media [2,3], molten oxide electrolysis [4,5] and even iron pyroelectrolysis [6,7]. While some of these approaches require the use of high temperature, acidic conditions lead to looping between iron valences (Fe²⁺ and Fe³⁺) and low process efficiencies [8,9].

Direct electrochemical reduction of iron oxides has been gaining attention [8–15] as a process allowing *in situ* reduction of the bulk ceramics at the cathode, under strong alkaline media. Low temperatures (90 - 110 °C) have been used for the electrochemical reduction of both bulk hematite or hematite particles in concentrated suspensions [14–17]. Such electrochemical reduction pathway also represents a new alternative for zero-valent iron (ZVI, Fe⁰) production, which has been frequently used for environmental treatments based on the flexible interplay between the redox states [18]. However, existing challenges include insufficient current efficiency of this process at relatively low temperatures and inherent electrically insulating nature of iron oxides in these conditions, especially for hematite. Recent works focused on the studies of bulk electroreduction mechanisms of hematite to metallic iron and on general improvement of the relevant cathode electrochemical issues, in order to decrease hydrogen evolution and, consequently, increase current efficiencies. Conductive materials such as molybdenum [19], nickel [12,15] grids/wires/foils enfolded the cathode or were glued to it with conductive paste, to trigger the reduction of hematite. Porous structures of the bulk electrodes seem to enable the entrance of the electrolyte and, thus to facilitate the diffusion of electrochemically active species. This fact was observed by Zou and his co-workers [15] when testing different sintering temperatures (700 - 1300 °C) for previously pressed Fe₂O₃ pellets. The higher residual porosity attained in the sample sintered at 1100 °C showed a pronounced impact on the reduction rate compared to the samples sintered at a higher temperature and possessing a lower residual porosity. However, lower sintering temperatures also lead to poor mechanical strength of the ceramics, showing the relevance of a balance between optimum sintering conditions for porosity, phase composition, and mechanical strength. Thus, an appropriate electrode design is especially important for facilitating the reduction of low-conductive ceramics, like hematite. A recent method for ceramics processing by the emulsification of ceramic powder suspensions [20–24] allows highly porous cellular microstructures, with interesting features for electrode applications. This approach was recently used for the first time for hematite [17]

and hematite-based materials containing aluminium [25], and it was also used as precursors for cathodes in the present work. Ivanova et al. [17] obtained up to 64% of open porosity in hematite ceramics by applying various processing conditions. Three pellets with different open porosities levels (9%, 44%, and 64%) were tested as cathodes for electrochemical reduction at different experimental temperatures (25 °C and 90 °C) and different electrolyte concentrations (1 and 10 M of NaOH). The highest electrochemical activity towards iron reduction was observed for the ceramics possessing 64% of open porosity at 90 °C and in 10 M of NaOH proving that, besides the microstructural design of the electrode, the temperature and the basicity of the alkaline media have a significant impact on the efficiency of the process. However, a total conversion to metallic iron was not yet attained, and the faradaic efficiency was around 39%.

The possible presence of other components may impose even more limitations on the electrochemical bulk reduction of iron oxides. For example, aluminium may be present in noticeable amounts in both natural iron oxide ore and, especially, in industrial wastes like red mud. Straightforward studies of electrochemical reduction of the red mud are not expected to be conclusive enough regarding the relevant mechanisms of the process due to the inherent complex chemical and phase composition of the bauxite residue. In the present work, Al-substituted hematite ($\text{Fe}_{1.8}\text{Al}_{0.2}\text{O}_3$) was tested as a model cathode material to assess the possible impacts provided by the aluminium presence. However, the particular novelty of this work is related to the assessment of different cathode concepts for the direct electrochemical iron reduction in alkaline medium, including various microstructural designs, supported configuration and preferred orientation towards counter electrode.

4.2. Experimental procedure

Hematite-based ceramics with designed porosity and containing a controlled addition of Al_2O_3 , $\text{Fe}_{1.8}\text{Al}_{0.2}\text{O}_3$, were prepared by the emulsification of Fe_2O_3 - Al_2O_3 powder mixture with liquid paraffin, using a procedure similar to that described in a previous work [25]. For the sake of comparison, dense pellets of the same composition were prepared by uniaxial pressing at 22 MPa. All samples were fired or sintered at 1100 °C and 1300 °C in air atmosphere (heating/cooling rates of 3 °C/min and 5 °C/min, dwell of 2 h). Open porosity of each sample was estimated by Archimedes method [21,25,26]. The fired ceramic samples retained a single phase solid solution, within the detection limits of XRD. Still, this is likely to be retained in a metastable condition, as found on extrapolating the boundaries of the single-phase region of the relevant phase diagram [27] to room temperatures.

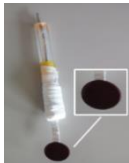




Before electrochemical reduction tests, the samples were polished until a thickness between 1.5 – 3.0 mm and a geometrical area of around 0.7 cm², washed with distilled water and ethanol and dried in the oven. Silver paste (Agar Scientific) was used to glue Ni supports (foil and mesh, acting as a current

collector) to the samples and provide reliable electrical contact. The area of Ni supports, which is not in the contact with the sample and exposed to the electrolyte was painted with lacquer (Lacomit Varnish, Agar Scientific) to avoid electrochemical contribution to the cathodic processes. After drying, the samples were soaked in the electrolyte (NaOH, 10 M) for 30 min to ensure a complete infiltration of the electrolyte inside of the porous cavities. Different electrode configurations with the prepared samples were tested. Table 4.1 presents those configurations and respective images of the electrodes. The $\text{Fe}_{1.8}\text{Al}_{0.2}\text{O}_3$ ceramics have a pellet form, with a lighter area corresponding to that covered with silver. In “front” orientation the pellet was turned to the counter electrode by the open surface side, without Ag paste and/or lacquer; the “rear” orientation corresponds to 180° reversed configuration. It is important to note that Ag-modified designation is related to the pellet having one full face completely painted by Ag paste. In all cases, Ag paste is always locally glued to the Ni support to ensure electrical contact. NF (nickel foil) and NM (nickel mesh) configurations are shown in Table 4.1, with the cathode support covered with Teflon tape for isolation purposes. In the case of NMAg-R, the nickel mesh was used as a support and current collector, in order to ensure a better distribution of the current through the entire electrode surface as compared to NF configuration. The wires of the mesh without the contact with the ceramics were covered with lacquer. One face and the lateral sides of ceramics were also isolated with lacquer, and the only face of the ceramic electrode, covered with Ag paste, was exposed to the electrolyte.

Electrochemical reduction studies were performed at 90 °C, with an Autolab potentiostat (PGSTAT 20) connected to the electrochemical cell in a Teflon reactor. A Pt wire was used as a counter electrode (CE) and $\text{Hg}|\text{HgO}|\text{NaOH}$ (1 M) (+0.098 V versus saturated hydrogen electrode) as a reference electrode connected by a Luggin capillary to the electrolyte as previously described in [9,17]. Cyclic voltammetry (CV) was performed starting from the open circuit potential (E_{oc}) with a scanning rate of 10 mV/s. The current density values were calculated from the geometric area of each electrode. Amperometry curves were performed in potentiostatic mode at -1.075 V, unless indicated otherwise. Electrochemical impedance spectra (EIS) were registered in a frequency from 1 Hz to 1MHz, 50 mV of amplitude and 50 points per decade.

In order to perform a post-mortem analysis after electroreduction, the cathodes were washed with distilled water to remove the excess of NaOH and afterward preserved in ethanol. The morphology of the cathodes was studied by scanning electron microscopy (SEM) with a Hitachi S-4100 microscope, with chemical analysis by Energy-dispersive X-ray spectroscopy (EDS), model Bruker Quantax 400. The phase composition was assessed by X-ray diffraction with a PANalytical XPert PRO diffractometer ($\text{CuK}\alpha$ radiation, $2\theta = 10\text{--}80^\circ$) with a graphite monochromator. Phase content was calculated using Rietveld refinement procedure in Panalytical HighScore Plus 4.7 (PDF-4) software.

Table 4.1. Electrode configurations studied.

Name	Configuration	Ag-modified	Sample orientation towards CE ¹	Sample type (porosity and processing conditions)	Scheme
NF-F	Ni-foil supported	No; Pellet borders and one face painted with lacquer	Front	Porous: 60%, $T_{\text{firing}}^2 = 1100\text{ }^\circ\text{C}$ 37%, $T_{\text{firing}} = 1300\text{ }^\circ\text{C}$	
NF-R	Ni-foil supported	No; Pellet borders and one face painted with lacquer	Rear	Porous: 60%, $T_{\text{firing}} = 1100\text{ }^\circ\text{C}$ 37%, $T_{\text{firing}} = 1300\text{ }^\circ\text{C}$	
NFAg-F	Ni-foil supported	Yes	Front	Porous: 37%, $T_{\text{firing}} = 1300\text{ }^\circ\text{C}$ Dense: 3%, $T_{\text{sint}}^3 = 1300\text{ }^\circ\text{C}$	
NFAg-R	Ni-foil supported	Yes	Rear	Porous: 37%, $T_{\text{firing}} = 1300\text{ }^\circ\text{C}$ Dense: 3%, $T_{\text{sint}} = 1300\text{ }^\circ\text{C}$	
NMAg-R	Ni-mesh supported	Yes	Rear	Dense: 3%, $T_{\text{sint}} = 1300\text{ }^\circ\text{C}$	

CE¹ – counter electrode; T_{firing}^2 – firing temperature of the porous pellet; T_{sint}^3 – sintering temperature of the dense pellet.

4.3. Results and discussion

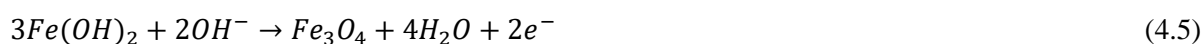
4.3.1. Electrochemical behaviour of $\text{Fe}_{1.8}\text{Al}_{0.2}\text{O}_3$ electrode: general aspects

Cyclic voltammetry curves (CV) obtained for $\text{Fe}_{1.8}\text{Al}_{0.2}\text{O}_3$ cathodes with 60% of open porosity in NF-F configuration are shown in Fig. 4.1. This configuration is rather typical for the electroreduction studies in bulk ceramics [9,17], and gives some general guidelines regarding the electrochemical processes taking place at the cathode. Before electroreduction (Fig. 4.1A), a well-defined cathodic peak C_1 was detected at -0.97 V , while a poorly defined shoulder C_2 is superimposed on the hydrogen

evolution region ($E < -1.10$ V). Higher cathodic polarizations than C_2 are associated with hydrogen evolution due to the water dissociation ($2H_2O + 2e^- \rightarrow H_2 + 2OH^-$). On the other hand, an anodic peak A_2 can be found at -0.65 V. A similar behaviour was observed in the voltammogram of Ivanova et al. [17], for Fe_2O_3 reduction with 64% of open porosity, in similar conditions (10 M of NaOH at $90^\circ C$). One can assign the reduction of $Fe_{1.8}Al_{0.2}O_3$ (Fe_2O_3) to Fe_3O_4 and consequent reduction to Fe (II) to the peak C_1 ($C_1 \approx -1.00$ V in [17]) and reduction of Fe (II) to Fe^0 to C_2 . Since there is no clear evidence from previous studies on the direct electroreduction of Fe_3O_4 to Fe^0 ($Fe_3O_4 + 8H^+ + 8e^- \rightarrow 3Fe^0 + 4H_2O$), as mentioned by Monteiro and co-workers [9], it seems plausible that a two-step reduction of $Fe_2O_3(Fe_{1.8}Al_{0.2}O_3) \rightarrow Fe_3O_4 \rightarrow Fe^{2+}$ takes place at potentials around C_1 . One also assumes ready segregation of alumina from the metastable solid solution ($Fe_{1.8}Al_{0.2}O_3$) upon its partial reduction. Assuming this reduction mechanism, Fe_3O_4 dissolution in a strong alkaline medium (*e.g.* NaOH) can lead to the formation of iron hydroxides precursors (equations 4.1, 4.2, 4.3) [9]:



It should be noticed that no C_2 shoulder was identified in the same CV spectrum in the work [17]. Since the CV scan from Fig.1A was obtained before the electroreduction of iron, the low definition of C_2 shoulder is related to the poor amount of Fe^0 reduced at that stage. At the reverse potential, the anodic peak A_2 is possibly related to the following oxidation of Fe (II) species (equations 4.4 and 4.5) [9,17,28]:



One can observe a significant increase in current density and only one cathodic peak at around -1.16 V (C_2), while also two anodic peaks at -0.82 V (A_1) and -0.56 V (A_2), when comparing the previous results with the voltammogram after reduction (Fig. 4.1B). An increase in the current density suggests a higher active surface area of the electrode [9], likely due to the presence of metallic Fe^0 . After the electroreduction, C_1 peak disappears from the voltammogram, thus confirming the processes previously attributed to the peaks C_1 and C_2 . The two anodic peaks are probably associated with the oxidation of Fe^0 to Fe (II) (A_1) and the oxidation of Fe (II) to FeOOH and/or Fe_3O_4 (A_2).

A cathodic and anodic peak can be found at potentials around 0.20 V (C') and 0.30 V (A'), respectively, in Fig. 4.1A. This behaviour can be associated with minor oxidation of the Ni foil used as

cathode support in the electrochemical cell, to form $\text{Ni}(\text{OH})_2$ and NiOOH , as observed at similar potentials by Skowroński and co-workers, in 6 M of KOH solution [29].

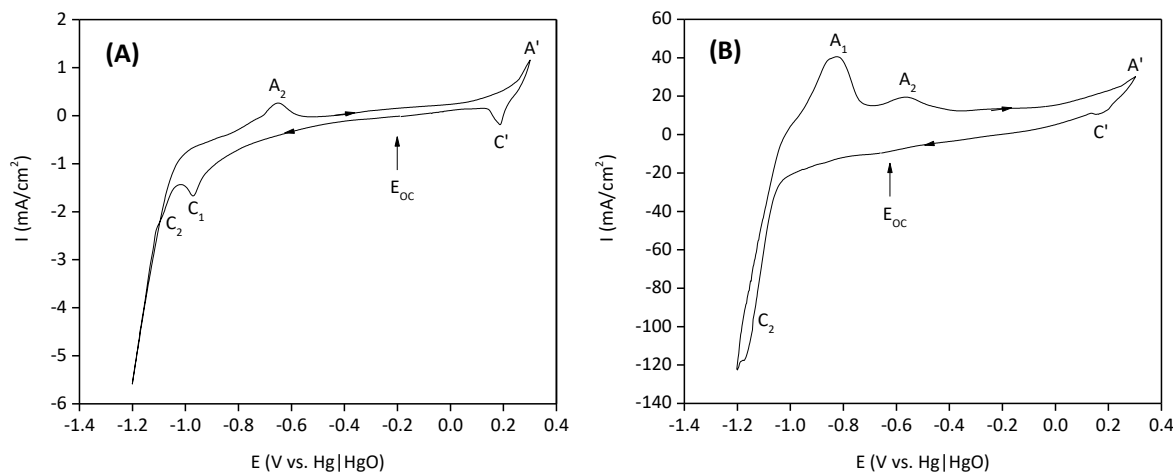


Fig. 4.1. CV curves recorded with a scan rate of 10 mV/s for porous $\text{Fe}_{1.8}\text{Al}_{0.2}\text{O}_3$ (60% of open porosity) electrodes in 10 M NaOH at 90 °C in NF-F configuration before (A) and after (B) reduction at cathodic potential $E_{\text{cath}} = -1.10$ V.

The results of EIS studies performed for the same porous (60%) $\text{Fe}_{1.8}\text{Al}_{0.2}\text{O}_3$ electrode before electroreduction and after 2.5 h and 5 h of the reduction are shown in Fig. 4.2. The low-frequency semi-circle, corresponding to the mixed diffusion-controlled region, almost merges with high-frequency semi-circle, indicating the charge transfer processes, making difficult to extract the latter contribution. Therefore, the low-frequency part of the Nyquist plots was not considered for further analysis. The equivalent circuit used for EIS investigation is showed in the same figure, where the following components are indicated: reference electrode (RE), resistance of solution/electrolyte (R_s), charge transfer resistance (R_1), double-layer capacitance (CPE_1) and working electrode (WE).

Table 4.2 shows the corresponding fitting parameters, where true capacitance values, CPE_1 ($\alpha=1$), were calculated attending to equation (4.6):

$$C = ((R_1 \times \text{CPE}_1)(R_1 \times \text{CPE}_1)^{1/n})/R \quad (4.6)$$

Despite the low values of R_s , this parameter seems to decrease with time indicating some ohmic contribution between RE and WE before reduction. The charge transfer resistance R_1 dramatically decreases upon the reduction, likely due to the formation of a percolating network of the highly-conductive Fe^0 particles and, possibly Fe_3O_4 . These results are in a good agreement with those obtained in [9]. CPE_1 ($\alpha=1$) values showed a significant increase from 0 to 5 h, which may indicate an expansion of the surface area of the WE due to the reduction to Fe^0 , again in a good agreement with the same study.

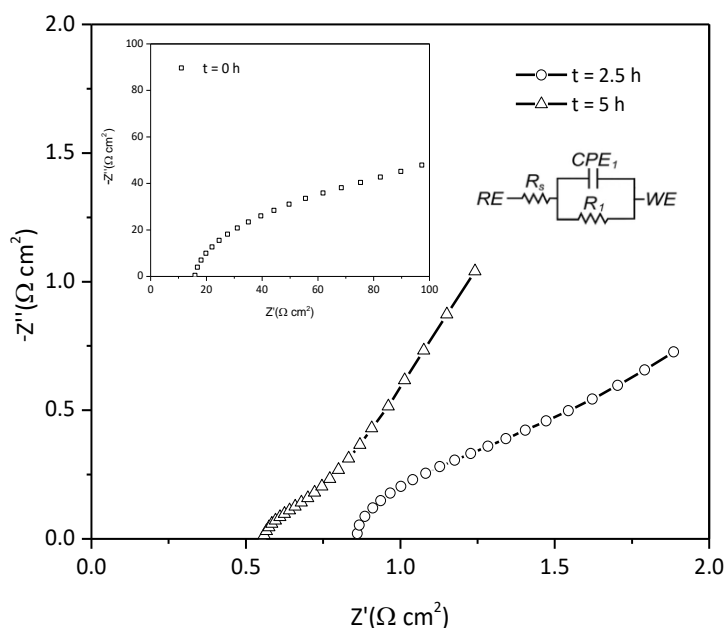


Fig. 4.2. Nyquist plots for non-reduced 60%-porous $\text{Fe}_{1.8}\text{Al}_{0.2}\text{O}_3$ sample ($t = 0$ h) and the same sample reduced during $t = 2.5$ h and $t = 5$ h at $E_{\text{cath}} = -1.10$ V (NF-F electrode configuration) at 90 °C in 10 M NaOH.

Table 4.2. Results of fitting of the EIS data: the parameters of the equivalent circuit.

Time	R_s ($\Omega \text{ cm}^2$)	R_1 ($\Omega \text{ cm}^2$)	CPE_1 ($\alpha=1$), $\mu\text{F}/\text{cm}^2$
$t = 0$ h	15.58	103.71	1.10×10^{-1}
$t = 2.5$ h	0.85	1.36	1.11×10^3
$t = 5$ h	0.55	0.69	5.60×10^2

4.3.2. Nickel-foil supported configuration

The CV curves shown in the Fig. 4.1A suggest that the iron reduction can be accomplished roughly in the cathodic potential range from -1.00 to -1.10 V, without risks of significant contribution from hydrogen evolution. Amperometry curves (currents vs. time) depicted in Fig. 4.3 were obtained for three different cathodic potentials (-1.00 V, -1.05 V and -1.10 V) during $\text{Fe}_{1.8}\text{Al}_{0.2}\text{O}_3$ reduction, in order to find a better estimation of another suitable potential for the cathodic reduction. Potential optimization also seems to be an important step to take into account when considering industrial needs, such as energy costs, suitable equipment for the range of potentials needed and time required for the electrochemical processes.

At lowest $E = -1.00$ V, the current density did not exceed the absolute value of -0.2 mA/cm^2 during 2.5 h, showing a weak tendency to increase. Thus, this cathodic potential was too low to promote

massive iron reduction and formation of more conductive phases than hematite [8,12,15,17]. By increasing the cathodic potential to $E = -1.05$ V, a slightly higher current density was observed (≈ -1.0 mA/cm²) at around 2.5 h of the reduction. At $E = -1.10$ V, a similar shape of the amperometry curve was observed. However, the current density increased considerably up to ≈ -24 mA/cm², which was the potential selected for the studies of iron oxide reduction in the Ni-foil supported configuration (NF).

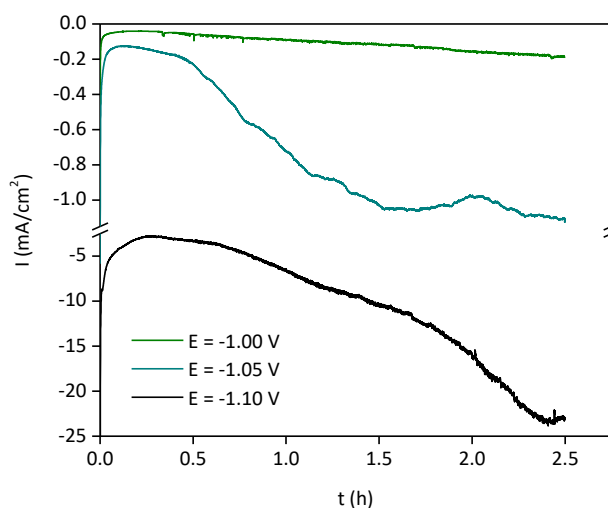


Fig. 4.3. Current vs. time curves at various cathodic potentials (-1.00 V, -1.05 V and -1.10 V) for 2.5 h (60% of open porosity).

A comparative study of different NF configurations was thus undertaken at $E_{\text{cath}} = -1.10$ V (Fig. 4.4), corresponding denominations are described in Table 1. In general, the amperometry curves have a similar shape. A short-time decrease of the current density is observed during the initial stage of reduction, which can be attributed to the formation of an electric double layer at the cathode-electrolyte interface [30]. The decrease and increase of current densities around the same short period of time was observed in other studies [15,17], which may be associated with the entrance of the electrolyte inside of the electrode, where an interface between the current collector|solid insulator pellet|electrolyte (three phase interlines mechanism - 3PIs) starts to be formed [31,32]. Once the interface is formed near Ni current collector, the hematite-based $\text{Fe}_{1.8}\text{Al}_{0.2}\text{O}_3$ phase starts to be reduced forming more conductive phases, Fe_3O_4 and Fe^0 , leading to an extension of the effective electrode area and increase of the cathodic current; this may explain the increase in nominal current density I/A_0 , which is based on the initial electrode area A_0 . In addition, volume changes on reducing hematite to metallic Fe^0 yield additional porosity, which also promotes further infiltration of the electrolyte inside the ceramic cathode. This minimizes ohmic losses by suppressing constrictions and also results in further increase of the current density (Fig. 4.4). In this case, the electrochemical reaction is self-sustained as long as the iron reduction takes place.

The NF-F configuration shows significant reproducibility, with current densities around -20 mA/cm^2 after 2.5 h of the reduction. On the contrary, NF-R configuration shows poor reproducibility: significant differences were found with the increase of the current density over time, where -13 mA/cm^2 (NF-R1) and -37 mA/cm^2 (NF-R2) were obtained. However, the current densities in both NF-F tests are comparable with NF-R1. On the other hand, NF-R2 demonstrates a higher current density. Since the reduction starts at the interface between the current collector and $\text{Fe}_{1.8}\text{Al}_{0.2}\text{O}_3$ cathode, the configuration where the current collector is facing the counter electrode (NF-R) is expected to have a lower ohmic resistance and better current distribution after the initial reduction. The latter facilitates the electrochemical reduction, but it can also result in losses of the mechanical integrity of the ceramic cathode. In particular, if few large pores with the access to the electrolyte are present at the interface between the current collector and $\text{Fe}_{1.8}\text{Al}_{0.2}\text{O}_3$ ceramics, this could result in very fast development of the reduction front, especially in the case of NF-R configuration. This might be responsible for high currents observed in the case of NF-R2 test.

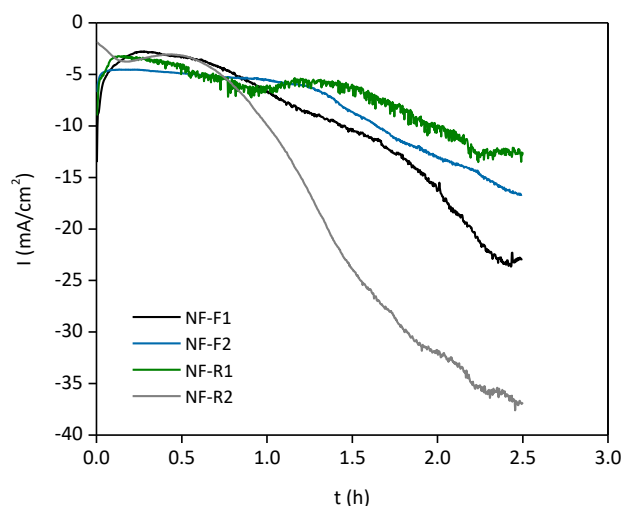


Fig. 4.4. Current-time transients recorded for NF-F and NF-R configurations at $E_{cath} = -1.10 \text{ V}$ for 2.5 h (60% of open porosity).

The above discussion of the cathodic processes during the electroreduction of $\text{Fe}_{2-x}\text{Al}_x\text{O}_3$ is further confirmed by the results of XRD and microstructural studies. Fig. 4.5 shows post-mortem studies of the NF-R electrode reduced at -1.10 V after 5 h. Ceramic cathodes can suffer significant physical stresses possibly due to pressure induced by hydrogen evolution, causing electrode delamination (Fig. 4.5), as the applied potential becomes cathodic relative to hydrogen evolution. In accordance with the XRD results (Fig. 4.5), Fe_3O_4 ($Fd\bar{3}m$) and Fe^0 ($Im\bar{3}m$) are found near the current collector (x). Indeed, SEM study reveals that large Fe^0 crystals (octahedron particles, $d \approx 3\text{-}12 \mu\text{m}$) are present in the sample analysed near Ni foil and are incorporated in finer microstructures, probably, composed of Fe_3O_4 . The initial cellular structure is not retained after reduction, suggesting that the reduction mechanism involves

diffusion and re-deposition of the iron species from the electrolyte. Note also that the reduced regions only retain residual Al-rich spots. This confirms that electrolysis in alkaline conditions offers prospects for direct electrowinning of Fe^0 from $\text{Fe}_{2-x}\text{Al}_x\text{O}_3$ solid solution, without previous separation and with relatively low residual contamination with alumina.

When analysing a sample in the bulk away from the Ni current collector, Fig.4.5 (*), one can observe very few Fe^0 crystals and greater evidence of cellular cavities, resembling the initial microstructure. At the same time, on the opposite side of the current collector (o), Fe^0 phase was not detected by XRD, and thus Fe_2O_3 -type phase is likely the dominant compound, indicating the absence of reduction.

The results highlight not only the fact that the reduction starts at the interface between Ni and the ceramic electrode, but also that the combination of poor mechanical strength of the pellet and high cathodic potentials applied might be an issue for the electrode integrity. These guidelines are essential for cathode design and were taken into account in another configuration, namely, Ag-modified concept described in the next section.

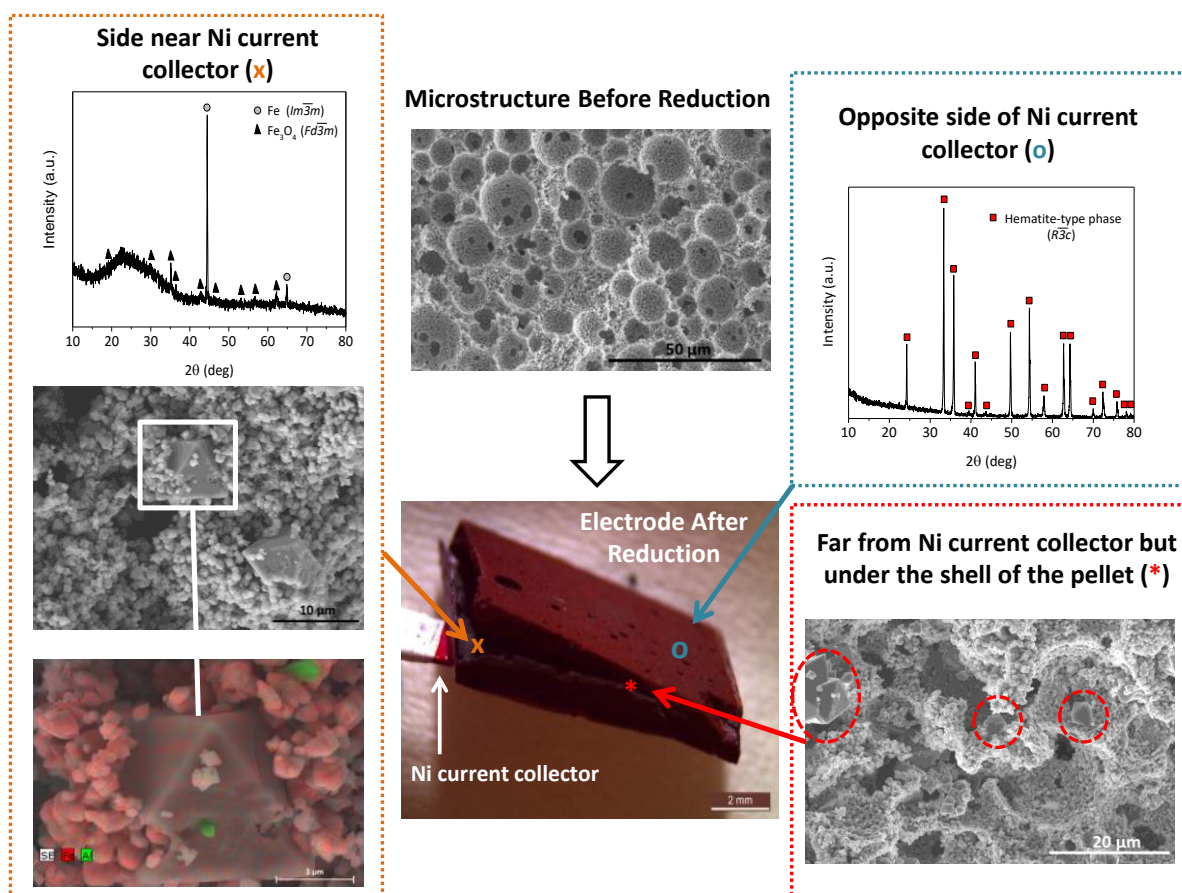


Fig. 4.5. Post-mortem studies of the NF-R electrode (60% of open porosity, $E_{\text{cath}} = -1.10$ V, 5 h of reduction).

4.3.3. Ag-modified nickel-foil supported configuration

This Ag-modified Ni-foil supported (NFAg) configuration is expected to be advantageous regarding the improvement of the contact area between the current collector and the electrode. Moreover, less porous, but mechanically stronger ceramic electrodes were used for testing this concept. Besides this, a lower cathodic potential was used in the reduction of the electrodes with Ag-modified configuration to further suppress the hydrogen evolution. The applied cathodic potential $E_{\text{cath}} = -1.075$ V was an intermediate value between conditions when current density was too low (at $E = -1.05$ V in Fig. 4.3) and conditions when hydrogen evolution may add difficulties ($E = -1.10$ V in Fig. 4.5). The present configuration was tested for $\text{Fe}_{1.8}\text{Al}_{0.2}\text{O}_3$ electrodes reduction, previously fired at 1300 °C, and retaining an intermediate value of porosity (37% of open porosity) in order to improve the mechanical strength. Amperometry curves are shown in Fig. 4.6, the cathodes were tested in NFAg-R (Fig. 4.6A) and NFAg-F (Fig. 4.6B) configurations. When using NFAg-R configuration, similar shape of the curves is observed when compared to the NF-R configuration. Since the face of the electrode with Ni-foil was completely painted with Ag paste and facing the counter electrode, more active surface for the electroreduction is available, leading to initial oscillations and higher currents over time. At 2.5 h, an increase of over 60% of the current density was observed for NFAg-R. One can distinguish three different periods on the current *vs* time dependencies during 5 h of the electroreduction. Namely, the first period (until ≈ 2 h) dominated by electrolyte entrance in the electrode pores and the formation of 3PIs; in the second period ($\approx 2 - 4$ h), a maximum cathodic current is achieved (≈ -75 mA/cm² and -85 mA/cm²), possibly due to almost complete reduction to Fe^0 in the locations with direct access to the electrolyte; and the third period (> 4 h), where a decrease of the current is noticeable and can be attributed to gradual exhaustion of precursor oxide in the ceramics bulk. Similar behaviour was observed in [15]. In fact, almost complete reduction of the NFAg-R electrodes was proved by XRD analysis (Fig. 4.6C), with a Faradaic efficiency close to 100%.

The front configuration NFAg-F is expected to provide better current distribution and more uniform reduction since the process starts at the interface between the current collector (Ni foil and Ag paste) and electrolyte. However, current oscillations occur on reaching nominal current densities of ≈ 80 mA/cm², (Fig. 4.6B), apparently as a result of less-homogeneous reduction, accumulation of stresses and partial disintegration of the electrode (Fig. 4.6D). Thus, Faradaic efficiency was not estimated for NFAg-F case due to the loss of a significant part of the ceramic electrode during the electrochemical tests.

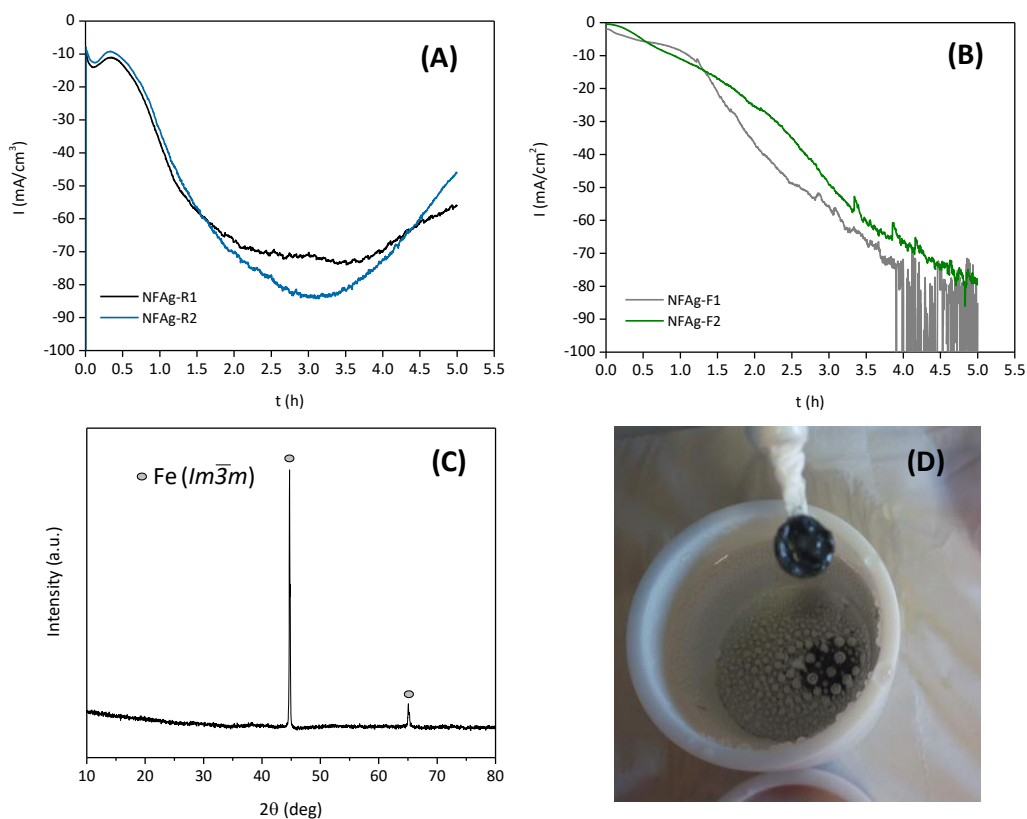


Fig. 4.6. Reduction of $\text{Fe}_{1.8}\text{Al}_{0.2}\text{O}_3$ electrode (37% of open porosity, 5 h), previously fired at 1300 °C, with $E_{\text{cath}} = -1.075$ V in different orientations towards CE: (A) NFAg-R and (B) NFAg-F; (C) XRD analysis of NFAg-R test; (D) pellet collapse during NFAg-F test.

Fig. 4.7 shows the microstructural evolution of the $\text{Fe}_{1.8}\text{Al}_{0.2}\text{O}_3$ electrode in NFAg-R configuration. The electroreduction results in significant microstructural reorganization (Fig. 4.7B) as compared to freshly sintered ceramics (Fig. 4.7A).

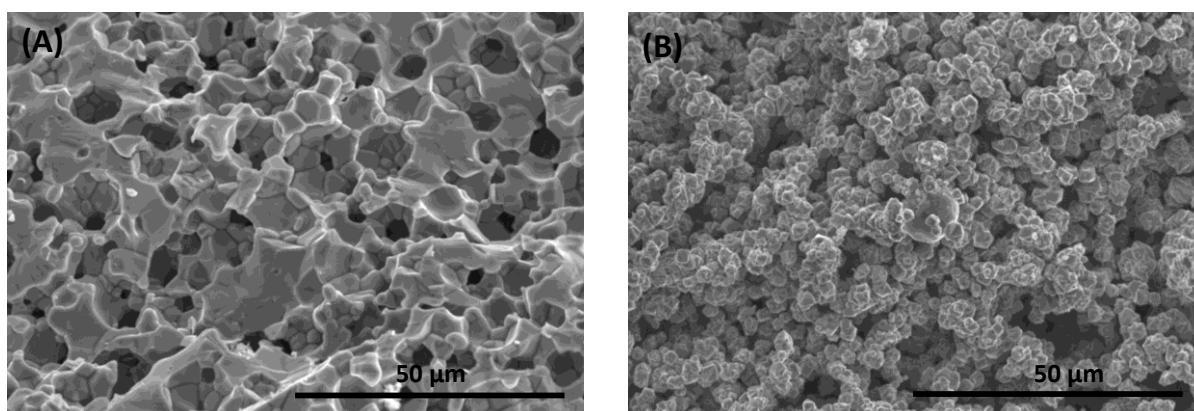


Fig. 4.7. Microstructural evolution after electroreduction of the electrode in NFAg-R configuration: (A) before reduction (37% of open porosity); (B) after 5 h of reduction (bulk of the electrode).

After 5h of electroreduction, one can observe only Fe^0 crystals (Fig. 4.7B), which is in agreement with the XRD studies (Fig. 4.6C). In fact, NFAg-R configuration allowed higher uniformity of electroreduction, as previously mentioned. Except for few bigger crystals ($\approx 12 \mu\text{m}$), the major part of Fe^0 is represented by smaller crystals (2 - 5 μm), also confirming a better homogeneity of the reduction in NFAg-R.

Dense ceramic electrodes ($\approx 3\%$ of open porosity) of the same composition were also assessed in NFAg configuration to confirm the role of porosity on electrolyte access to the reaction sites. The results of amperometry studies are shown in Fig. 4.8. In general, significantly lower current densities are achieved when using dense $\text{Fe}_{1.8}\text{Al}_{0.2}\text{O}_3$ electrodes; this highlights the fact that, if using low-conductive ceramics as a cathode, electrochemical reaction must occur at triple contacts, thus requiring access of the electrolyte to the interface between the ceramics and current collector; this determines the rate of the electrochemical reduction. Results in Fig. 4.8 also suggest that the NFAg-R configurations appear to outperform the NFAg-F configurations in terms of the current density. However, this is mainly found after major oscillations observed for NFAg-R2, likely originating from some pores and occasional defects, which may facilitate the electrolyte access to the interface with the current collector. Once electroreduction is started in such discontinuities, this may add porosity in the reduced layer, activating new electrochemical sites and setting higher currents. Still, reproducibility of electroreduction of highly dense samples is poor in both “front” and “rear” configurations (Fig.4.8), possibly because faster electroreduction depends mainly on discontinuous residual porosity or other microstructural heterogeneities, as shown in Fig. 4.9B, and also revealed by the diffused front between a fully reduced zone and a partially reduced front (Fig. 4.9C).

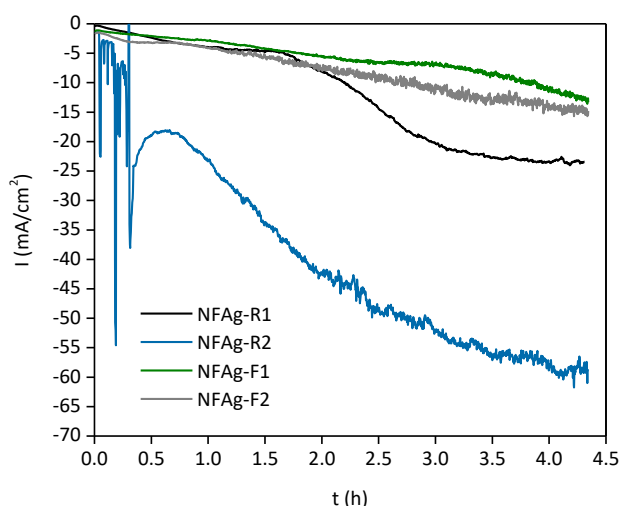


Fig. 4.8. Current-time transients obtained for dense $\text{Fe}_{1.8}\text{Al}_{0.2}\text{O}_3$ samples (3% of open porosity), $E_{\text{cath}} = -1.075 \text{ V}$, in NFAg-R and NFAg-F electrode configuration.

The XRD data and microstructural studies further confirm that the iron reduction takes place even in the case of the dense samples. Fig. 4.9 shows SEM micrographs of the initial $\text{Fe}_{1.8}\text{Al}_{0.2}\text{O}_3$ dense ceramics (Fig. 4.9A), post-mortem analysis results (Fig. 4.9B,C) and corresponding XRD pattern (Fig. 4.9D). Microstructural changes after the reduction are clearly visible and, again, are localized at the interface between the current collector (Ag paste) and ceramics. In these places, the formation of Fe^0 crystals similar to those shown in Fig. 4.5 for NF-R configuration takes place (Fig. 4.9B). Better visualization of the reduction front is given on the cross-section SEM micrograph, showing a transition from rather porous reduced part to the dense non-reduced ceramics microstructure.

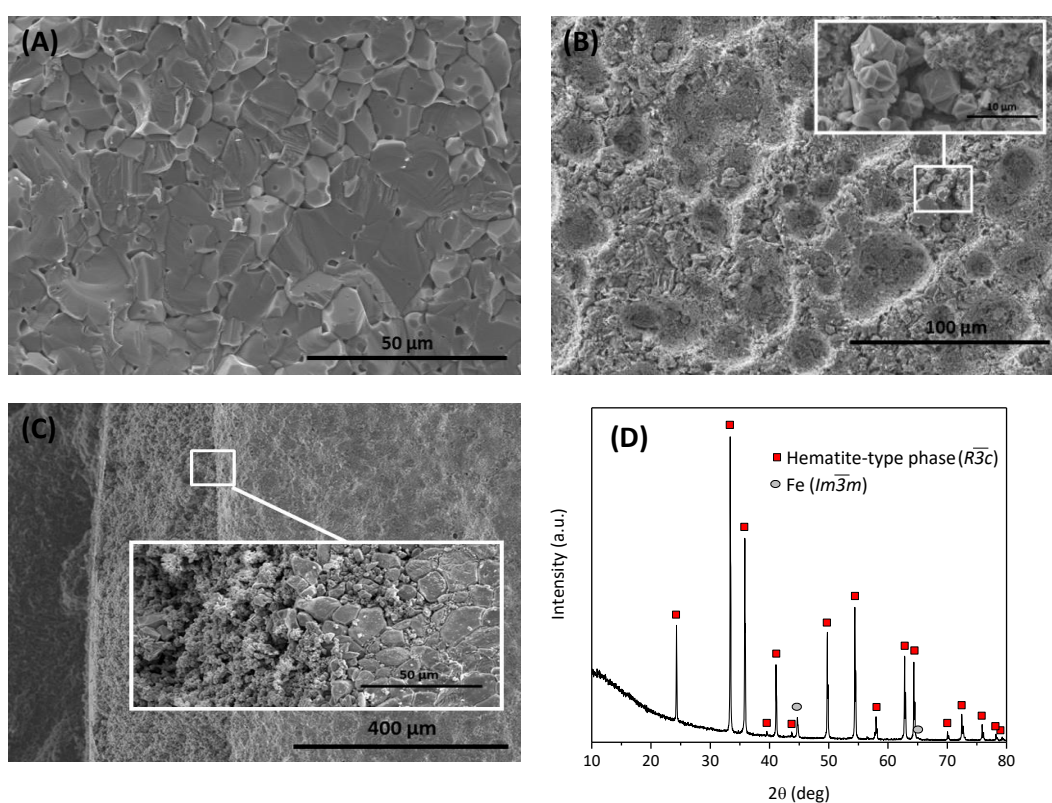


Fig. 4.9. SEM microstructures of dense $\text{Fe}_{1.8}\text{Al}_{0.2}\text{O}_3$ electrode in NF-Ag-R configuration (A) before reduction (3% of open porosity); and after reduction ($E_{\text{cath}} = -1.075$ V): (B) under the Ag layer near the Ni current collector; (C) cross-section starting from the current collector left to the ceramics bulk (right) (D) XRD pattern obtained for the whole ceramic electrode converted to powder.

4.3.4. Nickel-mesh supported configuration

Additional insight into the reduction mechanism in dense samples was obtained using a Ni-mesh supported electrode (NMAg-R), where the only surface of the ceramic electrode, exposed to the electrolyte, was the one covered with Ag paste, in contact with Ni mesh. Within this concept, the electrolyte access was further minimized and restricted to the boundaries between Ni mesh wires,

ceramics and Ag paste. The observed current densities are even lower than for NFAg configuration (Fig. 4.10A). As an example, around 3-times longer experiments were needed to achieve the currents comparable to those for NFAg (Fig. 4.8). Nevertheless, the amperometry curve shape suggests that the reduction still takes place in this configuration. When comparing the current density achieved in NFAg-F, one can suggest that the electrolyte diffusion through the lateral sides may significantly facilitate the process. This fact is highlighted by notably higher currents in the case of NFAg-R configuration. The microstructural results showed in Fig. 4.10B confirm the presence of reduction at the interface between the Ni-mesh current collector and the electrode (left part of Fig. 4.10B), while the opposite side located 1.5 mm further apart from the Ni-mesh shows no sign of reduction (right side of Fig. 4.10B). The reduction takes place at the whole surface, probably extending through a partially reduced layer with a typical thickness of about 20 μm , as revealed by differences in fracture cleavage at the surface layer marked by the yellow dash line in Fig. 4.10B. On integrating the current density one would expect reduced layers with a typical thickness of about 50 μm , suggesting relatively low Faradaic efficiencies.

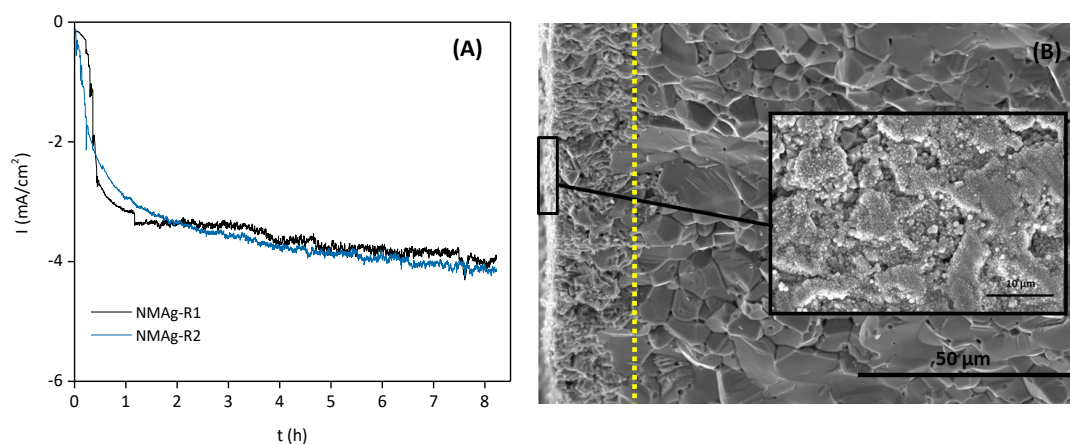


Fig. 4.10. (A) Current vs. time curves obtained for NMAg-R configuration at $E=-1.075$ V, using a dense electrode (3% of open porosity); (B) SEM images of the microstructural alteration in the cross-section of the electrode: at the surface beneath the Ag paste in the contact with Ni-mesh and electrolyte (left part) and structure without reduction (right part).

4.4. Conclusions

Microstructural aspects of the ceramic electrodes and their configuration in the electrochemical cell were investigated and proved to play an important role for the electroreduction of the hematite-based $\text{Fe}_{1.8}\text{Al}_{0.2}\text{O}_3$ in strong alkaline media (10 M of NaOH, at 90 °C). Various ceramic electrode concepts were tested, including front and rear orientation towards counter electrode, deliberate exposing/blocking the access of the electrolyte and different ceramics porosity. The highlights of the present work consist of:

- i. the electrochemical tests of the dense and porous low-conductive electrodes, with 3%, 37% and 60% of open porosity, proved that the reduction is triggered at the interface between the current collector|Fe_{1.8}Al_{0.2}O₃ ceramics|electrolyte;
- ii. the reduction of dense pellets was restricted to the area near Ni current collector, while the gradual self-propagation of the reduction front leads to nearly 100% Faradaic efficiency for the electrodes possessing 37% of open porosity;
- iii. the parasitic contribution of the cathodic hydrogen evolution resulted in the collapse of ceramic electrodes with high open porosity (60%);
- iv. electrowinning of dense samples was strongly affected by the electrolyte access through the lateral sides of the ceramic cathode or residual porosity at the propagation front.

Therefore, the novel methodology of direct electroreduction of Al-substituted hematite materials was proved to be successful for a complete reduction to Fe⁰ or zero-valent iron with medium open porosities.

Acknowledgements

This work was supported by the FCT grant PD/BD/114106/2015, by the European Commission (project SIDERWIN- DLV-768788 - Horizon 2020/SPIRE10) and CICECO-Aveiro Institute of Materials (ref. UID/CTM/50011/2019), financed by COMPETE 2020 Program and National Funds through the FCT/MEC and when applicable co-financed by FEDER under the PT2020 Partnership Agreement.

4.5. References

- [1] M.A. Khairul, J. Zanganeh, B. Moghtaderi, The composition, recycling and utilisation of Bayer red mud, *Resour. Conserv. Recycl.* 141 (2019) 483–498. doi:10.1016/j.resconrec.2018.11.006.
- [2] S.L. Díaz, J.A. Calderón, O.E. Barcia, O.R. Mattos, Electrodeposition of iron in sulphate solutions, *Electrochim. Acta.* 53 (2008) 7426–7435. doi:10.1016/j.electacta.2008.01.015.
- [3] C. wei Su, F. jiao He, H. Ju, Y. bin Zhang, E. li Wang, Electrodeposition of Ni, Fe and Ni-Fe alloys on a 316 stainless steel surface in a fluorborate bath, *Electrochim. Acta.* 54 (2009) 6257–6263. doi:10.1016/j.electacta.2009.05.076.
- [4] D.R. Sadoway, New opportunities for metals extraction and waste treatment by electrochemical processing in molten salts, *J. Mater. Res.* 10 (1995) 487–492. doi:10.1557/JMR.1995.0487.
- [5] H. Kim, J. Paramore, A. Allanore, D.R. Sadoway, Electrolysis of Molten Iron Oxide with an Iridium Anode: The Role of Electrolyte Basicity, *J. Electrochem. Soc.* 158 (2011) E101–E105.

doi:10.1149/1.3623446.

- [6] N.M. Ferreira, A. V. Kovalevsky, S.M. Mikhalev, F.M. Costa, J.R. Frade, Prospects and challenges of iron pyroelectrolysis in magnesium aluminosilicate melts near minimum liquidus temperature, *Phys. Chem. Chem. Phys.* 17 (2015) 9313–9325. doi:10.1039/c5cp00858a.
- [7] N.M. Ferreira, A. V. Kovalevsky, M.C. Ferro, F.M. Costa, J.R. Frade, A new concept of ceramic consumable anode for iron pyroelectrolysis in magnesium aluminosilicate melts, *Ceram. Int.* 42 (2016) 11070–11076. doi:10.1016/j.ceramint.2016.04.004.
- [8] A. Allanore, H. Lavelaine, G. Valentin, J.P. Birat, F. Lapique, Iron Metal Production by Bulk Electrolysis of Iron Ore Particles in Aqueous Media, *J. Electrochem. Soc.* 155 (2008) E125–E129. doi:10.1149/1.2952547.
- [9] J. Monteiro, Y. Ivanova, A. Kovalevsky, D. Ivanou, J. Frade, Reduction of magnetite to metallic iron in strong alkaline medium, *Electrochim. Acta.* 193 (2016) 284–292. doi:10.1016/j.electacta.2016.02.058.
- [10] K.H. Buob, A.F. Beck, M. Cohen, Study of the Cathodic Reduction of Oxide Films on Iron, *J. Electrochem. Soc.* 105 (1958) 74–78. doi:doi: 10.1149/1.2428501.
- [11] K.M. Gorbunova, L.I. Liamina, On the mechanism of iron reduction from alkaline solutions, *Electrochim. Acta.* 11 (1966) 457–467.
- [12] A. Allanore, H. Lavelaine, G. Valentin, J.P. Birat, P. Delcroix, F. Lapique, Observation and modeling of the reduction of hematite particles to metal in alkaline solution by electrolysis, *Electrochim. Acta.* 55 (2010) 4007–4013. doi:10.1016/j.electacta.2010.02.040.
- [13] M. Tokushige, O.E. Kongstein, G.M. Haarberg, Crystal Orientation of Iron Produced by Electrodeoxidation of Hematite Particles, *ECS Trans.* 50 (2013) 103–114. doi:10.1149/05052.0103ecst.
- [14] Q. Wang, Y. Zhu, Q. Wu, E. Gratz, Y. Wang, Low temperature electrolysis for iron production via conductive colloidal electrode, *RSC Adv.* 5 (2015) 5501–5507. doi:10.1039/C4RA14576C.
- [15] X. Zou, S. Gu, X. Lu, X. Xie, C. Lu, Z. Zhou, W. Ding, Electroreduction of Iron (III) Oxide Pellets to Iron in Alkaline Media : A Typical Shrinking-Core Reaction Process, *Metall. Mater. Trans. B.* 46B (2015) 1262–1274. doi:10.1007/s11663-015-0336-8.
- [16] Y. Ivanova, J. Monteiro, A. Horovistiz, D. Ivanou, D. Mata, R. Silva, J. Frade, Electrochemical deposition of Fe and Fe / CNTs composites from strongly alkaline hematite suspensions, *J. Appl. Electrochem.* 45 (2015) 515–522. doi:10.1007/s10800-015-0803-6.
- [17] Y. Ivanova, J. Monteiro, L. Teixeira, N. Vitorino, A. Kovalevsky, J. Frade, Designed porous microstructures for electrochemical reduction of bulk hematite ceramics, *Mater. Des.* 122 (2017)

- 307–314. doi:10.1016/j.matdes.2017.03.031.
- [18] F. Fu, D.D. Dionysiou, H. Liu, The use of zero-valent iron for groundwater remediation and wastewater treatment: A review, *J. Hazard. Mater.* 267 (2014) 194–205. doi:10.1016/j.jhazmat.2013.12.062 C2 - 24457611.
- [19] M. Gibilaro, J. Pivato, L. Cassayre, L. Massot, P. Chamelot, P. Taxil, Direct electroreduction of oxides in molten fluoride salts, *Electrochim. Acta.* 56 (2011) 5410–5415. doi:10.1016/j.electacta.2011.02.109.
- [20] N. Vitorino, J.C.C. Abrantes, J.R. Frade, Cellular PCM / graphite composites with improved thermal and electrical response, *Mater. Lett.* 92 (2013) 100–103. doi:10.1016/j.matlet.2012.10.025.
- [21] M.F. Sanches, N. Vitorino, J.C.C. Abrantes, J.R. Frade, J.B.R. Neto, D. Hotza, Effects of processing parameters on cellular ceramics obtained by paraffin emulsified suspensions, *Ceram. Int.* 40 (2014) 9045–9053. doi:10.1016/j.ceramint.2014.01.117.
- [22] N. Vitorino, C. Freitas, A. V Kovalevsky, J.C.C. Abrantes, J.R. Frade, Cellular MgAl₂O₄ spinels prepared by reactive sintering of emulsified suspensions, *Mater. Lett.* 164 (2016) 190–193. doi:http://dx.doi.org/10.1016/j.matlet.2015.10.169.
- [23] E. Lalli, N.M.D. Vitorino, J.G. Crespo, C. Boi, J.R. Frade, A. V Kovalevsky, Flexible design of cellular Al₂TiO₅ and Al₂TiO₅-Al₂O₃ composite monoliths by reactive firing, *Mater. Des.* 131 (2017) 92–101. doi:http://dx.doi.org/10.1016/j.matdes.2017.06.010.
- [24] N.M.D. Vitorino, A. V. Kovalevsky, M.C. Ferro, J.C.C. Abrantes, J.R. Frade, Design of NiAl₂O₄ cellular monoliths for catalytic applications, *Mater. Des.* 117 (2017) 332–337. doi:10.1016/j.matdes.2017.01.003.
- [25] D. V. Lopes, A. V. Kovalevsky, M.J. Quina, J.R. Frade, Processing of highly-porous cellular iron oxide-based ceramics by emulsification of ceramic suspensions, *Ceram. Int.* 44 (2018) 20354–20360. doi:10.1016/j.ceramint.2018.08.024.
- [26] S.W. Hughes, Archimedes revisited: a faster, better, cheaper method of accurately measuring the volume of small objects, *Phys. Educ.* 40 (2005) 468–474. doi:10.1088/0031-9120/40/5/008.
- [27] M. Maruyama, T. Fukasawa, S. Suenaga, Y. Goto, Vapor-grown carbon nanofibers synthesized from a Fe₂O₃-Al₂O₃ composite catalyst, *J. Eur. Ceram. Soc.* 24 (2004) 463–468. doi:10.1016/S0955-2219(03)00205-X.
- [28] R.S. Schrebler Guzmán, J.R. Vilche, A.J. Arvía, The potentiodynamic behaviour of iron in alkaline solutions, *Electrochim. Acta.* 24 (1979) 395–403. doi:10.1016/0013-4686(79)87026-7.
- [29] J.M. Skowroński, T. Rozmanowski, M. Osińska, Reuse of nickel recovered from spent Ni – Cd

- batteries for the preparation of C / Ni and C / Ni / Pd, *Process Saf. Environ. Prot.* 93 (2015) 139–146.
- [30] W. Gao, S. Cao, Y. Yang, H. Wang, J. Li, Y. Jiang, Electrochemical impedance spectroscopy investigation on indium tin oxide films under cathodic polarization in NaOH solution, *Thin Solid Films.* 520 (2012) 6916–6921. doi:10.1016/j.tsf.2012.07.092.
- [31] Y. Deng, D. Wang, W. Xiao, X. Jin, X. Hu, G.Z. Chen, Electrochemistry at conductor/insulator/electrolyte three-phase interlines: A thin layer model, *J. Phys. Chem. B.* 109 (2005) 14043–14051. doi:10.1021/jp044604r.
- [32] W. Xiao, X. Jin, Y. Deng, D. Wang, G.Z. Chen, Three-phase interlines electrochemically driven into insulator compounds: A penetration model and its verification by electroreduction of solid AgCl, *Chem. - A Eur. J.* 13 (2007) 604–612. doi:10.1002/chem.200600172.

5. Electrochemical deposition of zero-valent iron from alkaline ceramic suspensions of $\text{Fe}_{2-x}\text{Al}_x\text{O}_3$ for iron valorisation

Electrochemical reduction of iron oxides into zero-valent iron (ZVI, Fe^0) is a promising alternative to the traditional methods used for iron production. The electrochemical deposition of Fe^0 from hematite and hematite-based $\text{Fe}_{2-x}\text{Al}_x\text{O}_3$ ceramic in alkaline suspensions (10 M of NaOH) was assessed at relatively low temperature (90 °C). Ceramic compositions aimed to mimic the main components of red mud waste from the alumina refining industry for iron valorisation purposes. The impact of aluminium content on the electroreduction and microstructure of the deposited Fe^0 films was demonstrated and discussed. Trapping and following the leaching of the aluminium species during deposition causes drastic morphological changes and induces significant porosity. Faradaic efficiencies of the reduction to Fe^0 were found to decrease from 70% to 32% for Fe_2O_3 and $\text{Fe}_{1.4}\text{Al}_{0.6}\text{O}_3$, respectively. The results highlight possible effects imposed by aluminium presence during Fe^0 electrodeposition for future iron recycling from, for example, red mud or other aluminium containing wastes by electrowinning in alkaline conditions.

Keywords: Cathodic reduction; cellular ceramics; hematite; red mud; iron recovery.

This chapter is based on the following publication:

D.V. Lopes, A.V. Kovalevsky, M.J. Quina, J.R. Frade, Electrochemical deposition of zero-valent iron from alkaline ceramic suspensions of $\text{Fe}_{2-x}\text{Al}_x\text{O}_3$ for iron valorisation, J. Electrochem. Soc. 167 (2020) 102508. doi:10.1149/1945-7111/ab9a2b.

5.1. Introduction

Around 2 tons of CO₂ per ton of crude iron is generated by the traditional method of iron production in blast furnaces [1,2]. Thus, low-temperature electrolysis-based processes for iron electrodeposition, have emerged as an alternative route for the direct conversion of iron oxide suspensions to metallic iron (Fe⁰) without greenhouse gas emissions [1,3]. Another potential advantage is that these processes may be integrated to balance intermittent energy supply by conversion of renewable energies into metal and possibly also storable gas by-products. Due to the relatively low operating temperatures (≤ 110 °C), this technology is gaining more attention when compared with others for iron production, such as molten oxide electrolysis [3–5] or hydrogen flash smelting [6,7]. The loop of different valence states of iron (Fe²⁺ and Fe³⁺) between the cathode and the anode also prevents electrolysis in acid conditions. However, the Faradaic efficiencies of the process can be strongly affected by electrode overpotentials or current density and several other factors, such as the electrolyte concentration, solid load of iron oxide in suspension, temperature and stirring rate, mainly due to onset of hydrogen [8–10]. On the other hand, the high hydrogen evolution observed in alkaline media can have an impact not only on the process efficiency but also on the porosity of Fe⁰ deposits, leading to fragile structures [11]. To overcome this issue, around 18 M/19 M of an alkaline medium was frequently used as an electrolyte to suppress H₂ evolution near the working electrode [8,12–16]. Strong alkaline electrolytes (≥ 12 M) lead to stable Faradaic efficiencies above 50% during the electrochemical reduction of Fe₂O₃ (50 g/L) in alkaline suspensions at 90 °C [12]. More recently, about 70-80% of current efficiency was achieved in 10 M alkaline suspensions of hematite [9] and also in bulk hematite-based samples [17]. However, the insulating nature of Fe₂O₃ still raises questions regarding its electroreduction mechanism. Some guidelines are provided by the results obtained in [17]. In general, the works [8,16–18] highlight the possibilities for the complete electrochemical reduction of bulk hematite, also pointing out the formation of Fe₃O₄ as an intermediate product [8,16–18]. The use of compacted iron-containing ore as a cathode in the industry may represent a certain challenge due to insufficient electrical conductivity. On the other hand, other scenarios may exist where the electrochemical reduction of iron-containing suspensions can be rather relevant for the direct processing of industrial sludges or iron oxide-rich wastes towards iron recycling.

Though iron oxides, namely hematite, are abundant as natural raw materials, some industrial wastes are also Fe-rich in iron oxides and must be treated or recycled to avoid serious environmental problems. A notorious example is the red mud alkaline waste from the alumina refining industry; this generates about 170 million tons annually [19], which requires specific treatment and disposal. The main components of red mud are Fe₂O₃ (>30 wt%), combined with aluminium oxide/oxyhydroxides, and many others (*e.g.* SiO₂, CaO, Na₂O, and TiO₂) [20]. Despite the complexity and diversity of red mud, iron recovery and recycling bring new perspectives for alumina and iron industries.

In addition to the huge scale of cast iron and steel production, it is important to note that zero-valent iron (Fe^0 , ZVI) has gained attention due to its reactivity ($E^0 = -0.44$ V for Fe^{2+} and $E^0 = -0.04$ V for Fe^{3+} , at 25 °C) to reduce a vast list of contaminants, including nitrate [21], Cr(VI) [22], dyes from textile industries [23] and many other contaminants present in wastewaters [24] or in soils. Chemical [25,26] and carbothermal [27] reductions are some of the most used methods for ZVI production, whereas electrochemical methods have been less studied as an alternative to process ZVI for environmental applications.

The present work challenges the electrodeposition of ZVI/ Fe^0 from alkaline hematite-based suspensions, mimicking the main components of the red mud waste for iron valorisation and ZVI production to reduce other pollutants. In this way, one used synthetic mixtures of known composition, to understand the impact of alumina, and to assess prospects to process ZVI by direct electrolysis of red mud, without or with minimum pre-treatments. For the sake of comparison, the ceramics with a nominal compositions $\text{Fe}_{2-x}\text{Al}_x\text{O}_3$ ($x = 0, 0.2, 0.6$) were processed in the same way as described in [28], to result in highly porous materials with a cellular microstructure, which are further crushed into powder for the preparation of alkaline suspensions for the electroreduction studies. Particular novelty of this work includes the assessment of relevant effects imposed on the electroreduction process by the presence of aluminium oxide, as a main secondary component of the red mud waste.

5.2. Experimental procedure

Hematite, Fe_2O_3 , and hematite-based cellular ceramic pieces, $\text{Fe}_{2-x}\text{Al}_x\text{O}_3$, with designed open porosity and with nominal compositions $\text{Fe}_{1.8}\text{Al}_{0.2}\text{O}_3$ and $\text{Fe}_{1.4}\text{Al}_{0.6}\text{O}_3$ were used as the precursors for the powder suspensions studied in the present work. The ceramic samples were processed with precise structural and microstructural characteristics by emulsification with liquid paraffin from powder suspensions containing Fe_2O_3 (Gute Chemie, abcr GmbH, 99.8%) and the corresponding amount of Al_2O_3 (Alcoa CT3000, 99.8%), as described elsewhere [28]. After emulsification and subsequent firing, all samples were crushed into powder (< 15 μm) for the preparation of suspensions. Pure hematite-based cellular ceramics were sintered in air at 1100 °C, while both $\text{Fe}_{1.8}\text{Al}_{0.2}\text{O}_3$ and $\text{Fe}_{1.4}\text{Al}_{0.6}\text{O}_3$ ceramics were fired at 1300 °C. All firing conditions involved similar heating and cooling rate of 3 °C/min and 5 °C/min, respectively, and 2 h of dwell. The measurements of open porosity of the fired ceramic pieces were performed as described in [18,28,29]. Particle size distributions of all the three crushed iron oxide compositions were studied with a Coulter LS 230 (0.040-2000 μm).

A PTFE electrochemical cell filled with NaOH (100 mL, 10 M) electrolyte was used for the electrochemical studies. During the tests, the suspensions containing 67 g/L of iron in the ceramic powder were stirred with a magnetic stirrer (100 rpm) to avoid sedimentation. The electrochemical

reduction of the suspensions was performed at 90 °C. Platinum wire with a total area of 7.40 cm² in contact with the electrolyte was used as a counter electrode (CE), and Ni grid (4.20 cm² exposed to the electrolyte, 0.90 mm of aperture, 0.22 mm of Ni wire diameter, 0.45 mm of grid thickness) as a working electrode (WE), where the Fe⁰ deposition occurred. The distance between CE and WE was ≈2.5 cm. The reference electrode (RE), Hg|HgO|NaOH (1M) (+0.098 V versus saturated hydrogen electrode), was connected by a Luggin capillary to the electrolyte. The electrochemical reduction studies were conducted using a VersaSTAT 4 (AMETEK) connected to the electrochemical cell; these included cyclic voltammetry (CV) starting from the open circuit potential (E_{OC}) in the range of -1.2 V to 0 V, with a scanning rate of 10 mV/s and potentiostatic reduction to Fe⁰ at E = -1.08 V for 7 h. After electrodeposition, Ni grids were washed with distilled water for NaOH removal and ethanol, and left for drying in a vacuum desiccator. Faradaic efficiencies of the processes were estimated by weighing the Ni grid before and after the electrochemical deposition of Fe⁰, which was then correlated with the total electric charge passed in the cell during the 7 h of the electrochemical process.

Microstructural studies were performed both for the ceramic pieces before crushing and for the Ni grids after the electrodeposition, using scanning electron microscopy (SEM), Hitachi SU-70 coupled with energy dispersive spectroscopy (EDS) analysis (Bruker Quantax 400 detector). Phase composition was assessed based on the results of X-ray diffraction (XRD) analysis, employing a PANalytical XPert PRO diffractometer (CuK α radiation, 2 θ = 10–80°) with a graphite monochromator. Phase identification was performed with Panalytical HighScore Plus 4.7 (PDF-4) software.

5.3. Results and discussion

5.3.1. Structural and microstructural studies of ceramics and powdered samples

The presence of specific microstructural features that may facilitate an electrochemical process, such as open porosity and interconnectivity of the pores, is essential for the electroreduction of iron-based bulk ceramics [17,18]. While the larger pores are likely destroyed by the crushing procedure, the powder still can bear some inherent morphology of the parent ceramics. Porous structure also promotes comminution, with expected similar particle size and distribution in the resulting powder, if the same grinding procedure is applied for similar materials with comparable porosity. Fig. 5.1 shows typical microstructures of the prepared ceramic samples, again confirming the feasibility of the used emulsification method for producing cellular ceramics. In previous work, Lopes et al. [17] observed the collapse of Fe_{1.8}Al_{0.2}O₃ samples fired at 1100 °C due to the high porosity level (≈60%) and low

mechanical strength inappropriate for the bulk electrochemical reduction. On the contrary, 100% of Fe^0 conversion was obtained for $\text{Fe}_{1.8}\text{Al}_{0.2}\text{O}_3$ bulk samples fired at 1300 °C despite the lower open porosity level ($\approx 37\%$). Thus, in this work $\text{Fe}_{1.8}\text{Al}_{0.2}\text{O}_3$ and $\text{Fe}_{1.4}\text{Al}_{0.6}\text{O}_3$ samples were fired at 1300 °C before being crushed into powder. On the other hand, Fe_2O_3 cellular pieces were sintered at 1100 °C due to excessively high densification at 1300 °C observed in [28]. As a result, the selected firing conditions allowed to produce comparable levels of porosity in the prepared materials within the range of 35-49% (Table 5.1).

XRD patterns (Fig. 5.1D) show segregation of a secondary Al_2O_3 -based phase only in the case of $\text{Fe}_{1.4}\text{Al}_{0.6}\text{O}_3$ composition, as observed for all firing temperatures range tested (1100 – 1400 °C) in [28], in fairly good agreement with the phase diagram [30].

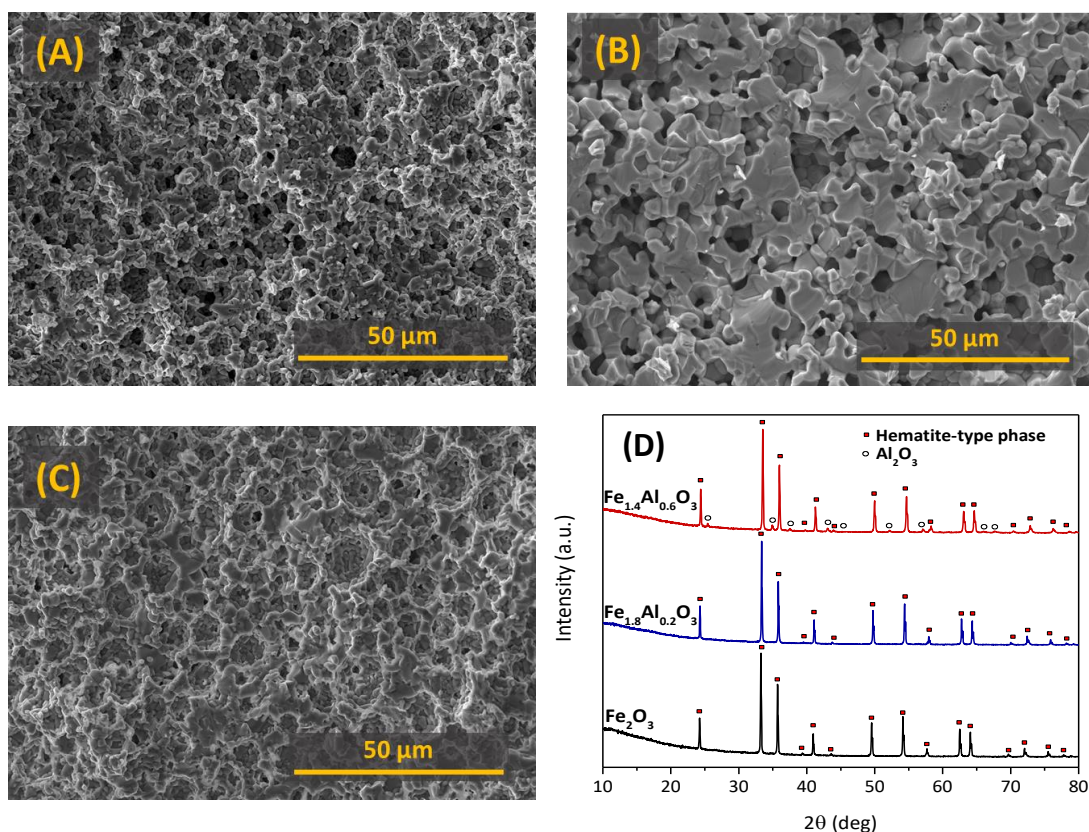


Fig. 5.1. SEM images of the fractured cellular ceramics: (A) Fe_2O_3 (1100 °C), (B) $\text{Fe}_{1.8}\text{Al}_{0.2}\text{O}_3$ (1300 °C), (C) $\text{Fe}_{1.4}\text{Al}_{0.6}\text{O}_3$ (1300 °C); (D) corresponding XRD patterns.

Table 5.1. Firing conditions and open porosities (x_0) of $\text{Fe}_{2-x}\text{Al}_x\text{O}_3$ cellular ceramics.

Nominal composition	T_{firing} (°C)	x_0
Fe_2O_3	1100	0.47 ± 0.04
$\text{Fe}_{1.8}\text{Al}_{0.2}\text{O}_3$	1300	0.35 ± 0.02
$\text{Fe}_{1.4}\text{Al}_{0.6}\text{O}_3$	1300	0.49 ± 0.02

Existing difference in the firing conditions for pure and Al-containing hematite does not affect significantly the particle size distribution (Fig. 5.2) of the powder after crushing, in accordance with the initial expectations based on comparable porosities. The average particle size corresponds to 5.1, 6.4 and 4.6 μm for Fe_2O_3 , $\text{Fe}_{1.8}\text{Al}_{0.2}\text{O}_3$ and $\text{Fe}_{1.4}\text{Al}_{0.6}\text{O}_3$ compositions, respectively. The D_{50} size distribution curves show that 50% of particles have diameters lower than 3.9, 5.3 and 3.5 μm for Fe_2O_3 , $\text{Fe}_{1.8}\text{Al}_{0.2}\text{O}_3$ and $\text{Fe}_{1.4}\text{Al}_{0.6}\text{O}_3$ samples. In all cases, D_{90} is lower than 15 μm .

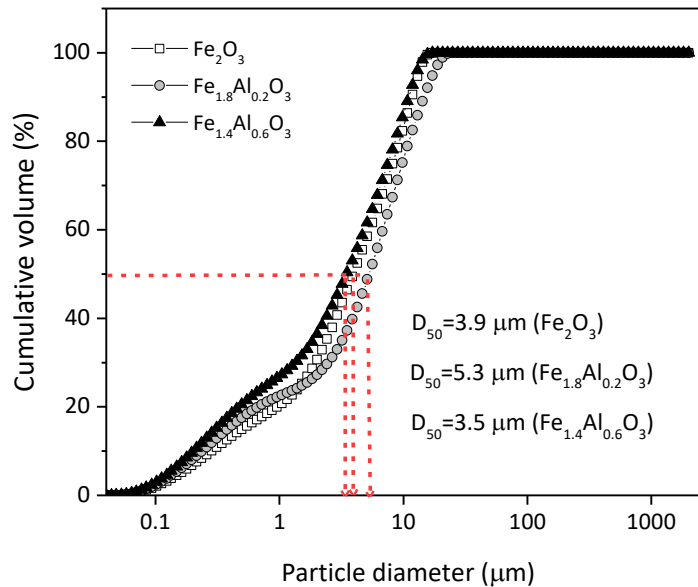


Fig. 5.2. Size distribution of the powder after crushing.

Typical microstructures of powders obtained by crushing cellular ceramic samples are shown in Fig. 5.3. Though the designed porosity in the cellular ceramics is no longer present after crushing (Fig. 5.3A), larger particles still resemble the previous morphology (Fig. 5.3B).

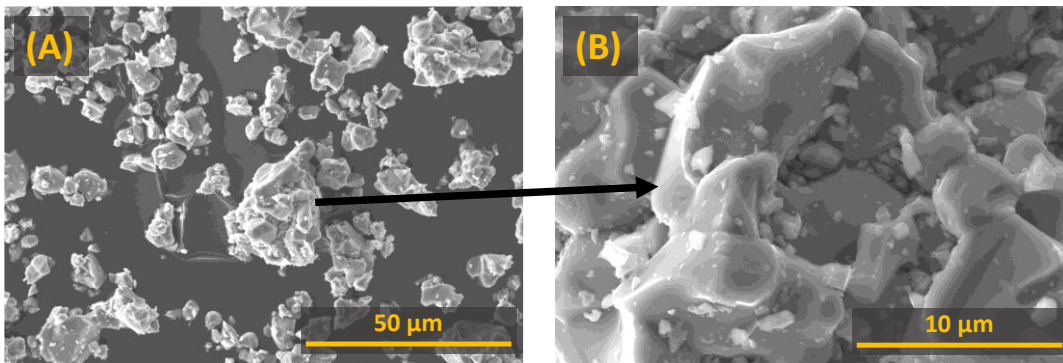


Fig. 5.3. Powders of $\text{Fe}_{2-x}\text{Al}_x\text{O}_3$ processed ceramics after crushing (A) general view and (B) walls of a previous cavity cell.

5.3.2. Electrochemical reduction to ZVI

The electrochemical processes occurring at the working electrode (WE) in the three alkaline suspensions were studied by cyclic voltammetry (CV). The corresponding curves show a sharp cathodic peak, and two broad peaks (Fig. 5.4). Hematite-based suspensions are known to have low electrical conductivity (10^{-14} S/cm) [31] revealing low current densities and no electrochemical reactions prior the electrochemical deposition (image not shown). No noticeable contribution of the redox reaction involving nickel cations was observed during the CV analysis since anodic potentials higher than 0.30 V are required for Ni oxidation [32]. When testing a bulk $\text{Fe}_{1.8}\text{Al}_{0.2}\text{O}_3$ electrode in the same electrochemical conditions before amperometry analysis, Lopes et al [17] observed a cathodic peak (C) at -0.97 V and an anodic peak (A) at -0.65 V. These peaks were related to a minor reduction of $\text{Fe}_{1.8}\text{Al}_{0.2}\text{O}_3$ to Fe_3O_4 , and consequently, to Fe(II) (C); and a minor oxidation of Fe(II) species to FeOOH and/or Fe_3O_4 (A). However, in the cited work a direct electrical contact between the ceramic $\text{Fe}_{1.8}\text{Al}_{0.2}\text{O}_3$ cathode and a nickel foil was provided by a silver paste, leading to a noticeable contribution of the redox reactions involving iron even prior to the electroreduction, highlighting principal differences of these approaches. A sharp current increase at cathodic potentials below -1.10 V can be attributed to the start of hydrogen evolution [9,17].

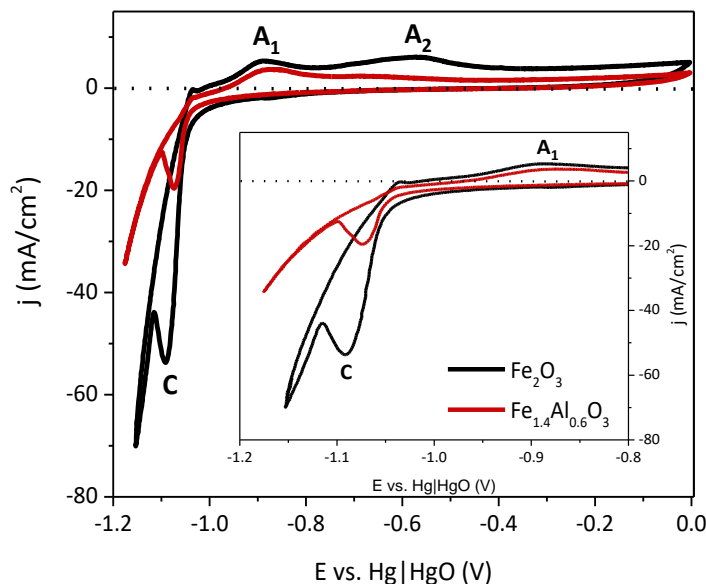


Fig. 5.4. Cyclic voltammetry performed at 0.01 V/s after Fe^0 deposition from Fe_2O_3 (black line) and $\text{Fe}_{1.4}\text{Al}_{0.6}\text{O}_3$ (red line). The insert image shows expanded scales of the main cathodic and anodic peaks.

After 7 h of Fe^0 electrodeposition, an intense peak (C) is present at ≈ -1.086 V for Fe_2O_3 and -1.071 V for $\text{Fe}_{1.4}\text{Al}_{0.6}\text{O}_3$ (Fig. 5.4). At the same potentials, no peak was present in [17] for bulk samples of $\text{Fe}_{1.8}\text{Al}_{0.2}\text{O}_3$ after electroreduction. However, one should notice that this cathodic peak lies in the range

of the potentials which correspond to C₂ observed in [17] and thus, likely, corresponds to complete reduction to Fe⁰. As an example, an onset potential at -1.1 V (vs. Hg|HgO) was attributed to a simultaneous Fe(II) reduction to Fe⁰ and H₂ evolution in similar experimental conditions in [9]; a peak at -1.06 V (vs. Hg|HgO) was associated with reduction to Fe⁰ [1]; and an onset potential of -1.1 V evolving to a peak reaching a maximum at -1.13 V was attributed to the reduction to Fe⁰ in [33]. The reduction of Fe(III) to Fe(II) species (*e.g.* Fe(OH)₃⁻, HFeO₂⁻) usually involves Fe₃O₄ as an intermediate phase, as previously demonstrated in bulk electroreduction [8,15,17,18]. However, in opposition to the latter case where the whole WE is composed of a Fe₂O₃/Fe₃O₄/Fe composite, the electrode in the present work after suspension electroreduction represents a metallic iron layer deposited on the nickel plate, presumably with a thin oxidised layer at the surface. Thus, the cathodic peaks corresponding to the formation of Fe₃O₄ and Fe(II) species might not be easily observed by cyclic voltammetry in this work. The high conductivity of Fe₃O₄ ($\approx 10^2$ to 10^3 S/cm) [31] may facilitate its fast conversion to Fe⁰ at the surface of the electrodeposited layer.

On sweeping the potential (Fig. 5.4), anodic peaks at ≈ -0.882 V (A₁) and ≈ -0.570 V (A₂) are essentially similar to those reported earlier for bulk electrodes [17], and can be attributed to the oxidation of Fe⁰ to Fe(II) species and, subsequently, its oxidation to FeOOH and/or Fe₃O₄. The area of A₂ peak noticeably decreases for the higher content of aluminium. Somewhat similar redox stabilisation effect of Al³⁺ addition on 2+ oxidation state of iron oxides was previously demonstrated for aluminium-containing ferrosinels [34,35].

Fig. 5.4 also shows sharp decay of the cathodic peak at the onset of intensive hydrogen evolution, allowing one to de-convolute these processes and to compute the stored charge ascribed to the reduction to Fe⁰ (j_{Fe}) as shown in Fig. 5.5, where j represents the current density in mA/cm². The hydrogen evolution current density, j_{H_2} , was extrapolated to obtain $j_{Fe} = j - j_{H_2}$, and the corresponding stored charge ascribed to the reduction to Fe⁰ was computed by the integration of the current density (Eq. (5.1)):

$$Q_{Fe} = \int j_{Fe} dt = \frac{1}{\beta} \int_{E_{on}}^{E_d} (j - j_{H_2}) dE \quad (5.1)$$

where the scan rate $\beta = dE/dt$ allows the transformation of time scale to potential $dt = dE/\beta$. Thus, an alternative representation of cyclic voltammograms (j/β vs E) is shown in Fig. 5.5, for a ready analysis of the stored charge, based on the cathodic peak area, integrated between the limiting values of onset and decay potentials (E_{on} and E_d). These results are summarized in Table 5.2, to emphasize not only the effects of alumina on the Fe⁰ deposition, as revealed by the corresponding stored charge (Q_{Fe}), but also the effects on hydrogen evolution at decay potential of Fe⁰-reduction. Thus, increasing the alumina content in the solid load of suspensions hinders the reduction to Fe⁰, with high correlation ($R^2=0.999$), as well as between alumina content and current density of hydrogen evolution, $j_{H_2,d}$, at the decay potential, E_d ($R^2=0.994$). This indicates that the fraction of alumina in the Fe_{2-x}Al_xO₃ suspensions

sets similar inhibitions on Fe⁰-deposition and H₂ evolution, probably by partial coverage of the conducting Fe⁰ surface with insulating alumina-based deposits, as it will be shown later. Note also that the values of decay potential shown in Table 5.2 are still insufficient to reduce trivalent aluminium species such as AlO₂⁻ to Al⁰ [36].

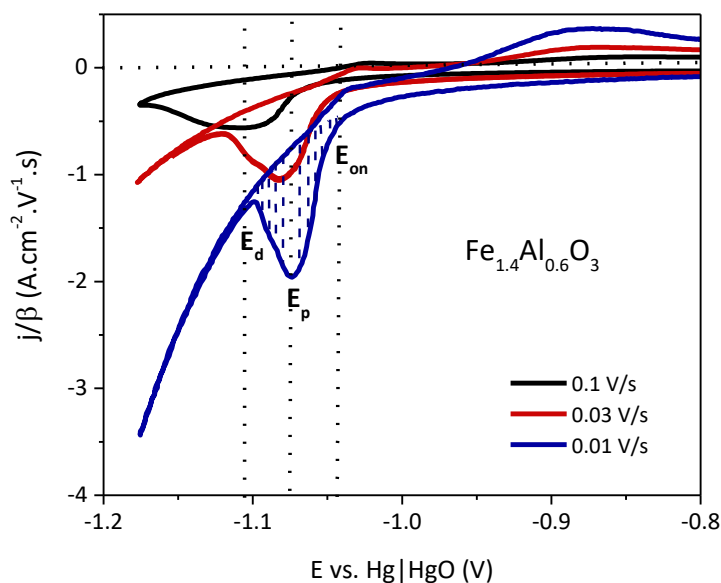


Fig. 5.5. Cyclic voltammograms of Fe_{1.4}Al_{0.6}O₃ suspensions at different scan rates. The shaded area represents the stored charge of the cathodic peak per unit area.

Table 5.2. Onset potential (E_{on}); peak potential (E_p); decay potential (E_d); stored charge of the Fe⁰-deposition peak (Q_{Fe}) and estimated current density of hydrogen evolution at the decay potential ($j_{H2,on}$).

	E vs Hg HgO (V)			Q_{Fe} (C/cm ²)	$j_{H2,on}$ (mA/cm ²)	
	β (V/s)	E_{on}	E_p			E_d
Fe ₂ O ₃	-0.01	-1.051	-1.086	-1.115	-0.093	-44
Fe _{1.8} Al _{0.2} O ₃	-0.01	-1.057	-1.090	-1.123	-0.076	-36
Fe _{1.4} Al _{0.6} O ₃	-0.01	-1.042	-1.073	-1.104	-0.039	-13
"	-0.03	-1.040	-1.083	-1.126	-0.032	-18
"	-0.1	-1.047	-1.109	-1.171	-0.023	-34

Fig. 5.5 also shows that by increasing the scan rates, a shift on the cathodic peak of reduction to Fe⁰ can be observed as well as a shift on the hydrogen evolution to higher cathodic polarizations. This is also revealed by the correlations between the peak potential and scan rate ($R^2=0.996$) and the correlation between the decay potential and scan rate ($R^2=0.988$). In addition, the stored charge varies

inversely with the hydrogen current density at the decay potential (Q_{Fe} vs $1/j_{\text{H}_2, \text{on}}$ with $R^2=0.991$). Thus, higher scan rates shift the operating conditions to higher cathodic polarization, and change the interplay between hydrogen evolution and Fe^0 -deposition, probably because H_2 bubbles restrict the contacts of $\text{Fe}_{2-x}\text{Al}_x\text{O}_3$ particles with the conducting Fe^0 -layer, and possibly also because a slight overpressure contributes to detachments of loosely bond Fe^0 -crystals from highly porous Fe^0 -deposits. In fact, it is well known that Faradaic efficiencies of the electrodeposition process decreases significantly when the WE is polarized from -1.09 V (vs. $\text{Hg}|\text{HgO}$) to higher cathodic polarizations [37], promoting the hydrogen evolution reaction ($2\text{H}_2\text{O}+2\text{e}^- \rightarrow \text{H}_2+2\text{OH}^-$), where the formation of Fe^0 competes with H_2 release, resulting in an overlapped shoulder in the CV.

Electrodeposition tests were performed for 7 h at -1.08 V in potentiostatic mode (Fig. 5.6), showing an increase in the cathodic current density with time for all samples. In general, the increase in the cathodic current can be ascribed to an increase in the effective area of the electrode, based on nearly cylindrical symmetry of the deposited Fe^0 layer, and probably its high porosity. These results can be compared to those obtained for bulk hematite-based cathodes, tested under similar conditions [17]. Despite the low conductivity of hematite-based materials, once the first Fe_3O_4 and/or Fe^0 crystals are formed in bulk electrode, the reaction is further boosted by these new conductive pathways. In the case of suspension, each particle reacts separately, while a gradual current increase is actually provided by an increase in the cathode area with time, as discussed below.

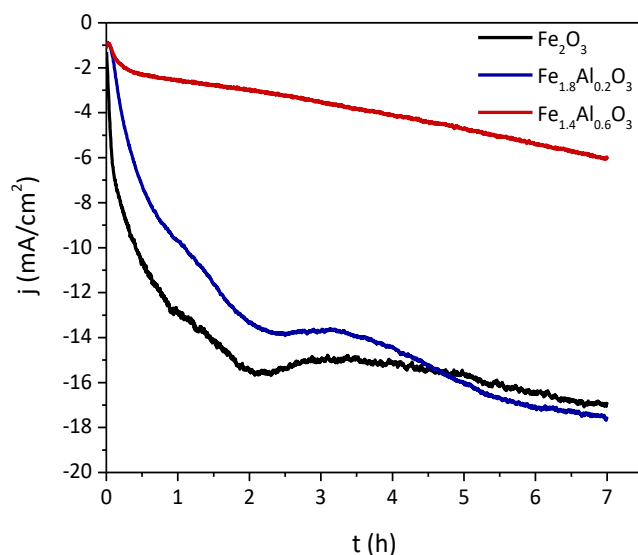


Fig. 5.6. Current vs. time curves of Fe^0 electrodeposition from Fe_2O_3 , $\text{Fe}_{1.8}\text{Al}_{0.2}\text{O}_3$ and $\text{Fe}_{1.4}\text{Al}_{0.6}\text{O}_3$ suspensions at -1.08 V (90 °C, NaOH 10 M).

The same potential was applied during the bulk reduction of $\text{Fe}_{1.8}\text{Al}_{0.2}\text{O}_3$ to Fe^0 in [17] for comparison purposes, where close to 100% of $\text{Fe}(\text{III})$ conversion to Fe^0 was obtained. However, this

may not be the case in the present study, as illustrated by extrapolating the hydrogen evolution current density (Fig. 5.5). The time dependence in Fig. 5.6 may also comprise enhanced hydrogen evolution, mainly for conditions when the deposited Fe⁰-layers are highly porous. This is confirmed by the limited Faradaic efficiencies of 70%, 55% and 32%, estimated for Fe⁰-deposition from suspensions of Fe₂O₃, Fe_{1.8}Al_{0.2}O₃ and Fe_{1.4}Al_{0.6}O₃, respectively. Note that literature studies report efficiencies in the range of 70%-94% [13,14,33] for Fe₂O₃ suspensions with 18 M of NaOH as an electrolyte and at 110-114 °C, with different CEs and WEs. Nevertheless, some results obtained in the present study, for the reference Fe₂O₃ suspension, may be explained by significant differences in operating conditions, namely the use of 10 M electrolyte concentration and 90 °C when compared to 18 M and higher temperatures in earlier studies, to minimize the impact of H₂ evolution [14]. Nevertheless, much lower Faradaic efficiency was obtained for the deposition of Fe⁰ from suspensions of Fe_{1.8}Al_{0.2}O₃ and Fe_{1.4}Al_{0.6}O₃, confirming the negative impact of increasing fractions of alumina.

The mechanism of the Fe₂O₃ electroreduction in alkaline suspensions is still uncertain in literature. The solubility of hematite and hematite-based suspensions in 10 M of NaOH, 90 °C should only be slightly higher than 1.1×10⁻³M (76 °C, 10 M) [38]. Despite the low solubility, the conversion of Fe₂O₃ to Fe(OH)₄⁻ has been proposed as a relevant step of Fe⁰-electrowinning in alkaline suspensions [13,14,33,39], as described by Eq. (5.2), and thermodynamic studies considered the hydrolysis of Fe₂O₃ to form Fe(OH)₄⁻ [40]. The Fe(OH)₄⁻ anions might be reduced to Fe(II) species, mainly as Fe(OH)₃⁻ (Eq. (5.3)), which is further electroreduced and deposited in the WE as Fe⁰ (Eq. (5.4)).



However, the contribution of such mechanism may be limited due to the low solubility of Fe₂O₃ particles. As an alternative, one can consider the electroreduction mechanism described for bulk electrolysis [16–18], including the following steps: Fe₂O₃→Fe₃O₄→Fe(II)→Fe⁰. An electroreduction mechanism based on the adsorption of Fe₂O₃ particles in contact with WE has been proposed by Siebentritt and his co-workers [39]. Though negative charge on the surface of Fe₂O₃ particles should be expected at strong alkaline conditions, since the isoelectric point (IEP) of hematite is in the pH range of 6-9.6, zeta potential measurements by electroacoustic methods [39] indicated a transition from negative to slightly positive values for 0.1 M to 10 M NaOH solution, respectively. In this case, positive charge by Na⁺ cations, surrounding the hematite particles, may promote their migration towards the cathodically polarized WE by electrostatic forces. Thus, one may consider a combination of the stated mechanisms above to the electroreduction of Fe₂O₃. For the reasons described above, the cathodic peak which corresponds to Fe(III) to Fe(II) reduction may be hidden.

The current densities in Fig. 5.6 remain below -18 mA/cm^2 even for electrodeposition from Fe_2O_3 suspension. These results are clearly lower than reported in previous studies, with up to 100 mA/cm^2 in some cases [14,33]. However, more concentrated electrolyte solution and higher process temperature ($110\text{-}114 \text{ }^\circ\text{C}$) were used in the cited work and both factors are expected to facilitate the electroreduction. In addition, the irregular shape of Fe_2O_3 particles obtained by grinding the precursor cellular ceramics (Fig. 5.3) may impose stereological restrictions on the contacts of particles with the current collecting Fe^0 -surface.

The XRD results in Fig. 5.7 confirm the formation of pure Fe^0 at the cathode for all studied suspensions, without any evidence of non-metallic inclusions, and possibly with preferential orientation. This is consistent with the characteristic morphology of Fe^0 crystals deposited on the Ni grid during the electrochemical reduction of Fe_2O_3 -based suspensions (Fig. 5.8), growing in columnar shape ($\approx 18 \text{ }\mu\text{m}$ of diameter). After 20 min of electroreduction, the smaller crystals evolve by growing on the top of previous nuclei (Fig. 5.8A). Columnar Fe^0 crystals grow perpendicularly to the Ni grid; the contrast between the layer of Fe^0 crystals and the Ni grid is well visible in Fig. 5.8B. After 7 h of electrodeposition, compact needle-like or dendritic crystals with $\approx 108 \text{ }\mu\text{m}$ of length (Fig. 5.8C, D) can be observed, similar to those observed in [14].

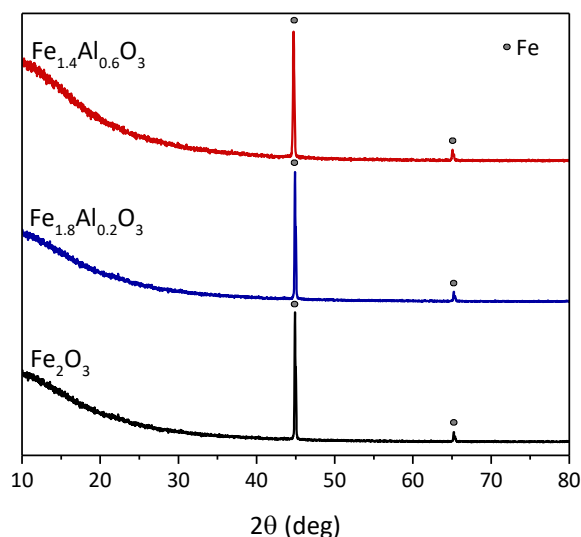


Fig. 5.7. XRD patterns of Ni grids after Fe^0 deposition from Fe_2O_3 , $\text{Fe}_{1.8}\text{Al}_{0.2}\text{O}_3$ and $\text{Fe}_{1.4}\text{Al}_{0.6}\text{O}_3$ suspensions.

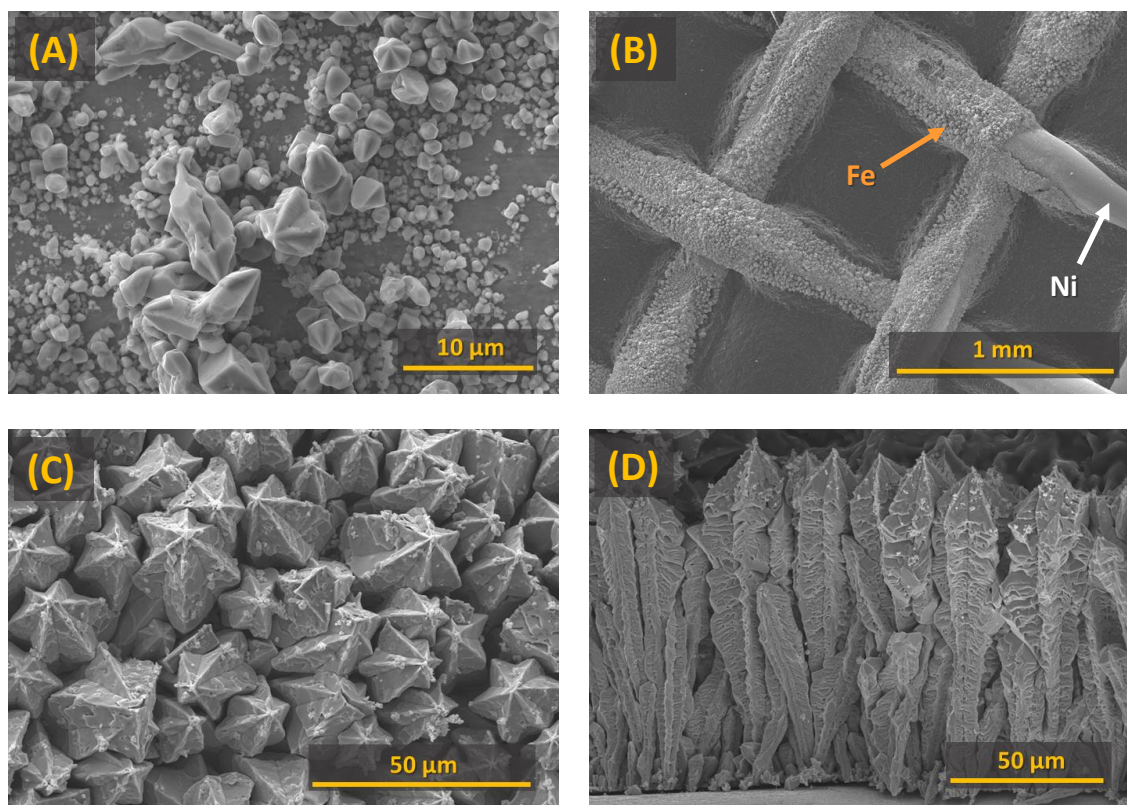


Fig. 5.8. Microstructural evolution of Fe^0 crystals deposited during (A) 20 min; (B), (C) and (D) 7 h of electroreduction of Fe_2O_3 -based suspensions, where (B) shows the Ni grid covered by Fe^0 crystals, while (C) represents a top view of Fe^0 crystals and (D) a side view.

Such dendritic morphology of the Fe^0 deposits is retained for all the alkaline suspensions tested (Fig. 5.9). Differences in morphology are likely provided by higher current densities observed for Fe_2O_3 containing suspension at the initial stage, which largely determines the landscape of the crystallite. However, these microstructures also mark a tendency to form smaller dendrites for a larger content of aluminium in the $\text{Fe}_{2-x}\text{Al}_x\text{O}_3$ suspension (Fig. 5.9A, B), finally resulting in entirely distinct morphology observed for the $\text{Fe}_{1.4}\text{Al}_{0.6}\text{O}_3$ suspension (Fig. 5.9C, D). Fe^0 dendrites electrodeposited from $\text{Fe}_{1.4}\text{Al}_{0.6}\text{O}_3$ suspensions (Fig. 5.9C, D) appear to be thinner ($\approx 13 \mu\text{m}$) and highly-porous, with an asymmetrical growth and shape. The high porosity shown in Fig. 5.9D is likely promoted by surface coverage by Al-rich precipitates, which may correspond to Al_2O_3 , AlOOH and $\text{Na}[\text{Al}(\text{OH})_4]$ species or mixture thereof. Note that these inclusions are barely observed after Fe^0 -electrowining from $\text{Fe}_{1.8}\text{Al}_{0.2}\text{O}_3$, which proved to be single-phase (Fig. 5.1D). Thus, one may assume that the extent of surface coverage by the alumina-rich precipitates is dictated mainly by the excess of alumina, present as a secondary corundum-based phase in the precursor powders with nominal composition $\text{Fe}_{1.4}\text{Al}_{0.6}\text{O}_3$, rather than by segregation of the alumina content dissolved in the hematite phase, during its electroreduction. Partial coverage of the current collecting and electrochemically active Fe^0 -surface by those Al-rich precipitates may explain simultaneous effects on Fe^0 -electrowining and on hydrogen evolution, as described above.

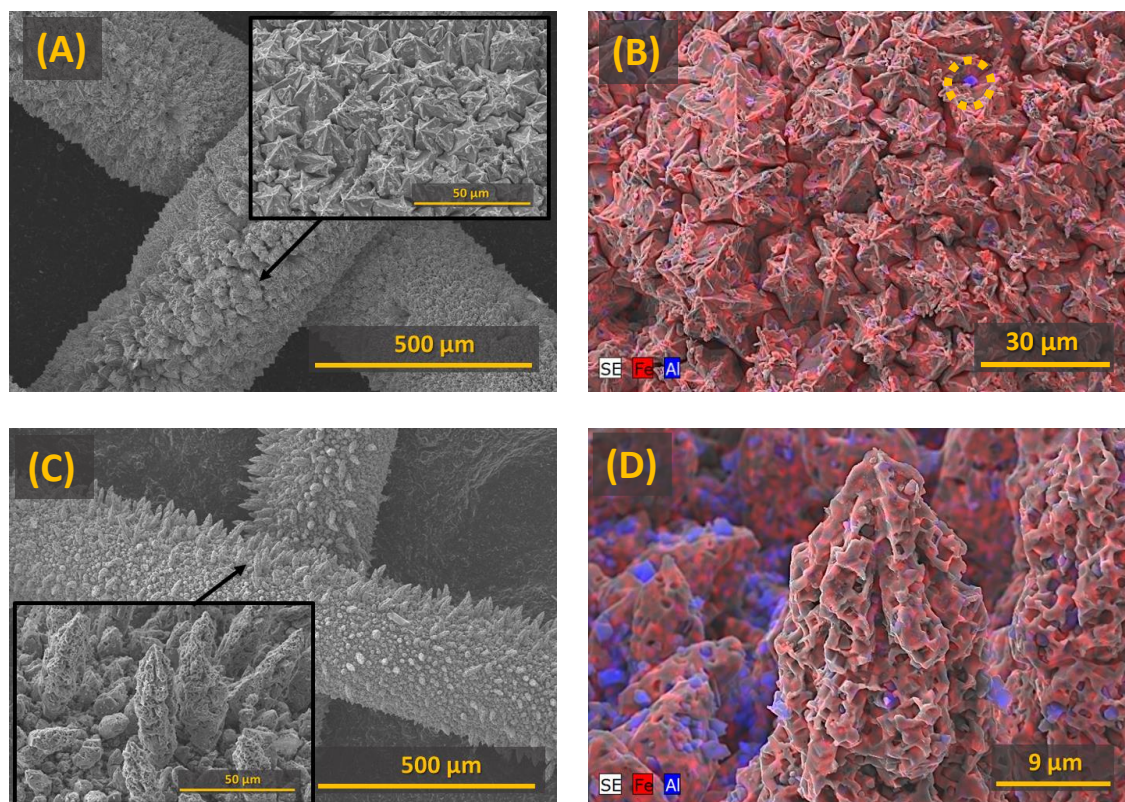
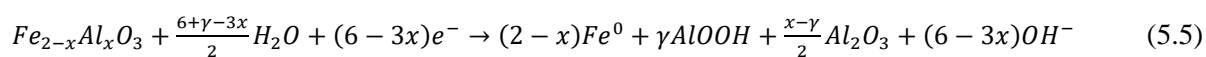


Fig. 5.9. SEM images of Fe^0 crystals after electrochemical reduction of suspensions containing (A) and (B) $Fe_{1.8}Al_{0.2}O_3$; (C) and (D) $Fe_{1.4}Al_{0.6}O_3$. Images (B) and (D) show EDS mappings.

Thus, the corresponding reactions of cathodic iron reduction, accompanied with aluminium redistribution, can be presented as follows (Eqs (5.5-5.6)):



where γ represents the fraction of $AlOOH$ formed.

Simultaneously, the highly alkaline electrolyte may still promote dissolution of the corundum phase:



which may also explain the corresponding porosity in the dendrites, observed mainly for Fe^0 -deposition from $Fe_{1.4}Al_{0.6}O_3$ (Fig. 5.9D). In addition, this may also contribute to enhance the relative contribution of hydrogen evolution at the inner porosity of Fe^0 -based electrodes [41], whereas Fe^0 -electrodeposition may be limited to the outermost surface of the Fe^0 -layer.

The obtained results generally suggest that the presence of aluminium in red mud is not expected to be a decisive obstacle towards the electrochemical reduction in suspensions with low Al content, but

may significantly determine the microstructure of the produced ZVI, while also impairing the electroreduction current and Faradaic efficiency. On the other hand, the presence of high concentrations of Al may have a direct impact on the electroreduction pathway. In fact, the addition of 30 wt% of kaolinite ($\text{Al}_2\text{Si}_2\text{O}_5(\text{OH})_4$) in Fe_2O_3 alkaline suspension, was responsible for lowering the Faradaic efficiency from 80% (0 wt% of kaolinite) to 38%, due to the possible phase formations of cancrinite or sodalite at the surface of hematite particles, hampering the electroreduction in [42]. At the same time, gradual leaching of aluminium-containing species may create additional flexibility for the functional design of the deposited films. Firstly, the dissolution rate can be adjusted by pH and the temperature of the electrolyte, to compensate for the formation of excessive porosity in the dendrites during fast film growth. Secondly, the controlled formation of the porosity may be even favourable for potential environmental applications of ZVI, where high surface area is often required. Thus, although these guidelines were obtained for synthetic compositions mimicking the main components of the red mud, they are still expected to contribute to the understanding of prospective conditions and possible outcomes for the process of the electrochemical reduction of iron-containing ores and industrial slugs.

5.3.3. Conclusions

Electrochemical reduction of hematite and hematite-based ($\text{Fe}_{2-x}\text{Al}_x\text{O}_3$) ceramic suspensions to zero-valent iron (ZVI, Fe^0) was assessed in strong alkaline conditions at relatively low temperature (90 °C) and proved to be feasible. Microstructural studies have shown that electrodeposition results in the formation of Fe^0 films having a columnar dendritic structure. The presence of alumina was found to affect the morphology of the dendrites and to promote the formation of significant porosity in crystallites when performing the electrodeposition from $\text{Fe}_{1.4}\text{Al}_{0.6}\text{O}_3$. This porosity is believed to result from mechanical trapping of the aluminium-rich species in the Fe^0 films during growth, followed by their dissolution promoted by highly-alkaline electrolytes. Increasing the aluminium content in suspensions depressed the electroreduction current and also affected the Faradaic efficiency of the electrodeposition from 70% (Fe_2O_3), 55% ($\text{Fe}_{1.8}\text{Al}_{0.2}\text{O}_3$) to 32% ($\text{Fe}_{1.4}\text{Al}_{0.6}\text{O}_3$), probably because partial surface coverage with alumina-based precipitates affects interactions of hematite-based particles with the current collecting Fe^0 -layer. Nevertheless, the results have demonstrated that the electrochemical deposition of Fe^0 may be a feasible process for iron recovery and recycling from aluminium-containing wastes, such as red mud.

Acknowledgements

The carried research was supported by the FCT grant PD/BD/114106/2015, the European Commission (project SIDERWIN- DLV-768788 - Horizon 2020/SPIRE10) and the project CICECO-

Aveiro Institute of Materials (ref. UIDB/50011/2020 and UIDP/50011/2020), financed by the COMPETE 2020 Program and National Funds through the FCT/MEC and when applicable co-financed by FEDER under the PT2020 Partnership Agreement.

5.3.4. References

- [1] Q. Wang, Y. Zhu, Q. Wu, E. Gratz, Y. Wang, Low temperature electrolysis for iron production via conductive colloidal electrode, *RSC Adv.* 5 (2015) 5501–5507. doi:10.1039/C4RA14576C.
- [2] E.A. Mousa, Modern blast furnace ironmaking technology: Potentials to meet the demand of high hot metal production and lower energy consumption, *Metall. Mater. Eng.* 25 (2019) 69–104. doi:10.30544/414.
- [3] A. Allanore, H. Lavelaine, G. Valentin, J.P. Birat, F. Lapique, Electrodeposition of metal iron from dissolved species in alkaline media, *J. Electrochem. Soc.* 154 (2007) E187–E193. doi:10.1149/1.2790285.
- [4] D.R. Sadoway, New opportunities for metals extraction and waste treatment by electrochemical processing in molten salts, *J. Mater. Res.* 10 (1995) 487–492. doi:10.1557/JMR.1995.0487.
- [5] H. Kim, J. Paramore, A. Allanore, D.R. Sadoway, Electrolysis of Molten Iron Oxide with an Iridium Anode: The Role of Electrolyte Basicity, *J. Electrochem. Soc.* 158 (2011) E101–E105. doi:10.1149/1.3623446.
- [6] A. Allanore, Features and Challenges of Molten Oxide Electrolytes for Metal Extraction, *J. Electrochem. Soc.* 162 (2015) E13–E22. doi:10.1149/2.0451501jes.
- [7] M.Y. Mohassab-Ahmed, H.Y. Sohn, H.G. Kim, Sulfur distribution between liquid iron and magnesia-saturated slag in H₂/H₂O atmosphere relevant to a novel green ironmaking technology, *Ind. Eng. Chem. Res.* 51 (2012) 3639–3645. doi:10.1021/ie201970r.
- [8] H.K. Pinegar, M.S. Moats, H.Y. Sohn, Flowsheet development, process simulation and economic feasibility analysis for novel suspension ironmaking technology based on natural gas: Part 3 - Economic feasibility analysis, *Ironmak. Steelmak.* 40 (2013) 44–49. doi:10.1179/030192312X13345671456897.
- [9] A. Allanore, H. Lavelaine, G. Valentin, J.P. Birat, F. Lapique, Iron Metal Production by Bulk Electrolysis of Iron Ore Particles in Aqueous Media, *J. Electrochem. Soc.* 155 (2008) E125–E129. doi:10.1149/1.2952547.
- [10] Y. Ivanova, J. Monteiro, A. Horovistiz, D. Ivanou, D. Mata, R. Silva, J. Frade, Electrochemical

- deposition of Fe and Fe / CNTs composites from strongly alkaline hematite suspensions, *J. Appl. Electrochem.* 45 (2015) 515–522. doi:10.1007/s10800-015-0803-6.
- [11] J. Monteiro, Y. Ivanova, A. Kovalevsky, D. Ivanou, J. Frade, Reduction of magnetite to metallic iron in strong alkaline medium, *Electrochim. Acta.* 193 (2016) 284–292. doi:10.1016/j.electacta.2016.02.058.
- [12] B. Yuan, G. Haarberg, Electrodeposition of Iron in Aqueous Alkaline Solution: An Alternative to Carbothermic Reduction, *ECS Trans.* 16 (2009) 31–37.
- [13] J.A.M. LeDuc, R.E. Lofffield, L.E. Vaaler, Electrolytic Iron Powder from a Caustic Soda Solution, *J. Electrochem. Soc.* 106 (1959) 659–667. doi:10.1149/1.2427465.
- [14] B. Yuan, O.E. Kongstein, G.M. Haarberg, Electrowinning of Iron in Aqueous Alkaline Solution Using a Rotating Cathode, *J. Electrochem. Soc.* 156 (2009) D64–D69. doi:10.1149/1.3039998.
- [15] A. Allanore, H. Lavelaine, G. Valentin, J.P. Birat, P. Delcroix, F. Lapique, Observation and modeling of the reduction of hematite particles to metal in alkaline solution by electrolysis, *Electrochim. Acta.* 55 (2010) 4007–4013. doi:10.1016/j.electacta.2010.02.040.
- [16] X. Zou, S. Gu, X. Lu, X. Xie, C. Lu, Z. Zhou, W. Ding, Electroreduction of Iron (III) Oxide Pellets to Iron in Alkaline Media : A Typical Shrinking-Core Reaction Process, *Metall. Mater. Trans. B.* 46B (2015) 1262–1274. doi:10.1007/s11663-015-0336-8.
- [17] D.V. Lopes, Y.A. Ivanova, A.V. Kovalevsky, A.R. Sarabando, J.R. Frade, M.J. Quina, Electrochemical reduction of hematite-based ceramics in alkaline medium: Challenges in electrode design, *Electrochim. Acta.* 327 (2019) 135060. doi:10.1016/j.electacta.2019.135060.
- [18] Y. Ivanova, J. Monteiro, L. Teixeira, N. Vitorino, A. Kovalevsky, J. Frade, Designed porous microstructures for electrochemical reduction of bulk hematite ceramics, *Mater. Des.* 122 (2017) 307–314. doi:10.1016/j.matdes.2017.03.031.
- [19] Y. Hua, K. V. Heal, W. Friesl-Hanl, The use of red mud as an immobiliser for metal/metalloid-contaminated soil: A review, *J. Hazard. Mater.* 325 (2017) 17–30. doi:10.1016/j.jhazmat.2016.11.073.
- [20] M.A. Khairul, J. Zanganeh, B. Moghtaderi, The composition, recycling and utilisation of Bayer red mud, *Resour. Conserv. Recycl.* 141 (2019) 483–498. doi:10.1016/j.resconrec.2018.11.006.
- [21] Y. Liu, J. Wang, Reduction of nitrate by zero valent iron (ZVI)-based materials: A review, *Sci. Total Environ.* 671 (2019) 388–403. doi:10.1016/j.scitotenv.2019.03.317.
- [22] C. Mystrioti, D. Sparis, N. Papasiopi, A. Xenidis, D. Dermatas, M. Chrysochoou, Assessment of polyphenol coated Nano zero Valent iron for hexavalent chromium removal from contaminated waters, *Bull. Environ. Contam. Toxicol.* 94 (2015) 302–307. doi:10.1007/s00128-014-1442-z.

- [23] C. Raman, S. Kanmani, Textile dye degradation using nano zero valent iron: A review, *J. Environ. Manag.* 177 (2016) 341–355. doi:10.1016/j.jenvman.2016.04.034.
- [24] R.C. Martins, D.V. Lopes, M.J. Quina, R.M. Quinta-ferreira, Treatment improvement of urban landfill leachates by Fenton-like process using ZVI, *Chem. Eng. J.* 192 (2012) 219–225. doi:10.1016/j.cej.2012.03.053.
- [25] C.B. Wang, W.X. Zhang, Synthesizing nanoscale iron particles for rapid and complete dechlorination of TCE and PCBs, *Environ. Sci. Technol.* 31 (1997) 2154–2156. doi:10.1021/es970039c.
- [26] J.T. Nurmi, P.G. Tratnyek, V. Sarathy, D.R. Baer, J.E. Amonette, K. Pecher, C. Wang, J.C. Linehan, D.W. Matson, R.L. Penn, M.D. Driessen, Characterization and properties of metallic iron nanoparticles: Spectroscopy, electrochemistry, and kinetics, *Environ. Sci. Technol.* 39 (2005) 1221–1230. doi:10.1021/es049190u.
- [27] M. Bystrzejewski, Synthesis of carbon-encapsulated iron nanoparticles via solid state reduction of iron oxide nanoparticles, *J. Solid State Chem.* 184 (2011) 1492–1498. doi:10.1016/j.jssc.2011.04.018.
- [28] D.V. Lopes, A.V. Kovalevsky, M.J. Quina, J.R. Frade, Processing of highly-porous cellular iron oxide-based ceramics by emulsification of ceramic suspensions, *Ceram. Int.* 44 (2018) 20354–20360. doi:10.1016/j.ceramint.2018.08.024.
- [29] S.W. Hughes, Archimedes revisited: a faster, better, cheaper method of accurately measuring the volume of small objects, *Phys. Educ.* 40 (2005) 468–474. doi:10.1088/0031-9120/40/5/008.
- [30] M. Maruyama, T. Fukasawa, S. Suenaga, Y. Goto, Vapor-grown carbon nanofibers synthesized from a Fe₂O₃-Al₂O₃ composite catalyst, *J. Eur. Ceram. Soc.* 24 (2004) 463–468. doi:10.1016/S0955-2219(03)00205-X.
- [31] K.K. Lee, S. Deng, H.M. Fan, S. Mhaisalkar, H.R. Tan, E.S. Tok, K.P. Loh, W.S. Chin, C.H. Sow, α -Fe₂O₃ nanotubes-reduced graphene oxide composites as synergistic electrochemical capacitor materials, *Nanoscale.* 4 (2012) 2958–2961. doi:10.1039/c2nr11902a.
- [32] J.M. Skowroński, T. Rozmanowski, M. Osińska, Reuse of nickel recovered from spent Ni – Cd batteries for the preparation of C / Ni and C / Ni / Pd, *Process Saf. Environ. Prot.* 93 (2015) 139–146. doi:10.1016/j.psep.2014.02.007.
- [33] V. Feynerol, H. Lavelaine, P. Marlier, M.N. Pons, F. Lapique, Reactivity of suspended iron oxide particles in low temperature alkaline electrolysis, *J. Appl. Electrochem.* 47 (2017) 1339–1350. doi:10.1007/s10800-017-1127-5.
- [34] A.V. Kovalevsky, E.N. Naumovich, A.A. Yaremchenko, J.R. Frade, High-temperature

- conductivity, stability and redox properties of $\text{Fe}_{3-x}\text{Al}_x\text{O}_4$ spinel-type materials, *J. Eur. Ceram. Soc.* 32 (2012) 3255–3263. doi:10.1016/j.jeurceramsoc.2012.04.040.
- [35] A.V. Kovalevsky, A.A. Yaremchenko, E.N. Naumovich, N.M. Ferreira, S.M. Mikhalev, F.M. Costa, J.R. Frade, Redox stability and high-temperature electrical conductivity of magnesium- and aluminium-substituted magnetite, *J. Eur. Ceram. Soc.* 33 (2013) 2751–2760. doi:10.1016/j.jeurceramsoc.2013.04.008.
- [36] M. Pourbaix, *Atlas of Electrochemical Equilibria in Aqueous Solutions*, 2nd Editio, Brussels, 1974.
- [37] P. Periasamy, B.R. Babu, S.V. Iyer, Electrochemical behaviour of Teflon-bonded iron oxide electrodes in alkaline solutions, *J. Power Sources.* 63 (1996) 79–85. doi:10.1016/S0378-7753(96)02449-4.
- [38] K. Ishikawa, T. Yoshioka, T. Sato, A. Okuwaki, Solubility of hematite in LiOH, NaOH and KOH solutions, *Hydrometallurgy.* 45 (1997) 129–135. doi:10.1016/S0304-386X(96)00068-0.
- [39] M. Siebentritt, P. Volovitch, K. Ogle, G. Lefèvre, Adsorption and electroreduction of hematite particles on steel in strong alkaline media, *Colloids Surfaces A Physicochem. Eng. Asp.* 440 (2014) 197–201. doi:10.1016/j.colsurfa.2012.09.002.
- [40] I.I. Diakonov, J. Schott, F. Martin, J.C. Harrichourry, J. Escalier, Iron(III) solubility and speciation in aqueous solutions. Experimental study and modelling: Part 1. Hematite solubility from 60 to 300°C in NaOH-NaCl solutions and thermodynamic properties of $\text{Fe}(\text{OH})_4(\text{aq})$, *Geochim. Cosmochim. Acta.* 63 (1999) 2247–2261. doi:10.1016/S0016-7037(99)00070-8.
- [41] C.I. Müller, K. Sellschopp, M. Tegel, T. Rauscher, B. Kieback, L. Röntzsch, The activity of nanocrystalline Fe-based alloys as electrode materials for the hydrogen evolution reaction, *J. Power Sources.* 304 (2016) 196–206. doi:10.1016/j.jpowsour.2015.11.008.
- [42] A. Maihatchi, M.-N. Pons, Q. Ricoux, F. Goettmann, F. Lapique, Electrolytic iron production from alkaline suspensions of solid oxides: compared cases of hematite, iron ore and iron-rich Bayer process residues, *J. Electrochem. Sci. Eng.* 10 (2020) 95–102. doi:10.5599/jese.751.

This Page Intentionally Left Blank

6. Direct processing and electroreduction of cellular red-mud-based ceramics for environmental applications

The feasibility of recycling red mud waste by its direct transformation into highly-porous cellular ceramics was successfully demonstrated. Ceramic materials with designed cellular porosity were processed by emulsification of red mud suspensions with liquid paraffin. Taguchi method was used to study the effects provided by varying the red mud load in the suspension, gelatine content and emulsion stirring time on the microstructural features of the cellular ceramics. Additional experiments analysed the effects of the organic to suspension ratio and firing temperature. Emulsification of paraffin followed by gelatine consolidation, drying, elimination of the droplets of the discontinuous organic phase and firing, allowed one to design cellular ceramic pieces with open porosity up to 75%, consisting in interconnected cells with adjustable cell size and low resistance to percolation. The adsorption capacity of the processed red mud was tested towards phosphate removal. These results allow one to consider prospective applications of red mud-based cellular ceramics with designed microstructures as highly-porous membranes for the capture of pollutants. Preliminary tests have shown that the direct bulk electrochemical reduction of the red mud is feasible despite relatively low current densities attained.

Keywords: Porous ceramics; waste valorisation; emulsification; Taguchi method

This chapter is based on the following publication, except sections 6.4 and 6.5:

D.V. Lopes, E. Durana, F.R. Cesconeto, P.V. Almeida, A.V. Kovalevsky, M.J. Quina, J.R. Frade, Direct processing of cellular ceramics from a single red mud precursor, *Ceram. Int.* 46 (2019) 16700–16707. doi: 10.1016/j.ceramint.2020.03.244.

6.1. Introduction

Around 1.5 tons of red mud waste are formed during the production of 1 ton of alumina by the Bayer process, reaching a worldwide production of 160 million tons in 2015 [1] without more recent production values reported in literature. The main components of this waste include Fe_2O_3 , Al_2O_3 , TiO_2 , SiO_2 , CaO , and Na_2O , often reaching pH in the order of 13 and making red mud highly alkaline, ecotoxic and challenging for recycling. Severe environmental problems worldwide have been caused by the high alkaline volume of red mud slurries formed and, in some cases, the presence of toxic and radioactive compounds [1–3]. Thus, much effort has been made to avoid landfill deposition of red mud and to find sustainable alternatives for its recycling. Red mud has been proposed as raw material for the production of bricks [4], cement [5] or tiles [6]. On the other hand, high contents of iron, aluminium and titanium increased the interest of red mud for metals extraction [7,8]. In addition, red mud has been used for environmental applications such as catalysts or adsorbents for soil remediation [2,9], wastewater treatments [10,11] and CO_2 sequestration [12]. The applications are often based on highly-porous membranes used in various processes involving gas and liquid transport, requiring flexibility in porosity design at an affordable cost. Similarly, porous ceramics with suitable porosity and other designed microstructural features are required for a variety of other applications from passive thermal insulation to different functionalities in catalysis, filters of molten metals or hot gases, sensors and electrodes for solid-state electrochemical systems fuel cells [13–16], and also a variety of ceramic membranes (*e.g.* alumina, zirconia or zeolite) to remove pollutants from wastewaters [17]. The use in hybrid systems combining several water treatment processes such as filtration, adsorption and catalytic degradation of pollutants, may also improve the overall membrane performance in water purification at industrial scale [18].

A suitable design of cellular microstructures combining mostly open porosity, high permeability to fluids, high surface area and mechanical strength is often required for such membrane applications. Particular attention has been given to the processing by emulsification of ceramic powder suspensions [13], due to its simplicity, flexibility and affordable cost, mainly based on low-cost raw materials or residues, with a variety of pore formers such as sawdust [19], starch [20], sunflower oil [21] or paraffin [22,23] to create the cellular microstructures. This method was recently used to process highly-porous membranes based on hematite [24] or iron-oxide based compositions [25], and the main goal of the present study is to adapt the suspension emulsification method for direct processing of highly-porous ceramic membranes from red mud suspensions, without blending with other natural or synthetic raw materials. Taguchi experimental planning [26] was applied to understand the relevant effects of the processing conditions on microstructural features and as a guideline for cellular microstructural design. Preliminary studies on the environmental application of such designed cellular membranes were performed to reveal the role of structural modifications imposed by the emulsification method. For this,

the processed red mud membranes were tested for phosphate removal, as agents to tackle the eutrophication problem. One also assessed the possibilities for direct electrochemical reduction of the red mud-based cellular ceramics to Fe^0 , aiming iron recovery and valorization from the iron-rich waste.

6.2. Experimental procedure

Red mud waste was kindly provided by Aluminium of Greece S.A. The powder was oven-dried for 24 h at 105 °C and grinded to obtain particle sizes below 3 μm . Cellular red mud ceramics were prepared by the emulsification of aqueous suspensions of red mud powder without additional treatments and without blending with other raw materials. Guidelines were taken from previous works on the processing of cellular ceramics with Fe_2O_3 or $\text{Fe}_{2-x}\text{Al}_x\text{O}_3$ compositions [24,25]. Solid loads of red mud (45% to 55% (v/v)) were added to distilled water, where Dolapix PC-67 (Zschimmer & Schwarz), 10% (v/v) relative to the volume of red mud suspension in water, was used as a dispersant. During emulsification, liquid paraffin (Valente e Ribeiro, Lda) was added with 1.5:1 paraffin:suspension volume ratio. Sodium lauryl sulfate (1 g/L, Sigma-Aldrich L-6026) was added as surfactant (6% (v/v) of the total volume of suspension with paraffin), and gelatine (Oxoid Lda., LP0008) was used as a shape stabilizer (2% to 5% related to water volume of the suspension). Emulsions were stirred at 1300 rpm with a mechanical stirrer (4 to 12 min), in a water bath (≈ 80 °C), then gel-casted in cylindrical form, at room temperature, and dried at 70 °C for two days. Flow and viscosity curves of red mud emulsified suspensions were studied in a rotational viscometer (Viscotester IQ, Thermo Haake, Germany), with concentric cylinders as sensors. The cycles were performed by increasing the shear rate until 1000 s^{-1} in 180 s and decreasing the shear rate in the same conditions. The burnout of paraffin was performed by slow heating (1 °C/min) until 300 °C (dwell of 3 h), heating at 1 °C/min up to 500 °C (dwell of 1 h), and cooling down to room temperature (5 °C/min); this yielded self-supported samples which were used to monitor the resulting cellular microstructures prior to high temperature firing. Ceramic samples were fired between 1100 °C to 1200 °C with a dwell of 2 h and 3 °C/min and 5 °C/min of heating and cooling rates, correspondently. The influence of the solid load of red mud powder in the suspension step (S), gelatine content (G) and stirring time (t) on the microstructural features of the produced cellular ceramics were studied according to the Taguchi method at three levels (Table 6.1).

Cellular microstructures and interconnectivity of the cells were investigated using a Hitachi SU-70 scanning electron microscopy (SEM) with energy dispersive spectroscopy (EDS) analysis (Bruker Quantax 400 detector). PANalytical XPert PRO diffractometer ($\text{CuK}\alpha$ radiation, $2\theta = 10\text{--}80^\circ$) with a graphite monochromator was used to analyse the phase composition by X-ray diffraction analysis (XRD) after the cellular processing. Panalytical HighScore Plus 4.7 (PDF-4) software was used for phase identification.

Table 6.1. Factors and levels used in Taguchi's planning: solid load (S), gelatine (G) and stirring time (t).

Factors	Level 1	Level 2	Level 3
S (%)	45	50	55
G (%)	2	3.5	5
t (min)	4	8	12

The average size of the porous cavities, \bar{d} , was measured by *Estereologia* software [27]. Open porosity (x_o) was calculated by the Archimedes method using water [28,29]. Values are given from 0 to 1, where 1 represents 100% of open porosity in volume fraction. Linear roughness of fracture surfaces (R_z , mean peak-to-valley height of the measured profile) of ceramic pieces was quantified by a profilometer (Hommel Tester T1000) with a diamond tip probe (stylus tip of 5 $\mu\text{m}/90^\circ\text{C}$, 0.75 μm of radius and 300 μm of measuring range) to study information regarding the total height of the porous cavities (ISO 4287), and prospective correlations with the cellular microstructures. Cell interconnectivity was studied by impregnating the cellular cavities with NaCH_3COO solution (5% w/w) under vacuum conditions and measuring the electrical response by electrochemical impedance spectroscopy (EIS) [22,23,25,30]. Samples were placed between two aluminium foil electrodes to provide electrical contacts and the measurements were performed by a Keysight E4980A impedance bridge in a frequency range from 20 Hz to 2 MHz, with 5 mV amplitude of the applied voltage.

Zeta potential measurements were performed in a Zetasizer Nano ZS (Malvern Instruments, UK) with diluted suspensions (100 mg/L). An inert electrolyte KCl (10^{-2} M) was used and the pH of the suspensions was determined by titration with HCl (10^{-2} M) and KOH (10^{-3} M). Adsorption studies were performed by adding 0.3 g of the initial and processed red mud powder, into 30 mL phosphate solutions of 20 and 400 mg $\text{PO}_4^{3-}/\text{L}$. The pH of the solutions was adjusted to 4 and 8, and adsorption trials were performed during 6 h, at 25 $^\circ\text{C}$ under stirring conditions (100 rpm). The final powder was removed from solutions by filtration with 0.45 μm filters and phosphorus (P- PO_4^{3-}) content was estimated by UV-Vis spectroscopy (T60 UV-Vis spectrophotometer) at 650 nm. The efficiency of PO_4^{3-} removal from the solutions (%) was quantified by Eq. (6.1), where C_0 and C_e are, respectively, the initial and equilibrium concentrations, $t_{\text{equilibrium}} = 6$ h, (mg/L):

$$R_{\text{PO}_4^{3-}}(\%) = \left(1 - \frac{C_e}{C_0}\right) \times 100 \quad (6.1)$$

Adsorbed PO_4^{3-} on the surface of the processed red mud powder was calculated according to Eq. (6.2):

$$q_e = \frac{V}{m}(C_0 - C_e) \quad (6.2)$$

where q_e is the amount of PO_4^{3-} adsorbed (mg/g), V is the volume of solution (L), m is the adsorbent mass (g); initial and $t_{\text{equilibrium}} = 6$ h of PO_4^{3-} concentrations.

Preliminary electrochemical studies were performed in the way similar to that described previously (Chapter 4 of the Thesis, [31]). The red mud pellets processed under the E1 experimental conditions (Taguchi line) were used as cathodes in the NFAg-R configuration. The pellets were glued to a Ni foil by Ag paste and tested in the rear position (e.g., against the counter electrode).

6.3. Results and discussion

6.3.1. Screening of paraffin-to-suspension ratio and firing temperatures towards microstructural cellular design

Different paraffin:suspension ratios ($p:s = 0.5:1$, $0.75:1$ and $1.5:1$) and firing temperatures ($1100\text{ }^{\circ}\text{C}$, $1150\text{ }^{\circ}\text{C}$ and $1200\text{ }^{\circ}\text{C}$) were used to assess their impacts on the microstructural design of the ceramic pieces. The resulting SEM micrographs are shown in Fig. 6.1, confirming the feasibility of the methodology used to process highly-porous ceramics with cellular-type microstructures. For all studied conditions (experiments E1 to E13, Table 6.2 in section 6.3.3), the results clearly indicate the formation of cellular microstructures with well-defined walls and interconnected cells.

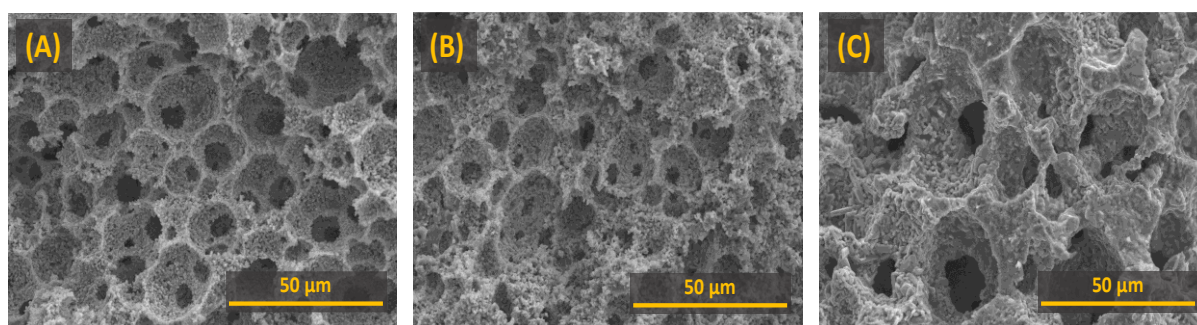


Fig. 6.1. Effects of paraffin:suspension volume ratio and firing temperatures on SEM microstructures for selected samples: (A) E2: $p:s$ 1.5:1; $G = 3.5\%$; $t = 8$ min; $T = 1100\text{ }^{\circ}\text{C}$; (B) E13: $p:s$ 0.5:1; $G = 3.5\%$; $t = 8$ min; $T = 1100\text{ }^{\circ}\text{C}$; (C) E11: $p:s$ 1.5:1; $G = 2\%$; $t = 4$ min; $T = 1200\text{ }^{\circ}\text{C}$.

Interconnectivity is an important feature required for fluids percolation inside the porous membrane. While decreasing the $p:s$ ratio from 1.50:1 to 0.50:1 without changing other processing conditions (Fig. 6.1A, B), one observes less defined cell walls and lower level of interconnectivity between the cells. Cell size (Table 6.2, in section 6.3.3) also seems to decrease slightly from E2 to E13 in Fig. 6.1 A to B when decreasing the paraffin load. Although this trend itself can be expected on decreasing the fraction of dispersed phase while keeping constant surfactant additions, paraffin droplet

sizes are comparable for emulsions with p:s= 0.50:1 through 1.50:1. Cell sizes are mainly defined by the surfactant and gelatine additions, with negligible droplet coalescence even at the highest paraffin contents. Inhomogeneous cavities distribution in the case of p:s 0.50:1 ratio (Fig. 6.1B) is combined with the presence of relatively dense areas, apparently originated from an insufficient amount of the organic phase to provide close packing of the droplets. The general agreement of the expectations with the experimental results, in accordance with [23], actually indicates that complex chemical composition and alkalinity of the red mud do not represent a severe obstacle for the implementation of ceramic suspension-based processing route.

Increasing firing temperature up to 1200 °C causes about 20% loss of open porosity (x_o) (Table 6.2), accompanied by the formation of thicker walls promoted by noticeable firing (Fig. 6.1A, C). To check further the limits for the formation of appropriate cellular ceramics from red mud, one attempted firing at temperatures below 1100 °C and above 1200 °C. However, lower firing temperatures resulted in very fragile samples, while temperatures above 1200 °C led to excessive degradation of the cellular microstructure and loss of interconnecting windows, similar to that observed in [25]. Nevertheless, one did not find important microstructural rearrangements strictly related to phase transformations, as reported elsewhere (e.g. [30]). Therefore, for obtaining further insights on the effects of the processing conditions, one selected 1.50:1 of paraffin:suspension ratio and 1100 °C as suitable fixed experimental conditions, providing a base for the appropriate microstructural design.

6.3.2. Microstructural development

The particular impacts of the processing parameters such as red mud solid load in the suspension (S), gelatine content (G) and stirring time (t) on the microstructural features and percolation were studied by Taguchi method on varying these factors in accordance with the Table 6.2. Some examples of the obtained microstructures are represented in Fig. 6.2.

Despite homogeneous cellular cavities with interconnectivity channels were found in all experiments, significant differences can be observed regarding the size of the cavities. While comparing the microstructural features for the same solid load content (Fig. 6.2A with B, C with D, and E with F), one can observe larger cavities in A ($\approx 42 \mu\text{m}$), followed by smaller in C ($\approx 17 \mu\text{m}$) and E ($\approx 17 \mu\text{m}$). This shows that cellular cavity size decreases for higher gelatine content and longer stirring time. For a long stirring time, gelatine is known as a good emulsifying agent for stabilizing oil-in-water emulsions [31–34], while stirring time promotes breaking the paraffin droplets to smaller ones. The effect of increasing the solid load from 45% (Fig. 2 A,B) to 50% (Fig. 6.2 C,D) or 55% (Fig. 6.2 E,F), can be ascribed to increasing viscosity of the continuous aqueous suspension, leading to smaller cavity size, in agreement with other studies [21–23].

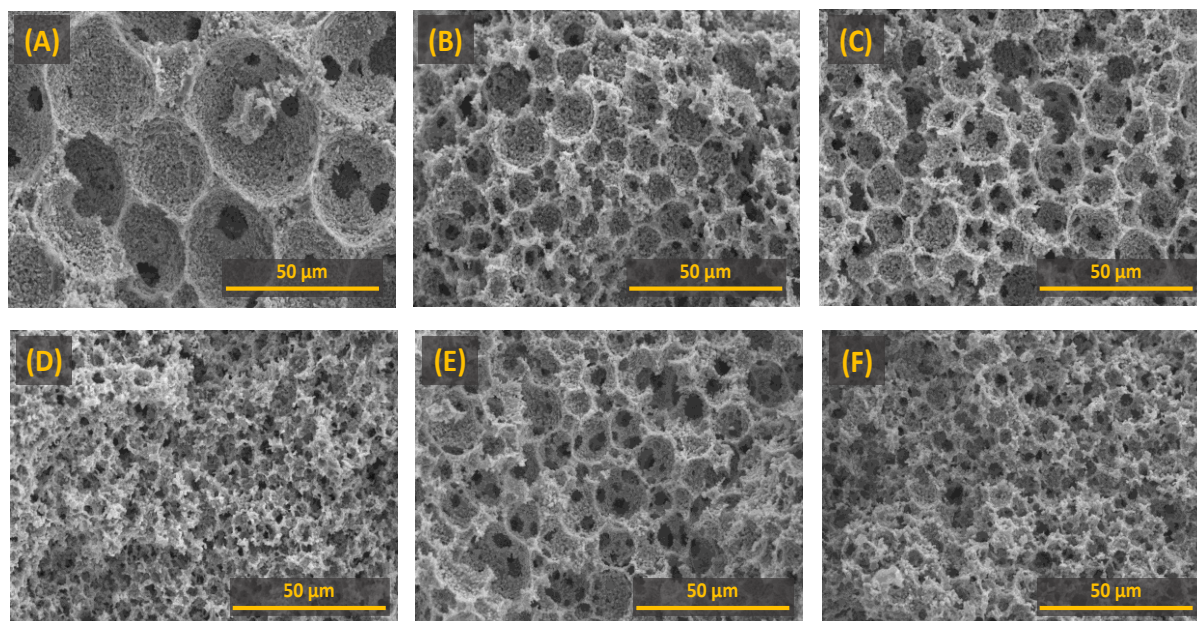


Fig. 6.2. SEM micrographs of red mud-based ceramics fired at 1100 °C, paraffin:suspension volume ratio of 1.5:1, with different experimental conditions attending to the Taguchi plan: (A) E1: S = 45%, G = 2%, t = 4; (B) E3: S = 45%, G = 5%, t = 12; (C) E4: S = 50%, G = 2%, t = 8 min; (D) E5: S = 50%, G = 3.5%, t = 12 min; (E) E8: S = 55%, G = 3.5%, t = 4; (F) E9: S = 55%, G = 5%, t = 8.

The role of gelatine and stirring time can be understood by taking into account their impact on the viscosity of emulsified suspensions; this is shown on comparing rheology of the ceramic suspensions and emulsions from Taguchi plan, E1 and E3, at a fixed solid load content of 45% (Fig. 6.3). Note that increasing gelation additions and stirring time yield much finer droplet sizes (Figs. 6.2A to 6.2B), which also contributes to increase the viscosity of sample E3. Flow and viscosity curves of the suspension (Fig. 6.3A), and of the emulsions E1 and E3 (Fig. 6.3B) are typical for non-Newtonian and pseudoplastic fluids. Moreover, all descendant curves from Fig. 6.3 show that the flow resistance and viscosity decrease with time, indicating a thixotropic behaviour. The area between the ascendant and descendent flow curves shows a possible rupture of the initial microstructure of the red mud suspension (Fig. 6.3A) when the shear rate increases, suggesting a high level of agglomeration between the particles in the waste, even with Dolapix addition as a dispersion agent.

A slight increase in the flow resistance and viscosity with shear rate can be observed in E1 (Fig. 6.3B) against S (Fig. 6.3A) due to the addition of the organic phase. However, a lower level of thixotropy was obtained with E1, suggesting that adding an organic phase with a surfactant, with a lower amount of gelatine (2%), causes a more homogenized emulsion relative to the starting suspension. Thus, fewer agglomerates and paraffin droplets suffered rupture or deformation of the cavities, and larger cavity cells were retained in the resulting cellular microstructures (Fig. 6.2A).

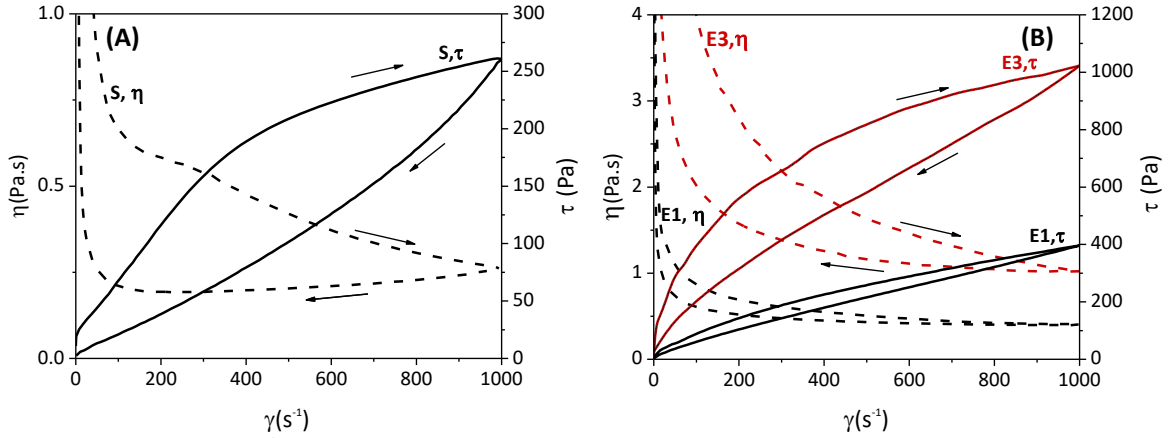


Fig. 6.3. (A) Flow and viscosity curves of the suspension (S) and (B) flow and viscosity curves for the emulsions from Taguchi plan, E1, and E3, for the red mud processing ceramics.

On the other hand, higher flow resistance and thixotropy behaviour was found in E3 when compared to E1, which may be related to higher concentrations of gelatine (2 to 5%) and higher stirring times (4 to 12 min) during the emulsification process. The ascendant flow curve in E3 shows a higher resistance due to the evolution of the gelling process caused by the highest amount of gelatine, and lower droplet size of the dispersed phase, related to a longer stirring time.

Shear thinning rheology behaviour of the emulsified suspensions can be described by the Herschel-Bulkley equation Eq. (6.3):

$$\tau = \tau_0 + k\dot{\gamma}^n \quad (6.3)$$

where τ , τ_0 , k , $\dot{\gamma}$ and n are, respectively, the shear stress, the yield stress, consistency index, shear rate, and pseudoplasticity parameter. This provided good fitting for E1 with $\tau \approx 8 + 3.8 \dot{\gamma}^{0.67}$ on ascending or $\tau \approx 12 + 0.81 \dot{\gamma}^{0.89}$ on descending. Similar differences between results obtained with increasing and decreasing shear rate have been reported previously for emulsified alumina suspensions [21]. However, greater hysteresis was found for sample E3, with $\tau \approx 2.1 \dot{\gamma}^{0.39}$ on ascending and $\tau \approx 11 + 1.46 \dot{\gamma}^{0.60}$ on descending, possibly because finer droplet sizes induce structural changes. In addition, one finds some deviations from the Herschel-Bulkley equation, as depicted in Fig.6.3, by extrapolating the slope at the inflection point; this suggests slight reversion from shear thinning, described by decreasing slope in the lower range of shear rate, to shear thickening, in the upper range of shear rate.

XRD patterns (Fig. 6.4) of the initial red mud waste (RM_i); green monoliths after drying and burn-out of the emulsions (G); and processed red mud after firing at different temperatures (1100 °C and 1200 °C) show the presence of Fe₂O₃ as the predominant phase for all materials. Since the phase composition of the red mud is quite complex, only the most significant phases are shown. In accordance with the literature data, the composition of red mud depends on the quality of bauxite and operation

parameters of the Bayer process; therefore, one may anticipate some differences with the literature data [36–38]. A similar type of red mud is reported in [11]. The initial powder is composed mainly of hematite (Fe_2O_3), boehmite (AlOOH), calcite (CaCO_3), calcium and sodium aluminosilicates, combined with an amorphous phase likely hindering other components. TiO_2 , SiO_2 , and $\text{Al}(\text{OH})_3$ were also identified as minor phases.

Burnout of the organic phase does not result in significant alteration of the phase composition, within the resolution of XRD. However, one cannot exclude significant changes within this intermediate temperature range, with emphasis on at least partial decomposition of hydrates or oxyhydrates, and possibly even carbonates according to relevant literature [39], and the onset of intermediate anhydrous phases. XRD also shows the onset of iron silicon oxide as silica-doped magnetite $\text{Fe}_{3-x}\text{Si}_x\text{O}_4$, probably assisted by oxygen deficient conditions imposed by the burnout of the high fractions of the dispersed organic phase.

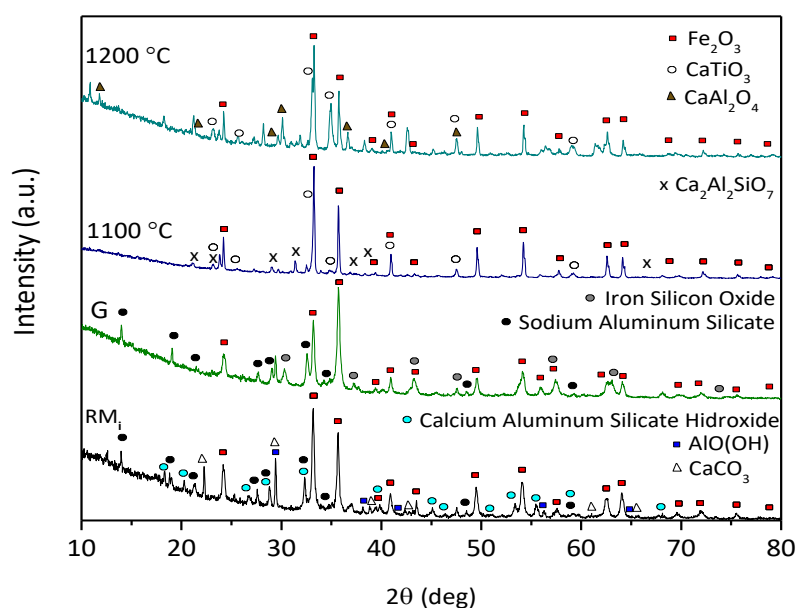


Fig. 6.4. XRD diffractograms of initial red mud waste (RM_i), processed green samples after burn-out of the organic phase (500 °C) (G) and processed samples after firing (1100 °C and 1200 °C).

High temperatures required to fire the red-mud based cellular ceramics promote new phases, with emphasis on perovskite (CaTiO_3) and calcium aluminates, probably due to the transformation of previous phases formed at intermediate temperatures. These processes are unlikely to become disruptive due to solid-state kinetic limitations, allowing some flexibility to fire the cellular ceramics in a significant temperature range, except for a gradual decrease in porosity and microstructural changes.

6.3.3. Effects of processing conditions on microstructural features and percolation

Taguchi method was used for assessing changes in cellular cavities size (\bar{d}), open porosity (x_o), linear roughness (R_z) and constriction factor (f_c) due to variations on three factors (S, G and t) according to Table 6.1. In general, the results indicate that the applied processing parameters mostly affect the cellular cavity size, while the effects on other parameters are rather minor, corresponding to less than 30% variation (Table 6.2). Lower solid load, gelatine content and stirring time (E1) favour larger cellular cavity sizes (42 μm), slightly higher values of open porosity (75%) and roughness (12.4 μm). Ceramics with smaller cellular cavity sizes, E5, E7 and E9 ($\leq 14.5 \mu\text{m}$) simultaneously show lower open porosity (70%) and lower roughness (8.1 μm in E5), also apparently correlated with higher solid load content and stirring time. Cavity sizes and open porosity decrease on increasing the firing temperature up to 1200 °C and on decreasing the paraffin content to 0.5:1 ratio, in good agreement with the discussion given in section 6.3.1. The roughness of fracture surfaces was measured to assess the feasibility of this method as a quick screening for approximate ranges of average cell size or other microstructural features. Though the obtained results suggest a moderate correlation between the roughness of fracture surfaces and cellular cavity size, significant discrepancies are likely due to tip entrance into the relatively small interconnection channels, resulting in $R_z < \bar{d}$, mainly for samples with the largest cell sizes.

The interconnection windows between large cavities are of special relevance for the permeability of the porous ceramics towards fluid flux; their impact can be quantified by a constriction factor f_c (Eq. (6.4)) [28,30]:

$$f_c = x_o \frac{A R}{L \rho} \quad (6.4)$$

This corresponds to a ratio between the measured resistance of soaked sample (R) and resistance of the ionic salt solution without constrictions, $R_I = L\rho/(Ax_o)$, where ρ is the resistivity of the salt solution (32.4 $\Omega \text{ cm}$ at 20 °C [40]), with thickness to area ratio (L/A), and open porosity (x_o). The effective resistance to ionic transport through the open porosity is likely to increase by constrictions at narrow interconnections between cellular cavities, as shown in Figs. 6.1 and 6.2, and due to tortuosity in the spatial distribution of the open porosity, corresponding to longer distances. In addition, the onset of microstructural rearrangements occurs on firing, with partial loss in open porosity, as found on comparing results for E1, E10 and E11, as well as thicker struts separating the remaining cellular cavities for samples fired at the highest temperature (sample E11 in Fig. 6.1C).

Table 6.2. L_9 orthogonal array of Taguchi plan used to study the effects of the solid load of red mud (S), gelatine content (G) and stirring time (t) on the response variables: cellular cavities size (\bar{d}), open porosity (x_o), linear roughness (R_z) and constriction factor (f_c). Additional experiments were performed with changes in firing temperature, while maintaining the other conditions of experiment E1, and changes in paraffin:suspension ratio, while maintaining conditions of E2.

	p:s	S (%)	G (%)	t (min)	T (°C)	\bar{d} (μm)	x_o	R_z (μm)	f_c
E1	1.5:1	45	2	4	1100	41.7±3.3	0.75±0.01	12.4±2.5	2.4
E2	“	45	3.5	8	“	20.5±1.4	0.74±0.004	11.5±2.9	2.4
E3	“	45	5	12	“	17.1±0.5	0.73±0.02	9.3±1.0	2.3
E4	“	50	2	8	“	17.4±0.3	0.71±0.002	10.6±1.5	2.9
E5	“	50	3.5	12	“	11.4±0.3	0.70±0.005	8.1±1.9	2.2
E6	“	50	5	4	“	16.8±0.6	0.72±0.02	10.3±1.2	2.4
E7	“	55	2	12	“	14.5±0.6	0.70±0.02	10.5±1.1	2.3
E8	“	55	3.5	4	“	17.4±0.7	0.72±0.004	8.7±1.2	2.8
E9	“	55	5	8	“	11.9±0.4	0.70±0.007	9.1±1.1	2.2
E10	“	45	2	4	1150	30.3±1.8	0.65±0.01	8.9±1.2	2.4
E11	“	45	2	4	1200	28.9±1.9	0.55±0.007	10.3±0.9	2.6
E12	0.75:1	45	3.5	8	1100	22.2±1.2	0.66±0.03	9.8±1.3	2.3
E13	0.5:1	45	3.5	8	1100	16.9±0.7	0.64±0.02	9.5±1.2	2.4

One attempted to get further insight into the impact of microstructural features on the constriction factor by relying on the ability of impedance spectroscopy to de-convolute contributions with different relaxation frequencies (ω_o), or in different capacitance ranges, as predicted for ideal resistor-capacitor (RC) contributions with ($\omega_o RC \approx 1$). However, the relaxation frequency of the highest microstructural contribution exceeds the frequency range of the equipment, and other contributions of Nyquist plots (Fig. 6.5A) are depressed and ill-resolved; this may be due to combination of different factors such as porosity of the samples [41] and charge transfer processes at the solid-liquid interface due to the complex composition of the red mud waste, containing different cations (Al^{3+} , Fe^{3+} , Ca^{2+} , and Si^{4+} , ...), and their interaction with the conductive salt solution. Thus, the depressed arc may correspond to overlapped processes with different relaxation times [42,43]. However, one may assume a simple empirical description by an equivalent circuit $R_s(RQ)_{bi}(RQ)_{el}$, consisting of a pure resistance at frequencies above the upper limit of the equipment (2 MHz), probably related to ionic transport in filled cellular cavities with the conductive salt solution, a depressed and poorly resolved arc in the upper frequency range of the impedance meter, probably due to internal blocking interfaces, and a very large arc in the lowest frequency range, ascribed to electrode processes.

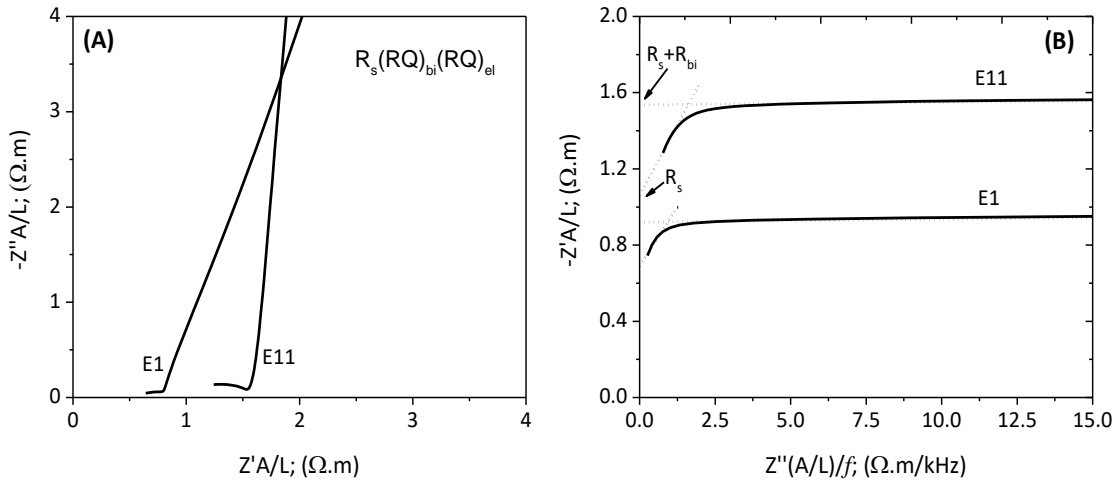


Fig. 6.5. (A) Impedance spectra for E1 and E11, and (B) the corresponding alternative representation of Z' vs Z''/f , to obtain the fitting parameters for the “bi” contribution.

Since standard codes (e.g. Z View) were somewhat in-suited to obtain good fitting for the constant phase elements (Q_{bi}), one relied on an alternative representation in the form of Z' vs Z''/f (Fig. 6.5B), with demonstrated ability to extract relevant values of resistance and relaxation frequencies of microstructural contributions [44]. The alternative representation shows separate trends in the upper frequency range (Eq. (6.5)) and for intermediate frequencies (Eq. (6.6)), which can be extrapolated to extract the relevant resistances and corresponding slopes provide information on relaxation frequencies, as follows:

$$Z' \approx R_s + f_{bi} \left(\frac{Z''}{f} \right) \quad (6.5)$$

$$Z' \approx R_s + R_{bi} + f_{el} \left(\frac{Z''}{f} \right) \quad (6.6)$$

For samples E1 one obtained average results of $\frac{AR_s}{L} = 0.69 \Omega.m$, $\frac{A(R_s+R_{bi})}{L} = 0.92 \Omega.m$, and $f_{bi} \approx 3$ MHz. The corresponding relative permittivity for the blocking interlayer was also estimated on combining the values of resistance and frequency, i.e.:

$$\frac{CL}{A\epsilon_o} = \left(\frac{L}{2\pi f_{bi} R_{bi} A \epsilon_o} \right) \approx 23 \times 10^3 \quad (6.7)$$

This is about 3 orders of magnitude higher than expected for the relative dielectric permittivity of aqueous solutions if one considered a bulk contribution. Thus, one must consider internal blocking interfaces, since their capacitance varies inversely with thickness. Similar ranges were obtained for E11, with $\frac{AR_s}{L} = 1.06 \Omega.m$, $\frac{A(R_s+R_{bi})}{L} = 1.54 \Omega.m$, $f_{bi} \approx 2.4$ MHz and $CL/(A\epsilon_o) \approx 15 \times 10^3$. In fact, the

“bi” contribution ($\frac{AR_{bi}}{L} = 0.23 \Omega \cdot m$ for sample E1) and ($\frac{AR_{bi}}{L} = 0.48 \Omega \cdot m$ for sample E11) can be ascribed to the microstructural differences shown in Fig. 6.1 and 6.2, with emphasis on discontinuous porosity and thicker struts. Thus, the contribution of blocking interfaces was included in the total resistance, responsible for the decreased percolation (Eq. (6.8)).

$$R = R_s + R_{bi} \quad (6.8)$$

The correlation matrix and corresponding coefficients listed in Table 6.3 again confirm the strongest negative correlation for solid load and open porosity. In general, the solid load content showed to be the most significant factor studied regarding the effect on cavity size and linear roughness, followed by stirring time, with a rather moderate negative correlation. On the other hand, practically no correlations were found between solid load and constriction factor, and between gelatine content and open porosity. Thus, lower solid load and shorter stirring times are essential for a flexible microstructural design of the ceramics based on red mud waste and attaining high open porosity ($\approx 75\%$). The amount of gelatine contributes to the development of the interconnecting windows, although this correlation is at the borderline of apparent.

Table 6.3. Correlation matrix of the effects of each factor studied (S, G, t) on the response variables (\bar{d} , x_o , R_z , f_c) and the coefficient of determination (R^2) of the mathematical models.

	Factors			Coefficient of determination
	S	G	t	R^2
\bar{d}	-0.57	-0.44	-0.52	0.95
x_o	-0.80	-0.11	-0.51	0.91
R_z	-0.50	-0.50	-0.38	0.67
f_c	0.08	-0.46	-0.41	0.35

Since open porosity, x_o , seems to be linearly dependent on the amount of solid load, stirring time and organic phase used (Table 6.2), one can assume a linear dependence described by multivariate least squares, leading to Eq. (6.9):

$$x_o = 0.908 - 0.330S - 0.001G - 0.003t \quad (6.9)$$

On the other hand, the low number of experiments required by the Taguchi plan does not take into consideration possible complex interactions between the different factors. The combination of the viscosity of paraffin, surfactant agent or gelatine, interfacial energy and shear stress between red mud

suspension with paraffin, may produce an additional impact on the size of the cellular cavities, linear roughness and its interconnectivity between cells. A linear multivariate model in this case may not be the most adequate. Thus, the experimental results were fitted by logarithmic models, based on general powder laws for the diameter of the cavities and linear roughness (Eq. (6.10) and (6.11), respectively), where α , β , and γ are fitting parameters obtained by the multivariable least squares method. The laws are related to the correlation between the factors observed in Table 6.3.

$$\bar{d} \propto (1 - S)^\alpha G^{-\beta} t^{-\gamma} \quad (6.10)$$

$$R_z \propto (1 - S)^\alpha G^{-\beta} t^{-\gamma} \quad (6.11)$$

After applying log-log scales (Eq. (6.12)), \bar{d} and R_z can be defined as indicated in Eq. (6.13) and (6.14).

$$\log(\bar{d} \text{ or } R_z) = \log(\bar{d}_0 \text{ or } R_z) + \alpha \log(1 - S) - \beta \log(G) - \gamma \log(t) \quad (6.12)$$

$$\bar{d} = 1.039 \times (1 - S)^{0.002} G^{-0.378} t^{-0.353} \quad (6.13)$$

$$R_z = 0.941 \times (1 - S)^{5.782} G^{-0.662} t^{-0.806} \quad (6.14)$$

As mentioned previously, percolation depends mainly on open porosity, with an additional constriction factor which depends mainly on microstructural evolution at the firing temperatures. Early results reported for alumina cellular ceramics [23] showed a decrease in f_c while increasing the porosity and cellular cavity size. The same was not observed in the present work. Despite the high levels of interconnectivity between cells and, consequently, a good level of permeability observed in all Taguchi lines, the experimental range tested for the Taguchi plan may be too narrow for conclusive analysis.

At the same time, suitable models were obtained for cellular cavities size and open porosity, with a R^2 near to 1, although a lower correlation was found for linear roughness, even at logarithmic scale. Again, this may originate from the relatively narrow experimental range, insufficient for clear observation of the impact on the linear roughness data.

The general processing mechanism relies on the organic phase addition which is responsible for the pores formation after its burn-out during thermal processing of the green ceramic pieces. In addition, relevant factors such as gelatine content, stirring time and solid load were proved to have an impact on the viscosity of the emulsions and, consequently, on the size of the cellular cavities. Corresponding guidelines are discussed along the manuscript. Importantly, the established role of gelatine does not encompass only the consolidation of the ceramic skeleton, but also consists of the development of suitable interconnecting channels between cells, allowing better percolation performance. In such a way, the applied processing routes are proved to result in high cavity sizes, high open porosity and linear

roughness, along with the good percolation between the cells, with a clear potential for further environmental applications.

6.3.4. Phosphate removal from water – preliminary studies

Considering possible environmental applications, the surface charge of RM_i and processed red mud (PRM, Taguchi line E1) was evaluated. The surface charge was investigated by zeta potential measurements in a pH range from 3 to 12 (Fig. 6.6).

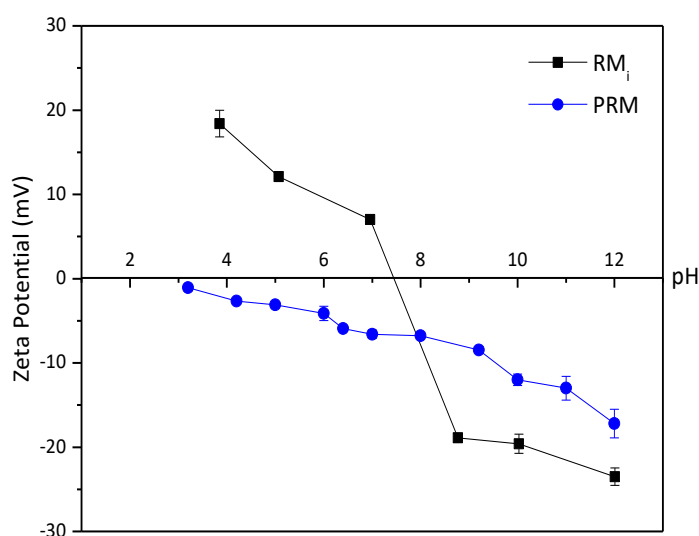


Fig. 6.6. Zeta potential as a function of pH for the initial red mud waste (RM_i) and the processed red mud (PRM).

The isoelectric region obtained ($-30 < \text{zeta potential} < 30 \text{ mV}$) corresponds to the unstable region, with high sedimentation tendency for both suspensions. This fact shows that it is reasonable to consider some level of agglomeration and sedimentation of the particles in the suspension before the emulsification in the rheology tests. The isoelectric point (IEP), corresponding to the pH at which the zeta potential is zero, was found to be 7.5 for RM_i . The particles are positively and negatively charged at pH, correspondingly, lower and higher than 7.5, which is within the range (6.4 – 8.7) reported by [45]. The IEP of red mud is related to the IEP of each phase present in the waste. Values of IEP of 8.4, 8.0 [45], 5.6 [46] and 2.0 [47] were reported for Fe_2O_3 , Al_2O_3 , TiO_2 and SiO_2 , respectively. Higher content of TiO_2 and, especially, SiO_2 in red mud is expected to decrease the IEP. On the other hand, negative values of zeta potential were found for the whole pH range tested in the PRM sample, revealing negatively charged particles. Nevertheless, the behaviour observed for PRM suggests a tendency for an IEP around pH 3. Attempts to perform the measurements at lower pH showed difficulties with pH

stabilization, apparently caused by the possible dissolution of cations (Fe^{3+} , Ca^{2+} , Na^+ , Al^{3+} , Ti^{4+} or Si^{4+}) into the suspension. The same characteristic negative zeta potential was found in a red mud sample from a combined Bayer and sintering process in [45]. Calcium titanate (CaTiO_3) was found both in [45] and in the present work for samples processed after firing ($T_{\text{firing}} \geq 1100$ °C). Presence of CaTiO_3 (IEP 3 - 4) [48–50] may be one of the causes for the lowering of IEP after the firing of the processed samples, since it is a major phase. However, the IEP of CaTiO_3 seems to be debatable in literature since some authors indicate a pH_{IEP} of ≈ 8 [45], but mainly acidic values are presented. Coreño and Coreño [48] obtained a $\text{pH}_{\text{IEP}} = 3$ with zeta potential determination and a $\text{pH}_{\text{IEP}} = 8.3$ when following another standard methodology. Lower particle concentrations during IEP determination may lower its value since a layer of acidic sites of TiO_2 ($\text{pH}_{\text{IEP}} \approx 5$) may be formed while Ca^{2+} is leached to the suspension. PRM sample seems to have a buffer behaviour since minor zeta potential changes occurred when adding higher contents of H^+ in suspension, suggesting the dissolution of soluble minerals at acidic pH [45].

Preliminary adsorption studies were performed for future hybrid water treatment systems with porous membranes. When using such membranes, the equilibrium of adsorption capacity is reached in longer periods of time due to longer diffusion pathways. Powder materials are frequently used for preliminary tests instead of granular materials, in order to minimize the diffusion processes during the adsorption of the pollutant at a first approach. Preliminary feasibility tests for the use of the highly porous membranes based on PRM powder were performed after grinding the cellular ceramics structure. Their performance was further compared to the RM_i for phosphate adsorption in water, in 6 h (equilibrium time). Fig. 6.7A shows the adsorption capacity for both powders under study and Fig. 6.7B, the corresponding phosphate removal from water. The contaminated water was previously adjusted for pH 4 and 8. Higher adsorption capacity (q_e) values (Fig. 6.7A) were obtained at 400 mg/L PO_4^{3-} concentration with both adsorbents at pH 4, with 12 mg $\text{PO}_4^{3-}/\text{g}$ and 4 mg $\text{PO}_4^{3-}/\text{g}$ for RM_i and PRM, respectively.

When pH increases from acidic to alkaline, the surface charged of the adsorbents change as well as the degree of ionization of the phosphate solution according to $\text{H}_3\text{PO}_4 \rightarrow \text{H}_2\text{PO}_4^- \rightarrow \text{HPO}_4^{2-} \rightarrow \text{PO}_4^{3-}$ [51,52]. Thus, pH can determine the phosphate species present in the water and the strength of the electrostatic forces between the pollutant and the surface of the adsorbents. Since the IEP of RM_i is 7.5 (Fig. 6.6), a pH below the IEP can enhance phosphate adsorption due to the positive charge around the surface of the adsorbents. Phosphate species compete with free HO^- ions present in the alkaline water, decreasing the efficiency of the adsorbent for alkaline pH [52]. On the other hand, PRM showed to have a possible IEP around pH 3. Since extreme acidic conditions promote the dissolution of cations present in both samples, the adsorption tests were performed at pH not lower than 4. However, in these conditions one can expect already lower adsorption capacities for PRM, since zeta potential at pH 4 is around -2.7 mV (Fig. 6.6), showing a negatively charged surface of the particles.

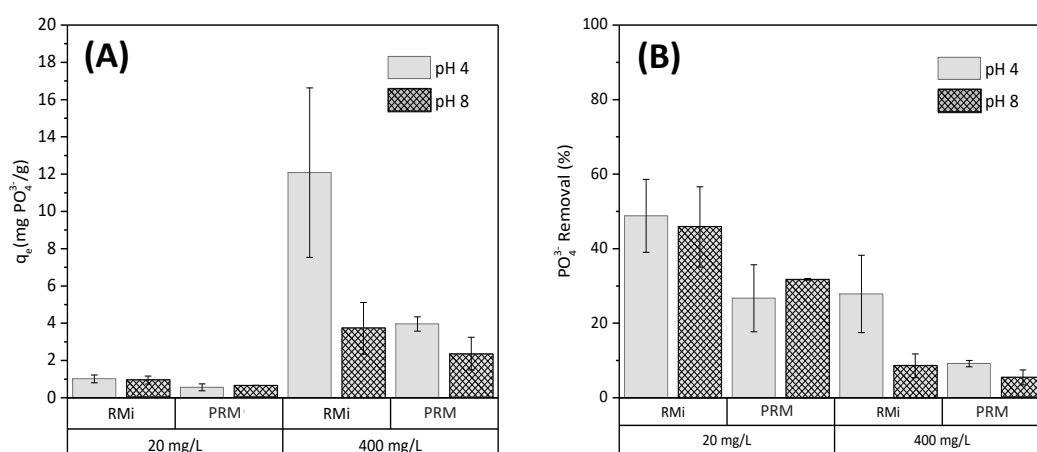


Fig. 6.7. Adsorption studies for 20 mg/L and 400 mg/L of phosphate solutions with RM_i and PRM at pH 4 and 8: (A) Adsorption capacity of the adsorbents; (B) phosphate removal (%) after 6 h.

The pH seems to be much less critical for q_e at lower PO_4^{3-} concentrations (20 mg/L). A poor contribution of the electrostatic forces between PO_4^{3-} and the surface of the adsorbents at lower phosphate concentrations promotes more active sites for adsorption. This results in higher rates of phosphate species removal in the water contaminated with 20 mg/L of PO_4^{3-} with both pH tested (Fig. 6.7B). While nearly 50% of removal rate was obtained for both pH tested with RM_i, around 30% was observed at pH 4 and 8 for PRM. Despite PRM might appear to have a slightly lower rate at pH 4 than pH 8 (27% against 32%), these values are within the standard deviation measured. On the other hand, lower removal rates were obtained at 400 mg/L of PO_4^{3-} , especially at pH 8, due to the presence of less active sites at the surface of the adsorbents.

Tangde et al. [53] obtained an adsorption capacity of 56 mg/g of PO_4^{3-} with red mud at pH 2 in 250 mg/L of PO_4^{3-} concentration, while 12 mg/g and 4 mg/g were obtained at pH 4 in the present study with RM_i and PRM, respectively, in 400 mg/L of PO_4^{3-} . Since the composition and morphology of the red mud can vary substantially with the source of bauxite and the processing technology, this will affect the specific BET surface area of the red mud. Without any pre-treatment, a BET surface area of 20.9 m^2/g was used in [53] justifying a better performance, since RM_i has a BET surface area of 0.6 m^2/g [11]. The use of stronger acidic conditions in [53], pH 2, could be another responsible factor of the improved adsorption capacity as well. PRM shows a lower capacity of adsorption of 4 mg/L in 400 mg/L of PO_4^{3-} when compared with the RM_i. After processing, the specific BET surface area of the red mud improved slightly but not significantly, leading to 1.8 m^2/g . Both BET surface areas obtained are considered relatively low for effective adsorption when compared with other materials in literature [52].

The concentration of both powders tested, 10 g/L, was proved to not be conclusive for a substantial increase in the treatment efficiency. Increasing the adsorbent load in the water will lead to

an increase in the adsorption capacity due to the presence of more active sites for adsorption. Consequently, higher phosphate removal rates from water can be attained [54]. An optimization study with a wider range of experimental conditions tested should be carried in the future for the materials considered. However, higher removal rates of phosphate species from water can be achieved by promoting not only adsorption effects on the processed red mud, but by combining it with redox and catalytical reactions.

While the preliminary adsorption tests were performed on the powders, one may anticipate an advantageous use of the cellular ceramic red-mud-based adsorbents, which allow preventing the particle removal by high fluid fluxes and their agglomeration, and generally, impart better mechanical stability to the whole system. Such supports are expected to be cheap and sustainable, provided by the massive scale of the worldwide alumina production using the Bayer process. Still, the results discussed above point out that the surface area of thus produced red-mud cellular ceramics may be insufficient for efficient adsorption. This likely can be tackled by using a hydrothermal modification of the red-mud ceramics, similar to the approaches described elsewhere [55,56], where, along with the surface development, one may also introduce additional functionalities, including catalytic.

6.3.5. Electrochemical reduction of the processed red mud in bulk – preliminary studies

Previous results on electrochemical reduction of the synthetic iron oxide-based ceramics have underlined the importance of open porosity for the electrolyte access, essential for the development of the reduction front. Thus, the ceramics having the highest open porosity, corresponding to E1 in Taguchi experimental planning (Table 6.2), was selected for the electrochemical tests.

Fig. 6.8 shows the cyclic voltammograms obtained for the E1 ceramic electrode before (black line) and after (red line) the electrochemical reduction. Both measured current densities (j) are in the same range, revealing that no significant evolution towards more conductive phases has occurred during the 20 h of reduction. In fact, a substantial increase in the current densities after the bulk electrochemical reduction of $\text{Fe}_{1.8}\text{Al}_{0.2}\text{O}_3$ was observed (Chapter 4, [31]) in the same experimental conditions. At the same time, notable similarities in onset potentials and evolution of cathodic (C) and anodic (A) peaks are evident as compared to [24,31]. Thus, C1 and C'1 peaks seem to be related to the reduction of some Fe(III) to Fe_3O_4 and Fe(II) aqueous species (e.g. $\text{Fe}(\text{OH})_3^-$, HFeO_2^- , between others) in the processed red mud, at around -0.93 V and -0.96 V, respectively. Onset potentials of around -1.05 V of cathodic polarizations are ascribed to H_2 evolution reaction (HER) in both cases, where it is also possible to observe C2 and C'2 cathodic shoulders superimposed in the HER region of the voltammogram at -1.10 V and -1.11 V, respectively. In agreement with the cited studies, the shoulders are related to the

conversion of the Fe(II) to Fe⁰, where a rather intensive peak was found after the 20 h of reduction. Two well visible peaks, A'₁ (-0.86 V) and A'₂ (-0.52 V), are related to the oxidation of Fe⁰ to Fe(II) species, and FeOOH and/or Fe₃O₄; where a single anodic peak, -0.65 V (A₂), is observed before the electrochemical reduction, in fair agreement with [31].

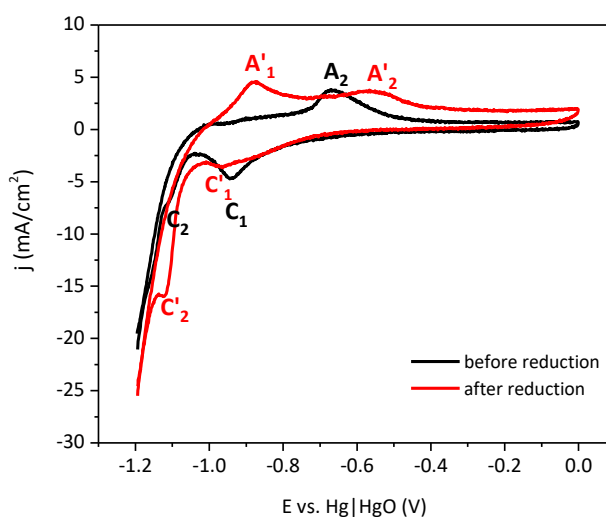


Fig. 6.8. Cyclic voltammograms of the E1– red-mud-based cathode before (black line) and after (red line) the electrochemical reduction (NaOH, 10 M at 90 °C).

Thus, the cyclic-voltammetry (CV) results suggest a possible reduction of iron oxide species in the red mud to Fe⁰ during 20 h of electroreduction. These results are in good agreement with Fig. 6.9, where the current density vs. time curves for two replicates (R1 and R2) are shown. In fact, a maximum of -3 mA/cm² is obtained (R2) when the sample was polarized at the same cathodic potential as in [31]. Due to the high porosity of E1 samples (75%), a suitable electrode|electrolyte interface is expected to occur. However, the presence of insulating phases, such as calcium-aluminium silicates (Fig. 6.4, processed samples at 1100 °C) may have a direct influence on the formation of the 3 phase interlines (3PIs) [31,57–59], including iron oxide from the red mud and the current collector (Ni foil). Both curves seem to progress towards around -2.5 mA/cm² in 20 h, showing a general reproducibility. However, different shapes were attained possibly due to the heterogeneity of the initial red mud sample.

Chapter 5 of the thesis, focused on the electrochemical reduction of Fe_{2-x}Al_xO₃ in alkaline suspensions, have revealed some guidelines suggesting that the presence of a significant amount of aluminium (hydro-) oxides phases may lead to the partial blocking of the iron-containing sites in terms of electrical contact with the electrolyte thus hampering the reduction. Similar results were observed by Maihatchi et al. [60] during the electrochemical reduction of a suspension based on Fe₂O₃ powder with 30 wt% kaolinite (Al₂Si₂O₅(OH)₄). Despite the low current densities, one can observe a similar trend in

the current-density vs. time curve of R2 as in [31,59]. A current decrease occurred during the 2.5 h (entrance of the electrolyte inside of the porous cavities and establishment of the 3PIs), followed by an increase of the current density to -3 mA/cm^2 until 5 h of the experiment, apparently promoted by the iron reduction. In the period of 5 h to 20 h, a very slight decrease of current is observed, possibly related to the blocking of the Fe_2O_3 by the non-conductive phases present in the processed red mud and impeding the expansion of the reduction front.

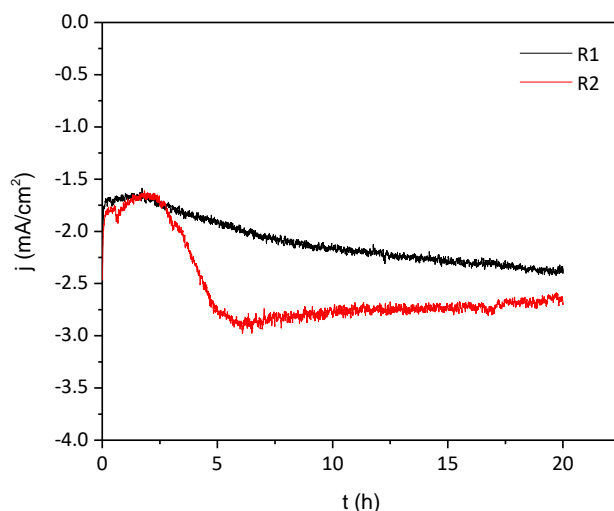


Fig. 6.9. Current-density vs. time curves (replicates R1 and R2) of the processed red mud sample (E1) in 10M NaOH at 90 °C)

Although iron reduction itself is accompanied by the formation of highly-conductive iron, the volume and surface fractions of the conductive species actually decrease on the reduction due to a significantly higher density of the metallic particles as compared to oxide. On the other hand, R1 might have more insulating phases in the contact with the current collector before the reduction. In general, these results suggest three guidelines regarding the prospects of the bulk electrochemical reduction of the red mud:

- i. a slow electroreduction occurs, although at a relatively slow reaction;
- ii. the reduction process may be significantly affected by the chemical inhomogeneities inherently present in the red mud;
- iii. the presence of insulating phases may impede the propagation of the reduction front in the red-mud-based ceramics even if the porosity provides a suitable contact with the electrolyte.

Fig. 6.10 shows the XRD pattern of a recovered piece of the ceramic electrode after the electroreduction, which was in contact with the current collector. The evolution of the phase composition as compared to non-reduced red mud (Fig. 6.4.) is visible. The presence of more conductive phases, such Fe_3O_4 and some Fe^0 were identified immediately under the silver paste, where a black coating was

clearly visible. However, comparing the microstructural evolution in the same spot (Fig. 6.11) to the iron crystals described in Chapter 4 ([31]), significant differences can be observed.

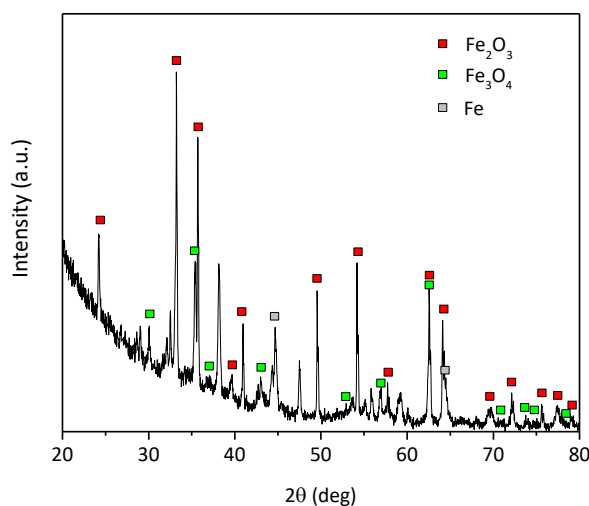


Fig. 6.10. XRD pattern of the processed E1 red mud pellet after the electroreduction.

The destruction of some cellular cavities is well visible in some parts of the black coating (Fig. 6.11A), these changes can be attributed to the partial dissolution of the red mud under employed experimental conditions. The morphology of iron crystals is entirely distinct as compared to the previous results (e.g., Figs. 4.5, 4.9). Several local large agglomerates showing iron excess are observed (Fig. 6.11 B-D) and can be possibly attributed to metallic iron, in agreement with the XRD results (Fig. 6.10). As an example, an agglomerate shown in Fig. 6.11C reveals some morphological similarities with the iron crystals obtained by electroreduction of the suspensions (Fig. 5.8 C, D, Fig. 5.9 C). This also suggests possible similarities in the iron reduction mechanisms from oxide suspensions and in the red mud, where the constituent phases are predominantly non-conducting. Such agglomerate (Fig. 6.11D) inclusions may preferably grow in iron-rich sites, provided by inherent chemical inhomogeneity of the red mud. Due to the high complexity of red mud, it was not possible to estimate the Faradaic efficiency of the electroreduction process.

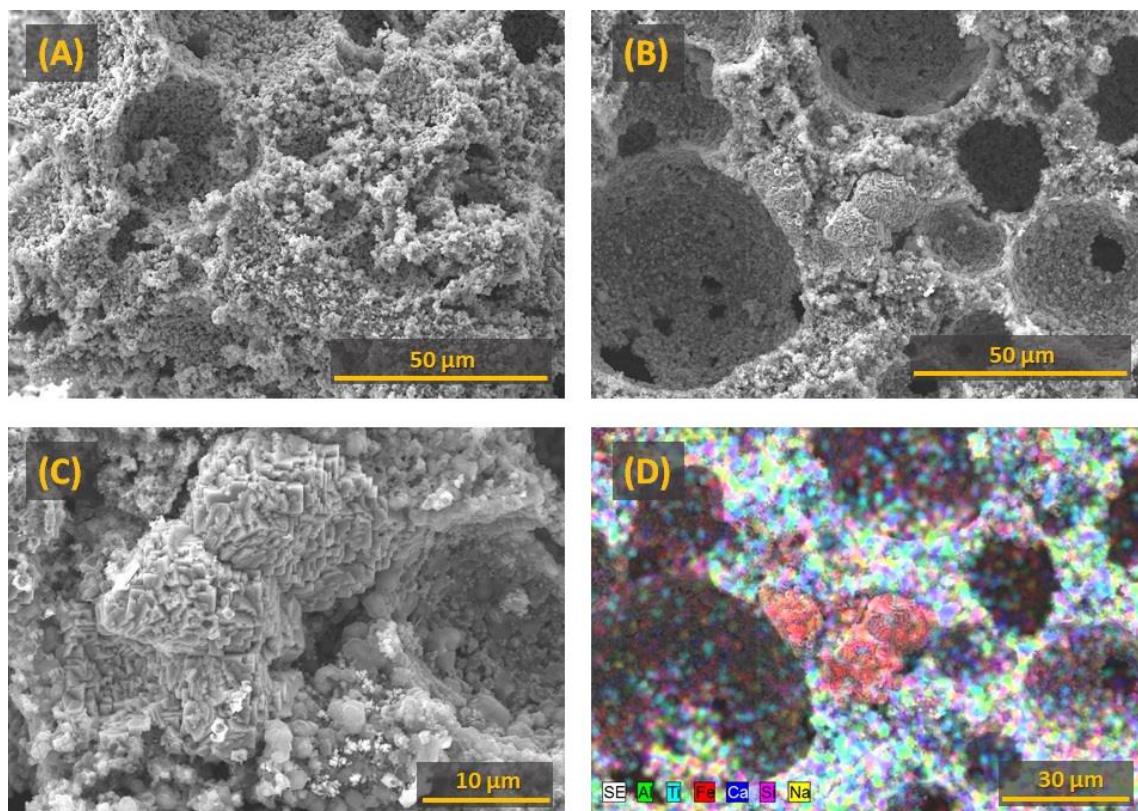


Fig. 6.11. SEM microstructures of the processed E1 red mud pellet after 20 h of electroreduction (NaOH, 10 M at 90°C): (A) destruction of the initial cellular cavities; (B) iron crystals; (C) iron crystals with higher magnification; (D) EDS mapping of the iron crystals observed in (B) and (C).

6.4. Conclusions

Red mud waste is a suitable precursor to process highly-porous cellular ceramics by emulsification of ceramic suspension with liquid paraffin. The impacts of the processing conditions, including the solid load of red mud, gelatine content and stirring time, on the microstructural features were studied by Taguchi method. Lower solid load (45%), gelatine content (2%) and shorter stirring time (4 min) were found as the optimal conditions for attaining the largest cellular cavity size (42 μm), and highest open porosity (75%) and linear roughness (12 μm). The cellular cavity size and open porosity were only slightly affected by the gelatine content. Gelatine was shown to be responsible for the consolidation of the cellular structure, while also playing an important role in the formation of interconnection channels between the cavities. The permeability towards fluid flow, defined as a constriction factor, varied only slightly within the range of applied processing conditions, suggesting that the proposed approach is flexible for producing highly-porous red-mud cellular ceramics with percolated porosity. These processing conditions, combined with the main dependence of porosity on paraffin:suspension ratio, are suitable guidelines for the microstructural design of highly porous membranes based on red mud waste, without blending with additional raw materials. In addition, the elemental and phase compositions of resulting cellular ceramics do not include hazardous components,

raising prospects for applications as membranes for filtration or capture of pollutants. Its open porosity is also suitable for subsequent functionalisation, if one considers catalytic applications. The alkalinity of red mud powder may be used as an advantage to neutralize very acidic water such as acid mine drainage [61,62] or a neutralization can be applied to the initial powder before processing as in [63]. Preliminary tests of the prepared materials for the phosphate removal from wastewater have shown a relatively low adsorption capacity, which corresponded to 12 mg/g and 4 mg/g for initial and processed red mud, correspondingly, at pH 4 in the solution containing 400 mg/L of PO_4^{3-} . The electrochemical reduction of the processed red-mud-based cellular ceramics revealed low current density (-3 mA/cm^2). Although the formation of metallic iron was confirmed by the XRD studies, the process is significantly affected by the presence of insulating phases and phase inhomogeneity of the red mud. The results indicate that a further pre-treatment of the red mud waste may be suitable in order to remove low-conductive components (e.g. silica and alumina) for the red mud valorisation. Moreover, using red mud waste as a raw material for processing highly-porous ceramics allows one to decrease processing costs and to promote waste valorisation, which is strongly encouraged by the European Commission for the Circular Economy.

Acknowledgements

This work was supported by the FCT grant PD/BD/114106/2015, NOTARGAS project (POCI-01-0145-FEDER-030661 and 30661-02/SAICT/2017) and CICECO-Aveiro Institute of Materials (ref. UID/CTM/50011/2019), financed by national funds through the FCT/MCTES. Additional funding was provided by the postdoctoral program abroad CAPES/EDITAL N° 46/2017. The authors kindly thank Artur Sarabando (University of Aveiro) for the support provided with XRD analysis.

6.5. References

- [1] E. Mukiza, L.L. Zhang, X. Liu, N. Zhang, Utilization of red mud in road base and subgrade materials: A review, *Resour. Conserv. Recycl.* 141 (2019) 187–199. doi:10.1016/j.resconrec.2018.10.031.
- [2] Y. Hua, K. V. Heal, W. Friesl-Hanl, The use of red mud as an immobiliser for metal/metalloid-contaminated soil: A review, *J. Hazard. Mater.* 325 (2017) 17–30. doi:10.1016/j.jhazmat.2016.11.073.
- [3] M.A. Khairul, J. Zanganeh, B. Moghtaderi, The composition, recycling and utilisation of Bayer red mud, *Resour. Conserv. Recycl.* 141 (2019) 483–498. doi:10.1016/j.resconrec.2018.11.006.

- [4] Y. Kim, Y. Lee, M. Kim, H. Park, Preparation of high porosity bricks by utilizing red mud and mine tailing, *J. Clean. Prod.* 207 (2019) 490–497. doi:10.1016/j.jclepro.2018.10.044.
- [5] W.C. Tang, Z. Wang, Y. Liu, H.Z. Cui, Influence of red mud on fresh and hardened properties of self-compacting concrete, *Constr. Build. Mater.* 178 (2018) 288–300. doi:10.1016/j.conbuildmat.2018.05.171.
- [6] W. Wang, W. Chen, H. Liu, C. Han, Recycling of waste red mud for production of ceramic floor tile with high strength and lightweight, *J. Alloys Compd.* 748 (2018) 876–881. doi:10.1016/j.jallcom.2018.03.220.
- [7] W. Liu, S. Sun, L. Zhang, S. Jahanshahi, J. Yang, Experimental and simulative study on phase transformation in Bayer red mud soda-lime roasting system and recovery of Al, Na and Fe, *Miner. Eng.* 39 (2012) 213–218. doi:10.1016/j.mineng.2012.05.021.
- [8] S. Rai, M.T. Nimje, M.J. Chaddha, S. Modak, K.R. Rao, A. Agnihotri, Recovery of iron from bauxite residue using advanced separation techniques, *Miner. Eng.* 134 (2019) 222–231. doi:10.1016/j.mineng.2019.02.018.
- [9] Z. Liang, X. Peng, Z. Luan, W. Li, Y. Zhao, Reduction of phosphorus release from high phosphorus soil by red mud, *Environ. Earth Sci.* 65 (2012) 581–588. doi:10.1007/s12665-011-1105-x.
- [10] S. Smiciklas, S. Smiljanic, A. Peric-Grujic, Sljivic-Ivanovic, M. Mitric, D. Antonovic, Effect of acid treatment on red mud properties with implications on Ni (II) sorption and stability, *Chemical.* 242 (2014) 27–35. doi:10.1016/j.cej.2013.12.079.
- [11] E. Domingues, N. Assunção, D. V. Lopes, J.R. Frade, M.J. Quina, R.M. Quinta-ferreira, R.C. Martins, Catalytic Efficiency of Red Mud for the Degradation of Olive Mill Wastewater through Heterogeneous Fenton's Process, *Water.* 11 (2019) 1–13. doi:https://doi.org/10.3390/w11061183.
- [12] V.S. Yadav, M. Prasad, J. Khan, S.S. Amritphale, M. Singh, C.B. Raju, Sequestration of carbon dioxide (CO₂) using red mud, *J. Hazard. Mater.* 176 (2010) 1044–1050. doi:10.1016/j.jhazmat.2009.11.146.
- [13] A.R. Studart, U.T. Gonzenbach, E. Tervoort, L.J. Gauckler, Processing routes to macroporous ceramics: A review, *J. Am. Ceram. Soc.* 89 (2006) 1771–1789. doi:10.1111/j.1551-2916.2006.01044.x.
- [14] L. Biasetto, P. Colombo, M.D.M. Innocentini, S. Mullens, Gas permeability of microcellular ceramic foams, *Ind. Eng. Chem. Res.* 46 (2007) 3366–3372. doi:10.1021/ie061335d.
- [15] S. Barg, C. Soltmann, M. Andrade, D. Koch, G. Grathwohl, Cellular ceramics by direct foaming

- of emulsified ceramic powder suspensions, *J. Am. Ceram. Soc.* 91 (2008) 2823–2829. doi:10.1111/j.1551-2916.2008.02553.x.
- [16] S. Barg, E.G. de Moraes, D. Koch, G. Grathwohl, New cellular ceramics from high alkane phase emulsified suspensions (HAPES), *J. Eur. Ceram. Soc.* 29 (2009) 2439–2446. doi:10.1016/j.jeurceramsoc.2009.02.003.
- [17] Z. He, Z. Lyu, Q. Gu, L. Zhang, J. Wang, Ceramic-based membranes for water and wastewater treatment, *Colloids Surfaces A*. 578 (2019) 123513. doi:10.1016/j.colsurfa.2019.05.074.
- [18] A. Ejraei, M.A. Aroon, A. Ziarati Saravani, Wastewater treatment using a hybrid system combining adsorption, photocatalytic degradation and membrane filtration processes, *J. Water Process Eng.* 28 (2019) 45–53. doi:10.1016/j.jwpe.2019.01.003.
- [19] W. Li, Z. Huang, Y. Wu, X. Zhao, S. Liu, Honeycomb carbon foams with tunable pore structures prepared from liquefied larch sawdust by self-foaming, *Ind. Crops Prod.* 64 (2015) 215–223. doi:10.1016/j.indcrop.2014.09.043.
- [20] E. Gregorová, Z. Zivcová, W. Pabst, Starch as a pore-forming and body-forming agent in ceramic technology, *Starch/Staerke*. 61 (2009) 495–502. doi:10.1002/star.200900138.
- [21] M.F. Sanches, N. Vitorino, C. Freitas, J.C.C. Abrantes, J.R. Frade, J.B. Rodrigues Neto, D. Hotza, Cellular ceramics by gelatin gelcasting of emulsified suspensions with sunflower oil, *J. Eur. Ceram. Soc.* 35 (2015) 2577–2585. doi:10.1016/j.jeurceramsoc.2015.03.008.
- [22] N. Vitorino, C.C.J. Abrantes, J.R. Frade, Cellular ceramics processed by paraffin emulsified suspensions with collagen consolidation, *Mater. Lett.* 98 (2013) 120–123. doi:10.1016/j.matlet.2013.02.020.
- [23] M.F. Sanches, N. Vitorino, J.C.C. Abrantes, J.R. Frade, J.B.R. Neto, D. Hotza, Effects of processing parameters on cellular ceramics obtained by paraffin emulsified suspensions, *Ceram. Int.* 40 (2014) 9045–9053. doi:10.1016/j.ceramint.2014.01.117.
- [24] Y. Ivanova, J. Monteiro, L. Teixeira, N. Vitorino, A. Kovalevsky, J. Frade, Designed porous microstructures for electrochemical reduction of bulk hematite ceramics, *Mater. Des.* 122 (2017) 307–314. doi:10.1016/j.matdes.2017.03.031.
- [25] D. V. Lopes, A. V. Kovalevsky, M.J. Quina, J.R. Frade, Processing of highly-porous cellular iron oxide-based ceramics by emulsification of ceramic suspensions, *Ceram. Int.* 44 (2018) 20354–20360. doi:10.1016/j.ceramint.2018.08.024.
- [26] G. Taguchi, S. Chowdhury, Y. Wu, *Quality Engineering: The Taguchi Method*, in: *Taguchi's Qual. Eng. Handb.*, John Wiley & Sons, Inc., Hoboken, NJ, USA, 2004: pp. 56–123.

doi:10.1002/9780470258354.

- [27] J.C.C. Abrantes, Estereologia software, (2001).
- [28] N. Vitorino, J.C.C. Abrantes, J.R. Frade, Cellular PCM / graphite composites with improved thermal and electrical response, *Mater. Lett.* 92 (2013) 100–103. doi:10.1016/j.matlet.2012.10.025.
- [29] S.W. Hughes, Archimedes revisited: a faster, better, cheaper method of accurately measuring the volume of small objects, *Phys. Educ.* 40 (2005) 468–474. doi:10.1088/0031-9120/40/5/008.
- [30] E.A. Moreira, J.R. Coury, The influence of structural parameters on the permeability of ceramic foams, *Brazilian J. Chem. Eng.* 21 (2004) 23–33. doi:10.1590/S0104-66322004000100004.
- [31] D. V. Lopes, Y.A. Ivanova, A. V. Kovalevsky, A.R. Sarabando, J.R. Frade, M.J. Quina, Electrochemical reduction of hematite-based ceramics in alkaline medium: Challenges in electrode design, *Electrochim. Acta.* 327 (2019) 135060. doi:10.1016/j.electacta.2019.135060.
- [32] E. Lalli, N.M.D. Vitorino, J.G. Crespo, C. Boi, J.R. Frade, A. V Kovalevsky, Flexible design of cellular Al₂TiO₅ and Al₂TiO₅-Al₂O₃ composite monoliths by reactive firing, *Mater. Des.* 131 (2017) 92–101. doi:http://dx.doi.org/10.1016/j.matdes.2017.06.010.
- [33] H.N. Holmes, W.C. Child, Gelatin as an emulsifying agent, *J. Am. Chem. Soc.* 42 (1920) 2049–2056. doi:https://doi.org/10.1021/ja01455a011.
- [34] L.F. Tice, Gelatin as a stabilizing colloid for oil in water emulsion systems, *J. Am. Pharm. Assoc.* 24 (1935) 1062–1069. doi:10.1080/01621459.1952.10483441.
- [35] J. Surh, E.A. Decker, D.J. McClements, Properties and stability of oil-in-water emulsions stabilized by fish gelatin, *Food Hydrocoll.* 20 (2006) 596–606. doi:10.1016/j.foodhyd.2005.06.002.
- [36] J.M.R. Mercury, A.A. Cabral, A.E.M. Paiva, R.S. Angélica, R.F. Neves, T. Scheller, Thermal behavior and evolution of the mineral phases of Brazilian red mud, *J. Therm. Anal. Calorim.* 104 (2011) 635–643. doi:10.1007/s10973-010-1039-7.
- [37] P. Wang, D.Y. Liu, Physical and Chemical Properties of Sintering Red Mud and Bayer Red Mud and the Implications for Beneficial Utilization, *Materials (Basel).* 5 (2012) 1800–1810. doi:10.3390/ma5101800.
- [38] C.-S. Wu, D.-Y. Liu, Mineral phase and physical properties of red mud calcined at different temperatures, *J. Nanomater.* 2012 (2012) 1–6. doi:10.1155/2012/628592.
- [39] V.M. Sglavo, R. Campostrini, S. Maurina, G. Carturan, M. Monagheddu, G. Budroni, G. Cocco, Bauxite “red mud” in the ceramic industry. Part 1: Thermal behaviour, *J. Eur. Ceram. Soc.* 20

- (2000) 235–244. doi:10.1016/S0955-2219(99)00088-6.
- [40] D.R. Lide, *CRC Handbook of Chemistry and Physics*, 87th Edition, Taylor&Francis, New York, 2007. doi:10.1080/08893110902764125.
- [41] F. La Mantia, J. Vetter, P. Novák, Impedance spectroscopy on porous materials: A general model and application to graphite electrodes of lithium-ion batteries, *Electrochim. Acta.* 53 (2008) 4109–4121. doi:10.1016/j.electacta.2007.12.060.
- [42] J.T.S. Irvine, D.C. Sinclair, A.R. West, *Electroceramics: Characterization by Impedance Spectroscopy*, *Adv. Mater.* 2 (1990) 132–138. doi:https://doi.org/10.1002/adma.19900020304.
- [43] E. Barsoukov, J. Macdonald, *Impedance Spectroscopy Theory, Experiment, and Applications*, Second Edition, John Wiley & Sons, Inc., Hoboken, New Jersey, 2005.
- [44] J.C.C. Abrantes, J.A. Labrincha, J.R. Frade, Alternative representation of impedance spectra of ceramics, *Mater. Res. Bull.* 35 (2000) 727–740. doi:10.1016/S0025-5408(00)00269-5.
- [45] Y. Liu, R. Naidu, H. Ming, Surface electrochemical properties of red mud (bauxite residue): Zeta potential and surface charge density, *J. Colloid Interface Sci.* 394 (2013) 451–457. doi:10.1016/j.jcis.2012.11.052.
- [46] M. Kosmulski, Compilation of PZC and IEP of sparingly soluble metal oxides and hydroxides from literature, *Adv. Colloid Interface Sci.* 152 (2009) 14–25. doi:10.1016/j.cis.2009.08.003.
- [47] C.B. Carter, M.G. Norton, *Ceramic Materials: Science and Engineering*, Springer Science+Business Media, LLC, New York, USA, 2007.
- [48] J. Coreño, O. Coreño, Evaluation of calcium titanate as apatite growth promoter, *J. Biomed. Mater. Res. - Part A.* 75 (2005) 478–484. doi:10.1002/jbm.a.30447.
- [49] Y. Zheng, Y. Cui, W. Wang, Activation mechanism of lead ions in perovskite flotation with octyl hydroxamic acid collector, *Minerals.* 8 (2018) 1–14. doi:10.3390/min8080341.
- [50] R. Tamayo, R. Espinoza-González, F. Gracia, U.P. Rodrigues-Filho, M. Flores, E. Sacari, As(III) removal from aqueous solution by calcium titanate nanoparticles prepared by the sol gel method, *Nanomaterials.* 9 (2019) 1–16. doi:10.3390/nano9050733.
- [51] H.H. Huang, The Eh-pH diagram and its advances, *Metals (Basel).* 6 (2016) 1–30. doi:10.3390/met6010023.
- [52] Z. Ajmal, A. Muhmood, M. Usman, S. Kizito, J. Lu, R. Dong, S. Wu, Phosphate removal from aqueous solution using iron oxides: adsorption, desorption and regeneration characteristics, *J. Colloid Interface Sci.* 528 (2018) 145–155.
- [53] V.M. Tangde, S.S. Prajapati, B.B. Mandal, N.P. Kulkarni, Study of Kinetics and

Thermodynamics of Removal of Phosphate from Aqueous Solution using Activated Red Mud, *Int. J. Environ. Res.* 11 (2017) 39–47. doi:10.1007/s41742-017-0004-8.

- [54] A.F. Santos, A.L. Arim, D. V. Lopes, L.M. Gando-Ferreira, M.J. Quina, Recovery of phosphate from aqueous solutions using calcined eggshell as an eco-friendly adsorbent, *J. Environ. Manage.* 238 (2019) 451–459. doi:10.1016/j.jenvman.2019.03.015.
- [55] N.M.D. Vitorino, A. V. Kovalevsky, J.C.C. Abrantes, J.R. Frade, Hydrothermal synthesis of boehmite in cellular alumina monoliths for catalytic and separation applications, *J. Eur. Ceram. Soc.* 35 (2015) 3119–3125. doi:10.1016/j.jeurceramsoc.2015.04.040.
- [56] N.M.D. Vitorino, A. V. Kovalevsky, M.C.C. Azevedo, J.C.C. Abrantes, J.R. Frade, Self-functionalization of cellular alumina monoliths in hydrothermal conditions, *J. Eur. Ceram. Soc.* 36 (2016) 1053–1058. doi:10.1016/j.jeurceramsoc.2015.11.017.
- [57] Y. Deng, D. Wang, W. Xiao, X. Jin, X. Hu, G.Z. Chen, Electrochemistry at conductor/insulator/electrolyte three-phase interlines: A thin layer model, *J. Phys. Chem. B.* 109 (2005) 14043–14051. doi:10.1021/jp044604r.
- [58] W. Xiao, X. Jin, Y. Deng, D. Wang, G.Z. Chen, Three-phase interlines electrochemically driven into insulator compounds: A penetration model and its verification by electroreduction of solid AgCl, *Chem. - A Eur. J.* 13 (2007) 604–612. doi:10.1002/chem.200600172.
- [59] X. Zou, S. Gu, X. Lu, X. Xie, C. Lu, Z. Zhou, W. Ding, Electroreduction of Iron (III) Oxide Pellets to Iron in Alkaline Media : A Typical Shrinking-Core Reaction Process, *Metall. Mater. Trans. B.* 46B (2015) 1262–1274. doi:10.1007/s11663-015-0336-8.
- [60] A. Maihatchi, M.-N. Pons, Q. Ricoux, F. Goettmann, F. Lapique, Electrolytic iron production from alkaline suspensions of solid oxides: compared cases of hematite, iron ore and iron-rich Bayer process residues, *J. Electrochem. Sci. Eng.* 10 (2020) 95. doi:10.5599/jese.751.
- [61] M. Paradis, J. Duchesne, A. Lamontagne, D. Isabel, Using red mud bauxite for the neutralization of acid mine tailings: A column leaching test, *Can. Geotech. J.* 43 (2006) 1167–1179. doi:10.1139/T06-071.
- [62] G. Kaur, S.J. Couperthwaite, B.W. Hatton-Jones, G.J. Millar, Alternative neutralisation materials for acid mine drainage treatment, *J. Water Process Eng.* 22 (2018) 46–58. doi:10.1016/j.jwpe.2018.01.004.
- [63] M. Taneez, C. Hurel, A review on the potential uses of red mud as amendment for pollution control in environmental media, *Environ. Sci. Pollut. Res.* 26 (2019) 22106–22125. doi:10.1007/s11356-019-05576-2.

7. General conclusions and forthcoming work

The electrochemical reduction of hematite-based ceramics in alkaline medium was investigated as a possible greener alternative for iron production, where O_2 (g) and H_2 (g) are the only by-products generated. The literature review not only highlighted the relevance of the electroreduction and electrowinning technologies for future industrial applications in the steelmaking industry, but also showed certain uncertainties regarding the mechanisms of iron oxides reduction in alkaline medium, increasing the relevance of the proposed study. On the other hand, the recycling and valorisation of red mud waste have been gaining attention due to the high environmental impacts caused by its high production and alkalinity. Thus, the iron recovery and valorisation of red mud by the electrochemical reduction to Fe^0 arose as the main target of the present thesis.

Hematite-based compositions mixed with controlled fractions of alumina, $Fe_{2-x}Al_xO_3$, the two main components often present in industrial iron wastes, were processed by a suspension emulsification method. This composition design was selected to simulate the red mud waste composition. Moreover, other compositions rich in iron and magnesium, $Fe_{3-x}Mg_xO_4$, were also processed for mimicking general metallurgical iron wastes. Highly-porous ceramic cathodes of $Fe_{2-x}Al_xO_3$ with the controllable cellular structure were successfully developed with a maximum of 60% of open porosity. The microstructure of the cathodes was deliberately adjusted to promote electrolyte impregnation during the electrochemical bulk tests and to allow better control of the microstructural features. The electrochemical experiments (NaOH, 10 M at 90 °C) were performed by using a platinum wire as a counter electrode and a reference electrode of Hg|HgO|NaOH (1 M). $Fe_{1.8}Al_{0.2}O_3$ cathodes were used as the working electrode in the bulk electroreduction in alkaline solutions, clearly demonstrating the feasibility of the proposed approach for the reduction. The XRD/SEM/EDS studies confirmed the presence of Fe^0 after the reduction of $Fe_{1.8}Al_{0.2}O_3$. The samples fired at 1300 °C (37% of open porosity), possessing an appropriate mechanical strength, revealed a possibility for an effective and complete bulk reduction to Fe^0 . The general bulk reduction mechanism consisted in establishing an interface between the three-phase interlines (3PIs), current collector| $Fe_{2-x}Al_xO_3$ ceramics|electrolyte, where the following consecutive reduction occurs: $Fe_{2-x}Al_xO_3 \rightarrow Fe_3O_4 \rightarrow Fe(II) (aq.) \rightarrow Fe^0$.

Ceramic suspensions were tested for the electrochemical reduction of $Fe_{2-x}Al_xO_3$ ($x=0, 0.2, 0.6$) to Fe^0 . The processed ceramic pieces were crushed to powder ($< 15 \mu m$) and used for Fe^0 electrodeposition at Ni grids (working electrode). The current efficiencies of the electroreduction process showed to decrease with aluminium content, attaining 70%, 55% and 32% for Fe_2O_3 , $Fe_{1.8}Al_{0.2}O_3$ and $Fe_{1.4}Al_{0.6}O_3$ suspensions, respectively. Higher aluminium content resulted in trapping

of Al_2O_3 particles inside the Fe^0 deposits and partial blocking of the further electrodeposition. The general mechanism apparently includes the following sequence: $\text{Fe}_{2-x}\text{Al}_x\text{O}_3 \rightarrow \text{Fe}(\text{OH})_4^-(\text{aq.}) \rightarrow \text{Fe}(\text{OH})_3^-(\text{aq.}) \rightarrow \text{Fe}^0$.

In the last decades, red mud waste has been frequently accessed regarding its potential for the applications in (electro)catalysis and environmental remediation. In this scope, the processing of red mud by the ceramic suspension emulsification route was successfully designed using Taguchi planning. The processing parameters of the waste-based porous ceramics were optimized regarding red mud load, gelatine content and emulsion stirring time, based on their microstructural features. A maximum of 75% of open porosity (1100 °C, 45% of solid load, 2% gelatine content and 4 min of stirring) was attained. Tests on the phosphate adsorption from contaminated waters revealed a low adsorption capacity in the processed red mud. However, the combination of other chemical treatments may be used to improve the adsorption for further water treatments. By the direct electrochemical reduction of the red-mud-based ceramics in alkaline medium, Fe_3O_4 and Fe^0 were obtained indicating the viability of electrochemical methods for iron waste recovery, despite low current (-3 mA/cm^2) was achieved.

In addition to the hydrogen evolution reaction, which decreases the Faradaic efficiency of the iron electroreduction at high cathodic polarization, other factors such as the choice of the working electrode material and the presence of non-conductive components in the iron oxide-based matrix should be taken into consideration when targeting the iron-rich wastes valorisation. Significant limitations are also imposed by the complex chemical composition and inhomogeneous morphology of the red mud, along with the presence of insulating phases. The first obtained guidelines for the electrochemical reduction of the red mud suggest that additional pretreatment might be necessary to increase the fraction of the conductive phases, if focusing on reasonable electroreduction current and efficiency. At the same time, the proposed method seems to be reliable for iron-rich waste recycling and valorisation without the presence of major non-conductive impurities, such as for the metallurgical iron waste. This technology is as well suitable for the regeneration of corroded iron surfaces and the recycling of metal scraps.

The general objectives of the proposed thesis are accomplished. Despite the fact that the proposed technology is still far from an industrial scale, the results bring a new perspective on the iron valorisation from industrial wastes and the impacts of possible contaminations during the electrochemical process. For the first time, detailed comparative studies on the iron oxide reduction in bulk porous form and suspensions were performed. The present thesis is expected not only to contribute to the development of the circular economy, but also to the scientific knowledge on the electrochemical reduction methods as a carbon-lean technology for waste valorisation.

Forthcoming work

Other important parameters should be further explored for establishing a robust electrochemical technology for iron recovery in the near future. The following aspects may be taken into consideration for the forthcoming work:

- i. to study Fe plates as working electrodes instead of Ni due to the relevance of having an entire piece of Fe that can be further processed for steel production without having to remove Fe⁰ crystals from other materials;
- ii. to study the influence of using Ni as the counter electrode instead of expensive Pt;
- iii. to implement porous membranes similar to the ones frequently used in alkaline water electrolysis to benefit from the simultaneous separation of H₂ and O₂ gases;
- iv. to implement sensors for measuring the amount of H₂ and O₂ produced during the electrochemical reduction;
- v. to assess the capture and storage possibilities for generated hydrogen, as a source of intermittent renewable energy production, and consider its use as an energy source during the process;
- vi. to simulate the parameters related to the electrolyte flow, electrolyte/cathode interface, gas bubbles, and particle distribution in the electrochemical reactor.

The impact of the above factors must be analysed taking into account the Faradaic efficiencies. When considering the H₂ gas production for storage, the use of 10 M of NaOH electrolyte at 90 °C seems to be more interesting as experimental conditions, due to the higher production of the gas when compared with 18 M, for example. However, highly-concentrated electrolyte might be considered as well for further improvement of the current efficiencies. When considering waste valorisation, metallurgical waste and other less complex iron-rich waste, with lower levels of contamination may be studied as a potential iron feedstock.

The Fe⁰ or ZVI produced by the electroreduction method has been frequently used as a strong reducing agent of several pollutants in soils and for water treatments involving redox mechanisms. The proposed method implies certain flexibility for growing the Fe⁰ crystals of different shapes and dimensions. These can be further applied for a wide range of pollutants, such as dyes or pesticides, among many others, to end the proposed symbiotic cycle.

